Tectonic pattern and evolution of the Easter microplate, based on GLORIA and other geophysical data

Ruth I. Rusby

Tectonic Pattern and Evolution of the Easter Microplate, Based on GLORIA and other Geophysical Data

by

Ruth I. Rusby

A Thesis submitted in partial fulfilment of the
requirements for the degree of
Doctor of Philosophy

Department of Geological Sciences

University of Durham
Epiphany 1992

ABSTRACT

Tectonic Pattern and Evolution of the Easter Microplate, Based on GLORIA and other Geophysical Data

Ruth I. Rusby, University of Durham 1992

The GLORIA and other geophysical data obtained during this study have enabled the entire present-day tectonic pattern of the Easter Microplate to be determined. The complex nature of all of the plate boundaries has been revealed, and there is evidence of rapid plate boundary evolution. Earthquake focal mechanisms together with GLORIA data have provided the first unequivocal evidence that thrust faulting is taking place along the northern boundary of the microplate. On the Nazca plate to the north of the Easter Microplate, the GLORIA images have disclosed a series of prominent east-west trending ridges which earthquake focal mechanisms and plate tectonics of the region imply are the first known case of intraplate thrusting in young oceanic lithosphere. Slightly younger Nazca plate lithosphere to the north is overthrust over marginally older lithosphere to the south, in order to accommodate the tectonic shortening predicted in the region.

Interpretation of magnetic anomaly data and the complex structural information offered by the GLORIA images have permitted a detailed history of the microplate to be determined. Three-plate Nazca-Pacific, Nazca-Easter and Pacific-Easter Euler poles have been calculated and used to rotate the Easter Microplate and surrounding major plates back in time since the East Rift of the microplate first started to propagate northwards at around 5.25 Ma. The microplate has evolved in two stages. The first is from 5.25 Ma to around 2.5 Ma, and involved continuous northward propagation of the East Rift, while the West Rift became segmented along new transform faults as it adjusted to keep the overall Nazca-Pacific velocities constant. The transpressive northern boundary migrated with the East Rift tip, while the transtensional southern boundary remained more or less still. At sometime after 2.5 Ma, the East Rift ceased northward propagation and the Southwest Rift began to open up along the transtensional Pacific-Easter transform. A convergent northern boundary formed involving southward overthrusting of the Nazca plate to the north over the microplate. No more Nazca plate lithosphere from the north of the microplate was transferred to the microplate interior, and the Pito Deep region was caused to open up by pervasively rifting apart pre-existing Nazca plate lithosphere. This study predicts that the Easter Microplate will be transferred onto the Pacific plate within the next 2-5 myr, when the Southwest Rift has propagated through to the southern EPR, and the shear couple on the microplate has ceased.

ACKNOWLEDGEMENTS

I would like to thank the following individuals and institutions for their support during this research project:

My supervisors, Prof. Roger Searle and Dr. Lindsay Parson, for their enthusiastic encouragement and guidance throughout the last three years. Thanks for enabling me to work with such a fantastic data set and for allowing me to participate in so many cruises. Thanks also for thorough criticisms of earlier drafts of this thesis.

Prof. Graham Westbrook, who supervised me during the first year of my Ph.D. and allowed me to participate in the GLORIA survey of the Chile Triple Junction area (cruise Charles Darwin 36), which ended with a passage through the Magellan straits and a visit to the penguins near Punta Arenas.

Vesna Marchig, of Bundesanstalt fur Geowissenschaften und Rohstoffe, Hannover, for inviting me to participate in the first leg of the Geometep 5 program (cruise Sonne 62) to study ore formation along the EPR and the Easter Microplate, from which this study has greatly benefitted. Also for providing me with colour copies of all the Seabeam maps obtained from the Easter Microplate region during Geometep 4 and 5. Thanks also to Helgard Rask and Gerhild Holler at BGR for all their help and the fun we had both at sea and in Hannover.

Dick Hey, Dave Naar and Jean Francheteau for copies of the SeaMARC II and Seabeam data sets discussed in this thesis.

Joe Engeln, Dick Hey, Dave Naar, Marty Kleinrock and numerous others for their help in the form of thought-provoking and stimulating ideas and criticisms at various times and places both at sea and on land during the last three years.

Roger Larson and all his other co-chief scientists for allowing me to participate in the GLORIA survey of the Juan Fernandez microplate cruise (Maurice Ewing EW9104), when I should have been writing up this thesis.

All the people at I.O.S.D.L. who have helped me throughout the last three years. Especial thanks go to Gwyneth for her endless patience as I first attempted to write Fortran programs, and all the rest of the Local Support Group who have helped me at

various times. Thanks to Tim LeBas for greatly assisting in the processing of the GLORIA mosaic. Thanks also to Mike Conquer for photography.

All those who have supported this project at Durham, particularly Dave Stevenson for computer support, and Gerry and Alan for photography. Thanks to all the postgrads and other hangers-on for all the completely wild times we've had during the last two years. Thanks especially to Gary for putting up with me all this time.

The late Master of RRS Charles Darwin, Captain Sam Mayl, and the rest of the company and technicians of the Charles Darwin for making the Easter Microplate cruise (Charles Darwin 35) possible, the data from which forms the basis for this thesis.

Funding for this research (CASE studentship) was provided by the Natural Environment Research Council. Additional funding was provided by NATO to allow international collaboration with J.F. Engeln and others.

Finally, thanks go to my parents, Stuart and Vigdis, for supporting me both financially and morally during the exceedingly long years of my education. I'm sure they're as glad as I am that its all finally coming to an end. Thanks to both of them for encouraging my interest in science. I dedicate this thesis to them.

DECLARATION

I declare that this thesis, which I submit for the degree of Doctor of Philosophy at the University of Durham, is my own work and is not substantially the same as any which has previously been submitted for a degree at this or another university.

January 1992

CONTENTS

CHAPTER 1
THE EAST CENTRAL PACIFIC OCEAN AND THE EASTER MICROPLATE

1.1 Introduction

The Easter Microplate is about 400 km across and is situated on the East Pacific Rise at around 25°S, in an anomalously shallow region of extremely fast spreading rates, of the order of 160 mm/yr (e.g Naar & Hey, 1989). To the east of the microplate the Easter-Sala y Gomez island seamount chain extends towards the South American coast, and to the west lies the Tuamoto Hotspot Chain (e.g. the islands of Ducie, Henderson and Pitcairn, Fig. 1.1). The general morphology of the Easter Microplate is illustrated by the colour bathymetric map in Fig. 1.2. The Easter Microplate lies between the Pacific and Nazca plates, where two actively spreading limbs of the East Pacific Rise (EPR) have propagated past each other and are known as the East and West Rifts.

Microplates are known to play a key role in facilitating major reorganisations of accretionary plate boundaries. They undergo rapid and complex evolutions involving large and fast rotations which lead to changes in the patterns of global tectonics. Different models have been developed for microplate behaviour. If microplates are merely the mechanism by which major changes in orientation of fast-spreading mid-ocean ridges occur, then it is essential that a full understanding is gained of all the processes involved in the formation, growth and eventual death of a contemporary microplate. Though much attention has been focussed on the Easter Microplate in recent years (e.g Engeln & Stein, 1984; Hey et al., 1985; Naar & Hey, 1986; 1989; Francheteau et al., 1988), prior to this study, much of the present tectonic pattern and behaviour of the microplate was still poorly understood, and little was known about the overall evolution of the microplate. This thesis documents the present tectonic pattern and history of the Easter Microplate, based principally on GLORIA data together with bathymetric and magnetic data.

In Chapter 1, an outline is given of the present-day tectonics and geology of the East Central Pacific Ocean. A description is given of the history of the East Pacific Rise since 24 Ma, and the role that microplates play in facilitating plate boundary reorganisations. Previous work on the Easter Microplate and other microplates within the Pacific basin is discussed.

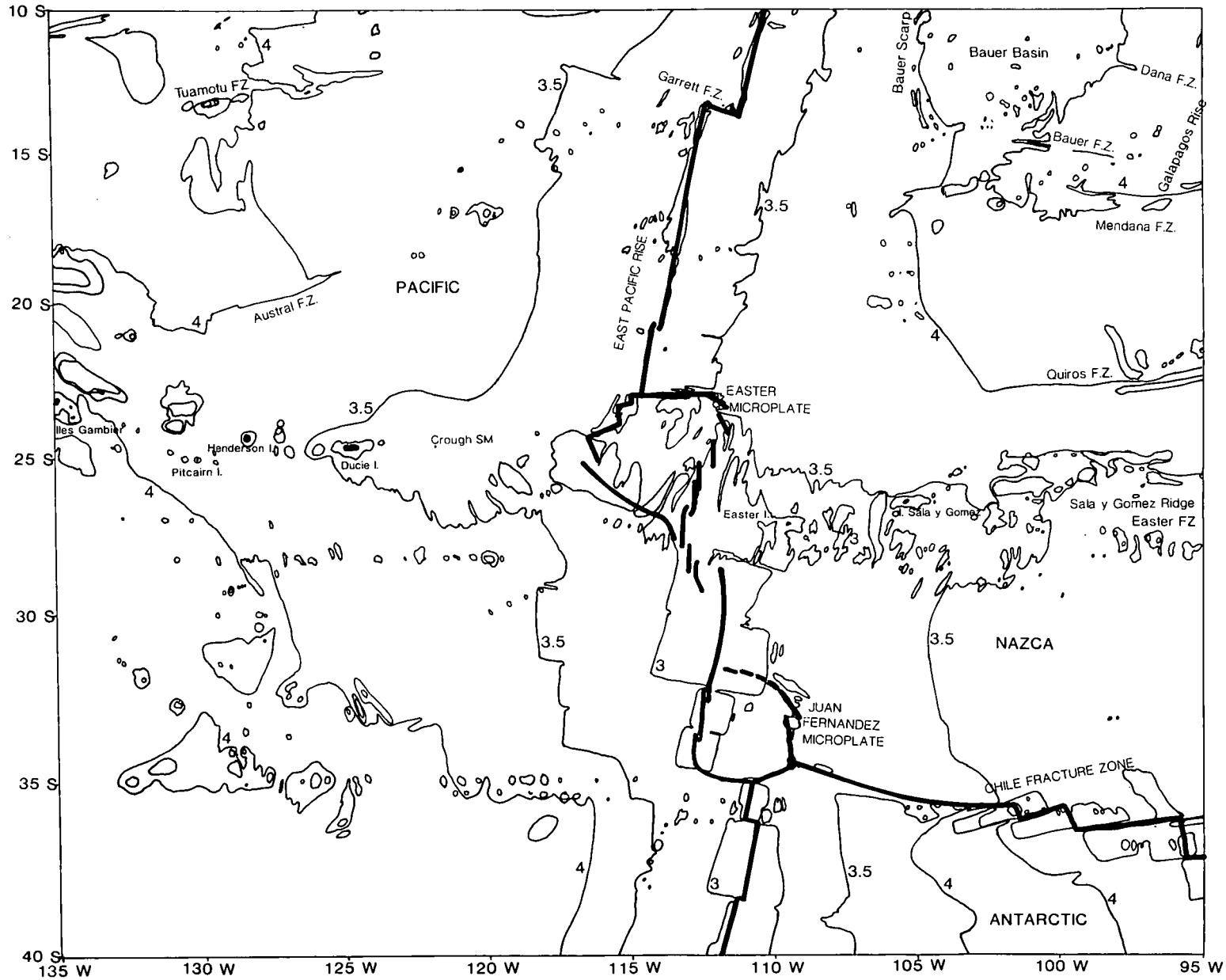

Figure 1.1 Location Map of the Easter Microplate, southeast Pacific. Heavy lines are plate boundaries. Bathymetric contours are from GEBCO chart 5.11 (Mammerickx et al., 1980) and are labelled in km.

Figure 1.2 Hand-contoured colour bathymetric map of the Easter Microplate using all the bathymetric data available from the World Data Center, Boulder, Colorado, and including the Sea MARC II bathymetric data (after Naar & Hey, 1991). Plate boundaries are shown by thin black lines, while dashed lines mark pseudofaults. Contour interval as shown in the key.

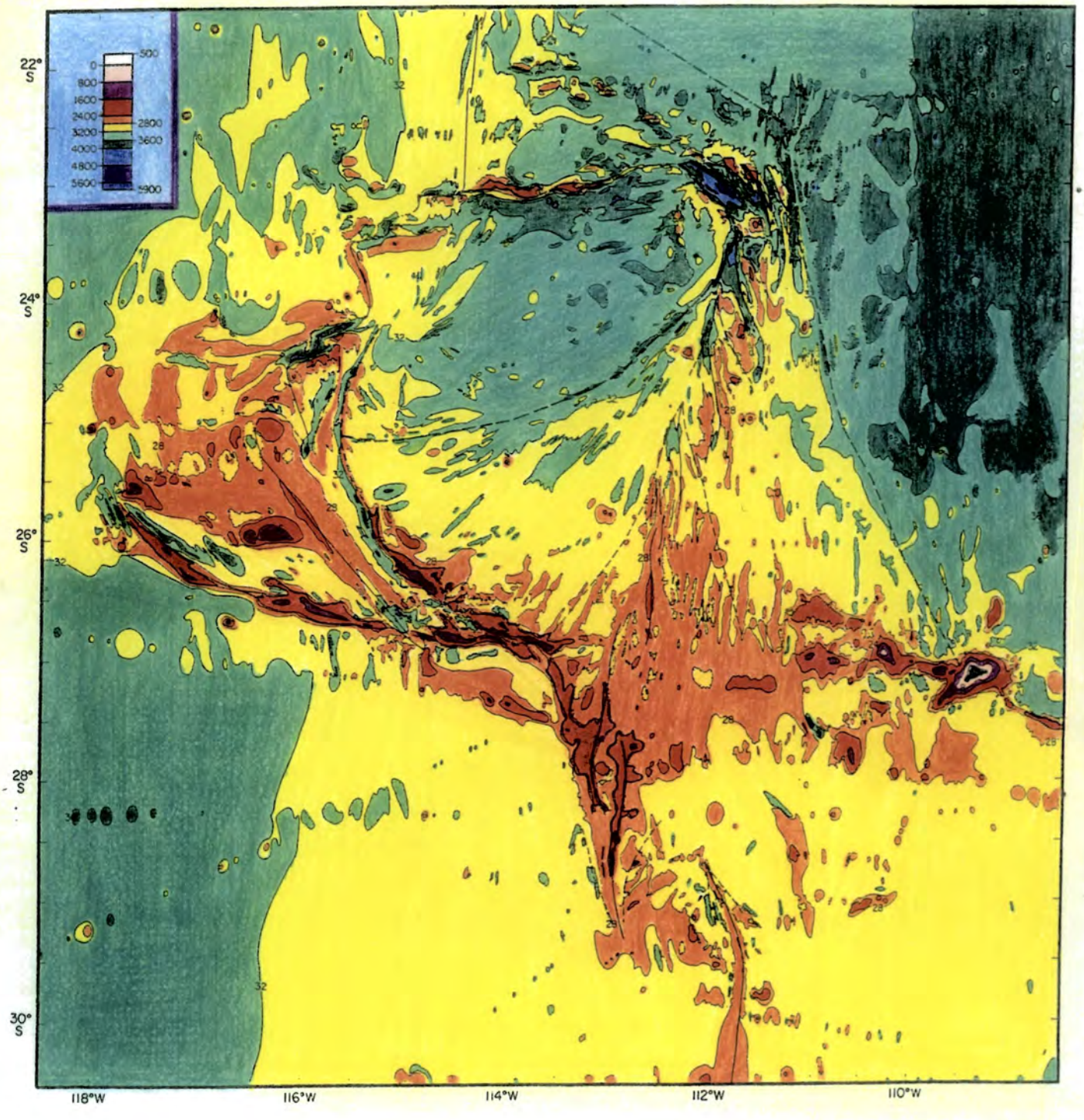
500
0
800
1600
2400
3200
4000
4800
5600
2800
3600
5900
22° S
24° S
26° S
28° S
30° S
118°W
116°W
114°W
112°W
110°W

Chapter 2 is mainly concerned with the regional scale geology within the region of the Easter Microplate and introduces the area for later, more detailed studies. The geology is illustrated with a combined data base of bathymetry, gravity and magnetics data from many cruises, and the acquisition and processing of this data is described.

In Chapter 3, a description is given of the GLORIA system and the acquisition of GLORIA data. The processes that are involved in enhancing the GLORIA data for improved appearance and ease of interpretation are discussed and the methods of interpreting the GLORIA images are introduced. In addition, the acquisition and interpretation of Seabeam data is described.

In the first main part of Chapter 4, the morphology and tectonic pattern of the Easter Microplate is discussed in detail, based on GLORIA and Seabeam data. Much of this description will shortly be published (Rusby, 1992). In the second part of this chapter, geological data from around the Easter Microplate are examined in the light of their tectonic setting and proximity to the Easter hotspot.

In Chapter 5, magnetic anomaly profiles are modelled along the East Pacific Rise and the East, West and Southwest Rifts of the Easter Microplate. Spreading rate data, together with transform fault and seismic slip vector azimuths are inverted using the Minster and Jordan (1978) algorithm to obtain three-plate closure and best fit Euler vectors for Nazca, Pacific and Easter plate motions. Earthquake seismicity and focal mechanisms are then examined in the light of known and predicted plate motions.

In Chapter 6, the three-plate Euler poles calculated in Chapter 5 are used to reconstruct the history of the Easter Microplate, from the present day back to the time of its initiation at around 5.25 Ma. Three digital data sets, namely digitised magnetic isochrons, digitised lineaments interpreted from the GLORIA data and the digitally processed GLORIA data itself are rotated around the Euler poles as if the plates were rigid.

In Chapter 7, a series of prominent east-west trending ridges imaged by GLORIA on the Nazca plate to the north of the Easter Microplate are examined in detail, together with bathymetry, seismicity and spreading rates from the region. The earthquake focal mechanisms and predicted plate motions suggest that these prominent ridges are thrust faults that involve southward overthrusting of slightly younger Nazca crust from the north over that to the south. This is the first known case of intraplate thrust faulting within young oceanic lithosphere, and the ideas presented in this chapter have been submitted to Geology (Rusby & Searle, submitted 1991).

A discussion of the principal findings of this thesis is given in Chapter 8, and in Chapter 9, the main conclusions are listed.

1.2 Studies of other microplates

In recent years there has been a growing awareness of the occurrence of microplates, and of their role in the evolution and reorganisation of major plate boundaries. Three microplates presently exist along the fast-spreading East Pacific Rise (EPR), namely the Galapagos, Easter and Juan Fernandez microplates (e.g. Lonsdale, 1989; Searle et al., 1989; Francheteau et al, 1987) (see Fig. 1.3). These are all relatively young, with estimated ages of 1 Ma, 4 Ma and possibly 6 Ma, respectively. The Orozco Transform on the EPR has recently been referred to as a "picoplate" (e.g. Hey et al., 1989), implying that it may be forming an incipient microplate, as the southern EPR axis in the east propagates northwards to overlap with the northern EPR axis in the west. Where the EPR approaches the Gulf of California, the Rivera microplate is thought to exist (Mammerickx & Carmichael, 1989). In the southwest Pacific, the Caroline plate is proposed to exist within the Caroline Sea area (Weissel and Anderson, 1978), based on marine seismic and geophysical data. This microplate occurs within a region dominated by plate subduction and thrusting, and the lithosphere is thought to have formed during the Oligocene. A contemporary example of a continental microplate may be in the Afar region at the Nubia-Somalia-Arabia triple junction (Acton et al., 1991), where with propagation of the Gulf of Aden spreading centre into eastern Afar within the last 2Ma+, continental rifting has resulted in block rotations of the "microplate" interior.

Several "palaeoplates", or abandoned microplates, have also been recognised, such as the Bauer palaeoplate in the southeast Pacific (Mammerickx et al., 1980), which was formed as the Bauer Scarp and the Galapagos Rise (Fig. 1.4) were active at the same time, between 8.2 Ma and 6.5 Ma, during a reorganisation of the EPR. The Mathematician palaeoplate (Fig. 1.3) (Mammerickx et al., 1988) has been identified south of the Rivera microplate by its distinctive morphology and well developed magnetic anomalies, and was active for about 7 myr, during an episode of spreading centre reorganisation, becoming extinct at around 3.15 Ma. The evolution of the Mathematician palaeoplate has been likened to that of the Easter Microplate, involving the northward propagation of a fast Eastern rift replacing a slowing western rift, and enabling a large scale ridge-jump to take place. In the western central Pacific, the Magellan palaeoplate (Fig. 1.3) was revealed by a pair of opposite-sensed, fanned magnetic lineation patterns defining the boundaries (Tamaki & Larson, 1988). Magnetic anomaly data suggest this palaeoplate evolved by propagation of the Phoenix-Farallon ridge through the Pacific plate at around 138 Ma, and

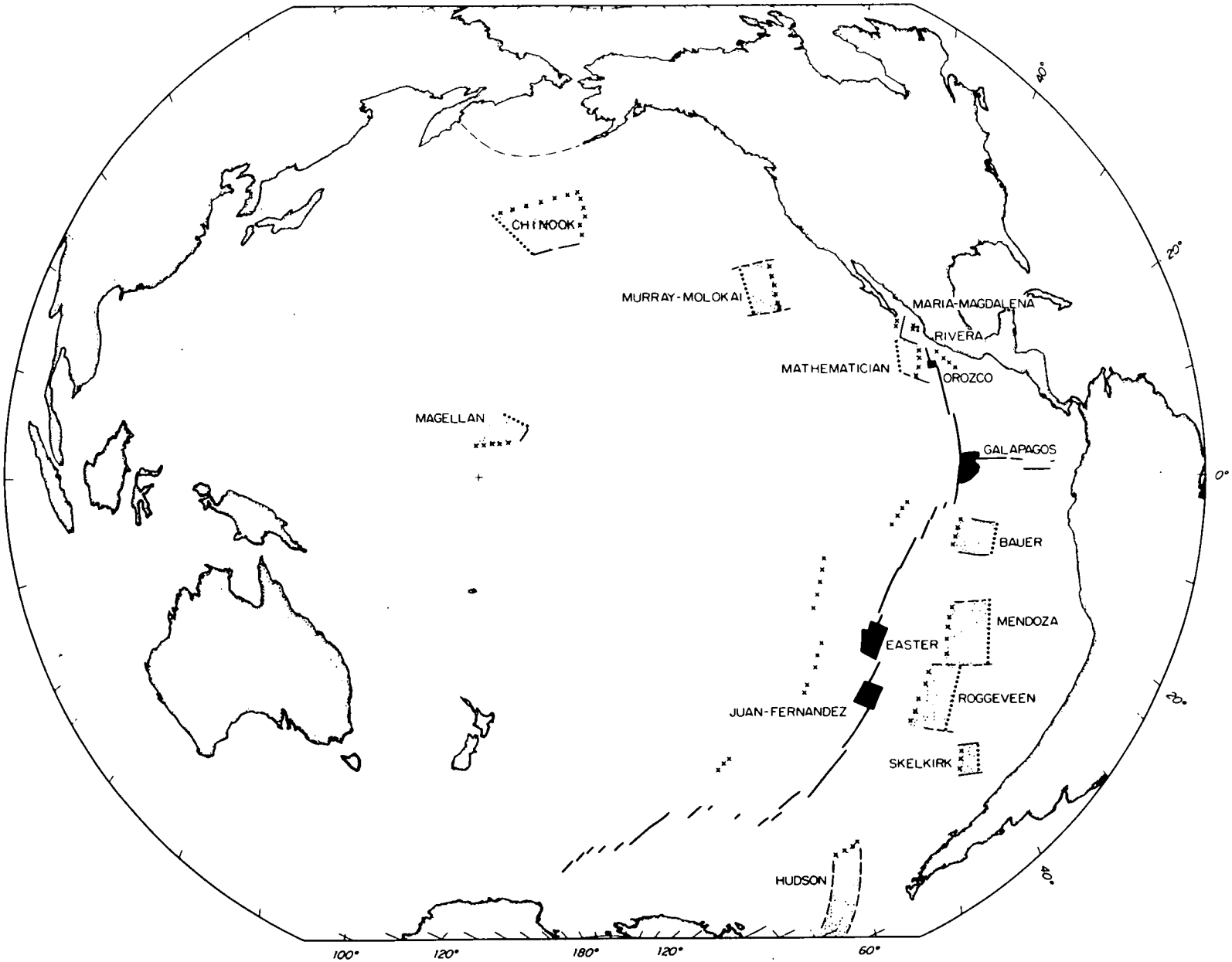

Figure 1.3 Map showing the location of active microplates (black) and abandoned palaeo-microplates (open boxes) within the Pacific basin. Dotted lines are abandoned spreading ridges, crosses are pseudofaults (from Mammerickx et al., 1988).

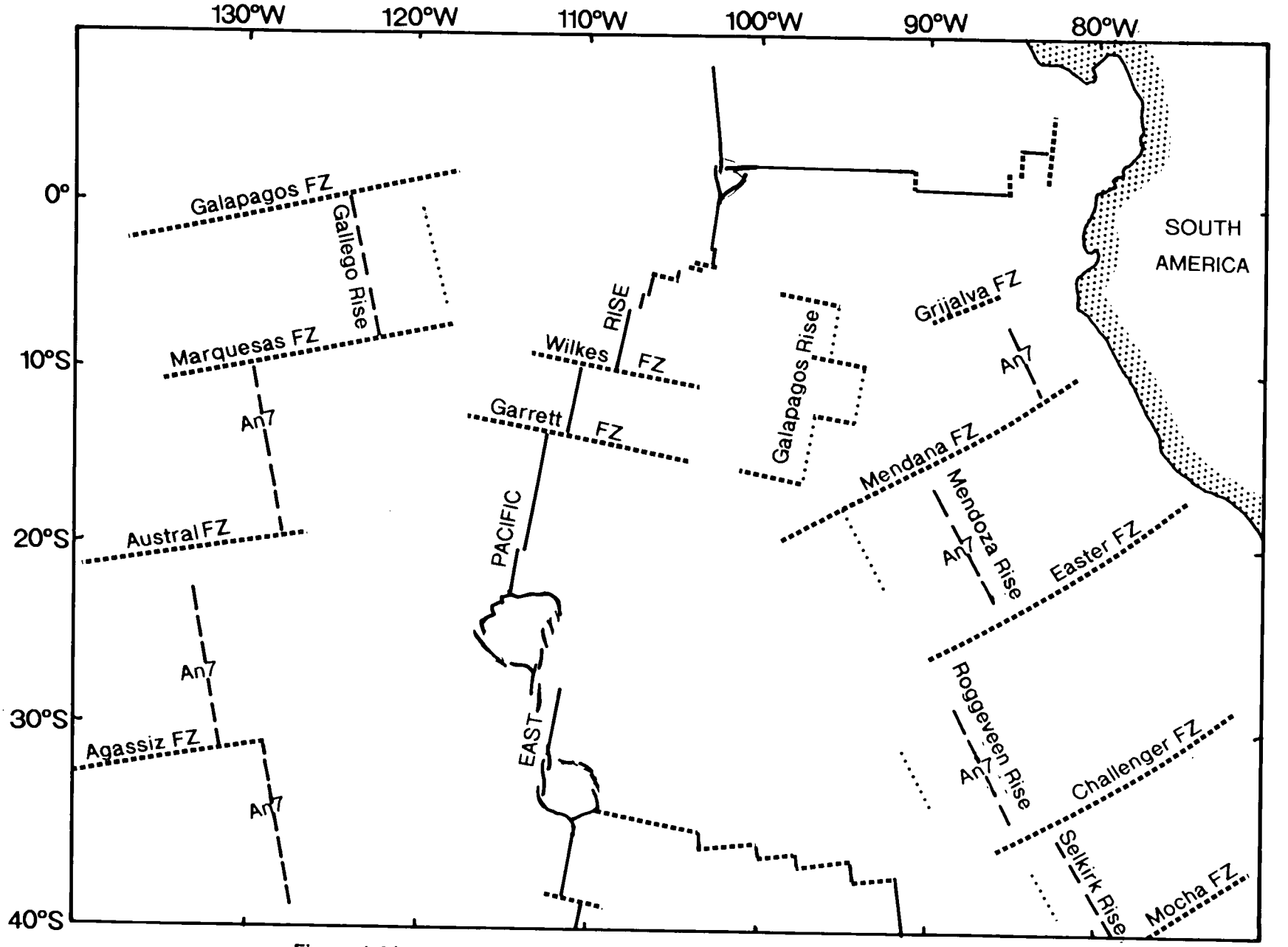

Figure 1.4 Location map of past and present spreading centres and fracture zones within the southeast Pacific, with magnetic anomaly 7 shown for reference. (From Mammerickx et al., 1980).

lasted for about 9 Ma. At 131.5 Ma (anomaly M10n) a reorganisation of the Pacific, Farallon and Phoenix plates took place, marking the end of the active history of the Magellan palaeoplate, and coinciding with the breakup of Gondwanaland. The largest palaeoplate yet observed is the Chinook plate in the northwest Pacific (Mammerickx and Sharman, 1988), which supposedly involved a 2000 km triple junction "jump" at 80 Ma (Fig. 1.3).

It is becoming increasingly apparent that ridge propagation and the formation of microplates play an essential part in the evolution and reorganisation of major plate boundaries. However, despite our growing understanding of present day microplates, and abandoned palaeoplates, the precise cause of the formation of these complex systems is still poorly understood. The Juan Fernandez and Galapagos microplates have formed at presumed unstable triple junctions, as did the Magellan and Chinook palaeoplates. The Easter and Juan Fernandez microplates, and the Bauer palaeoplate were formed in areas of very fast spreading rates (>140 mm/yr), and the formation of the Easter Microplate may have been influenced by the Easter hotspot (e.g. Anderson et al., 1974). The Rivera microplate is experiencing oblique subduction, and hence strong slab pull, as is the Caroline plate, whereas the Orozco "picoplate" has not evolved near a triple junction, hotspot or subduction zone.

1.3 The Evolution of the Pacific-Nazca Spreading System since 24 Ma

The origin and history of the Pacific-Nazca plate boundary has been the subject of study for over two decades. In 1972, Herron suggested that the East Pacific Rise (EPR) formed only during the last 9 myr, while prior to this a northwest trending rise had existed. Mammerickx et al. (1980) then produced a more comprehensive understanding of the region and drew attention to a fossil Pacific-Farallon spreading axis (the Farallon plate was the precursor to the Nazca and Cocos plates prior to 24 Ma), the Gallego Rise on the Pacific plate, and three fossil spreading axes found on the Nazca plate, namely the Mendoza, Roggeveen and Selkirk Rises (see Fig. 1.4) whose ages of extinction have been determined as 18.5 Ma, 20 Ma and 23 Ma respectively. An almost simultaneous extinction of all Pacific-Farallon segments was thought to have occurred between 20-18.5 Ma, as the northern plate boundary jumped eastwards, abandoning the Gallego Rise (Fig. 1.4) on the Pacific plate, and the southern plate boundary jumped westward, leaving the Mendoza, Roggeveen and Selkirk Rises on what is now the Nazca plate. Mammerickx *et al.* (1980) found that the Galapagos Rise (Fig. 1.4) was originally a spreading centre of an early phase of the Pacific-Nazca system between 18.5 Ma - 6.5 Ma, when 100 km of lithosphere was accreted at the spreading centre. At 8.2 Ma, while the Galapagos Rise was still active, spreading began on the Bauer Scarp (part of the present day EPR) (Fig.

1.1), thus forming the Bauer plate between the two ridges. Further reorganisation then took place at 6.5 Ma.

The most recent and extensive understanding of the region has been determined by Lonsdale (1989) who examined along-axis Seabeam data from the present day Pacific-Nazca plate boundary, and discussed the historical development of the ridge segmentation in the light of plate boundary reorganisations of the Pacific-Farallon (prior to 24 Ma) and Pacific-Nazca (post 24 Ma) spreading centres. His limited data set allowed him the following hypothesis on the origin of the Pacific-Nazca plate boundary, which is summarised in Figs. 1.5a-h and based on his interpretation of present structural patterns. His hypothesis relies on analogy with the modern Easter Microplate and the older Mathematician palaeoplate (Mammerickx et al., 1988) on the northern EPR.

At 24 Ma the Pacific-Nazca plate boundary originated as a consequence of the splitting of the Farallon plate along a fracture zone which intersected its eastern (subducting) margin (Figs. 1.5a,b). The motion of the southern fragment of the plate (now the Nazca plate) changed from northeast- to eastward as the spreading axis on its westem margin rotated 20-30°clockwise, as recorded by the abyssal hills and magnetic lineations (Hey, 1977; Lonsdale & Klitgord, 1978). This rotation of the spreading axes may have occurred by differential asymmetric spreading or by subtle rift propagation (Caress et al., 1988). Near 20°S, Handschumacher (1976) noted that the east flank magnetic anomalies had rotated from NW to N between chron 7 (25.5 - 26Ma) and chron 6B (22.6 - 23 Ma). The identification of anomaly 6B on the first crust produced at the Cocos-Nazca spreading centre, north of the Grijalva Scarp (Fig. 1.5a), is further evidence for the 24 Ma initiation time of the Nazca plate.

Nearly all of the present Pacific-Nazca spreading centres south of the Quebrada-Gofar transforms (3-5°S) are younger than 24 Ma, and originated by ridge propagation during the formation of short-lived East Pacific Rise microplates (such as the Mendoza and Bauer microplates). As the eastern boundaries of the microplates failed and eventually stopped spreading, the western boundaries became the new Pacific-Nazca spreading axes and the microplates were incorporated into the Nazca plate (Figs. 1.5d-g).

Fossil transforms, such as the Dana Fracture Zone (Fig. 1.1) segmented these ridges prior to their extinction, as they rotated some 30° from their original strike to accommodate new microplate-plate motions. The Galapagos and Mendoza Rises followed a similar evolution to the Mathematician Rise, with rotation and transform fault segmentation of the ridges before their death, due to adjustments of relative motion of the plate fragments. The interior of the Mendoza and Bauer microplates consists of lithosphere originally formed on the west flank of the Pacific-Nazca spreading centre, which has rotated in an

Figure 1.5 Development of the northern part of the Pacific-Nazca plate boundary, according to Lonsdale, 1989. (a) A Pacific-Farallon plate boundary with northwest striking spreading axes. (b) After fission of the Farallon plate along Grijalva fracture zone (at 24 Ma, i.e anomaly 6c), EPR spreading axes rotate clockwise to become orthogonal to the new Pacific-Nazca motion and by 20 Ma a spreading segment had propagated across the right-stepping transform(s) of the Austral/Easter system. (c)-(d) Northward ridge propagation extends >1000 km to the South Marquesas fracture zone, isolating the Mendoza microplate on the east flank of the rise. Crust transferred from the west to the east of the rise is rotated anticlockwise, and the former Pacific-Nazca axes at the eastern margin of the microplate rotate clockwise as it fails. Meanwhile the northernmost Pacific-Nazca spreading axis is extending northward because of rapid migration of a Nazca-Cocos-Pacific RRR triple junction. (e) The Mendoza microplate has become abandoned and attached to the Nazca plate. Between 15-10 Ma the southern Pacific-Nazca segment propagates northward to the North Marquesas fracture zone. (f) Continued propagation creates part of Bauer Scarp rift and Bauer microplate, which spins anticlockwise. The Galapagos Rise slows and rotates, and Bauer transform fault dies. (g) Western margin of Bauer microplate has propagated north to Gofar fracture zone. Galapagos Rise stops spreading and the Garrett, Wilkes (W) and Yaquina (Y) transforms develop. (h) Since 5 Ma, the northermost 100 km of the Pacific-Nazca boundary has become the western margin of a 1 myr old Galapagos microplate, the Discovery and Quebrada transforms developed, and the Easter Microplate formed.

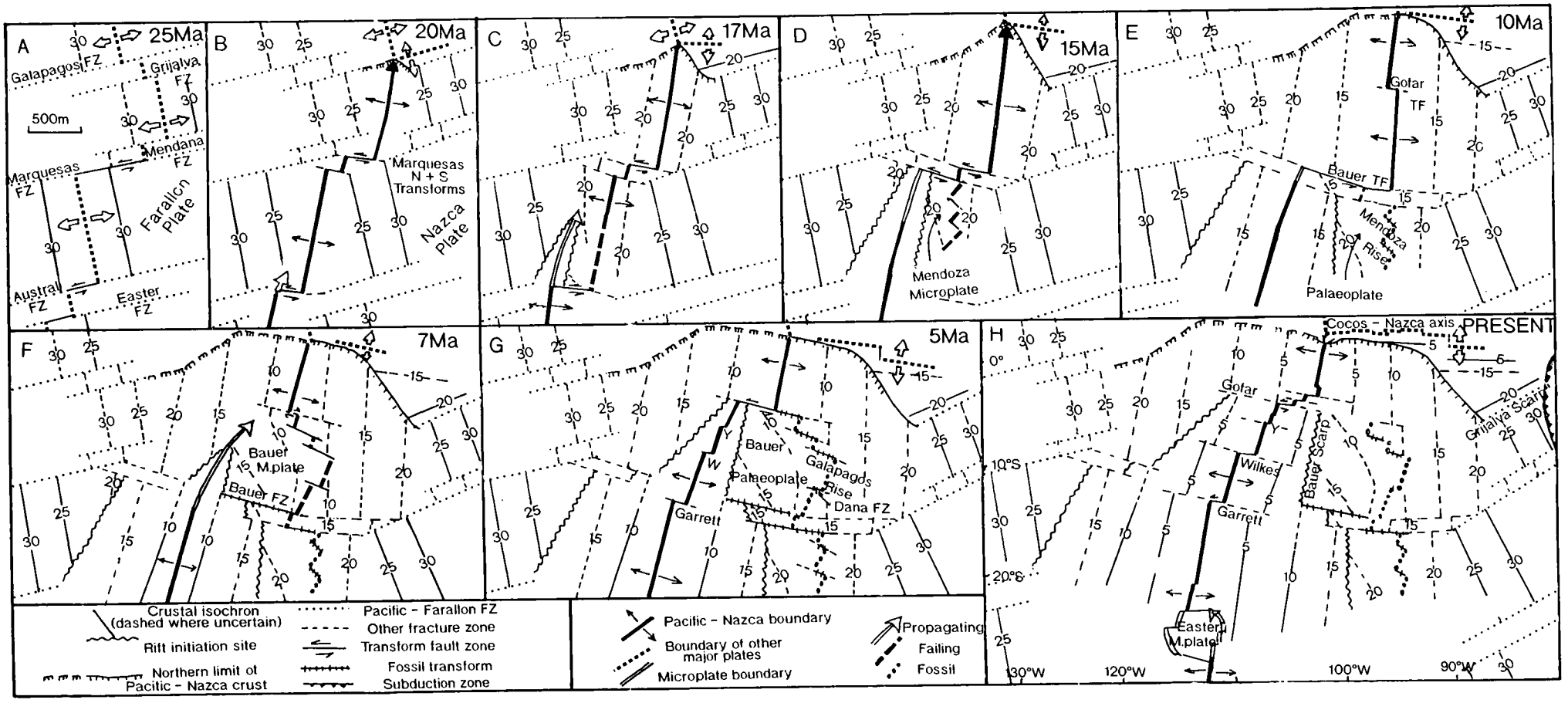
A
25Ma
Galapagos FZ
Grijalva FZ
500m
Mendana FZ
Marquesas FZ
Farallon Plate
Austral FZ
Easter FZ
B
20Ma
Marquesas N + S Transforms
Nazca Plate
C
17Ma
D
15Ma
Mendoza Microplate
E
10Ma
Gofar TF
Bauer TF
Mendoza Rise
Palaeoplate
F
7Ma
Bauer M.plate
Bauer FZ
G
5Ma
Bauer
Palaeoplate
Galapagos Rise
Dana FZ
Garrett
H
Cocos - Nazca axis
PRESENT
Gofar
Wilkes
Garrett
Bauer Scarp
Grijalva Scarp
Easter M.plate
10°S
20°S
130°W
120°W
100°W
90°W
Crustal isochron (dashed where uncertain)
Rift initiation site
Northern limit of Pacific - Nazca crust
Pacific - Farallon FZ
Other fracture zone
Transform fault zone
Fossil transform
Subduction zone
Pacific - Nazca boundary
Boundary of other major plates
Microplate boundary
Propagating
Failing
Fossil

anticlockwise sense to a NW trend, i.e. the opposite of the present day Easter Microplate interior.

The new EPR crest between the Easter Microplate and the Gofar transform grew by spurts of northward propagation between 20-5 Ma, and in so doing, eliminated the long offsets inherited from the Pacific-Farallon boundary, e.g the right-steps of the Austral/Easter and Marquesas/Mendana transforms. The propagating ridges grow in a direction orthogonal to the Pacific-microplate motion, and when they then once again become part of the Pacific-Nazca boundary, a staircase of new right-lateral offset transforms develops as they reorientate themselves to the new direction. In this way the Yaquina, Garrett and Wilkes transforms were created as the Galapagos Rise ceased spreading at 6.5 Ma.

A small (5°-10°) post-5 Ma clockwise rotation of Pacific-Nazca spreading direction is inferred to have taken place to produce the en echelon fault strands and transtensional troughs within the Wilkes and Garrett fault systems (Lonsdale, 1988), but this is in the opposite sense to the 5-3.2 Ma anticlockwise rotation proposed by Pollitz (1986). A recent clockwise rotation would explain the left-stepping nontransform offsets along the northern and southern parts of the EPR, while the right-stepping offsets in the central EPR region can be explained by a post 6Ma clockwise rotation of the boundary as it evolved from a microplate boundary (Lonsdale, 1988).

Thus the evolution of EPR microplates appears to be closely involved with changes in spreading rate and direction of the main Pacific-Nazca plate boundary. The history of the spreading centre has had a major influence on the modern pattern of segmentation and the history of individual segments provides further insights on how and why these patterns change.

Okal and Cazenave (1985) used Seasat altimetry data to investigate plate tectonic evolution of the east-central Pacific. They studied an area northeast of Pitcairn Island (Fig. 1.1) which was involved in a Miocene ridge-jump and reorientation of the EPR. They mapped two fracture zones (FZ1 and FZ2) to the east of the Austral Fracture Zone (Fig. 1.1) which were found to strike 095°, i.e. intermediate in trend between the Pacific-Farallon Austral Fracture Zone (070°) and the present day Pacific-Nazca spreading direction (110°). They produced a model of the evolution of spreading during the last 40 Ma, in which the Austral Fracture Zone is deactivated, and its offset transferred to FZ1 by rift propagation, triggered by a northern Tuamotu hotspot, so that an intermediate stage of east-west spreading existed between the extinction of the Pacific-Farallon spreading centre and the formation of the present day Pacific-Nazca spreading centre. They also suggested that FZ2, 300 km south of FZ1, coincides with the eastward lineament of the

Oeno-Ducie chain (Fig. 1.1) and that this chain is the surface expression of a southern Tuamotu hotspot, deviated 15° in azimuth by the presence of a young and fresh fracture zone. The uncompensated, intraplate seamounts of Ducie and Crough are given possible ages of formation of 8 Ma and 4 Ma respectively, while the lithosphere on which they are formed is 14 Ma and 1 0 Ma. By extrapolation, Okal and Cazenave infer that the present location of the hotspot that formed the Oeno-Ducie chain now lies some 300 km south of the Southwest Rift of the Easter Microplate. They also suggested that FZ2 should be continuous with the Southwest Rift of the Easter Microplate itself.

During the RRS Charles Darwin's passage from Tahiti to the Easter Microplate (Cruise CD35, 1988) the opportunity was taken to obtain a GLORIA swath and other data relevant to the history of the region, in order to improve our knowledge of the distribution of fracture zones and volcanic chains between Tahiti and the Easter Microplate (Searle et al., 1989b). The passage track (Fig. 1.6) was planned so that the N/O Jean Charcot's Seabeam data (Francheteau et al., 1988) would lie within the GLORIA swath as much as possible, allowing the acquisition of two offset, parallel magnetic anomaly profiles. The principal findings from the results of this passage track (Searle et al., in prep) were as follows:

The first significant observation is that mid-plate volcanism is common even on old deep seafloor hundreds of kilometres from major hotspot lines of seamounts and islands. The second is that the Austral Fracture Zone is found at 21°20'S, 139°30'W and 21°45'S, 138°0'W, as observed by Okal & Cazenave (1985) on their Seasat data, and trending 070°-077°. It consists of five distinct fossil transform traces within a zone 90 km wide. The total relief of the fracture zone valley is 1500 m. Thirdly, to the west of 130°30'S, the tectonic fabric strikes NNW. However, east of 130°30'W until 124°W, the tectonic fabric, as imaged by GLORIA, becomes disordered, and a whole range of abyssal hill lineations are observed, varying from 300° to 021° in trend. From 124°W eastwards, the predominant trends are once again NNW, with a few local ENE trends. This confused fabric begins just after chron 6C (ca. 23 Ma) which is just after the supposed formation of the Pacific-Nazca spreading system. The fabric may have resulted from a series of ridge propagations and microplate formations as suggested by Lonsdale's (1989) work. It thus appears that Handschumacher's (1976) general observation that the magnetic anomalies were rotated between chron 7 and chron 6B is correct, except that he does not realise that the NNE abyssal hill direction never gets well established and that several further oscillations in spreading fabric direction occur.

The fourth major observation is that a series of six sharp-crested ridges, trending ENE, were found between 123°30'W and 118°30'W. They appear, on the GLORIA images, to

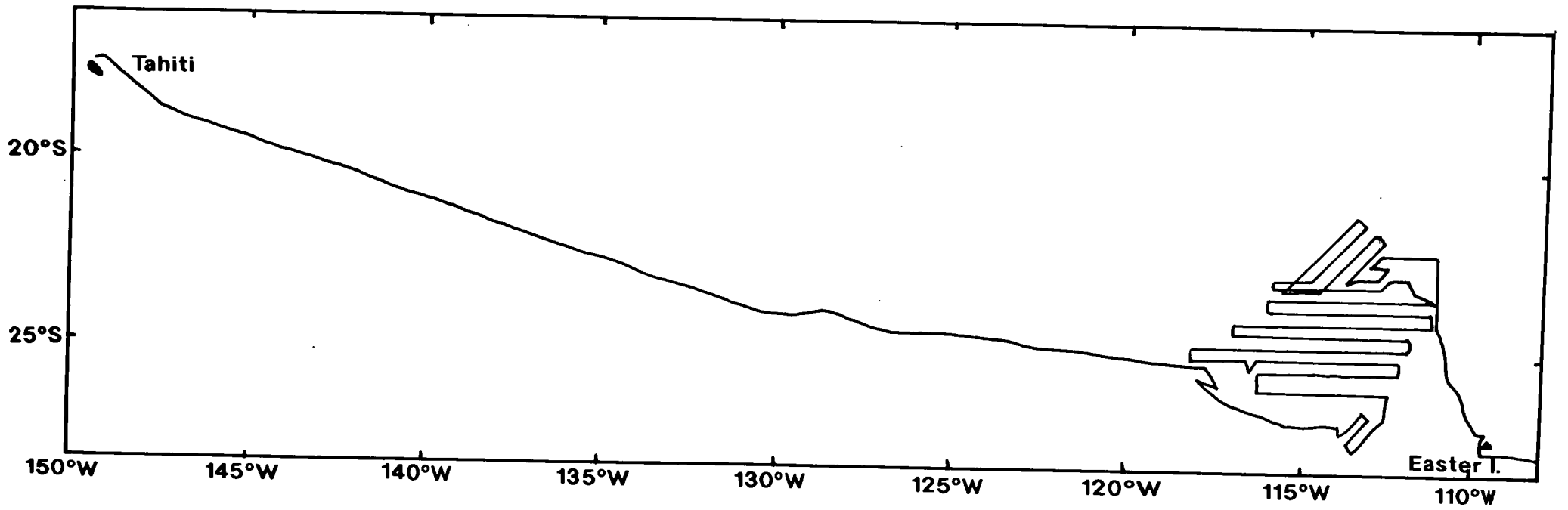

Figure 1.6 Track chart for Charles Darwin Cruise 35, October - November 1988. Tahiti to Easter Island is shown, where GLORIA coverage was continuous. (Not shown is passage leg from Easter Island to Valparaiso, along which no GLORIA data were collected.)

be built almost entirely of small volcanic cones. The ridges were between 60-120 km long, 500-2500 m high and 10-25 km wide, with numerous small (1-3 km diameter) volcanic cones associated with them, as well as fresh-looking lava flows. These ridges are roughly orthogonal to the main NNW tectonic trends of the region, but are not orthogonal to the local tectonic fabric, and hence are not considered to be fracture zones. The nature of their origin is unclear, but it has been suggested (Searle et al., in prep) that they may correspond to Winterer and Sandwell's (1987) "cross-grain" ridges seen elsewhere in the Pacific, and represent lines of weakness and magma leakage along a geoid high, that mirrors the Easter-Sala y Gomez "hot-line" of Bonatti et al. (1977).

No evidence was found to support Okal and Cazenave's (1985) suggestion that the fracture zone FZ2 extends from the Oeno-Ducie chain eastwards as far as the Easter Microplate, or is continuous with the Southwest Rift of the microplate. Possible remnant fracture zone lineaments were imaged by GLORIA along track, with trends of 054° and 082° (orthogonal to local spreading fabric), but the 095° trend of Okal and Cazenave's (1985) FZ2 was not found in its predicted position. However, Okal and Cazenave based their identification of FZ2 on its gravity signature, which is more like that of a fracture zone than a series of seamount. It is possible that it is the series of ENE-trending ridges that have given rise to this gravity signal.

1.4 Hotspots and Island-Seamount Chains in the East Central Pacific

Various models have been offered to explain the existence of the Tuamotu hotspot chain and the Easter-Sala y Gomez island-seamount chain (Fig. 1.7) and their relationship to the formation of the Easter Microplate. Morgan (1971; 1972) was the first to propose the existence of a hotspot fixed relative to the mantle at Easter Island, such that the linear trend of seamounts and islands to the east, with a systematic increase in volcanic age with distance from the hotspot, records the absolute motion of the Nazca plate relative to the hotspot. Morgan (1972) modelled the rotation of the Pacific plate backwards in time over four hotspots (near Cobb Seamount, Hawaii, MacDonald Seamount, and the Easter hotspot) and found a close agreement of predicted hotspot trends with the trends of the Gulf of Alaska seamount chains, the Hawaiian-Emperor chain, and the Tuamotu-Line chain. A closer agreement was achieved by allowing the hotspot to migrate a nominal 5 mm/yr.

Since Herron's discovery of two small crustal plates in the south Pacific (1972a), attempts have been made to link the formation of the northern (Easter) microplate with the presence of the Tuamotu hotspot chain and the Easter-Sala y Gomez island-seamount chain (Fig. 1.7) (Anderson, et al., 1974). They suggest that the presence of a mantle

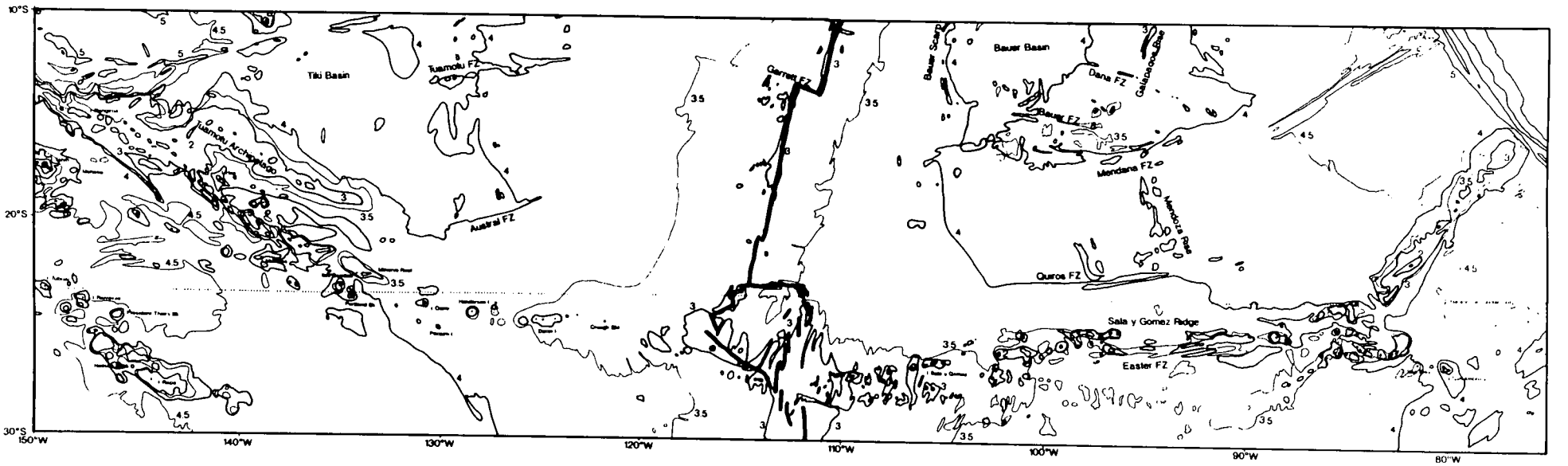

Figure 1.7 Location Map of Easter Microplate, showing its relation to East Pacific Rise, Tuamotu Hotspot Chain (Oeno-Henderson-Ducie) and Easter-Sala y Gomez island seamount chain. Bathymetric contours are from GEBCO chart 5.11 (Mammerickx et al., 1980) and are labelled in km.

plume beneath Easter Island might stress the overlying plate above it and cause it to break along more than one zone.

Clark and Dymond (1977) examined two hypotheses, that either the Sala y Gomez Ridge traces the motion of the Nazca lithosphere over a deep mantle plume near Easter Island (Morgan, 1972), or that volcanism has taken place within a leaky fracture zone transverse to the East Pacific Rise (Herron, 1972a). Herron (1972a) suggested that the Sala y Gomez Ridge is the result of shearing during a temporary break-up of the Nazca plate between 5-10 Ma. A mantle plume would imply that the ages of the shield volcanoes must increase with distance from the hotspot, and display a similarity of basalt composition and style of volcanism, whilst describing a small circle about the pole of absolute motion for the Nazca plate. A fracture zone, however, would trace the direction of Pacific-Nazca movement, and would display nearly contemporaneous volcanism and increased chemical variability.

Although Clark and Dymond (1977) only recovered one sub-aerial basalt sample from Sala y Gomez island, along with several sub-marine samples, all the samples were found to be alkaline (hawaiites and mugearites) and undersaturated in silica (i.e. nepheline normative) having fractionated from a parent liquid of alkaline olivine basalt composition. In contrast, most of the basalt lavas from Easter Island are transitional tholeiites that are almost exactly saturated in silica. The alkaline nature of the Sala y Gomez liquid indicates a lesser degree of partial melt generated at greater depths than the tholeiites, while the tholeiites derive from shallow melting and magma segregation at relatively low pressures. This suggests that while the transitional tholeiite basalts of Easter Island were formed on or near the EPR, the dredged alkaline rocks from Sala y Gomez either represent waning volcanism as the island was swept off the plume, or a flank eruption on the periphery of the plume. Clark and Dymond also suggest that if there was channelling of the plume material along a pre-existing fracture zone such as the Easter Fracture Zone, the alkaline character of the Sala y Gomez liquids could still be derived from magma segregation at the base of thicker lithosphere. The mantle plume hypothesis requires an age difference of 4.4 myr between Easter Island and Sala y Gomez, based on rotation of the Nazca plate relative to the mantle (Minster, et al., 1974), but the samples recovered from the two islands suggest that, if anything, Easter Island may be older than Sala y Gomez (the oldest rocks retrieved from Easter Island are 2.5 - 3 Ma and the oldest from Sala y Gomez are only 2 Ma). However, older rocks than these may exist below sea-level. Clark and Dymond (1977) suggest that even if the alkaline rocks dredged from Sala y Gomez are just a cap on tholeiitic volcanism beneath, it is unlikely that such an age difference exists.

Bonatti et al. (1977) collected igneous rock samples from Easter Island and from a number of seamounts along the Easter Seamount Chain. The petrochemistry of the extrusive rocks and the isotopic data obtained ($^{87}Sr/^{86}Sr$ and $^{206}Pb/^{204}Pb$ and $^{207}Pb/^{204}Pb$ ratios) all suggest that a hotspot or mantle plume is present beneath Easter Island. The samples indicate that the basalts from the seamounts have also been derived from a mantle plume source, with a somewhat shallower mantle depth of derivation suggested for the basalts from Easter Island. K/Ar age determinations were made for samples from Easter Island and also the dredge samples. The rhyolites from Easter Island were found to be <0.2 Ma, while the upper age given for the basalts is higher (<10 Ma), due to their low K content, although Baker et al. (1974) report a 3 Ma basalt from Poike (the assumed oldest volcano on Easter Island). A fresh mugearite sample from Sala y Gomez island gave an age of 1.7 Ma. Samples from three seamounts lying to the east of Sala y Gomez island give ages that are older than Sala y Gomez, but younger than the adjacent oceanic crust (the samples are strongly altered so these ages must be treated with caution). In order to explain recent (<2 Ma) intermittent mantle plume type activity along the Easter Seamount Chain, Bonatti et al. proposed an alternative to the leaky fracture zone model: Richter and Parsons (1975) have suggested that convective rolls may occur parallel to the direction of spreading during mantle convection, and Bonatti et al. suggest that it is these that produce "hotlines" such as the Easter Seamount Chain.

Pilger & Handschumacher (1981) developed a simple hotspot model for the evolution of the Easter Seamount Chain and the Nazca and Tuamotu Ridges (but kinematic problems were encountered when trying to fit this into a unified Pacific-Nazca-hotspot model). They outlined earlier ideas that aseismic ridges (such as the Nazca and Tuamotu) are formed by on-ridge hotspots and are smoother and more continuous features, underlain by thickened crust in near isostatic equilibrium with the adjacent seafloor (Kogan, 1979). In contrast, generally island-seamount chains (such as the Easter-Sala y Gomez chain) form just after the plate by a few or several million years and are more irregularly spaced and uncompensated. If the Easter-Sala y Gomez chain is entirely intraplate, then they suggest the hotspot must have been located east of the Pacific-Nazca spreading centre when it formed, since there is no "mirror image" immediately to the west of the EPR. However, the Oeno-Henderson-Ducie-Crough chain may be a more subdued "mirror image" of the Easter-Sala y Gomez chain.

Pilger & Handschumacher's simple hotspot model for the evolution of the area is as follows: From sometime before anomaly 19 time, until anomaly 11 time, the "Easter" hotspot was located beneath the Pacific-Farallon Ridge, and between the Marquesas-Mendana and Austral-Sala y Gomez fracture zones. Both plates had a weak northward

component of motion with respect to the hotspot. At about anomaly 11 time, the Austral-Sala y Gomez fracture zone (with right-lateral offset) passed over the hotspot, so that the hotspot was no longer in contact with the Pacific plate. The Tuamotu Ridge stopped growing, and a change in the morphology of the hotspot trace meant that the regular Nazca Ridge was replaced by an irregular set of seamounts to the southwest. Soon after anomaly 7 time, there was a major change in plate motion, the Pacific-Nazca spreading centre replaced the Pacific-Farallon spreading centre, and the Nazca plate started moving in a more easterly direction, while the hotspot formed the irregular trace of the Sala y Gomez seamount chain. Magnetic anomaly identifications between anomalies 7 and 3, however, require either asymmetric spreading or ridge jumps, as the EPR was found to asymmetrical with respect to anomaly 7 on the Pacific and Nazca plates.

Since anomaly 3 time the hotspot was inferred to lie on the East Rift of the Easter Microplate, and Easter Island was assumed to be 3 Ma old. The Tuamotu and Nazca Ridges appeared to correspond very well, and were reconstructed for magnetic anomalies 7 through to 13, and 16.

The main problem with this model was that the bend on the Tuamotu Ridge occurred at anomaly 25 time (i.e. 55 Ma, using La Breque et al. (1977) timescale), according to Herron's (1972a) identification. The corresponding change in Pacific plate motion recorded by the bend in the Hawaiian-Emperor Chain is given as 42-43 Ma (from dredge samples of Jarrard and Clague, 1977). Therefore, either Pilger and Handschumacher's model is wrong and the Easter Hotspot is located much further east of Easter Island, or one or both of the ages of the Tuamotu and Hawaiian-Emperor bends are wrong.

In 1983, expedition Pascua (Hey et al., 1985) sampled basalts at sites on the East Rift of the Easter Microplate. The first is at 26°26'S, where the ridge is shallowest (only 2080 m water depth) and channelling from the hotspot is thought to intersect the spreading axis (Hey at al., 1985). Nine other sites were also sampled from 25°S to 34°S. A very high $^{3}He/^{4}He$ anomaly as well as strong Sr and Nd anomalies were found at 26°30'S compared to elsewhere along the East Pacific Rise (Craig et al., 1984), which suggests the influence of a plume. Macdougall and Tanzer (1984) also found that the isotopic and chemical evidence (elevated $^{87}Sr/^{86}Sr$ and LIL element contents and low $^{230}Th/^{232}Th$ and $^{143}Nd/^{144}Nd$) suggested a recent or present day plume component, and comparison with Easter Island basalts suggested that the compositions were consistent with mixing between normal MORB (mid-ocean ridge basalts) and an Easter Island plume-like composition.

Schilling et al. (1985) also sampled basalts from around the Easter Microplate and found that those on the East Rift closest to Easter Island were most enriched in K_20 and

light rare earth elements, and were also much lower in CaO/Al_2O_3 than expected. Preliminary $(La/Sm)_n$ variations along the East Rift were found to peak at around 27°S where the ridge is shallowest and closest to Easter Island, and increased amounts of incompatible elements such as TiO_2 and P_2O_5 suggest the influence of a hotspot to the east of the Easter Microplate. Using an empirical relationship established for slow spreading Mid-Atlantic Ridge hotspots, based on anomalous ridge elevation and width of geochemical anomaly, Schilling and co-workers have suggested that the hotspot is 725 km from the East Rift of the Easter Microplate, under Sala y Gomez island. However, they also suggest that if the width of the geochemical anomaly is inversely related to the spreading rate, the hotspot may lie near or beneath Easter Island. Hanan and Schilling (1989) carried out Pb isotope analyses on the same basalt samples, and found a major anomaly at 27°S on the East Rift, where the ridge is shallowest and closest to Easter Island, and also a smaller anomaly at the same latitude on the West Rift. The radiogenic Pb content covaries with the $(La/Sm)_n$ ratios and Hanan and Schilling suggest a binary mixing process between two end-member sources, one a plume source enriched in large ion lithophile elements (LILE) and radiogenic Pb, and the other a normal MORB source, depleted in LILE and radiogenic Pb. Although Sala y Gomez has a very high $(La/Sm)_n$ ratio and may be close to the hotspot end member, this ratio may result from the smaller degrees of melting required for the hawaiites and mugearites of the island. Whether the hotspot is situated near Easter Island or Sala y Gomez, Schilling et al.'s (1985) migrating ridge-sink hotspot-source model provides a reasonable explanation for the region (Fig. 1.8) allowing channelled flow from the hotspot to the rift.

Seasat altimeter investigations of the east-central Pacific by Okal and Cazenave (1985) revealed several seamounts along the Oeno-Henderson-Ducie lineament (Fig. 1.7), and the isostatic compensation of these features suggests that they have formed off-axis from a plume or hotspot, though on relatively young crust. On the basis of age estimates for Crough Seamount of 4 ± 1 Ma for the seamount, and 10 Ma for the underlying crust, Okal and Cazenave locate the southern Tuamotu hotspot about 300 km south of the southwest boundary of the Easter Microplate. They also note that the azimuth of the seamount chain from Crough Seamount to Oeno differs by 15° from the absolute motion of the Pacific plate (as indicated by the nearby Pitcairn-Gambier-Duke of Gloucester chain) and suggest that the presence of a young fresh fracture zone (their FZ2) has caused the surficial expression of the hotspot to be "trapped" and the lineament of the chain deviated.

Bonatti's (1977) hotline model, in which upwelling limbs of mantle convective rolls lie along the seamount chains, would allow simultaneous volcanism to occur along the seamount chains, as would the "leaky" fracture zone model (Herron, 1972a; Clark &

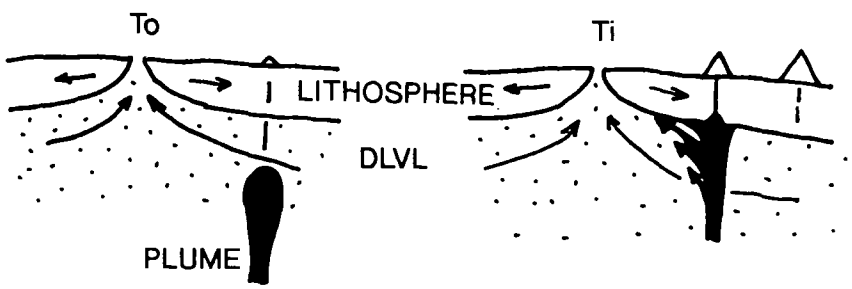

Figure 1.8 Schematic representation of a mantle flow plate motion model which may explain LILE spikes at the ridge axis. Material from a near-ridge plume would be deflected towards the ridge axis, smeared and dispersed as it penetrates the asthenosphere. (from Schilling et al., 1985).

Dymond, 1977). The latter model has been disputed (e.g. Hagen et al., 1990) because there is no obvious fracture zone trace or offset of magnetic anomalies to the west of Easter Island, although further to the east there is certainly evidence of this. Hagen et al. (1990) use their SeaMARC II survey of recent submarine volcanism near Easter Island to tentatively suggest that a hotspot may exist just to the west of Easter Island. Recent volcanism in the region (forming the Ahu Volcanic Field) could then be attributed to the motion of the Nazca Plate over the hotspot. Hagen et al. (1990) also conclude that the presence of a hotspot on the EPR axis 4.5 myr ago may have initiated the rift propagation that created the microplate. The association of a hotspot with Easter Island and the Easter-Sala y Gomez ridge, combined with extremely fast spreading rates in this region, relatively thin lithosphere, and an unusually warm and strongly convecting mantle (with a broad region of low velocity in the upper mantle as shown by surface wave propagation (Woodhouse and Dziewonski, 1984; Craig et al., 1984) may provide optimum conditions for non-rigid plate behaviour or plate boundary reorganisations to develop (Hey, et al., 1985). This would occur especially if the EPR segment nearest to the hotspot tended to jump back towards the hotspot, instead of migrating west with the rest of the EPR, in a way which has been proposed near Iceland (Burke et al., 1973) and Galapagos (Hey, et al., 1973).

1.5 The Easter Microplate

The existence of both the Easter and Juan Fernandez microplates was first deduced by Herron (1972) and Forsyth (1972) simultaneously from two rings of earthquake epicentres and from anomalous magnetic anomaly patterns. Anderson et al (1974) was the first to note that the existence of the Easter Microplate may be related to (i) its close proximity to Easter Island (a proposed hotspot) and (ii) the thin lithosphere and very high plate velocities. Handschumacher et al. (1981) studied magnetic and bathymetric data from the region, and suggested that the microplate was 3.2 Ma old, based on the magnetic anomalies observed on the East Rift. They recognised the fanning of magnetic anomalies about the East Rift, implying rapidly changing extension rates along it and consequent rotation of the microplate. They speculated that the East Rift is assuming a more dominant kinematic role relative to Nazca-Pacific plate divergence, and may be incorporated as a segment of the Pacific-Nazca spreading centre, whilst spreading on the West Rift would cease. They also suggested that there might be a generic relationship between the Easter Microplate and the Easter-Sala y Gomez island-seamount chain.

More recent work using earthquake focal mechanisms (Engeln & Stein, 1984) and Seabeam and SeaMARC II data (e.g. Francheteau et al., 1988; Zukin, 1990; Hey et al., 1985; Naar & Hey, 1986; Naar, 1990) has established much of the nature of the present

plate boundaries and tectonics of the region. Engeln & Stein (1984) presented the first tectonic model of the Easter Microplate and proposed that a rigid microplate had formed between the propagating East Rift and the dying West Rift as a result of rift propagation. Euler poles for Easter-Nazca and Pacific-Nazca motion were calculated which lie close to the Easter Microplate, which is compatible with the rapid changes in spreading rates and direction of motion along the plate boundaries. Engeln and Stein (1984) realised that as the new eastern spreading centre develops, the old western spreading centre must adjust to keep the total spreading rate and direction constant between the two large plates, and so since the propagating rift spreads orthogonally, the dying ridge not only slows, but also changes direction. The relative motion across the original sinistral offset transform or group of transforms (Handschumacher et al., 1981) must change, and evolve into a leaky transform, eventually forming a nearly orthogonally spreading ridge. The northern boundary is a site of compression, and if propagation is continuous, the boundary will continually migrate northwards and the very young age of the crust will prevent the formation of a subduction zone. Also, since the transforms on the West Rift must remain parallel to the direction of relative motion, they must reorient themselves anti-clockwise, cutting across previous trends, while the ridge segments also rotate.

The acquisition of further data from the region of the Easter Microplate (Hey et al., 1985; Francheteau et al., 1988; Marchig & Gundlach, 1987) led Engeln et al. (1988) to investigate further the consequences of a rigid microplate model versus a shear zone model (see Fig. 1.9a,b). If the microplate behaves entirely rigidly, the southern and northern boundaries require a complex evolution (Fig. 1.9a), whereby the southern transform evolves through a leaky transform stage, and convergence takes place across the northern boundary, which moves northward. With the shear zone model, the entire overlap region of the microplate deforms by evenly distributed simple shear parallel to the spreading direction and displacement is parallel to the original transform orientation (Fig. 1.9b). Thus only the rate of motion would change on the dying rift, not the rate and direction, and spreading would not be predicted on the southwest rift, nor convergence along the northern boundary. Engeln et al. also examined, by inversion of plate motion data, what would happen if a shear couple overlap zone is treated as a rigid plate. The rapid variation in spreading rates along the east and west rifts would favour Euler poles near their tips, while the uniform east-west spreading directions, and supposed transform motion would favour distant poles. The resulting poles would represent a compromise between these two extremes, found by locating the pole with the least squared errors. Thus an orderly sense of misfit would be found, by assuming that the plate is rigid when it is in fact non-rigid. Also, the best fit vectors derived separately for the three plate pairs would fail to close when combined, as the rigid plate assumption would be invalid.

Figure 1.9 (a) Schematic evolution of a rigid microplate between two major plates. Since the plate is rigid, no relative motion occurs between points within the microplate; relative motion only occurs at points on the boundaries. Note the rotation of the microplate, the reorientation of the two ridges, the formation of the northward converging boundary, and the conversion of the initial transform into a slow spreading ridge. The change of spreading rates along the overlapped spreading axes is accomplished by letting the microplate rotatae and having compressive deformation in the north. Spreading rates along the east and west rifts never reach the full major plate separation rate. Isochrons are only reoriented because of microplate rotation. For seafloor created at the growing (eastern) ridge, the boundaries separating pre-existing seafloor from that created during propagation are pseudofaults. At time T_4 the southern part of the west rift has stopped spreading, so that the southern boundary of the microplate has started to migrate northward, transferring seafloor from the microplate to the major plate to the west. After Engeln et al. (1988). (b) Evolution of a continuous zone of simple shear between two major plates. Here the entire overlap region deforms in simple shear parallel to the spreading direction as a response to the differential spreading along the growing and dying ridges. Isochrons within the overlap zone reorient by differential translation of seafloor. In contrast to the rigid case, both northern and southern boundaries remain transforms in the shear case. This shear geometry would predict neither the spreading observed along the southwestern ridge nor the contraction along the northern plate boundary. After time T3, spreading has slowed and then finally stopped along the west rift, allowing the east rift to take over as the major plate boundary, while the northern boundary becomes the transform between two major plates and the shear zone vanishes. After Engeln et al. (1988).

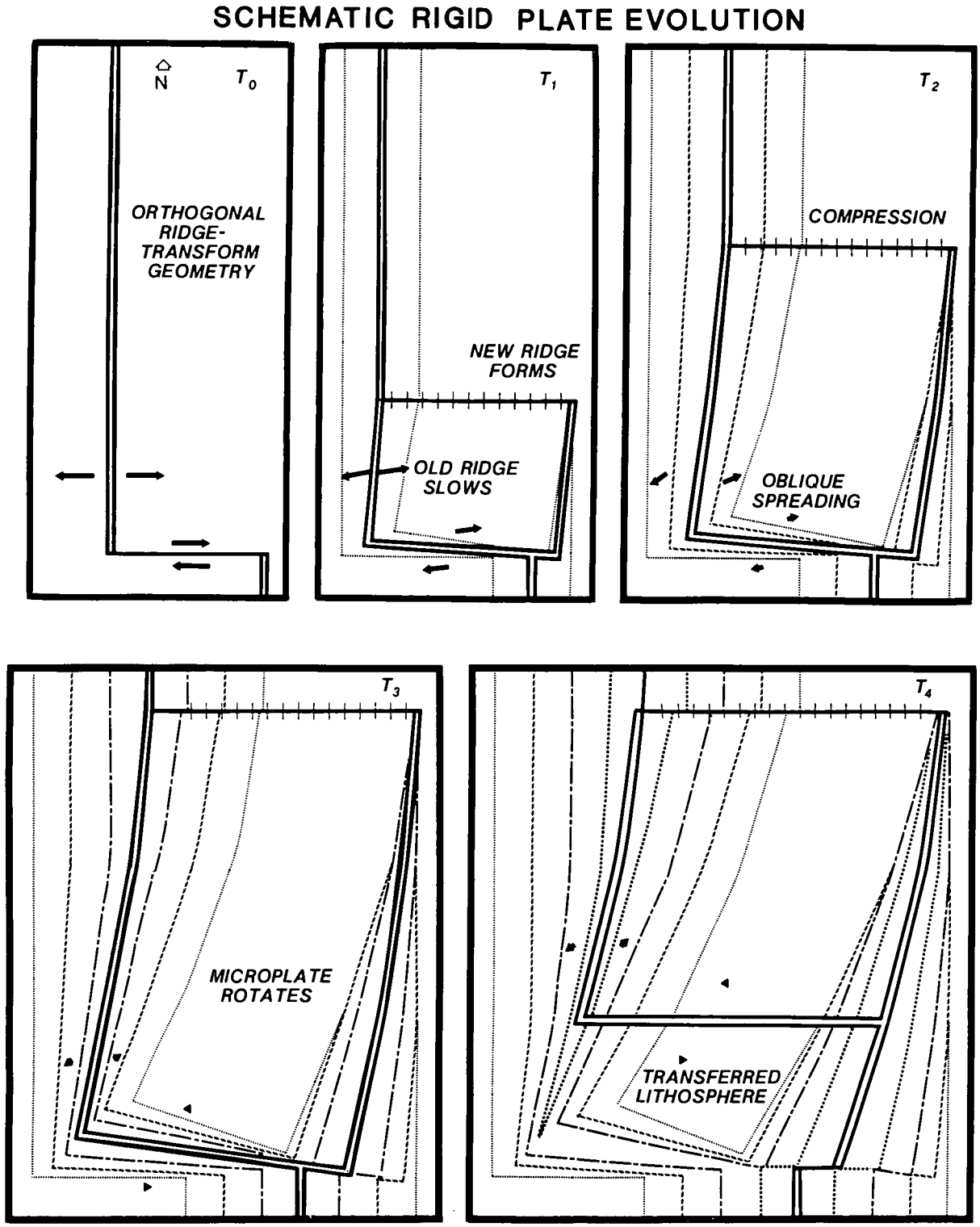
SCHEMATIC RIGID PLATE EVOLUTION
N
T_0
ORTHOGONAL RIDGE-TRANSFORM GEOMETRY
T_1
NEW RIDGE FORMS
OLD RIDGE SLOWS
T_2
COMPRESSION
OBLIQUE SPREADING
T_3
MICROPLATE ROTATES
T_4
TRANSFERRED LITHOSPHERE

a

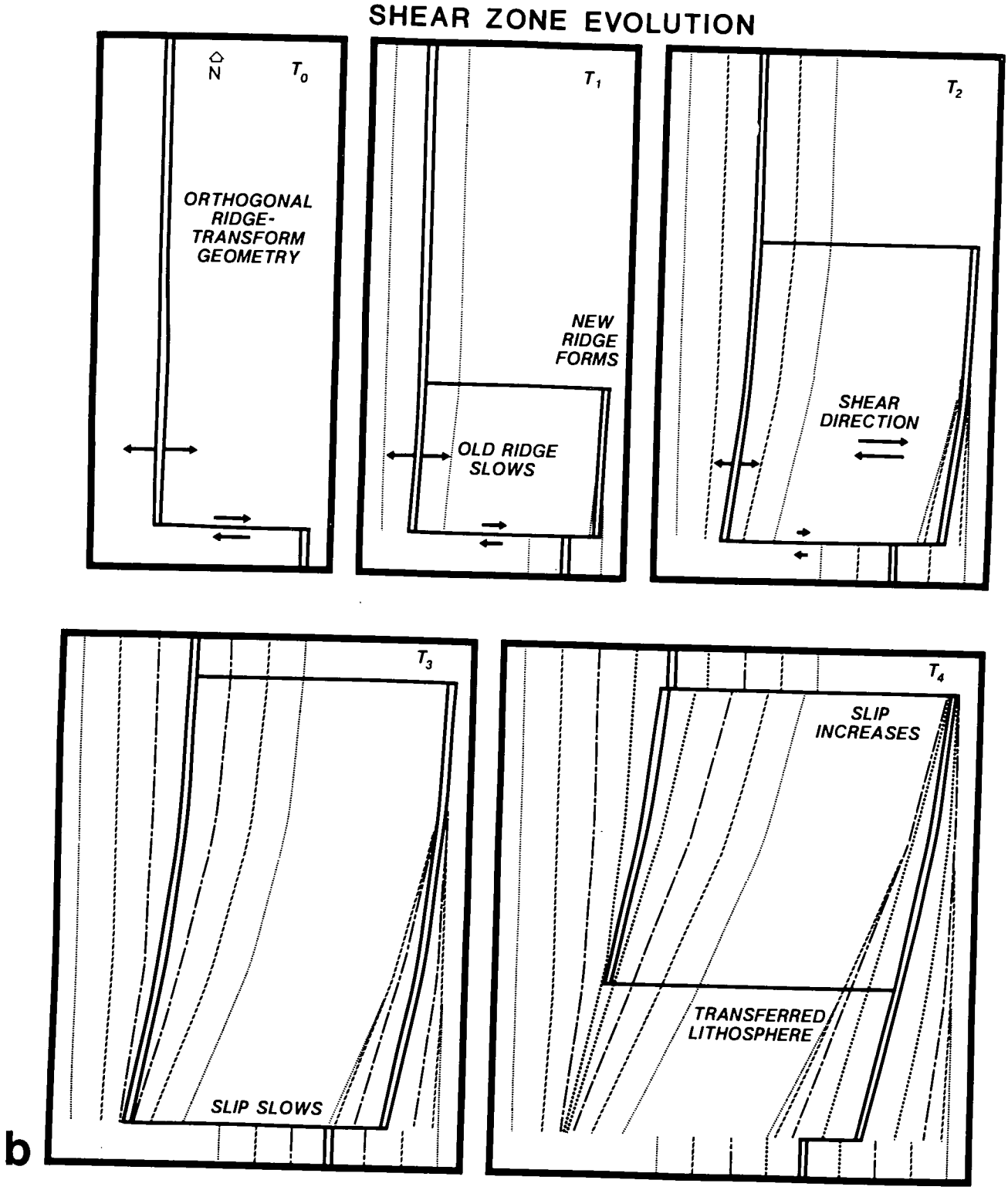
SHEAR ZONE EVOLUTION
N
T_0
ORTHOGONAL RIDGE-TRANSFORM GEOMETRY
T_1
NEW RIDGE FORMS
OLD RIDGE SLOWS
T_2
SHEAR DIRECTION
T_3
SLIP SLOWS
T_4
SLIP INCREASES
TRANSFERRED LITHOSPHERE
b

Schouten et al. (1990) have provided a thought-provoking analogue for the behaviour of microplates between major lithospheric plates, by suggesting that they rotate rigidly like roller-bearings between two planks of wood moving in opposite directions (Fig. 1.10a-c). A microplate's instantaneous relative rotation axes are assumed to lie on or near the boundaries, and represent unique points where the roller-bearing does not move relative to the respective planks, and where to one side there is compression, while to the other extension. Second order motion of the microplate is required, whereby the microplate rotates with constant angular velocity around an axis within its interior, while at the same time this axis rotates around the globe. Propagation of the two rifts is assumed to occur passively as the microplate rotates, and the resulting pseudofaults formed on the seafloor trace the location of the microplate's instantaneous relative rotation axes back in time, and can be used to constrain the past motion of the microplate. Their model was applied to the Easter Microplate (Fig. 1.10d,e), but though their model works in a general sense, the start and end times they give for the different phases contradict the magnetic anomaly evidence (see Chapter 6, section 6.5.2) and growth of the microplate is not permitted. Schouten et al. suggest the East Rift propagated northward between 5.0 and 3.4 Ma. During this time, the Pacific-Easter instantaneous rotation axis was fixed with respect to the Pacific plate, and acted as a hinge between the Easter and Pacific plates (Fig. 1.10d). From 3.4 Ma to the present the roller-bearing model was used to explain the curvature of pseudofaults surrounding the Southwest Rift and Pito Deep (the southwest and northeast corners of the Easter Microplate, see Fig. 2.1 and section 2.1, Chapter 2).

Although the roller-bearing model as it stands does not completely describe the kinematics of the Easter Microplate, Schouten et al. (1990) note some interesting points. If the instantaneous relative rotation axes are on the northern and southern boundaries of the microplate, there will be no slip between the microplate and the Pacific and Nazca plates. If slip is taking place, the microplate would rotate more slowly and the axes would lie some distance from the boundaries. Schouten et al. suggest that if the rotation of the microplate is driven by the shear flow of the mantle underneath, then it would rotate at half its present angular velocity (which Schouten et al. give as around18°/myr) (McKenzie & Jackson, 1983). The instantaneous relative rotation axes would then be located a distance apart that is approximately twice that between the present boundaries of the microplate, and slip would take place. Since the model assumes that no slip is occurring, Schouten et al. (1990) propose that microplate rotation could be driven by drag of the major plates on the microplate boundaries (like a roller-bearing) so that a change in relative major plate velocities would result in a change in the microplate rotation rate. In the case of the Easter Microplate, however, they allow the asymmetry of the microplate's rotation to be explained by the drag of the mantle on the base of the microplate, ideally in the direction of the fixed-hotspot reference frame. They also conclude that as the Southwest

Figure 1.10 The roller-bearing model of Schouten et al. (1990). (a) the ball bearing: straight arrows give the motions of the major plates, the circular arrows give the motion of the microplate relative to the plates about the instantaneous relative rotation axes. (b) representation in velocity space of the motions of the plates (P: Pacific; N: Nazca) and of the microplate rotation axis M. (c) schematic illustration of a second order motion of the Easter Microplate between the Pacific and Nazca plates. Since extension and accretion occur along the boundaries of the microplate, the microplate will grow with time and eventually become unstable. (d) Continuous kinematic solution for the motion of the Easter Microplate shown with the calculated paths of the Easter-Nazca and Easter-Pacific instantaneous rotation axes at the tips of propagating rifts, from the time of their common origin at ~5.0 Ma in O to the present location of these axes in N2 and P2 respectively. These are compared with observed pseudofaults (heavy black lines) for a two phase evolution of the microplate. The first phase of the evolution is from 5.0 - 3.4 Ma, and involves continuous northward propagation of the East Rift (from O to N1), with rapid microplate rotation of >> 17°/myr. The second phase is from 3.4 Ma to the present, and involves rigid rotation of the microplate as a ball-bearing, at a rotation rate of 17.7°/myr, while the Southwest Rift and Pito Rift regions open up due to rift propagation along the plate boundaries (from P1 to P2 and N1 to N2, respectively). According to Schouten et al. (1990), the fit of the calculated paths of instantaneous relative rotation axes to the observed pseudofaults shows that a complete kinematic history of microplate evolution can be deduced solely from its pseudofaults. (e) Simplified tectonic interpretation of the Easter Microplate (Searle et al., 1989) used to generate the model in (d).

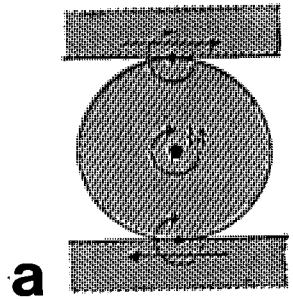

a

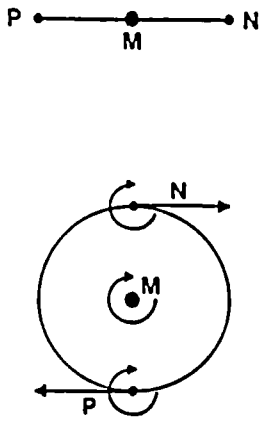
P
M
N
N
M
P

b

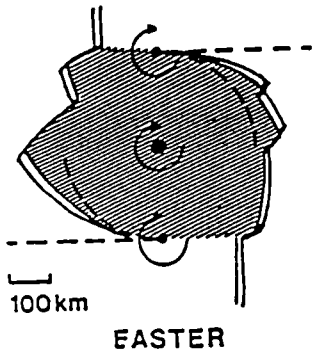
100km
EASTER

c

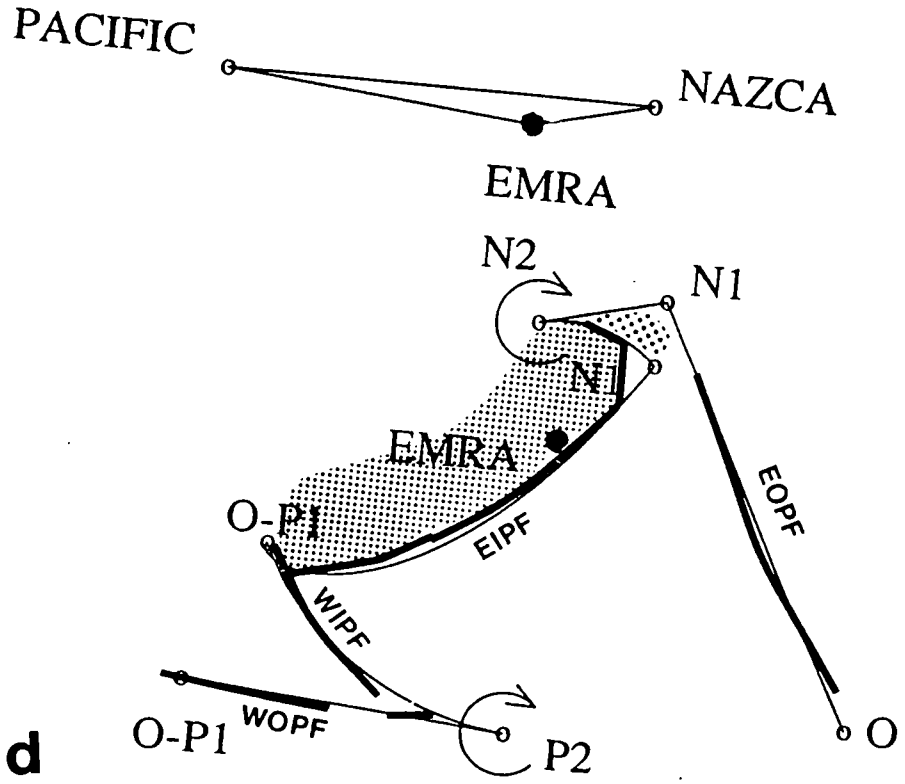
PACIFIC
NAZCA
EMRA
N2
N1
N1
EMRA
O-P1
EIPF
WIPF
EOPF
O-P1
WOPF
P2
O

d

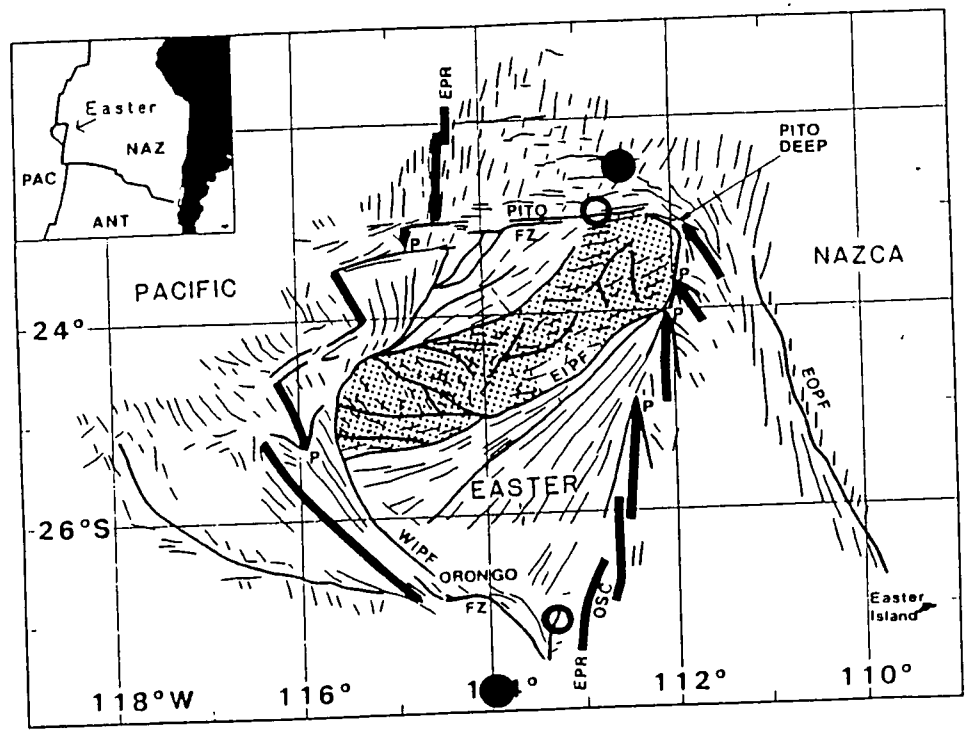
Easter
NAZ
PAC
ANT
EPR
PITO DEEP
PITO
FZ
NAZCA
PACIFIC
24°
EIPF
EOPF
EASTER
26°S
WIPF
ORONGO
FZ
OSC
EPR
Easter Island
118°W
116°
112°
110°

e

The work of Naar, Zukin and Martinez represents the most recent studies of the intensively examined Easter Microplate, but nevertheless leave many questions unanswered.

1.6 RRS Charles Darwin Cruise 35, 1988

RRS Charles Darwin cruise 35 in 1988 (Fig. 1.6) provided most of the data for this study. The main objective of the cruise was to image and assess the present structure of the microplate and adjacent areas, using underway geophysical data, consisting of GLORIA sidescan imagery, 3.5 kHz and 10 kHz bathymetric data and magnetic and gravity data. After leaving Papeete, Tahiti on October 13th, 1988, GLORIA was launched immediately, in order to survey the extent of the Teahetia-Mehetia hotspot while on passage to the Easter Microplate, and to improve knowledge of the distribution of fracture zones and other volcanic chains between Tahiti and the Easter Microplate. The principal findings from the results of this passage track are reported in Searle et al. (in prep.) and Searle et al. (1989b) and have been described above in section 1.3. Virtually all of the microplate was then imaged by GLORIA in just 18 days, using mainly east-west tracks over the East and West Rifts and the microplate interior, spaced 30-35 km apart to obtain good acoustic coverage, and allowing readily interpretable magnetic data. The area to the north of the microplate was then surveyed, using NE-SW tracks, to investigate a possible northern extension of the microplate. On November 9th, after following the trace of the initial outer pseudofault of the East Rift to Easter Island, and surveying the west and south sides of the island, GLORIA was recovered, and we then set course for Valparaiso at full speed, arriving on November 17th, 1988.

1.7 The objectives of this study

The main objectives of this study were to use the GLORIA and other geophysical data to determine the present day tectonic pattern and history of the Easter Microplate. This includes:

(1) Determining the position and nature of all of the present day microplate boundaries in both gross and fine detail.

(2) Examining evidence of short term evolution (<1 myr) of the various plate boundaries.

(3) Confirming and confining the current plate tectonics model at both local and regional scales.

(4) Inferring the past positions and types of plate boundary, and hence to determine the history of the development of the Easter Microplate.

(5) Using the magnetic anomaly data available to determine the age of the sea floor, and hence to enable spreading rates to be calculated.

(6) Calculating Euler poles for Pacific, Nazca and Easter motion using all the available spreading rate, transform and seismic slip data.

(7) Determining as far as possible the tectonic history of the microplate from its inception to the present.

(8) Ascertaining to what extent the microplate behaves as a rigid body, and how much intraplate deformation in the form of shear and compressional mechanisms is required for the microplate to evolve.

(9) Resolving what role the evolution of microplates have played during the widespread reorganisation of the EPR between about 25 Ma and the present.

CHAPTER 2
UNDERWAY GEOPHYSICAL DATA AND THE EASTER MICROPLATE

2.1 Introduction

This chapter is mainly concerned with the regional scale geology within the area of the Easter Microplate, and introduces the area for later, more detailed studies. The geology is illustrated with a combined data base of bathymetry, gravity and magnetic anomaly measurements from many research cruises within an area extending from 21°S to 28°S, and from 118°W to 110°W (and to 109°W near Easter Island). Attention is drawn to the main features associated with the Easter Microplate, which are then described in greater detail in Chapter 4. Fig. 2.1 introduces and names the main features associated with the microplate.

2.2 Collection and Processing of Data

2.2.1 RRS Charles Darwin cruise CD35, 1988

Throughout cruise CD35, magnetic, bathymetry and gravity data were collected concurrently with the GLORIA sidescan data. Bathymetry data were digitised manually from 10 kHz wide-beam precision echo-sounder records at two minute intervals and corrected for sound speed variations using the Carter tables (Carter, 1980). A 3.5 kHz echosounder was towed throughout the cruise, and data was collected in analogue form. A LaCoste and Romberg marine gravity meter was used to measure relative gravity, and the data were tied to the International Gravity Standardization Net (IGSN 71) (Morelli, 1974) in Papeete and Valparaiso. The final Free Air Anomaly was averaged using an 8 minute moving window. Total magnetic field intensity was measured at intervals of 6 secs by a towed proton magnetometer. These data were transformed into magnetic anomaly at two minute intervals using the 1985 International Geomagnetic Reference Field (IGRF) (IAGA, 1986).

2.2.2 Navigation

The transit satellite system was the main navigational aid used during the cruise. Positions between satellite fixes were dead-reckoned using an electro-magnetic log. In addition, positions were recorded with a Global Positioning System (GPS) receiver for

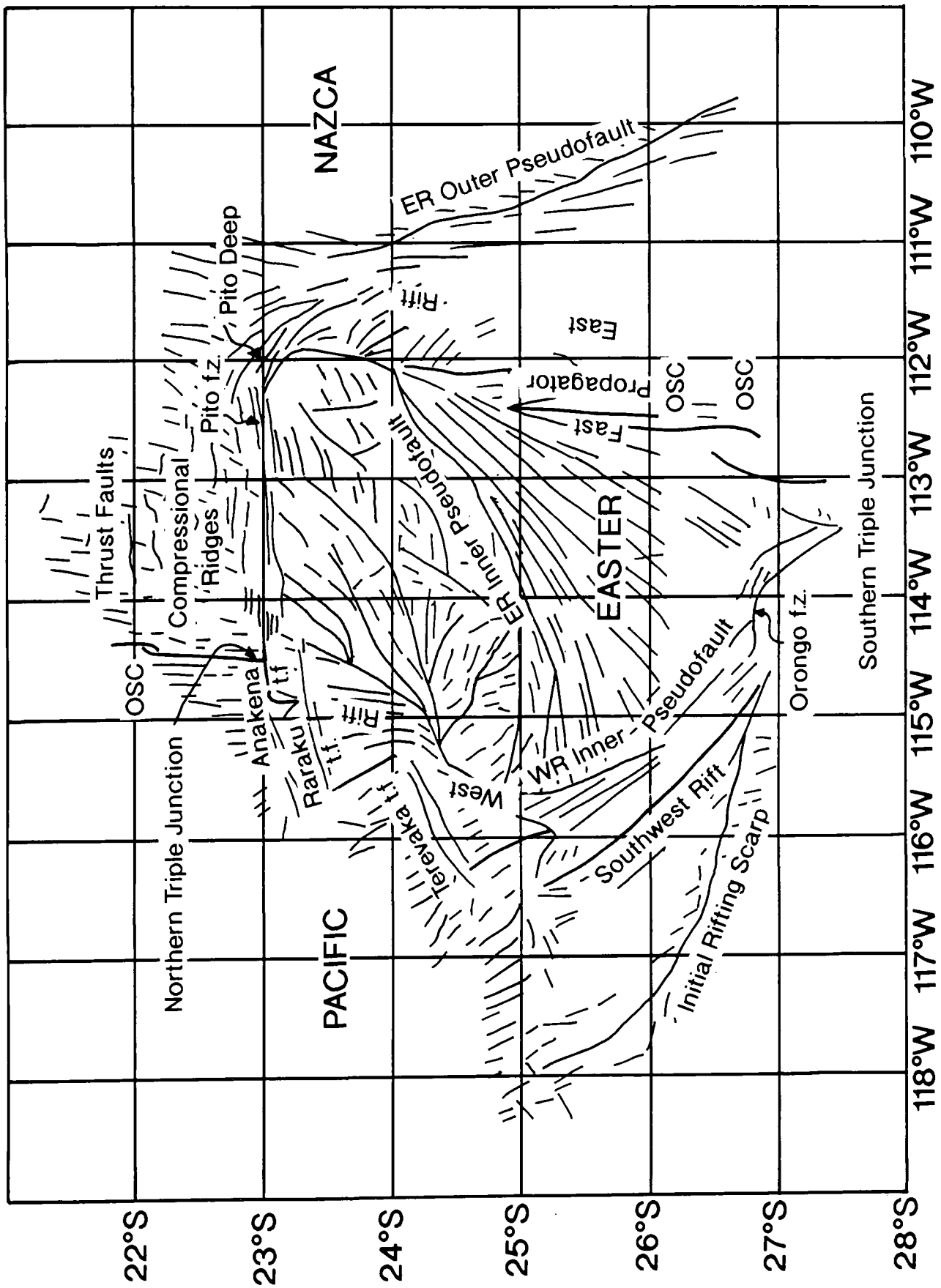

Figure 2.1 Simplified tectonic interpretation of the Easter Microplate based on GLORIA sidescan sonar data (see Plate 1) showing the main features associated with the microplate. Location names used throughout this thesis are indicated. ER and WR denote East Rift and West Rift respectively; OSC indicates an overlapping spreading centre; t.f indicates an active transform fault; f.z. indicates a fracture zone.

much of the time, but these were used to correct the dead-reckoned navigation only where there were large gaps of several hours between the transit satellite fixes. Normally the difference between the two navigational sets was less than 700 m. Comparison of features on adjacent GLORIA swaths does not significantly reduce this error.

2.2.3 Data base compilation and assessment

The data from cruise CD35 were supplemented by a large amount of data from the World Data Center, Boulder, Colorado (Fig. 2.2). Magnetic, bathymetry and gravity data were also supplied by J. Francheteau (Institut de Physique du Globe, Universite de Paris VII) from the Rapanui cruise in January, 1988, as well as from the Pascua cruises (Hey et al. 1985). Centre beam bathymetry from German Seabeam data (Cruises SO40 and SO62, Marchig et al., 1987; Marchig et al., 1989) were also added to the data set.

Crossover errors for the magnetic data were calculated using a program CROSOVER written by T.P. LeBas of IOSDL. Crossover errors were not calculated for gravity or bathymetry, since the main source of inaccuracy for both of these data types is navigational error. This program takes the cruise data and expands it into one minute values, corrects the magnetics with the appropriate Definitive Geomagnetic Reference Field (DGRF), and assigns an index number to each data value which corresponds to an area about 1 km square (101 points per degree). The data is then sorted with respect to the index number, thus bringing together all the points within the same area. The program then identifies crossovers, and calculates the data offsets. The cross-overs are then collated and compared. Using a least squares algorithm a datum level is found (for each cruise) which when added to the data value brings all the cruises to a common datum level. This correction factor is then tested with the mean values creating a new cross-correlation table. The original data is then re-read and the appropriate correction factor applied.

2.3 Grand-Scale Morphology

2.3.1 Presentation of Bathymetric Data

All the bathymetric data available were compiled as described in section 2.2 above (Sea MARC II data (Hey et al., 1987) were not included). These data were binned into 5 km bins and gridded using a program written by D.L. Stevenson, which in this case used a distance weighted average. The resulting data coverage is plotted in Fig. 2.3a, using a contour interval of 100 m and a "topographic" colour scale, ranging from red/brown above 2000 m to dark green below 4000 m. These data were then used to interpolate between

Figure 2.2 Compilation of all the ships' tracks with underway geophysical data used to supplement CD35 data. The majority of this data was obtained from the World Data Center, Boulder, Colorado. Additional magnetic, bathymetry and gravity data from the Rapanui cruises were supplied by J. Francheteau (Institut de Physique du Globe de Paris) and from the Pascua cruises by R.N. Hey (University of Hawaii at Manoa).

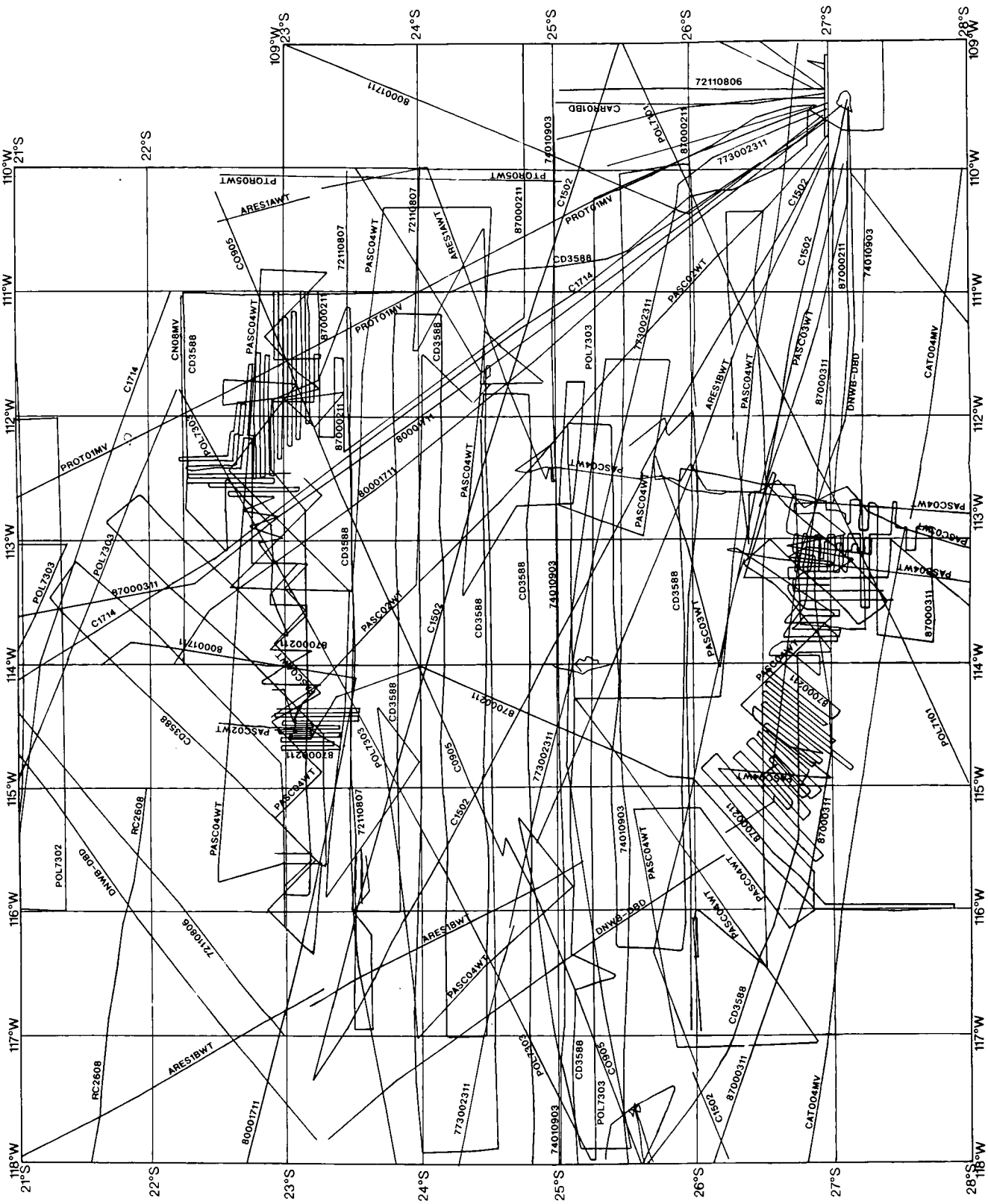
109°W
110°W
111°W
112°W
113°W
114°W
115°W
116°W
117°W
118°W
21°S
22°S
23°S
24°S
25°S
26°S
27°S
28°S
PROTO1MV
ARES1AWT
ARES1BWT
PASC04WT
PASC02WT
PASC03WT
CD3588
C1502
C1714
POL7303
POL7302
POL7101
CAT004MV
DNWB-DBD
DNWB-DBP
CN08MV
C0905
RC2608
72110806
72110807
74010903
87000211
87000311
87000711
80001711
80001911
81000211
773002311
CAR01BD
PTOR05WT

Figure 2.3 (a) Colour shaded contour map of bathymetric data. Data are in 5 km bins and gridded on to a 5 km grid. Contour interval is 100 m, ranging from below 4000 m water depth to above 2000 m. Actual maximum and minimum depths are 5980 m at Pito Deep and 640 m near Orongo fracture zone (see Fig. 2.1). (b) Bathymetric data as in (a) with interpolation of data between grid points.

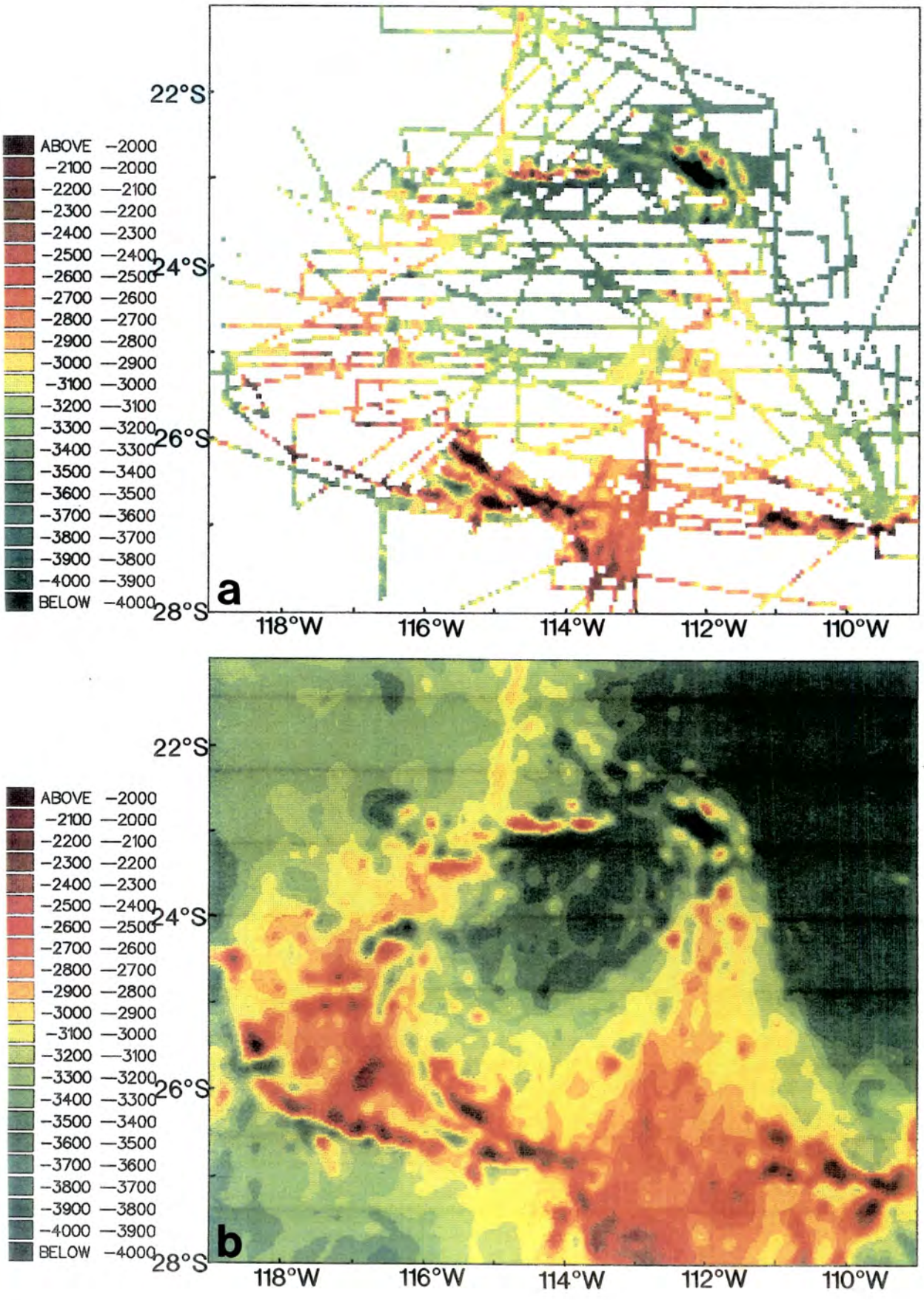
ABOVE −2000
−2100 −2000
−2200 −2100
−2300 −2200
−2400 −2300
−2500 −2400
−2600 −2500
−2700 −2600
−2800 −2700
−2900 −2800
−3000 −2900
−3100 −3000
−3200 −3100
−3300 −3200
−3400 −3300
−3500 −3400
−3600 −3500
−3700 −3600
−3800 −3700
−3900 −3800
−4000 −3900
BELOW −4000
22°S
24°S
26°S
28°S
118°W
116°W
114°W
112°W
110°W
a
b

the ship's tracks, using a distance weighted method, to produce the machine-contoured map shown in Fig. 2.3b.

Naar (1990) has compiled a hand-contoured bathymetric map using all the bathymetric data available as listed above and including the Sea MARC II data (Fig. 1.2, Chapter 1). This map was produced independently from my own, and has been recently published (Naar & Hey, 1991), making it unnecessary for me to repeat the exercise using the same data set.

2.3.2 Bathymetry and the Easter Microplate

The main features associated with the Easter Microplate are shown in Fig. 2.1. The microplate is some 400 km across and lies between two spreading rifts, known as the East and West Rifts, which accommodate Easter-Nazca and Easter-Pacific spreading respectively.

The West Rift consists of four spreading segments, three of which are connected by dextral offset (i.e. sinistrally slipping) transforms, which I have named the Anakena, Raraku and Terevaka transforms (after prominent features on Easter Island), from north to south. South of the Terevaka transform a fairly recently formed propagating rift has been mapped using GLORIA (Chapter 4, section 4.2.2), but is not quite picked out by the bathymetry. This propagator overlaps the northwestern end of the Southwest Rift, forming the only non-transform offset on the West Rift. The Southwest Rift forms part of the West Rift, but differs in morphology and origin from that of the northern part of the West Rift (as will be seen later). Tectonic fabric formed at the Southwest Rift is enclosed within two prominent ridges which converge to become one near 26°46'S, 114°13'W. These shallow ridges (which are known as initial rifting scarps, or IRSs, see Chapter 4) can be clearly seen in Fig. 2.3b and Fig. 1.2, Chapter 1, curving southeastwards from around 25°S, and rising some 2000 m above the surrounding seafloor.

The precise location of the Southern Triple Junction is not known, despite an abundance of data in the area, but is thought to be around 28°S, 113°W (see Chapter 4, section 4.2.4), although Francheteau et al. (1988) place it further north than this. The bathymetric data reveal that the whole area between 27°S and 28°S around 113°W is anomalously shallow, and tectonically very complex. Detailed examination of Seabeam and GLORIA data (see Chapter 4) indicate the presence of several overlapping spreading centres (OSCs), and the sidescan data show the whole area to be covered in recent lava flows and volcanic cones.

The overall trend of the East Rift can be seen from the bathymetric data to be east of north. However, the spreading axis is divided into at least four segments, three of which, on the GLORIA images, can be seen to have recently propagated northward to the inside (west) of the axis they are replacing. North of these the axis becomes a deep graben and probably passes through Pito Deep at 23°0'S, 111°56'W, with its maximum depth of 5890 m (Francheteau et al., 1988).

The Northern Boundary has been described in detail by Zukin (1990) based on the Seabeam data collected during the Rapanui expedition. Although named Pito Fracture Zone by Francheteau et al. (1988), this name is not used here as pure strike-slip movement only occurs at the eastern end of the boundary, see Chapters 4 and 6. It can be picked out in Fig. 2.3b (and Fig. 1.2, Chapter 1) as a fairly prominent almost east-west trending ridge extending from 112°W to 114.5°W, roughly along latitude 23°S, i.e. from Pito Deep in the east to the Northern Triple Junction in the west. South of this ridge and parallel to it the seafloor is anomalously deep, forming a slight trough. As will be seen later (Chapters 4 and 7) this anomalous trough-ridge feature is caused by closure of the Nazca and Easter plates along this boundary, without the formation of a subduction zone.

The Northern Triple Junction is not the straightforward ridge-fault-fault (R-F-F) triple junction that it immediately appears to be (Fig. 1.2, Chapter 1). It is located at 23°28'S, 114°32'W, at the near orthogonal intersection of the roughly north-south East Pacific Rise with the almost east-west Anakena Transform and Northern Boundary, and as will be seen later (Chapters 4 and 7), it has a ridge-fault-trench (R-F-T) configuration.

Relatively little information about the microplate interior is revealed by the bathymetric data. The major East Rift inner pseudofault (EIPF) is picked out by the 3200 m contour line in Fig. 1.2, Chapter 1. Insufficient data are available to show the complex nature of the rotated structures between the West and East Rifts of the microplate. Also the changes in spreading ridge orientations implied by the juxtaposition of different tectonic domains (revealed by the GLORIA data, Chapters 4 and 6) cannot be seen from the bathymetry alone.

Between the southern end of the East Rift, and Easter Island (at around 27°S, 109°W), the bathymetric data reveal another anomalously shallow region of the seafloor. Within this region lies the Ahu Volcanic field of Hagen et al. (1990), mapped by the Sea MARC II sidescan sonar and swath bathymetry system. This is an area of recent voluminous lava flows and the formation of numerous volcanic edifices, that is thought to be associated with the Easter Hotspot (see Chapter 1, section 1.4, and Chapter 6, section 6.5.4).

There are few ship's tracks on the Nazca plate to the north of the microplate (Fig. 2.2). They are barely sufficient to reveal the prominent series of almost east-west trending ridges that extend in an en echelon fashion southeasterly from around 22°S, 114°W to the Pito Deep region at around 23°S, 112°W. After these features were first revealed by GLORIA, a broad Seabeam zig-zag was made across them (during the passage leg of the second part of the German Geometep 5 leg) which has given some insight into the morphology and nature of these ridges. Chapter 7 is entirely devoted to the understanding of these ridges, which I believe are the first known occurrence of intraplate thrust faulting within young oceanic lithosphere.

Overall, the Easter Microplate is considerably shallower in the south than in the north. The anomalous relief of the scarps bounding the Southwest rift increases with decreasing distance towards the East Rift. The area between 27° and 28°S is remarkably shallow compared to other parts of the East Pacific Rise, and must be related to the nearby presence of the Easter Hotspot.

2.4 Gravity data and the Easter Microplate

The free air anomaly gravity data are shown in Fig. 2.4. These data were binned into 5 km bins and gridded as for Fig. 2.3 and the resulting data coverage is plotted in Fig. 2.3a, using a contour interval of 5 mgal and a "topographic" colour scale, ranging from red/brown above 50 mGal to dark green below -50 mGal. These data were then used to interpolate between the ship's tracks, using a distance weighted method, to produce the machine-contoured map shown in Fig. 2.3b. In regions where there are few or no data, such as to the southwest of the Southwest Rift, the machine contours produced should be ignored.

A visual comparison of the gravity data with the bathymetry data in Fig. 2.3 reveals that many of the small-scale variations correlate. The anomalously deep region of Pito Deep has a corresponding gravity low associated with it, as does the axial graben at the tip of the Southwest Rift. The shallow northern boundary of the microplate has an equivalent gravity high, an so do the initial rifting scarps which bound the Southwest Rift. A small-scale variation in gravity which does not correlate with the bathymetry is a slight gravity low which extends from Easter Island (27°S, 109°W) westwards to the East Rift. However, this apparent lineament is only along one ship's track, and since the data have not been adjusted for crossover errors, it is not likely to be a true anomaly.

The large-scale variations in the bathymetry, however, are not matched by ones in the gravity. The gravity does not reflect the increase in water depth with age.

In addition, there is an obvious regional decrease in water depth towards

Figure 2.4 (a) Colour shaded contour map of free air anomaly gravity data. Data have been binned and gridded as for Fig. 2.3. Contour interval is 5 mgal and ranges from below -50 mgal to above +50 mgal. (b) Free air anomaly gravity data as in (a) with interpolation of data between grid points.

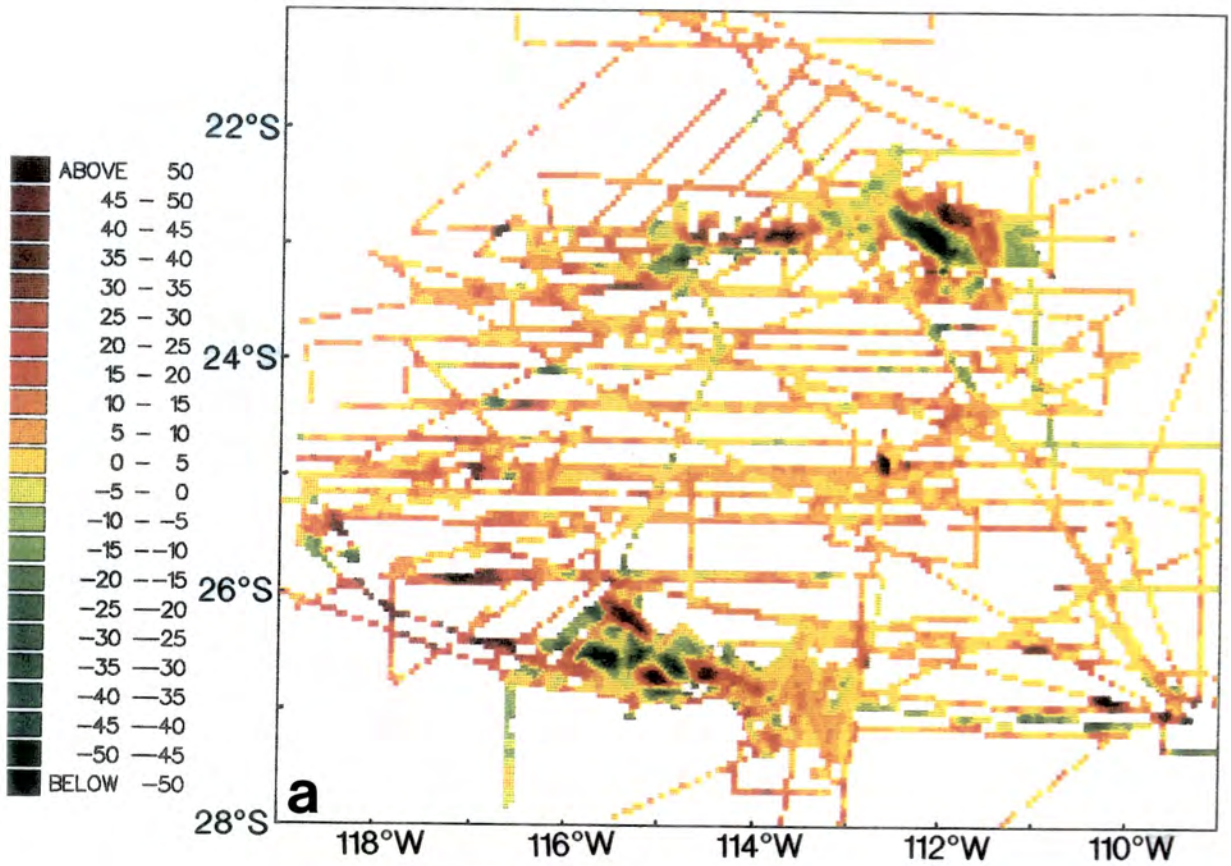
ABOVE 50
45 – 50
40 – 45
35 – 40
30 – 35
25 – 30
20 – 25
15 – 20
10 – 15
5 – 10
0 – 5
–5 – 0
–10 – –5
–15 – –10
–20 – –15
–25 – –20
–30 – –25
–35 – –30
–40 – –35
–45 – –40
–50 – –45
BELOW –50
22°S
24°S
26°S
28°S
118°W
116°W
114°W
112°W
110°W
a

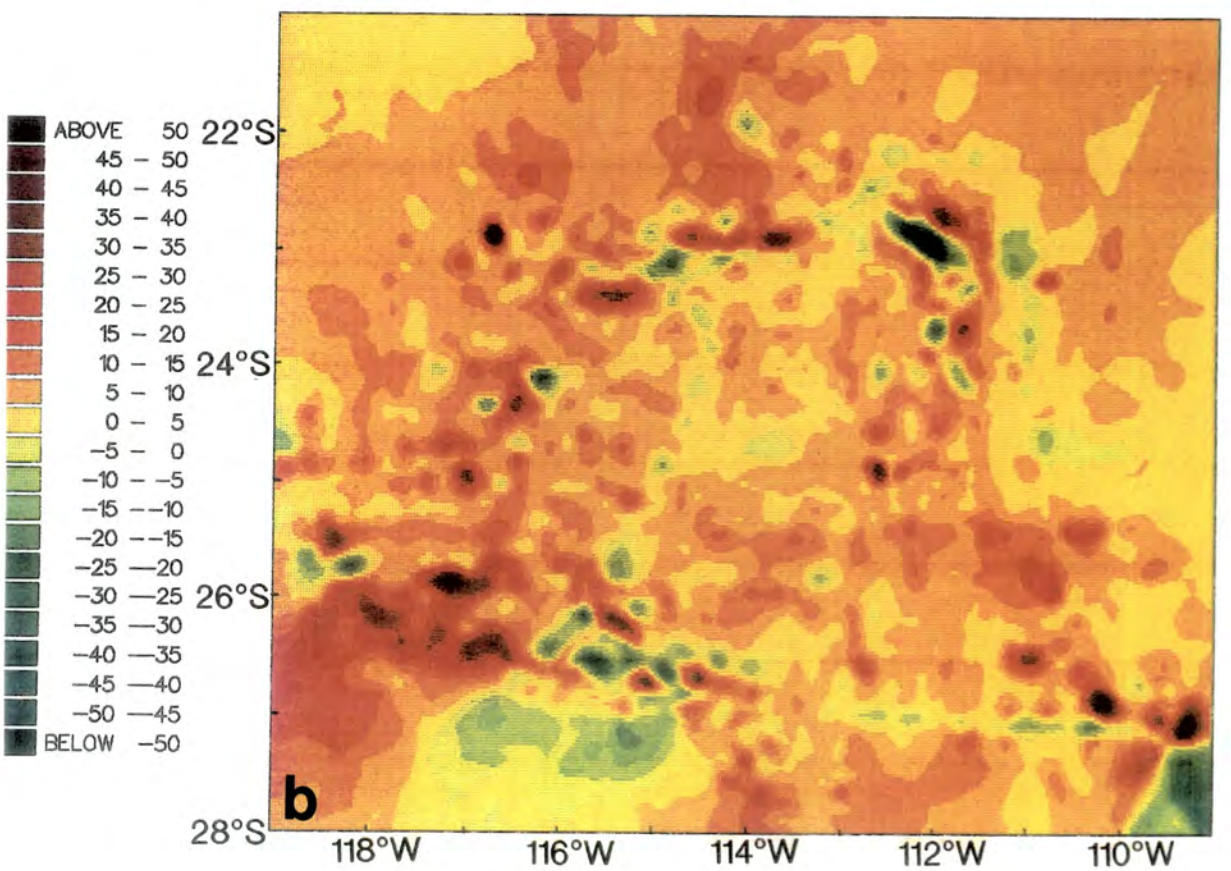
ABOVE 50
45 – 50
40 – 45
35 – 40
30 – 35
25 – 30
20 – 25
15 – 20
10 – 15
5 – 10
0 – 5
–5 – 0
–10 – –5
–15 – –10
–20 – –15
–25 – –20
–30 – –25
–35 – –30
–40 – –35
–45 – –40
–50 – –45
BELOW –50
22°S
24°S
26°S
28°S
118°W
116°W
114°W
112°W
110°W
b

the south of the Easter Microplate region which has no corresponding increase in free air anomaly. This suggests that the region as a whole has been isostatically compensated at spatial wavelengths of 100 km and above (McKenzie & Bowin, 1976; Watts, 1982), but is compensated by crustal thickness variations and by the flexural rigidity of the mechanical lithosphere at smaller scales. The small-scale variations in gravity and bathymetry at around the Pito Deep region and the Southwest Rift have been examined and modelled in detail by Martinez et al., (1990, submitted) in relation to the apparent rifting apart and propagation through older, pre-existing lithosphere that is occurring in these regions, and so are not further discussed here.

2.5 Magnetic Anomalies

2.5.1 Magnetic data and models

The magnetic anomaly data were compiled and crossover errors calculated as described in section 2.2.3. The data are plotted as profiles along the ships' tracks in Fig. 2.5, with positive to the north and negative to the south, as the majority of the ships' tracks are oriented east-west. The ships' tracks themselves are not drawn, but their position is implicit as the positive parts of the anomalies are coloured black. To aid identification of the magnetic anomalies, corresponding models were calculated using the program MAGIC (written by R.C. Searle). This is described in detail in Chapter 5.

The colour overlay for Fig. 2.5 shows the magnetic anomaly identifications made, with the colours representing different anomalies, or the reversals between the anomalies, as given in the key. The lines represent isochrons, the corresponding ages of which are given in Fig. 2.6 in millions of years, according to the Harland et al. (1990) timescale, and the magnetic anomaly picks are given in Table 2.1.

The magnetic anomaly data are displayed as a colour shaded contour map in Fig. 2.7. Data were binned into 5 km bins and gridded, as with the bathymetric and gravity data. These gridded data are shown in Fig. 2.7a without interpolation, and with interpolation (using a distance weighted function) in Fig. 2.7b. The advantage of displaying the magnetic anomaly data in contoured form is readily appreciated in areas such as the interior of the microplate. Here the lithosphere has been rotated by several tens of degrees, as have the magnetic anomalies, while the majority of the ships' tracks run roughly east-west, making the interpretation of anomalies from the magnetic profiles extremely difficult. However, from the contoured data I have identified anomalies 2A and 3 at around 23.5°S, 113°W and 24.5°S, 114°W, on crust whose fabric is presently oriented ENE and ESE, respectively. Further support for this interpretation is given by an

TABLE 2.1 *Magnetic Anomaly Picks*

Anomaly	*Age (myr)*
B/M	0.72
J	0.94
2	1.77
2r-1	2.08
2A (y)	2.45
2A (m)	3.03
2A (o)	3.40
3 (y)	3.87
3 (o)	5.08

Figure 2.5 Magnetic anomaly profiles plotted along the ships' tracks with positive to the north and negative to the south. Positive anomalies are shaded black. Although the ships' tracks are not shown their location is implicit from the black and white colouring of the anomalies. Colour overlay indicates the magnetic isochrons interpreted from the anomalies. Red indicates Brunhes anomaly (0 - 0.72 Ma); orange is from Brunhes/Matuyama reversal to Jaramillo anomaly (0.72 - 0.94 Ma); yellow is from Jaramillo to Chron 2 (0.94 - 1.77 Ma); green is from Chron 2 to start of anomaly 2A (1.77 - 2.45 Ma); blue indicates anomaly 2A (2.45 - 3.40 Ma); purple is from the end of anomaly 2A to the start of anomaly 3 (3.40 - 3.87 Ma); wine red indicates anomaly 3 (3.87 - 5.08 Ma). Magnetic anomaly picks according to Harland et al. (1990) timescale.

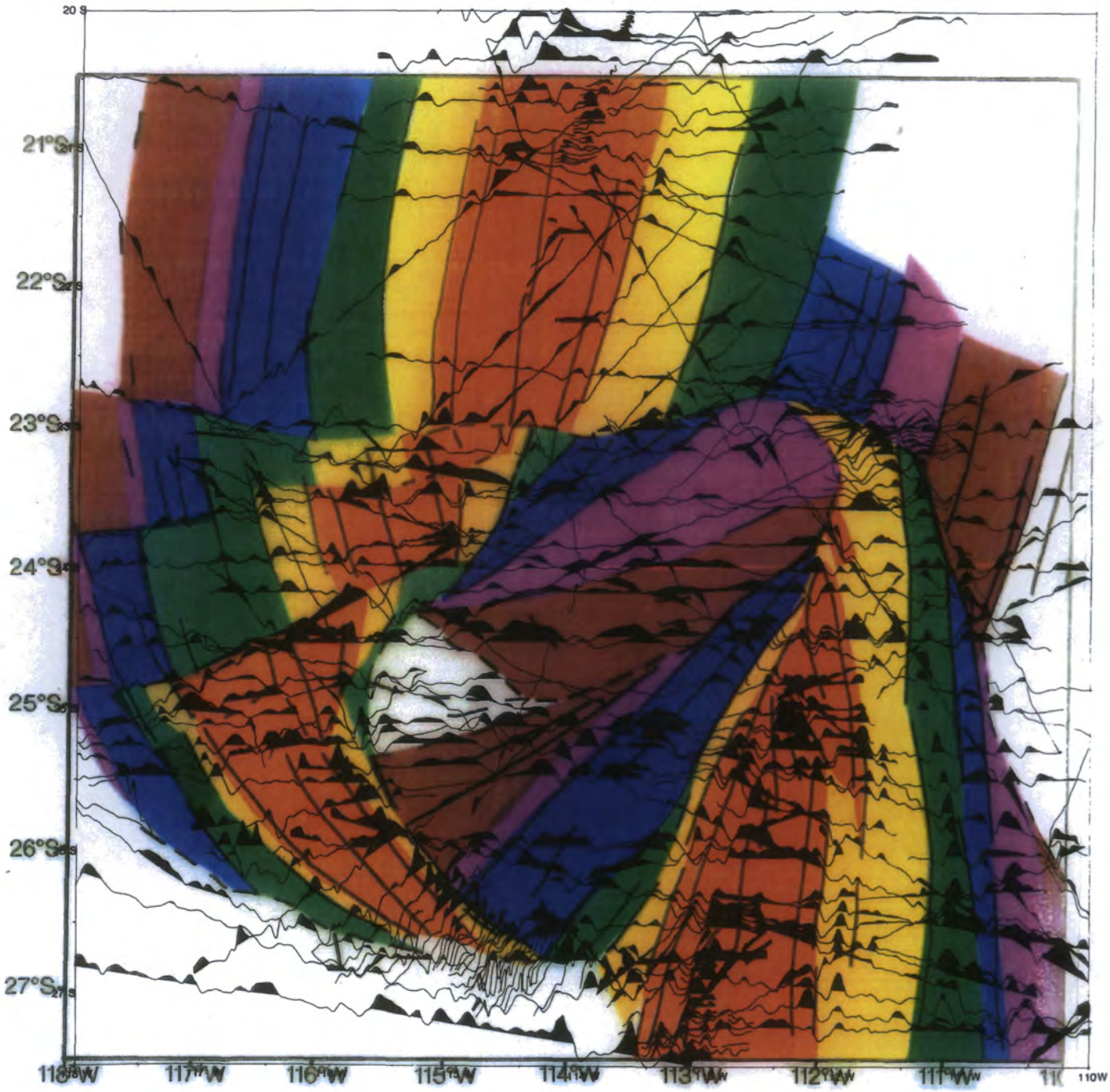
20°S
21°S
22°S
23°S
24°S
25°S
26°S
27°S
118°W
117°W
116°W
115°W
114°W
113°W
112°W
111°W
110W

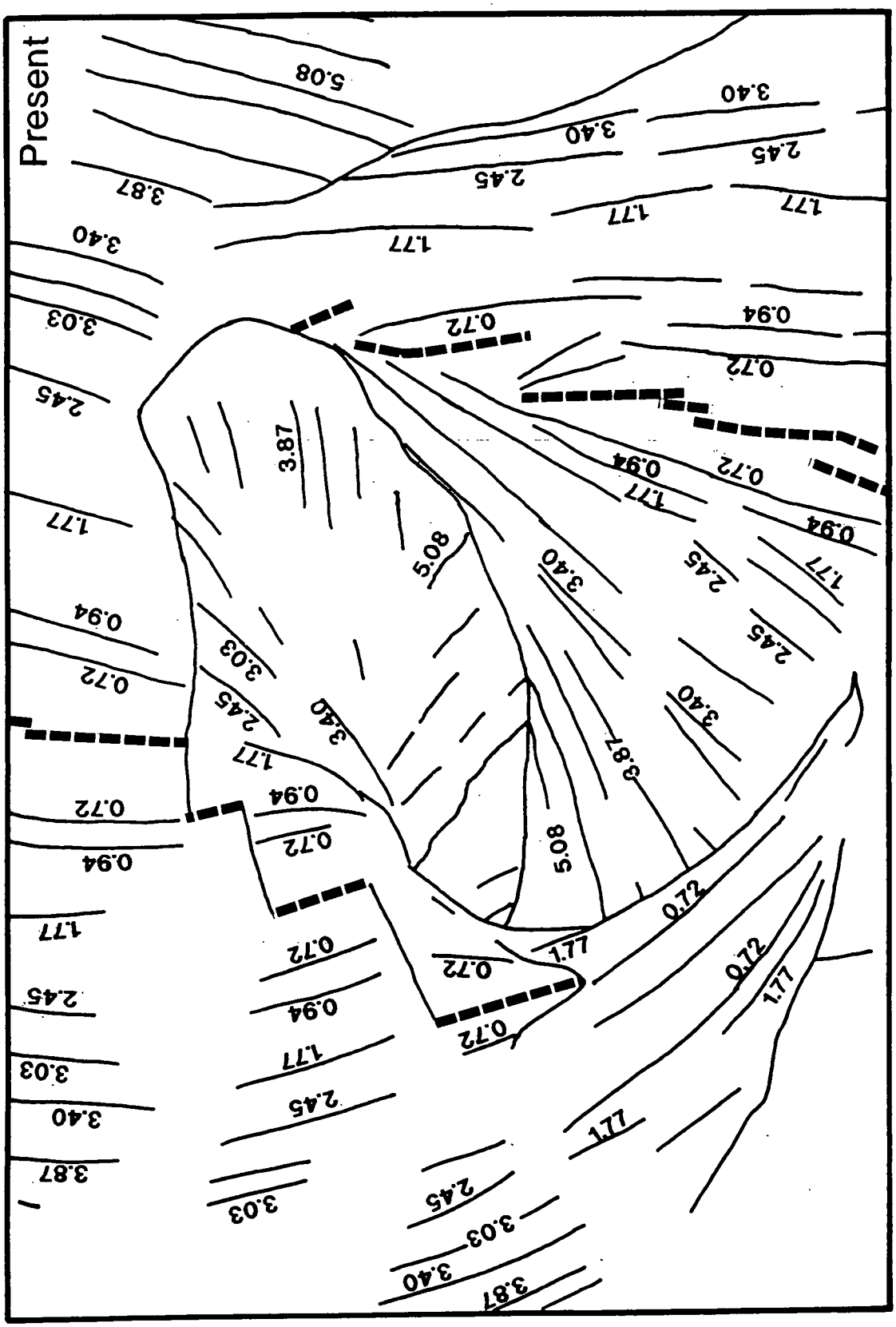

Figure 2.6 Magnetic isochrons interpreted from anomaly data in Fig. 2.5. Ages of isochrons are given in millions of years according to the Harland et al. (1990) timescale.

Figure 2.7 Colour shaded contour map of magnetic anomaly data. Data have been binned and gridded as for Fig. 2.3. Contour interval is 25 nT and ranges from below -250 nT to above +250 nT. (b) Magnetic anomaly data as in (a) with interpolation of data between grid points.

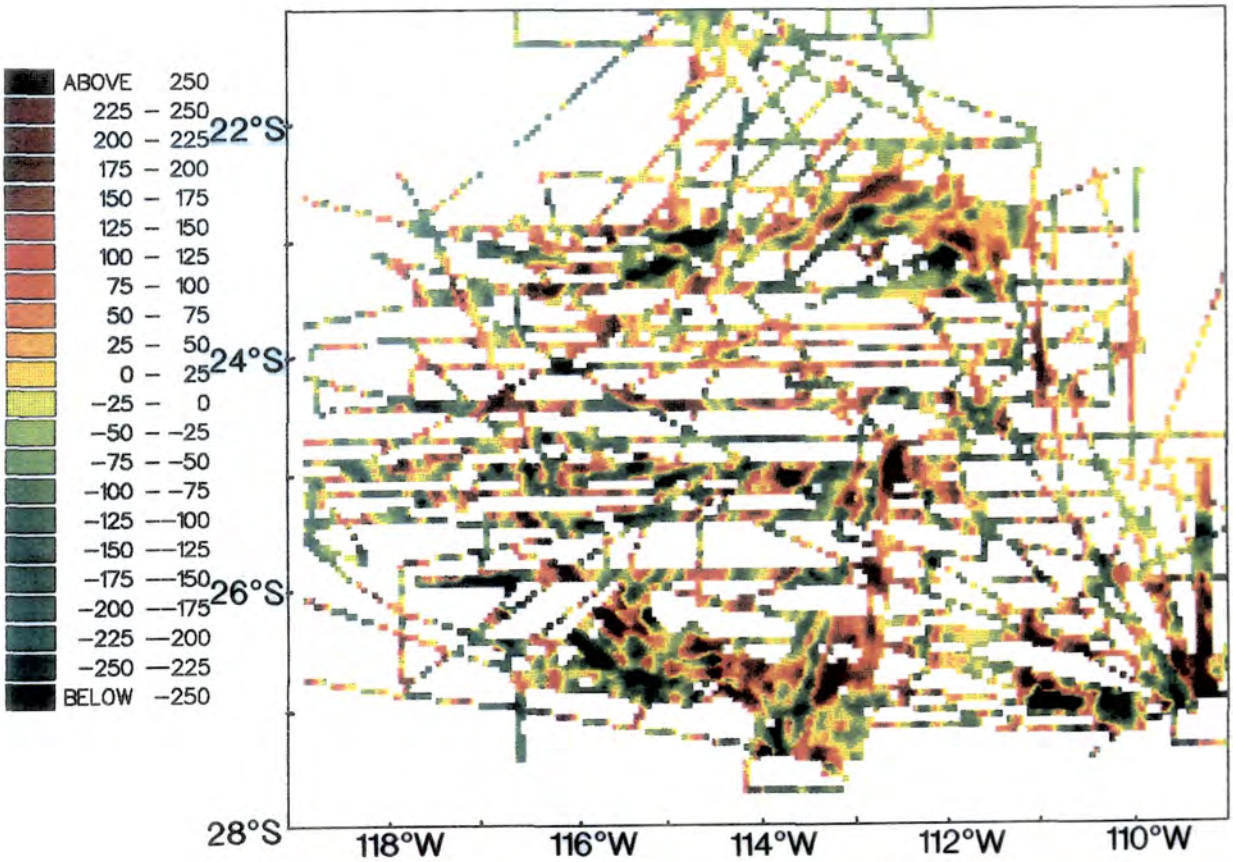
ABOVE 250
225 – 250
200 – 225
175 – 200
150 – 175
125 – 150
100 – 125
75 – 100
50 – 75
25 – 50
0 – 25
−25 – 0
−50 – −25
−75 – −50
−100 – −75
−125 – −100
−150 – −125
−175 – −150
−200 – −175
−225 – −200
−250 – −225
BELOW −250
22°S
24°S
26°S
28°S
118°W
116°W
114°W
112°W
110°W

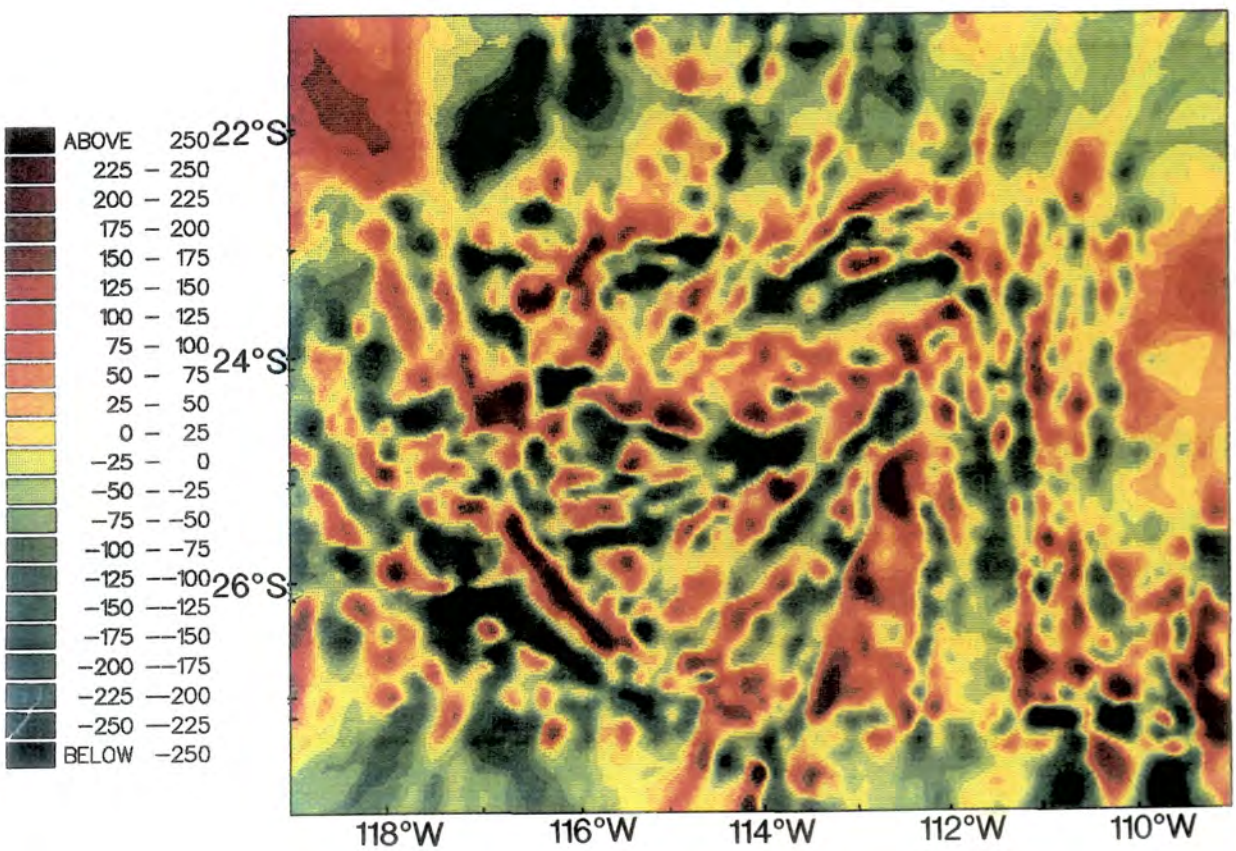
ABOVE 250
225 – 250
200 – 225
175 – 200
150 – 175
125 – 150
100 – 125
75 – 100
50 – 75
25 – 50
0 – 25
−25 – 0
−50 – −25
−75 – −50
−100 – −75
−125 – −100
−150 – −125
−175 – −150
−200 – −175
−225 – −200
−250 – −225
BELOW −250
22°S
24°S
26°S
118°W
116°W
114°W
112°W
110°W

"eyeball" comparison of variation in backscatter strength on the processed GLORIA mosaic (see Chapter 3) which appears to be of similar strength in these areas to others known to be of age 2A or 3. This assumes that sedimentation rates around the microplate are roughly similar.

2.5.2 Magnetic anomalies and the Easter Microplate

A discussion of the detailed magnetic anomaly identifications in this region can be found in Chapter 5, but a general overview of the anomalies is provided here for completeness.

Brunhes Anomaly

The Brunhes anomaly is generally well defined on all the different spreading segments on both the East and West Rifts, as well as on the EPR to the north and south of the microplate. On the West Rift, the Brunhes is not easily located between the Anakena and Raraku transforms, although the tectonic structures and backscatter levels observed on the GLORIA mosaics indicate that crust has been continuously accreted at this ridge since at least anomaly 2 time (1.77 Ma). Also, south of the Terevaka transform (Fig. 2.1, and Chapter 4), the Brunhes anomaly at the location of the southward propagator and the overlapped tail of the Southwest Rift can be seen, though its exact configuration is not clear. The Southwest Rift itself, oriented some 50° west of north, has an extremely antisymmetric anomaly associated with it, as expected, with the positive peak of the Brunhes to the northeast of the axis, and the negative trough to the southwest. On the East Rift, at 25°S, the "fast propagator" (Naar & Hey, 1986) has a clearly defined central anomaly associated with it, and the ridge to the east of this lies within a moderately well defined Brunhes anomaly. However, the spreading axis to the north of this, which is believed to be magmatically active (Marchig et al. unpublished manuscript), appears to have only recently evolved, as the Brunhes/Matuyama reversal boundary can not be located with confidence. The rift axis which passes through Pito Deep is thought to be only tectonically active (Naar & Hey, 1991; Martinez et al., in press), and hence no magnetic anomaly is expected or found.

Jaramillo Anomaly

The Jaramillo is located with confidence either side of the EPR, the spreading centre separating the Raraku and Terevaka transforms, and the "Fast Propagator". Elsewhere it is not well defined. On the Southwest Rift, where spreading rates are relatively slow (from 110 mm/yr down to 60 mm/yr, see Chapter 5), the Jaramillo can just be made out to the southwest of the axis, but not to the northeast.

Anomaly 2

Anomaly 2 (1.77 Ma) is the most easily recognised peak of the whole magnetic anomaly data set, and can be located with reasonable confidence either side of all the spreading segments on the West Rift, and along most of the length of the East Rift, as well as the EPR. One of the places where its interpretation is ambiguous is to the west of the southern end of the East Rift. Here two small peaks are found in place of anomaly 2. I interpret the small peak nearest the East Rift to be anomaly 2, while the other small peak is subchron 2r-1 (Harland et al., 1990). Either side of the Southwest Rift, anomaly 2 can be located with confidence, but the peaks to the northeast of the ridge axis almost follow the trend of the West Rift Inner Pseudofault (WIPF, see Fig. 2.1) and are the oldest anomalies found to the northeast associated with the Southwest Rift. Anomalies formed prior to chron 2 must presently lie to the southwest of the axis, having been rafted off during later stages of propagation.

Anomaly 2A

It is during chron 2A (at 2.45 Ma) that major changes occur in the evolution of the microplate, according to the model presented in Chapter 6 (see sections 6.3 and 6.4). At this time, the East Rift ceases to propagate northward, and the Southwest Rift begins to propagate in a southeasterly direction from the Terevaka transform. This is the start of Schouten et al.'s (1990) Phase Two (see Chapter 1, section 1.5, and Chapter 6, section 6.5.2). Since this is such a pivotal time within the history of the microplate, it is essential that anomaly 2A be recognised with confidence.

Either side of the East Pacific Rise, standard 2A anomalies can be picked out, while to the west of the East Rift, 2A appears as a very broad anomaly lacking in the small central peak, and to the east is a relatively narrow anomaly, also lacking in the small central peak (see Chapter 5). To the west of the West Rift, anomaly 2A can be recognised in several places. However, it is only where sufficient magnetic data and/or GLORIA data are available that there is enough structural control to determine the north-south extent of these anomalies, i.e. where they can be seen to abut earlier fracture zone traces or obvious offsets in overall GLORIA backscatter strength. To the east of the West Rift, anomaly 2A is harder to pick out. In Chapter 6 (section 6.2) reference is made to the fact that in the northeast of the microplate, two domains exist that are juxtaposed against each other, with the same variation in backscatter across them, despite differing trends of basement fabric. I have interpreted the magnetic anomalies in both these domains as the peaks of 2A (Fig. 2.5, Fig. 2.6 and Fig. 2.7b). The western domain (presently trending NE-SW) formed at the northern end of the West Rift during chron 2A, while the eastern

domain (trending almost east-west) formed during the same interval, but at the southern end of the northern East Pacific Rise.

As mentioned above, the oldest lithosphere lying to the northeast of the Southwest Rift and having formed at that axis is of anomaly 2 age. Since the southern initial rifting scarp (IRS, see Fig. 2.1) encloses lithosphere of a greater age than this, and is inferred to have formed at around 2.5 Ma, I suggest that this lithosphere is of early anomaly 2A age, and includes that originally accreted on the Easter Microplate, which has since been transferred to the Pacific plate by rift propagation. Unfortunately, the magnetic anomalies available there can not be interpreted unambiguously.

Anomaly 3

The oldest identifiable anomaly associated with the Easter Microplate is anomaly 3. In Chapter 6, I propose that the microplate formed at around 5.25 Ma, i.e. just prior to chron 3. Anomaly 3 is best recognised either side of the East Pacific Rise north of the microplate, at around 117.5°W on the Pacific plate and near 110.5°W on the Nazca plate. It can also be identified with reasonable confidence to the west of the various spreading segments associated with the West Rift. To the east of the East Rift, as the outer pseudofault approaches Easter Island, there is one profile that extends east-southeastwards from 26°40'S, 110°06'W, that exhibits all of the peaks associated with anomaly 3. Parts of this anomaly 3 can be correlated with the more oblique profiles to the north and south. This one profile is the single piece of evidence that supports the idea presented in Chapters 5 and 6 that the crust on which Easter Island is sited is older than anomaly 3 age, and hence that the oldest crust accreted by the newly formed East Rift, and presently lying on the Nazca plate, is also older than anomaly 3.

The chron 3 fabric formed at the East Rift and accreted to the microplate is harder to identify, since most of the ships' tracks run east-west, while the fabric trends NE-SW. One anomaly identified on several profiles is thought to be the youngest peak of anomaly 3 that originally formed on the Nazca plate and has since been transferred to the microplate. This isochron lies between 3.40 and 3.87 in Fig. 2.6. West of this, the positive peaks are identified as all belonging to anomaly 3 (Fig. 2.5).

In the centre of the microplate, where the abyssal hill fabric trends almost east-west, anomaly 3 is even harder to pick out. The fabric centred around 24.5°S, 113.5°W is thought to have formed at the East Pacific Rise as the Nazca plate, before being transferred to the microplate. Unfortunately, there are no north-south track lines, and the east-west running lines reveal nothing of the characteristic shapes of the magnetic anomalies. However, the reconstructions carried out in Chapter 6 suggest that this fabric

may be of anomaly 3 age and the contoured magnetic data in Fig. 2.7b show that these positive anomalies may in fact be those of anomaly 3.

Microplate Core

The remaining core of the microplate is of uncertain age. The lithosphere centred around 24.5°S, 114.5°W may be of anomaly 3A age (5.69-6.33 Ma), while that found in the domain to the southwest may be much older than this. 3.5 kHz records show the sediment thickness to be around 15-20 m. The average sedimentation rate, based on the examination of foraminifera and coccoliths biostratigraphies for all the cores recovered from the Easter Microplate region, is about 270cm/myr (Weiss, pers. comm.; Marchig et al., 1989). This suggests that this region must be at least 5.5 Ma, and possibly 7.5 Ma .

CHAPTER 3
ACQUISITION AND PROCESSING OF GLORIA AND SEABEAM DATA

3.1 Introduction

In this chapter, the acquisition of GLORIA data and the GLORIA system itself are described. The processes that are involved in enhancing the GLORIA data for improved appearance and ease of interpretation are discussed. Much attention is focussed on the use of the MIPS (Mini Image Processing System) software because the application of this software has not been adequately described elsewhere. The method of interpreting GLORIA images is introduced, and the hazards of wrongly interpreting artifacts of GLORIA data are discussed. Finally, the acquisition and interpretation of Seabeam data are described.

3.2 GLORIA data acquisition

3.2.1 The GLORIA system

The GLORIA system used is a digitally recorded long-range sidescan sonar system (Somers et al., 1978; Searle et al., 1990). During the survey a 2-sec. long pulse of about 6.5 kHz (6.2875 kHz to starboard and 6.7625 kHz to port) was transmitted at a 30 second cycle rate. Under ideal conditions for signal propagation in deep water this configuration gives a maximum swath width of 45 km (22.5 km to either side of the survey vessel). However, in practice the effective range was limited to about 15-20 km either side of the ship.

The GLORIA sonar vehicle is towed some 400 m behind the ship, and is neutrally buoyant at the surface, so that as the cable is unwound, the vehicle sinks to a depth of around 40 m below sea level. The vehicle itself consists of two transducer arrays (one port and one starboard), each with 2 x 30 transducers divided into six horizontal sections of 5 x 2 transducers. Usually only three sections per side are used for transmission, while all sections are used for reception. The signals from the separate sections are then used to steer the beam normal to the heading of the vehicle, which allows for yaw of up to •5°. High sea states of 6 and above may produce greater yaw, giving "dropouts" in the records. The range resolution for a 30-sec. pulse repetition rate is 45m, while at 10 knots,

the near-ship along track resolution is 150 m. The finite (2.7°) beam-width leads to far range resolution (along-track) of about 1200 m (Fig. 3.1).

3.2.2 Acquisition of GLORIA data

The Easter Microplate GLORIA survey was conducted on board the RRS Charles Darwin during October-November 1988 (Searle et al., 1989b). Ship's speed during the survey averaged about 10 knots, and the track was fixed by satellite navigation (see Chapter 2). Most of the ship's tracks were positioned about 18 nm (33 km) apart in order that good acoustic coverage was obtained throughout. However, due to the limited survey time, in the southern part of the microplate, where the tectonics of the region were considered well understood, and in the Pito Rift area, where there is comprehensive Sea MARC II coverage (Hey et al., 1987), the ship's tracks were positioned further apart.

The data were recorded in 6 hour files or "passes" of 720 scans (see raw GLORIA pass, Fig. 3.2a). Using navigation and along-track depth measurements, slant-range corrections were routinely carried out by the GLORIA technicians on board the ship (Fig. 3.2b). Further processing of the replayed GLORIA data was carried out aboard ship by T.P. LeBas and R.C. Searle (Searle et al., 1989b). Filtering was used to smooth the appearance of the ship's track down the centre of the image, to remove the line dropouts and striping noise, and also to smooth the image by reducing high-frequency random noise. (These processes are described in detail in section 3.3.2). "Shading" corrections were also applied to compensate for the variation in overall brightness across GLORIA images (this is also described in detail in section 3.3.2). The application of a shading correction results in an enhanced image with a more uniform contrast across each pass from left to right. Previously unseen information in the weak near- and far-range areas (the centre of the image, and the extreme left and right, respectively) may be revealed, enabling better comparisons between features at different ranges. The final stage of shipboard processing involved correcting for along-track variations in the ship's velocity, and the resulting image is shown in Fig. 3.2c.

The data thus processed were used to compile an initial shipboard GLORIA mosaic, which was subsequently presented (Rusby et al., 1988) and published (Searle et al., 1989).

3.2.3 Artifacts of GLORIA images

The interpretation of GLORIA images requires an awareness of any artifacts remaining in the data. Few of these were noticed on the GLORIA sonographs collected during cruise CD35, but are mentioned here for the sake of completeness.

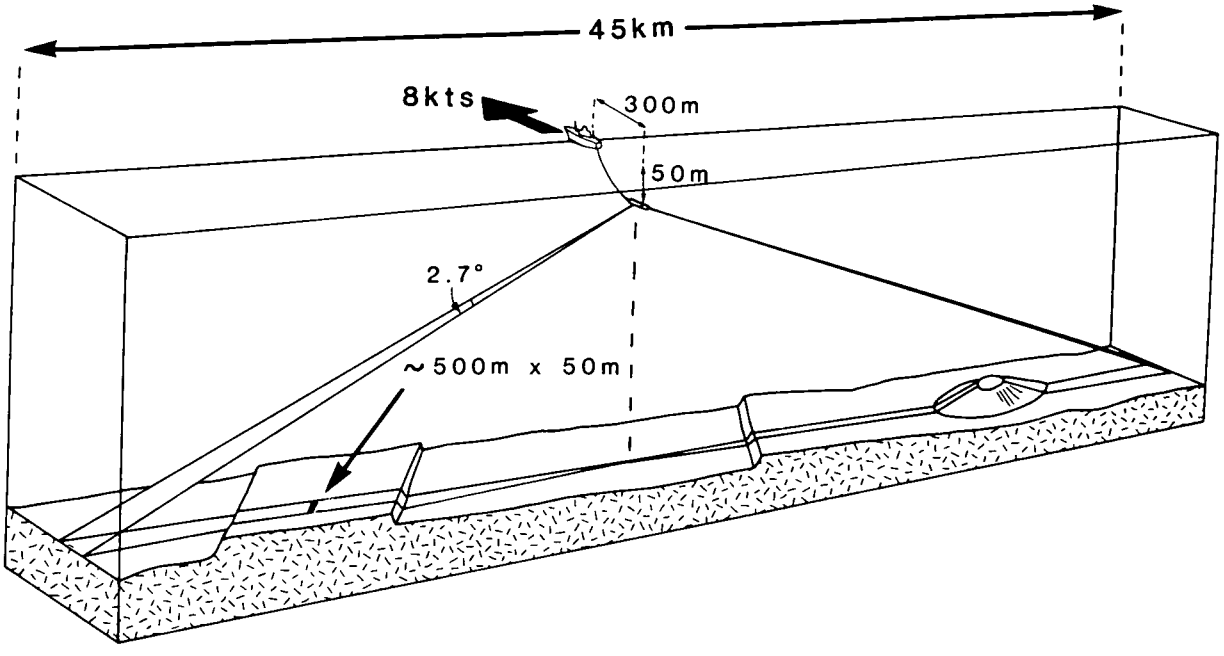

Figure 3.1 Schematic diagram of the GLORIA tow-vehicle and its sound swath, with principle dimensions (from Searle et al., 1990).

Figure 3.2 (a) Example of the 'raw' GLORIA pass as it is stored on magnetic tape prior to any corrections being carried out. This pass is from 24.8°S, 116°W, just to the south of the Terevaka transform, showing the northern end of the southward propagating rift. Various geometric and radiometric problems can be seen in the image. The extreme edges (left and right) are the far-range locations, and the centre of the image is the near-range or nadir location (ship's track). (b) This image shows the results of applying the slant-range to ground-range corrections to the image in (a). Due to the extreme difference between the near- and far-range depression angles, the pixels at near range (nadir) are expanded much more than the pixels at far- or mid-range. (c) The final GLORIA image produced after filtering and shading corrections have been applied to the data, as well as corrections for variations in ship's velocity in the along track direction. The low-frequency brightness variations that occur in the across-track direction have been eliminated by the shading corrections. The filtering has smoothed the 'blocky' appearance of the near-nadir pixels of the ship's track, and if there were any line dropouts and striping noise, or speckle noise, these would have been removed.

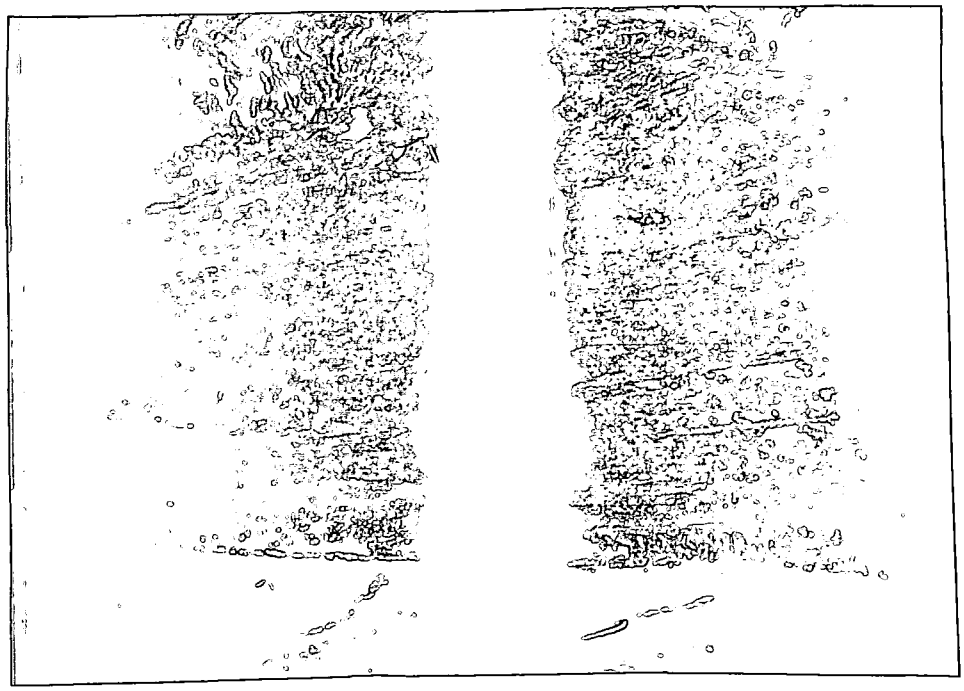

a

b

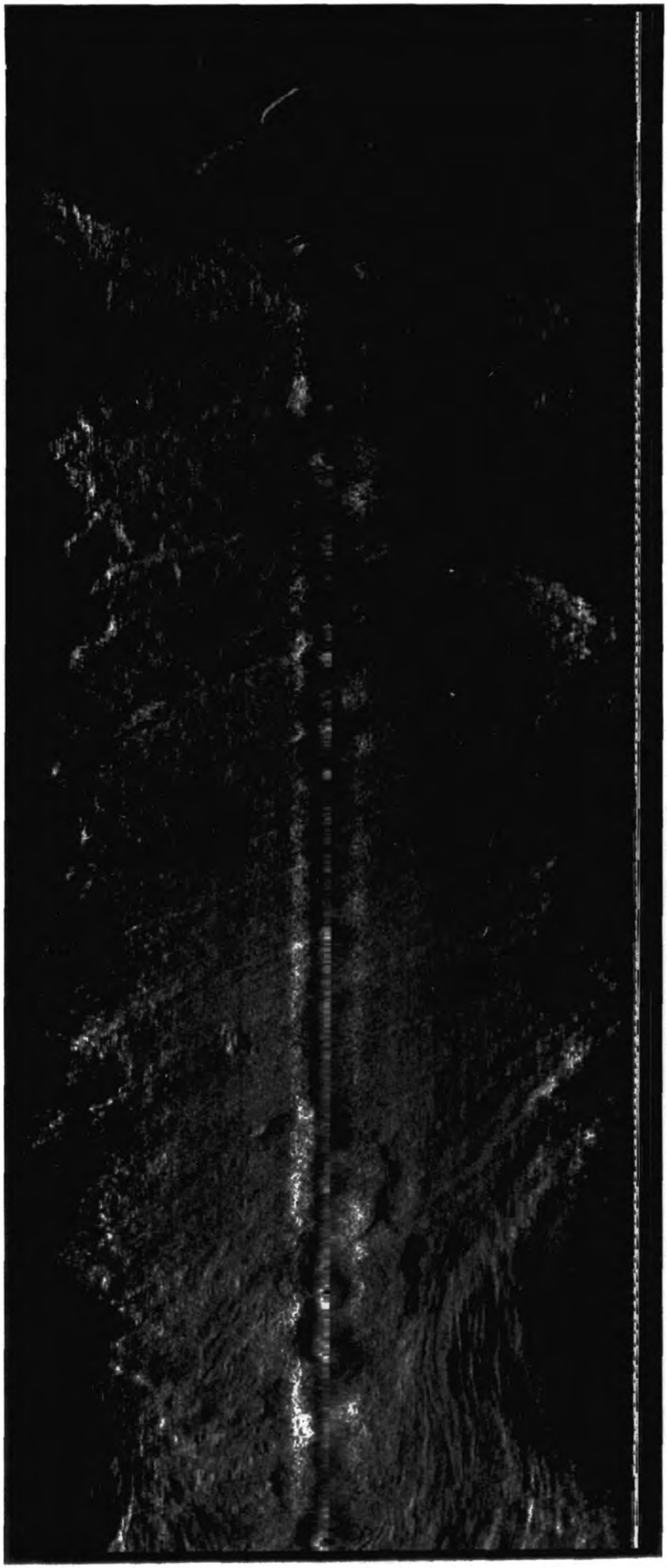

C

Geometrical distortions have mostly been removed during the preprocessing stages, although foreshortening and "layover" (which results in the top of the slope appearing closer than its base) (see Mitchell, 1991) may result, in areas of extreme topography, from the use of only central water depth data in slant-range to ground-range conversions. This assumption that the sea floor is flat results in shortening of slopes facing towards the sonar vehicle, and lengthening of slopes which face away (see Mitchell, 1991). This may have occurred on the CD35 data along the Initial Rifting Scarps (Fig. 2.1 and Fig. 4.5a) and the fracture zones (Fig. 2.1 and Fig. 4.1a).

Multiple backscatter (equivalent to peg-leg multiples in seismic sections) is found on GLORIA images when the returned signal makes two or more reflections in the water column. This produces pale, diffuse features imitating the primary image, which are situated progressively further away from the ship's track. These features are more common in the far range of GLORIA images, especially when the primary reflection is particularly strong, and can be seen at around 26.6°S, 115.5°W in Fig. 4.5a from the Southwest Rift.

The use of different frequencies for the port and starboard signals is designed to reduce the occurrence of "cross-talk" across the sonar vehicle, which would result in mirror images of strongly backscattering lineaments appearing on opposite sides of the sonographs. This effect is rarely observed and was not seen on any of the data used here.

The effects of yaw, resulting in dropouts in the images, and the use of filters to correct for this, has been discussed above, as has the use of shading corrections to compensate for the variation in overall brightness across GLORIA images. Other artifacts, such as refraction of the sound by internal waves in density interfaces in the near-surface waters, or scattering of sound by fish shoals were not observed on any of the CD35 data.

3.3 Processing of GLORIA data using the MIPS (Mini Image Processing System) software

3.3.1 Introduction

Further processing of the GLORIA data collected on cruise CD35 was carried out at IOSDL, Wormley, using the United States Geological Survey's MIPS (Mini Image Processing System) software (Chavez, 1984) run on a Micro Vax II. This software was originally developed to process data from ground mapping satellites such as Landsat, but has subsequently been altered for use with sidescan sonar. The processing was carried

out in two main stages. Firstly, the "pre-processing", which involves geometric corrections and image enhancement, and secondly, the geographical registration and digital mosaicking of the pre-processed segments. Many of the programs used now in the MIPS system are run from command files which enable the programs to be run in batch, and the need for time consuming manual entering of parameters has been reduced considerably.

Before processing begins, it is necessary to subdivide the total area surveyed into manageable regions. The most convenient size for the region of the Easter Microplate is 2° latitude x 2° longitude "squares", which results in final mosaics of about 4776 lines (pixels in the vertical, y, direction) by 4454 samples (pixels in the horizontal, x, direction), depending on the latitude. The Easter Microplate region was divided into 10 main areas, and two additional smaller areas.

3.3.2 Pre-processing of the GLORIA image data

Because the results of the shipboard processing had not been digitally stored, the raw digital data had to be "pre-processed" from scratch in a similar manner to that employed at sea. This had the advantage that improved parameters, e.g. edited navigation and depth data, could be applied.

The raw data from CD35 are stored on seven magnetic tapes. A program GLO87 was used to read the files required for one pass from tape and write them on to disk in the standard MIPS format (an array of 720 lines and 1024 samples per pass). Files were then selected to be "tacked" together to form an unbroken straight line ship's track (or "segment") through the mosaic area, and joined using the program MOSAIC. (Note, this does not mosaic the data in the usual sense of juxtaposing them in their correct geographical locations.) A ship's track chart of the cruise, marked with date and time at ten minute intervals, was used to determine the start and end times of the track being processed. Typically two or three passes were tacked together to form a continuous east-west image across the mosaic area (resulting in files 1440 or 2160 lines long). Program SSHDR was run to find the corresponding start and end line numbers, as given by the header information stored in the raw data files. Data lying outside these start and end line numbers was then trimmed using DK2DK. The resulting file is now ready for processing.

A suite of thirteen MIPS programs have been combined into one command file (called PROCOM), which deals with all the pre-processing stages in turn, i.e. merging the navigation data, shading and filtering corrections, and anamorphic corrections for changes in the ship's velocity along track. The programs may be run individually if preferred, but it is usually convenient to submit several of these batch jobs to be run

overnight, for instance. Before running PROCOM, it is important to ensure that all the parameters given are correct. Firstly, a NAVIGATE.DAT file must exist, which contains all the navigation and bathymetric data from the cruise to be merged with the image files. Secondly, a file containing shading correction factors must be produced. The default is to use the SHADE2 function, whereby an along-track average of a single 6-hour pass is used to automatically make the corrections, but the results from this are rarely satisfactory (see Searle et al., 1990). A better method is to use the SHADE3 function which applies a user-defined shading correction factor for the whole region. In order to determine the appropriate correction factor, several passes from different terrains were examined in order to produce a "standard" across track profile. In particular, three sample passes were examined. These were: Pass 70, from around 24.5°S, 116°W, i.e. an area of young, strongly reflective seafloor; Pass 68, from around 24.5°S, 114°W, i.e. an area of older, sedimented seafloor that is weakly reflective; and Pass 95, from north of the microplate, where there is a gradual spread of reflectivity. From the "standard profile" constructed from these passes, its inverse, the correction factor, was determined (see Fig. 3.3) and stored in a SHAD3.DAT file created for use with the GLORIA data.

In addition to these two data files, five possible arguments may be given along with the command to run the programs. These are the map (or mosaic) number, the segment number, the shading method (e.g. SHADE3), the pulse repetition rate, and a yes/no flag indicating whether or not the intermediate files produced should be deleted. The thirteen different stages run by PROCOM are as follows:

(1) MRGNAV inserts the navigation data into the header information of the GLORIA sonar image data. The original header contains information on date, time and line number and also "fish" heading, and so position and depth information for each "ping" must be added, by matching times and interpolating the navigational data when required.

(2) SLR2GR applies two corrections simultaneously to the data. The true nadir pixels, as recorded, in a raw data file are offset to the sides of the ship's track as a function of the water depth. Using the bathymetric value, this offset is removed. Secondly, a slant-range to ground-range correction is applied to the data.This is achieved by computing the horizontal range for a given slant-range, assuming a plane horizontal seafloor whose depth is that below the ship. As a result, the near range pixels are "stretched", while the far range ones remain almost unaltered. This stretch is achieved by the duplication of some pixels. The resulting file now contains only 924 samples in the across track direction instead of the original 1024, as the pixel width has been changed from 46 m to 50 m.

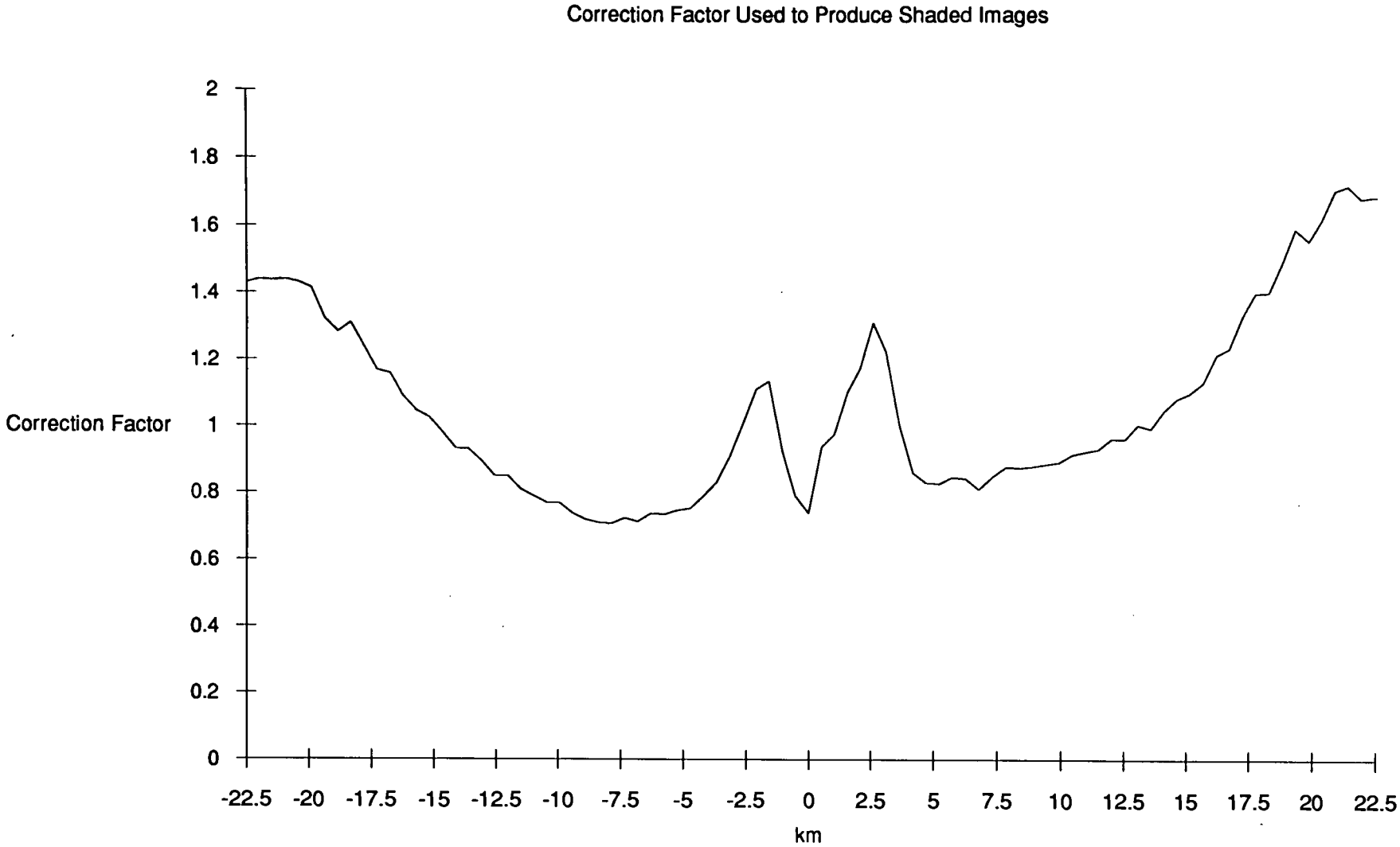

Figure 3.3 The correction factor used to correct the GLORIA passes for across-track variations in 'illumination'. This was calculated by producing plots of average and maximum response for each range pixel for several passes, so that a 'standard profile' could be calculated. Three passes in particular were chosen to produce this 'standard profile' (Pass 70, from an area of young, strongly reflective seafloor; Pass 68, from an area of older, sedimented seafloor that is weakly reflective; and Pass 95, from an area where there is a gradual spread of reflectivity). From this resulting 'standard profile', the inverse correction factor shown was calculated.

(3) SHADE3 applies a pre-determined shading correction given in SHADE3.DAT to the image file by multiplying each sample in a line by a correction coefficient. The effect of this is to reduce the across-track variation in overall brightness due to the change of system response with range (through attenuation and transmitter power distribution patterns). This program is the first to alter the DN (digital number) values of the pixels rather than just change their location.

(4) The next three programs are used to filter out the effects of the near-nadir pixels of the ship's track. The duplicated pixels are smoothed so that they have a less "blocky" appearance. This method was only introduced to the MIPS system fairly recently by the U.S.G.S. and seems to be very successful in reducing the distracting nature of the near-nadir pixels. FILTER8 is a general filtering program and is first used to apply a low pass "box-car" filter (LPF) of 151 lines by 401 samples. For a "low pass" filter, all the pixels within the "box-car" are averaged, and the pixel in the central position is replaced by this average value. FILTER8 is then used again to apply a high pass "box-car" filter (HPF) of 151 lines by 31 samples. For a "high pass" filter, all the pixels within the box-car are averaged, and the central pixel is replaced by the difference between the average value and the actual value of the central pixel. Program WTCMB08 simply adds the two new values of each pixel together to give a final value, justified by the equation:

DN_{new} =Average in LPF + (DN_{old} - Average in HPF)

If there is no difference between the average of the low pass filter and the average of the high pass filter, the DN value of the central pixel will remain unchanged.

(5) The same three programs are run again. This time the main effect is to remove the line dropouts and striping noise, using a combination of high- and low-pass filtering. First FILTER8 is used to apply a low pass filter of 9 lines by 71 samples. This produces an image that represents the low-frequency spectrum of varying geological field and range dependent variation, that is the regional effects, except for the noise frequency. Secondly, FILTER8 is used to apply a high pass filter of 1 line by 71 samples. This image represents the high frequency spectrum of detailed topological changes and geological differences, that is the localised effects, without the noise. WTCMB08 is used to combine the two images in the same way as described in (4) to create an image very similar to the original, but without the noise, which effectively removes the line dropouts.

(6) MGHEAD is used to replace the headers that have been removed during the filtering stages. It uses the header information stored in the file produced by SHADE3, and overlays this header onto the output of the second WTCMB08. The filtering programs were originally designed for use with data sets other than GLORIA images, which did not require the use of header information.

(7) DELTAV corrects the GLORIA sonar image data for changes of the ship's velocity and aspect ratio distortions using the latitudes and longitudes supplied with the navigation data. This results in the image being "stretched" in the along-track direction so that the across- and along-track scales are the same. An average velocity calculation is made over every 30 minute period. The distance covered by the ship during each period in a 6 hour pass is calculated, and so the amount by which the file needs to be "stretched" through the duplication of lines is determined. The resulting file is usually some three times the length of the original.

(8) LPF2B2 smooths the image using a 2-pixel by 2-pixel moving average low-pass filter. It is used to reduce high-frequency random noise or "speckle" and also helps smooth the blocky appearance that the image will have from the pixel duplication in the along track direction due to the aspect ratio correction. This again destroys the header information.

(9) MGHEAD is used to replace the headers removed in stage (8) using the header information in the output file from DELTAV. The final output file resulting from this program is suffixed by .MG2. This file is then backed-up before using in the transformations described below.

The final image produced in stage (9) is displayed on the TV monitor to check that the pre-processing has been satisfactory. The procedure described above is then repeated for all the other ship's tracks that pass through the mosaic area, before proceeding with the second major stage of processing, i.e. the geographical registration and digital mosaicking of the pre-processed segments.

3.3.3 Geographical registration of the pre-processed GLORIA images

Another suite of MIPS programs has been combined into a command file known as TRANSFORM. This deals with all the processes involved in the geographical registration of a segment (i.e. the resulting .MG2 image) of pre-processed GLORIA data within the mosaic area. Previously, this process was a very time consuming and tedious, involving a lot of manual typing-in of control point line and sample numbers, and their corresponding latitudes and longitudes, and x and y coordinates. Only four control points were used to register each segment within the 2° latitude x 2° longitude mosaic, using a second or third order polynomial. Results were often unsatisfactory, as the ship's track was not well approximated, resulting in geological features from separate segments failing to match up. The second- or third-order polynomials could only accommodate very small changes in the vehicle heading (3 - 4°), whereas often larger changes than this are found to exist in a "straight" ship's track. The vehicle heading information then had to be

edited to remove these small glitches, and the process repeated. Mosaics 1 to 4 of the CD35 data were processed in this way. Using this method it took about a week to process a whole 2° x 2° mosaic.

Fortunately, as the British Antarctic Survey were encountering the same difficulties in processing their GLORIA image data using the MIPS system, J. Thomlinson and R. Livermore (from B.A.S.) decided to modify the existing procedure, and the resulting TRANSFORM suite of programs has been adapted for use at IOSDL by T.P. LeBas. This group of programs is now able to accommodate a considerably larger number of control points, sampling the segment, say, every 20th, 30th or 40th line. A standard .MG2 file containing over 2000 lines, if sampled every 20th line, would result in over 100 control points being used. These control points are used to approximate the ship's track using a polynomial of degree 2. Initially the command file was set up to allow polynomials of a higher order to be applied to particularly long segments, but this was found to be unnecessary and is no longer used.

One of the arguments given when submitting the command file concerns the maximum course deviation allowed, before the segment is automatically divided into separate files (each with its own polynomial fit). The default value is set at 15°, although for the CD35 data, 20° was used throughout. Although it takes longer to transform the data to its geographical position using such a large number of control points, far more time is saved by removing the tedious chore of entering control point information manually. Running the process as a batch job also means that several TRANSFORMs may be setup to run overnight (if disk space exists), along with the PROCOM routines described above. This considerably reduces the number of days needed for the processing of the digital GLORIA images. Thus most of the normal working day can now be spent carefully stencilling the processed segments together, a process which will always be best done manually, to ensure that the most useful data is extracted from overlapping GLORIA segments.

The procedure presently employed using TRANSFORM is thus as follows. Firstly a MAPn.DAT file must be created, where n corresponds to the number given to the mosaic being produced. This file requires seven values concerning the 2° x 2° mosaic area: the minimum and maximum latitude; the minimum and maximum longitude; the map projection code (e.g. 1=UTM, 5=Mercator) and the standard latitude and longitude. Again, up to five arguments may be given when submitting the program. These are: the mosaic and segment number; the pulse repetition rate (default is 30 seconds); the line increment parameter (default is every 20th line will be used as a control point), and the maximum

course deviation allowed, before the segment is automatically divided into separate files (default is 15°). The different stages executed by TRANSFORM are as follows:

(1) The mosaic limits and other arguments are read from the file MAPn.DAT to be input as parameters.

(2) IMCUT reads the header information from the last file output from PROCOM (.MG2). Every 20th (default) line heading is printed into a file (BMERKY.INP) and this header information is used to locate the segment geographically within the 2° x 2° square. Where the variation in successive headings is greater than 15° (default), the segment is divided into separate pieces, and each piece is then processed separately. The number of lines in the .MG2 file and the starting line number are found.

(3) DK2DK is run to trim the first 32 pixels of header information from the .MG2 file, so that the number of samples in one line of data is now 892.

(4) BMERKY converts the latitude and longitude position of all the control points stored in BMERKY.INP into new line and sample numbers. With a pulse repetition rate of 30 seconds, the sample number for each control point along the ship's track will always be 446 (since the total number of samples in each line is 892 once the header has been removed). Vehicle heading information is also retrieved and is used to produce two further control points at far range port and starboard (pixel 1 and 892). The results are stored in a file TFGEN.INP.

(5) TFGEN generates a transformation file (TFILE) for the program GEOM using polynomial curve/surface fitting techniques. Control point information is read in from TFGEN.INP, along with the vehicle headings. Other parameters are entered from the TRANSFORM command file. These are usually: nrow=40, ncol=40 (number of rows and columns in the transformation matrix); degree=2 (degree of polynomial used); proj=5 (for Mercator projection); clon=0 (standard longitude is not required for a Mercator projection); clat=-25 (standard latitude of 25°S for Easter Microplate region); pixres=50 (pixel resolution of 50 m); starting and ending latitudes of the mosiac and starting and ending longitudes of the mosaic.

For each line for which control point information has been obtained, the positions of the extreme port and starboard pixels are determined, in terms of x and y coordinates (referred to, rather confusingly, as sample and line numbers once again, although these are different form those used for a .MG2 file) within the 2° x 2° mosaic, using the vehicle heading and the parameters given. Thus the original hundred or so control points have been increased to over three hundred. These pixel control points are linked to geographic

coordinates using the ship's navigation and heading which in turn are linked to the pixel coordinates on a mosaic map. This gives a pixel to pixel transformation for any given map projection. The resulting transformation file is TFILE.DAT which contains all the information necessary to place the GLORIA image within the geographical reference of the mosaic.

(6) GEOM is run, which uses the image segment and the output from TFGEN (i.e. TFILE.DAT) to create the final image segment (or geom), with all the GLORIA data correctly positioned within the map area.

If IMCUT has not subdivided the .MG2 data file in stage (2), stages (3) - (6) will be carried out once. Otherwise the procedure is repeated for each segment.

3.3.4 Digital stencilling and mosaicking of geographically registered GLORIA images.

Each geom exists as a complete image covering the entire map area, including the insonified area of the processed GLORIA image along the ship's track. In order to combine two images, which in general will have overlapping coverage, both are displayed in separate colours (usually red, and green) on the TV monitor. TVSTCL is used to carefully stencil around the useful sonar data of one geom using a trackball. The stencil line is displayed on the monitor as it is being drawn. The line can be undone at any stage, and the program allows one to zoom in to up to 8 x magnification to enable detailed examination of individual pixels. Each colour can be switched on and off so that comparisons can be made between the geoms.

In a well-planned survey area, where sufficient time is available, ship's tracks are usually run parallel to each other, and positioned an optimum distance apart, allowing a small overlap of data, but not unnecessary duplication of data. In the case of CD35, the ship's track were positioned 18 nm apart (33 km) over the majority of the region, except where lack of time prevented this from being done. The resulting mosaics within the interior of the Easter Microplate were relatively easy to stencil together. In contrast, the area between 22° - 23°S and 112°-113°W, within mosiac 2, was extremely difficult to piece together, when at one time there were twelve adjacent pieces requiring stencilling. Also in mosaic 8 (which was right at the start of the survey), between 25° - 26°S and 117° - 118°W, nine short overlapping segments required stencilling. Extreme care must be taken to ensure that the most useful data from each segment is being retained. The mosaicking process is such a time consuming and expensive process, that mistakes made in haste may not usually be rectified.

Once a stencil line has been drawn completely around one of the geoms (taking care that the first and last pixels do actually meet up), the resulting vector file can be converted to raster format using VEC2RAS. MASKIM takes the original image and the stencilled line and converts all the DN values of the image outside the stencil line to zero, to produce an edited geom. This "masked" image can then be mosaicked on to the other non-edited geom using MOSAIC. If the "input" parameter is given, where the two images overlap, the DN values of the "masked" image are written to the output file, except where these are zero, when the DN values of the non-edited geom are taken.

Other parameters that may be given instead of "input" are: "average" (where the average DN value of the two images is taken); "minimum" (where the minimum DN value of the two images is taken); "maximum" (where the maximum DN value of the two images is taken); and "output" (where the DN values of the output file are taken except where these are zero). The use of, say, "average", or "maximum" is useful for a hasty mosaicking of two adjacent tracks, as stencilling and the production of a masked image is not required and a considerable amount of time is saved. However, the results are not very satisfactory. In mosaic 2, (see Fig. 4.16a, Chapter 4) "average" was used to join the two most northwesterly tracks together. As the average DN value is taken, where the DN value of a pixel from one geom image is 1 (where data is very small at the far range of the image), and on the other it is, say, 99, the output DN will of course be 50 DN. Along the join of the two images, therefore, the DN values are consistently less than they would otherwise be if one of the images had been stencilled, producing a dark band down the join between the two images. The next two adjacent ship's tracks were joined using "maximum". This has resulted in a rather bright band of pixels along the join between the adjacent images. So although the stencilling procedure is so time consuming, it is obviously well worth the effort.

Several geoms are joined together in the manner described, to produce the final composite mosaic. Care must be taken to back-up all the geoms and "masked" files at every stage, so that potential disasters may be avoided.

The final hard-copies are obtained by outputting the sonar images on to film by laser scanning. Presently this is done using the Spectrascan system at the National Remote Sensing Centre in Farnborough (Hants). The images are written onto film at a scale of usually 20, 25 or 30 microns per pixel. Before this is done, a contrast stretch is applied to the final mosaic on disk, to make the DN values more compatible with the resolution of photographic paper. A program HSTGRM is run, which generates a statistical histogram on the terminal screen (used as a quick look histogram). The mean, median and mode of the DN values from the whole mosaic are given, along with the standard deviation.

HSTGRM was run for all eleven of the final mosaics produced from the Easter Microplate CD35 data. The mean and standard deviation were noted for all of the mosaics. The averages of the means and standard deviations (S.D.s) were found to be 64 and 32 respectively. These were used to provide a linear contrast stretch to the image data as it was being written to magnetic tape using the program SPECTR. The stretch is usually calculated so that: the zero and 255 values stay the same; the values 1 to "the mean minus the S.D." (=32) are stretched between 1 and 25; values from "the mean minus the S.D. plus one" (=33) to "the mean" (=64) are stretched between 26 and 50; values from "the mean plus one" (=65) to "the mean plus the S.D." (=96) are stretched between 51 to 75; values from "the mean plus one" (=97) to 255 are stretched between 76 and 255. A grey scale of 16 equally-spaced brightness levels is produced on each Spectrascan negative, in order that the prints may be printed consistently. A final version of the processed GLORIA data is given in Plate 1, which is only about one seventh of the size (linearly) of prints normally required for GLORIA interpretation (a usual working scale is about 1:375 000).

3.4 Interpretation of GLORIA Images

10 kHz, 3.5 kHz and magnetic anomaly data collected concurrently with the GLORIA data, and that available from the World Data Center, Boulder, Colorado, were used to assist the interpretation of the sonar mosaic. The scale of the mosaics I used for the initial interpretation was 1:375,653. Different geological features are recognised on the GLORIA images from their shape, form, and textural characteristics. On the mosaics used in this thesis, bare lava backscatters acoustic energy strongly, producing very white records (Plate 1). Conversely, smooth sediments backscatter poorly and produce dark-grey to black areas on the records. Also, targets aligned parallel to the ship's track are usually well imaged, while those orthogonal to it are less well imaged, due to the anisotropic sampling of the side-scan system. Acoustic shadows are produced on the far side of prominent scarps, ridges and volcanic cones, which appear black on the records.

Fresh lava generated at spreading axes produces very strong backscattering. However, spreading rates are so fast in this region (up to 160 mm/yr) and sedimentation rates are so low (about 3 m/myr), that it is often difficult to determine the precise location of the spreading axis from surrounding lavas of up to about 0.5myr old. Therefore the use of magnetic and bathymetric data together with the sidescan data is of particular importance.

Long, narrow, strongly reflecting (white) lineaments are interpreted as fault scarps facing towards the sonar vehicle, while slightly broader ones are interpreted as volcanic

ridges. These linear trends are probably caused by acoustic scattering from fault scarps and rough breccia and talus formed along steep slopes and faults. Recent work by Mitchell (1991) has shown that the effect of bottom slope on the backscatter is secondary to the effect of changing bottom type. Scarps facing away from the sonar are sometimes revealed by narrow, linear shadows. Differentiation between scarps resulting from lateral strike-slip movement and those from vertical dip-slip is often impossible. Pseudofaults were recognised from their V-shaped plan pattern and from the presence of variations in orientation of spreading fabric between the propagating and dying rifts (Kleinrock & Hey, 1989b). There is also usually a distinct change in backscatter across the pseudofaults, due to the change in age, and hence sediment thickness, of the crust either side of them. Transform and thrust faults were identified as prominent topographic features usually oriented parallel/sub-parallel to the spreading direction and seamounts are well defined by their shapes.

3.5 Acquisition of Seabeam Data and Interpretation

All Seabeam data described in this thesis were obtained on cruises SO40 and SO62, on board the F/S Sonne in 1985 and 1989 (Marchig & Gundlach et al., 1987; Marchig et al., 1989) as part of the Geometep program (parts 4 and 5). These cruises aimed to investigate ore formation at rapidly diverging plate margins, including the East and West Rifts of the EPR, and the Seabeam multibeam sonar system was used as a tool for locating sites of possible hydrothermal venting and sulphide formation.

The Seabeam data from the Pascua cruises of the R/V Thomas Washington in 1983 (Hey et al., 1985), and mostly published in Naar & Hey (1986), and studied by Naar for his doctoral thesis (1990), is not described here, although this data has been incorporated in Naar's (1990) bathymetric map (Fig. 1.2, Chapter 1) which is used as a general reference. The data from the Rapanui expedition (Francheteau et al., 1988) has been described in detail by Zukin (1990) for her doctoral thesis, and is not further studied here.

The Seabeam system is hull-mounted and measures depth in 16 beams athwart-ships over a swath width equal to 75% of the water depth (Renard & Allenou, 1979; Farr, 1980) (see Fig. 3.4). The effective surface area or "footprint" covered by each beam is the ellipse formed by the intersection of the cone of the narrow fan-shaped beam with the seafloor. The beams are formed such that their outer edges abut, making the across-track component of the footprint and the across-track spacing the same. The receiver transducer array is normal to the transmitting array, producing a reception beam pattern that is wide athwart-ships but narrow fore-and-aft. The actual depth value recorded is an average depth, weighted by the backscatter strength of each small patch of seafloor and

SEABEAM

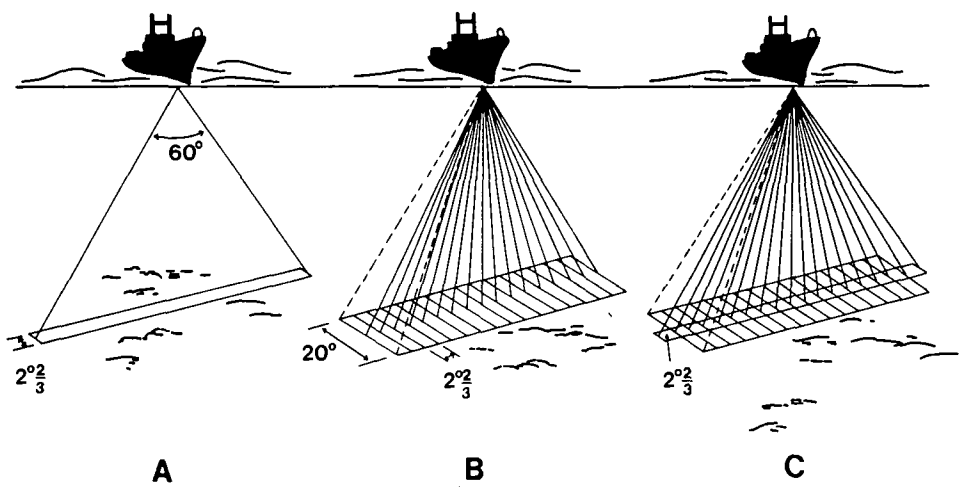

Figure 3.4 Configuration of the Seabeam beam pattern. (a) The transmission beam is 60° wide athwart-ships, which enables an effective swath width of 75% of the water depth to be mapped, and is only 2.7° wide in the along-track direction. (b) The receiver transducer array is arranged to receive a beam pattern of 16 beams that are 20° wide in the along-track direction and only 2.7° wide athwart-ships. (c) Transmission and reception beams overlap to form an effective beam for the whole cycle of 2.7° x 2.7°.

the effective beam directivity function. The drawback of the hull-mounted system is that data tend to be acoustically noisy due to near-surface turbulence and ship noise, especially during bad weather. Also variations in the sound velocity versus depth profiles produce errors in the depth and position values.

During surveys, realtime contour plots of along track variations in depth within the typically 2 km wide swath (for 3 km water depth) are produced, which can then be merged with navigation usually at daily intervals. The contour interval generally used for the resulting bathymetric maps is 20 m for location of camera, grab and core sites, though for the purpose of general tectonic interpretation used in this thesis, a contour interval of 100 m is most useful. Colour shaded bathymetric maps at a scale of 1:100 000 and contour interval of 100 m were later produced by Bundesanstalt für Geowissenschaften und Rohstoffe, Hannover. Copies of these maps were made available for my interpretation (see example in Fig. 3.5), although the contour maps used to illustrate this thesis (especially in Chapter 4) have been redrawn in black ink from these colour shaded maps and interpolated between Seabeam swaths by hand.

Geological interpretation of the swath bathymetry data is based on the recognition of the morphology of various elements. For instance, circular, close-contoured features are usually interpreted as seamounts, and closely spaced linear contours indicate the fault scarps that form the abyssal hill fabric. Overlapping spreading centres and propagating rifts are recognised from their distinctive patterns (e.g. Macdonald et al., 1988), and transform faults are usually orthogonal to the spreading fabric and are represented by extreme changes in topography. Flat uniform topography may result from either ponded sediments in basins, or from lava lakes.

Most of the German Seabeam data available is from the East and West Rifts of the microplate, since these were the sites being investigated for possible sulphide formations. These data complement the Seabeam data collected by the French (e.g. Francheteau et al., 1988) along the northern and southern boundaries of the microplate, and within the Pito Deep region. However, only preliminary attempts have been made so far to combine digitally the sidescan sonar and swath bathymetry data sets. The region where this has been most readily achieved is in the Pito Deep area (T.P. LeBas, unpublished work), where there is dense coverage of both French Seabeam and GLORIA data. Unfortunately, little additional geological information was obtained from this exercise. The extremely rugged morphology and texture of the area is poorly represented by the GLORIA sidescan data. Recently processed Sea MARC II side-scan sonar data and bathymetry data provide a much better insight into the tectonic processes occurring there (see Naar, 1990; Naar et al., in press).

Figure 3.5 Example of colour shaded bathymetry map produced by Bundesanstalt für Geowissenschaften und Rohstoffe, Hannover. This map is from the western ridge-transform intersection of the Raraku transform at around 23°30'S, 115°35'W. Contour interval is 100m, with colour changes every 200m.

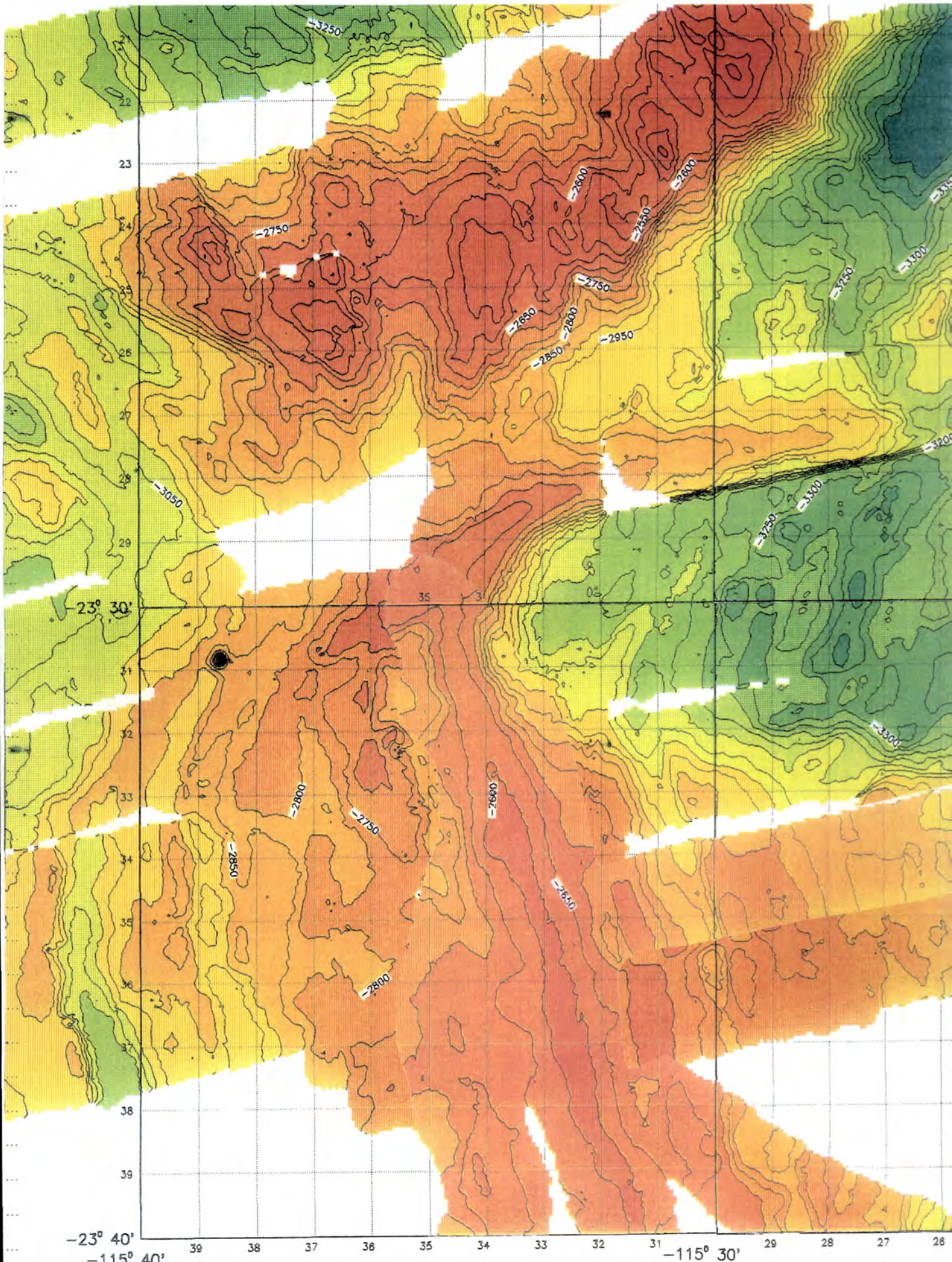
-3250
-2750
-2600
-2650
-2750
-2650
-2600
-2850
-2950
-3300
-3250
-3050
-3300
-3250
-2800
-2750
-2650
-2850
-2800
-2650
-2800
-3300
-23° 30'
-23° 40'
-115° 40'
-115° 30'
22
23
24
25
26
27
28
29
31
32
33
34
35
36
37
38
39
39
38
37
36
35
34
33
32
31
29
28
27
26

In areas where there are insufficient Seabeam data to warrant attempts at digital combination of the data sets, nevertheless, combined interpretation of the tectonic elements of the plate boundaries using the two data sets is considerably more useful than the interpretation of each data set in isolation. GLORIA data provides no direct information on depth, and semi-quantitative estimates of topography inferred from acoustic shadows is dependant on orientation of features relative to the ship's track, and original correct assumptions that "shadows" are not ponded sediments, etc., as well as an awareness of the effects of foreshortening, mentioned earlier. Likewise, swath bathymetry data only provides information on depth of the seafloor, and not backscatter strength, and so the type and texture of the seafloor, such as the difference between sheet lava flows, and ponded sediments, for example, cannot be determined from them alone.

CHAPTER 4
MORPHOLOGY, TECTONIC PATTERN AND GEOLOGY OF THE EASTER MICROPLATE

4.1 Introduction

In the first main part of this chapter, the morphology and tectonic pattern of the Easter Microplate is described, based on both the GLORIA data obtained during cruise CD35, and the Seabeam data acquired during the German Geometep 4 and Geometep 5 cruises (SO40 and SO62; Marchig et al., 1986; Marchig et al., 1989). The final processed GLORIA mosaic (see Chapter 3) is shown in Plate 1, with an interpretation at the same scale. Fig. 4.1 also shows a simplified interpretation of the GLORIA mosaic, with various features labelled.

The GLORIA data indicate that all of the microplate boundaries are evolving rapidly. Seabeam data are used to examine in detail the complex morphology of individual spreading segments and transform fault traces on both the East and West Rifts, as well as the complex Southern Triple Junction region, and thrust faults on the Nazca plate to the north of the microplate. On the West Rift, where the spreading segments are mostly offset by more than 50 km, sinistral strike-slip movement is usually taken up along rapidly evolving, right-lateral offset transform faults. On the East Rift, the spreading segments are offset by less than 50 km and no transform faults exist. Instead, as the northern ends of each spreading segment propagate northwards and overlap each dying rift to the east, the required sinistral strike-slip movement between each segment is accommodated by a "bookshelf" faulting mechanism (see Kleinrock and Hey, 1989), whereby the fabric between the spreading axes is progressively rotated from its original north-south orientation in an anticlockwise manner. As propagation takes place, a V-shaped pseudofault may form, separating fabric formed at the "doomed" rift (Searle & Hey, 1983) from that formed at the new propagating rift.

In the second main part of this chapter, geological data from around the Easter Microplate are examined. Published geochemical data from rock samples are examined in the light of their tectonic setting and proximity to the Easter hotspot.

Figure 4.1 Tectonic interpretation of the Easter Microplate based on GLORIA and SeaMARC II sidescan sonar data. Heavy lines show plate boundaries; medium lines mark pseudofaults and other discontinuities in crustal accretion; light lines are fault scarps of the tectonic spreading fabric. P indicates a propagating rift tip; WIPF, EIPF and EOPF are the West Rift inner and East Rift inner and outer pseudofaults respectively; three active transform zones are labelled Anakena, Raraku and Terevaka transforms; TZ denotes the sites of active strike-slip movement along the Pito and Orongo fracture zones of Francheteau, et al. (1988) i.e. at the northern and southern boundaries; FZ indicates a fossil fracture zone; OSC indicates an overlapping spreading centre. IRS indicates the Initial Rifting Scarp (see text); NTJ and STJ are the northern and southern triple junctions respectively.

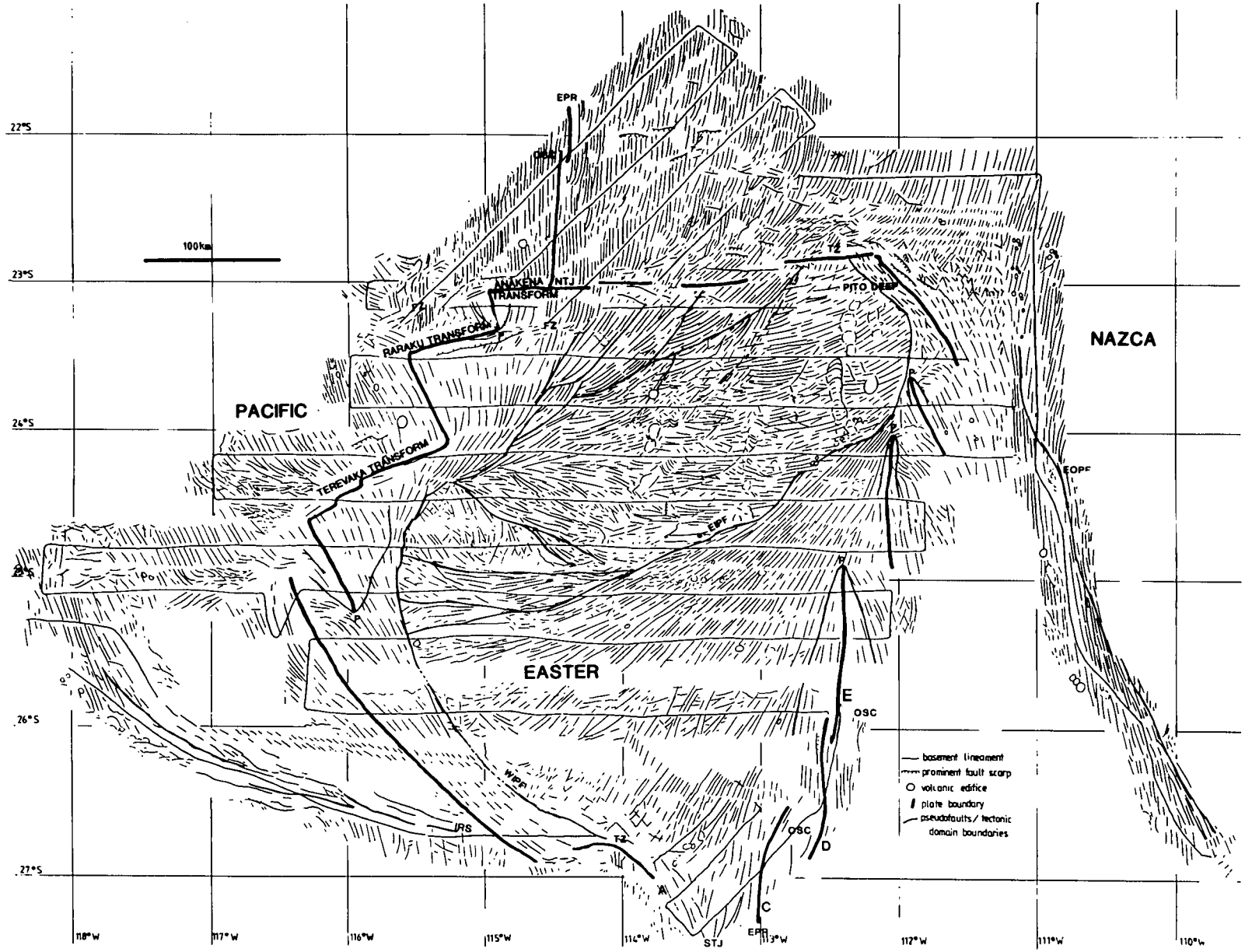
EPR
100km
ANAKENA TRANSFORM
NTJ
PITO DEEP
RARAKU TRANSFORM
FZ
PACIFIC
NAZCA
TEREVAKA TRANSFORM
EOPF
EPF
EASTER
E
OSC
IRS
WIPR
OSC
D
C
STJ
EPR
basement lineament
prominent fault scarp
volcanic edifice
plate boundary
pseudofaults / tectonic domain boundaries
22°S
23°S
24°S
26°S
27°S
118°W
117°W
116°W
115°W
114°W
113°W
112°W
111°W
110°W

4.2 Morphology and Tectonic Pattern

4.2.1 West Rift

The GLORIA image of the West Rift of the Easter Microplate is shown in Fig. 4.2a, and its interpretation is given in Fig. 4.2b. The West Rift consists of four spreading segments, three of which are connected by dextral offset (i.e. sinistrally slipping) transform faults which are herein named the Anakena, Raraku and Terevaka Transforms, after major features on nearby Easter Island (Fig. 4.1).

To the west of the Northern Triple Junction (NTJ), there exist a series of strike-slip fault strands which comprise the Anakena Transform. These fault strands have become progressively more rotated (up to about 10°) in an anticlockwise sense west of the NTJ. The overall trend of the Anakena Transform is 086°, i.e. almost east-west, and it is about 35 km in length. One of these fault strands can be seen to intersect with the start of the northernmost spreading segment of the West Rift (at 23°04'S,114°51'W) and is thought to be the most recent site of strike-slip movement.

At around 115°50'W, to the west of the Anakena Transform, amongst disturbed tectonic fabric, the remains of a fracture zone can be seen. EPR parallel fabric appears to have overwritten part of the ridges and valleys that make up this feature at a later date. This fracture zone trace is assumed to be an older continuation of the Anakena Transform.

South of the Anakena Transform, the northernmost spreading segment of the West Rift extends in a SSE direction, with an average depth of 3000 m, and typically fairly smooth topography. This segment is about 24 km long, and appears to have propagated southwards fairly recently. No clear pseudofaults are identified either side of the axis, but the characteristic rotated pre-existing fabric to the west of the most recently formed crust can be seen. This spreading segment intersects the Raraku transform fault orthogonally at 23°17'S, 114°51'W, with curvature of the neovolcanic zone towards the transform zone occurring only during the last 5 km.

The overall trend of the Raraku Transform is 072°, and its length is 78 km. It consists of two fault strands separated by an oblique extensional basin. The western fault strand (trending 080°) and extensional basin can be seen in Fig. 4.3, and the actual plate boundary appears to coincide with the edges of two ridges separated by a saddle. During the last 1 myr or so, the spreading axis to the south of this fault strand appears to have migrated 9 km northwards, abandoning a previously active site of strike-slip movement (Wilke & Lonsdale, 1987). To the northwest of the present day transform fault zone an

Figure 4.2 (a) GLORIA image of the West Rift, with line drawing interpretation in (b). The Anakena, Raraku and Terevaka transforms separate spreading segments that are progressively more offset to the south. Note: the remains of a fracture zone to the west of the Anakena transform; fracture zone traces to the east of the Raraku transform, indicating that it has existed for at least 1.5 myr; the oblique lineaments to the west of the Terevaka transform that are interpreted as evidence of earlier phases of rift propagation; and strongly rotated fabric to the east of the West Rift, i.e. within the microplate interior.

a

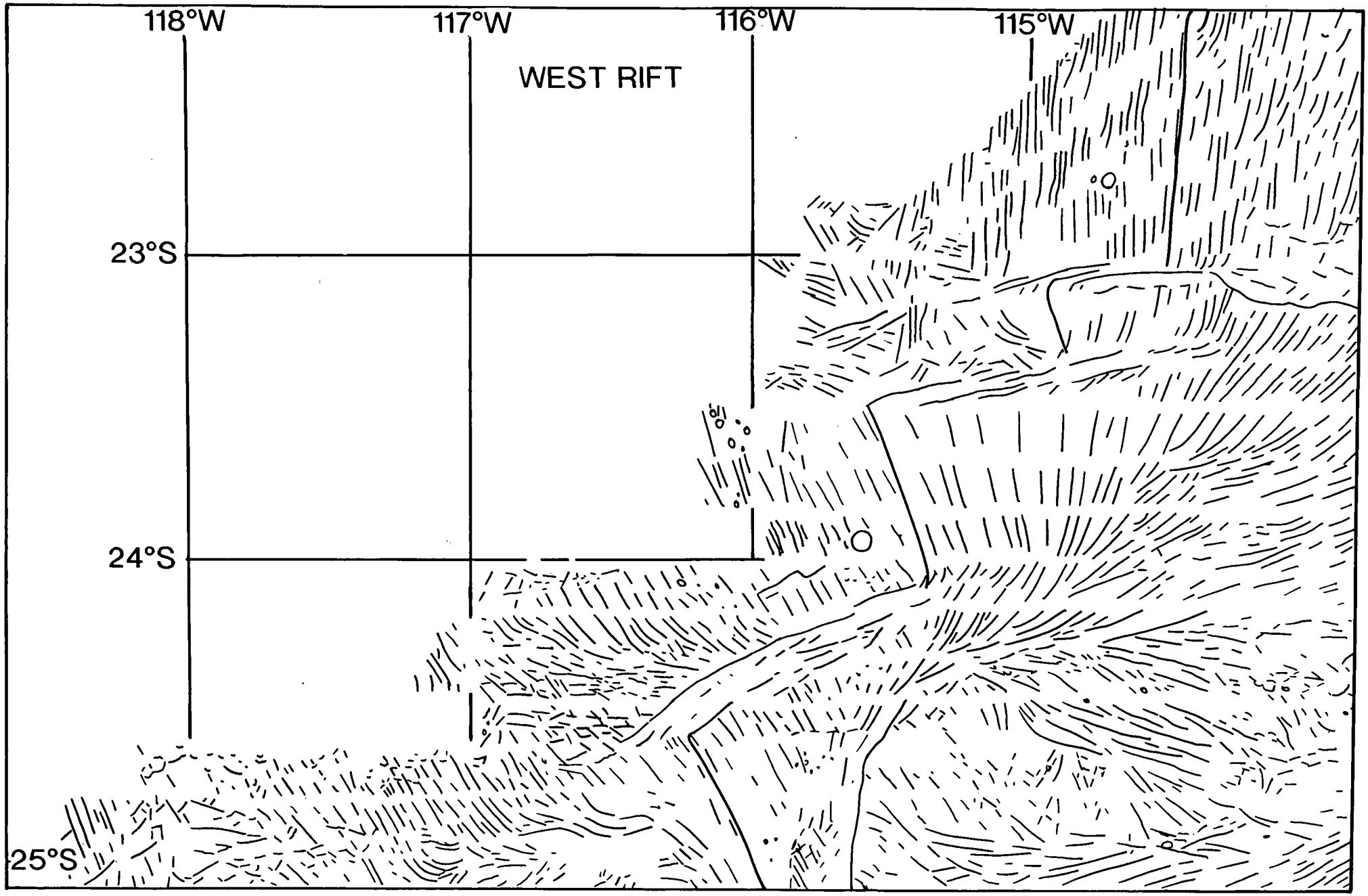

b

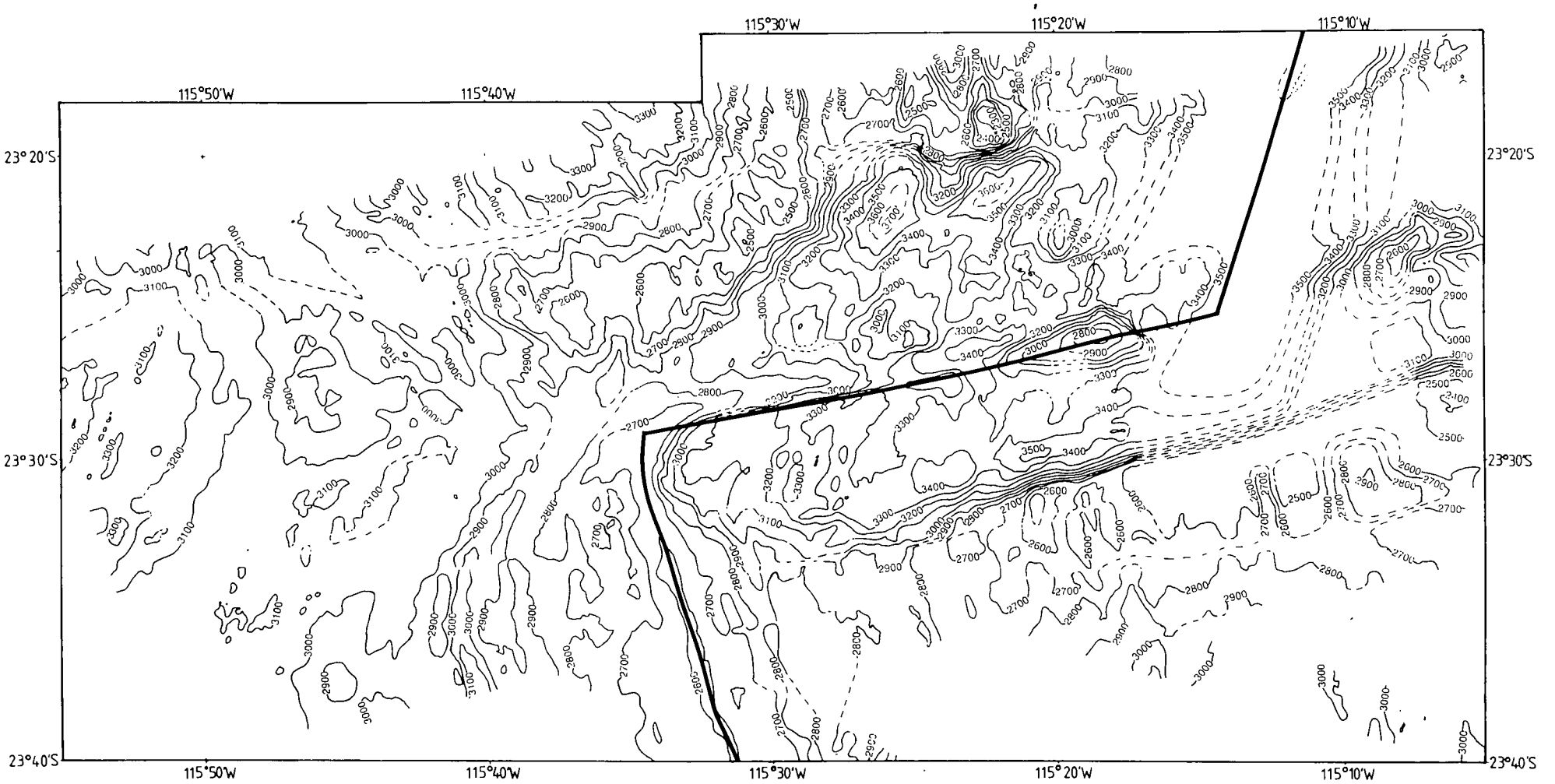

Figure 4.3 Seabeam bathymetric data at the western end of Raraku transform. In this and other Seabeam diagrams, heavy lines show plate boundaries; contour interval is 100 m; broken lines indicate extrapolated contours. Note: the present plate boundary has migrated 9 km northwards recently, abandoning the previously active site of strike-slip movement; complicated spreading fabric exists to the north of the transform which may be related to other plate boundary reorganisations; and curvature of spreading fabric to the west of the western ridge-transform intersection (RTI) into the transform.

area of complicated tectonic fabric exists (see Plate 1 and interpretation, and Fig. 4.2a,b) that may be related to earlier expressions of the Anakena Transform or other ridge jumps in the area. To the east of the transform, the GLORIA mosaic (Fig. 4.2a) reveals a fracture zone extending to 114°30'W, implying that the Raraku Transform has existed for at least 1.5 myr. The ridge-transform-intersection (RTI) at the western end of the Raraku Transform is at 23°29'S, 115°35'W.

The next spreading segment trends southeastward along a bearing of 153°. It is 70 km long, and forms a ridge along its length which deepens slightly towards the Raraku and Terevaka transform faults. Detailed examination of the GLORIA mosaic (Fig. 4.2a,b) indicates that this axis has not propagated southwards recently, but rotated spreading fabric seen to the west of 24°23'S, 116°13'W indicates that the ridge ceased southward propagation at about 1.5 Ma. The present day spreading axis intersects the Terevaka transform at 24°06'S, 115°21'W.

The Terevaka transform fault consists of at least two en echelon active transform valleys, separated by a N-S trending depression (Fig. 4.4). The northern active fault trace lies within the deep 11km wide transform valley trending 250°. On the GLORIA mosaic, the transform valley appears to extend to around 115°54'W where it intersects a north-south depression which is assumed to be extensional in nature. This type of oblique depression joining two en echelon strands of active transform faults is typical of medium- to fast-slipping long offset fracture zones (Fox and Gallo, 1984). The southern end of this basin intersects the southern active fault trace at 24°24'S, 115°54'W. This fault trace has an overall trend of 245° and at 116°10'W shoals rapidly to the RTI at 24°33'S, 116°13'W (Fig. 4.4).

Although older offsets of the magnetic lineations suggest that transform faults have existed in this area in the past, no obvious fracture zone trace is seen immediately west of the Terevaka transform, which would imply that the transform fault has remained in its present orientation for not more than 2 myr (corresponding to the age offset at the eastern RTI). However, several fault strands imaged by GLORIA southwest of 25°S, 117°W, all with similar trends to the Terevaka transform, may be relicts of a Terevaka Fracture Zone trace (Fig. 4.2a,b). Rotated spreading fabric, similar to that found further to the northeast at 24°23'S, 116°13'W, is seen abutting these fracture zone remains, and suggests the occurrence of older episodes of southward rift propagation at around 3Ma.

The spreading axis south of the Terevaka Transform (see Fig. 4.5) is in the form of a graben of over 3100m depth near the RTI, which then shoals to become a ridge at 24°43'S. This ridge then continues with a bearing of 150°and a depth of more than 2600m, becoming progressively deeper from around 24°58'S southwards, whilst

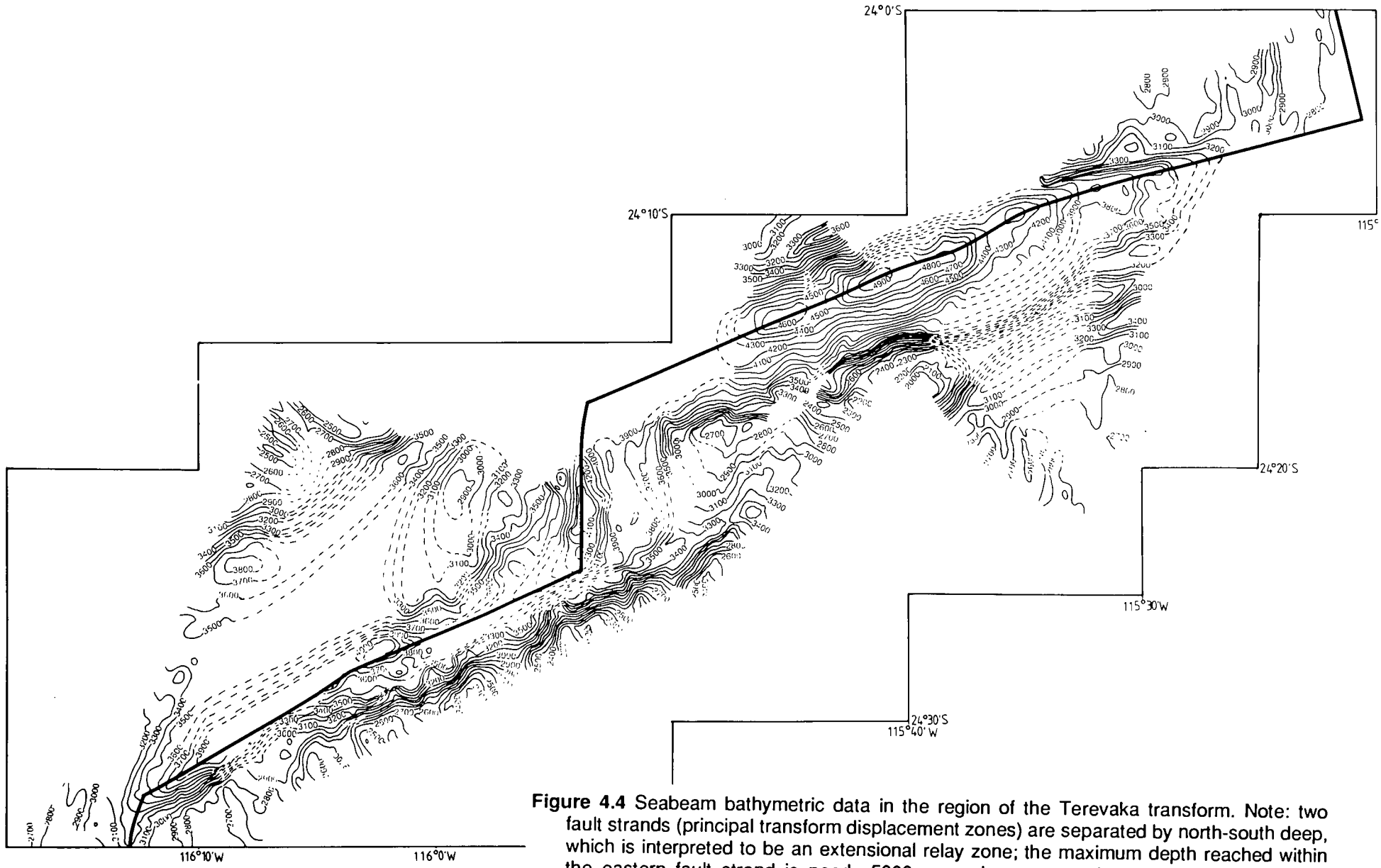

Figure 4.4 Seabeam bathymetric data in the region of the Terevaka transform. Note: two fault strands (principal transform displacement zones) are separated by north-south deep, which is interpreted to be an extensional relay zone; the maximum depth reached within the eastern fault strand is nearly 5000 m; and curvature of spreading fabric into the western RTI.

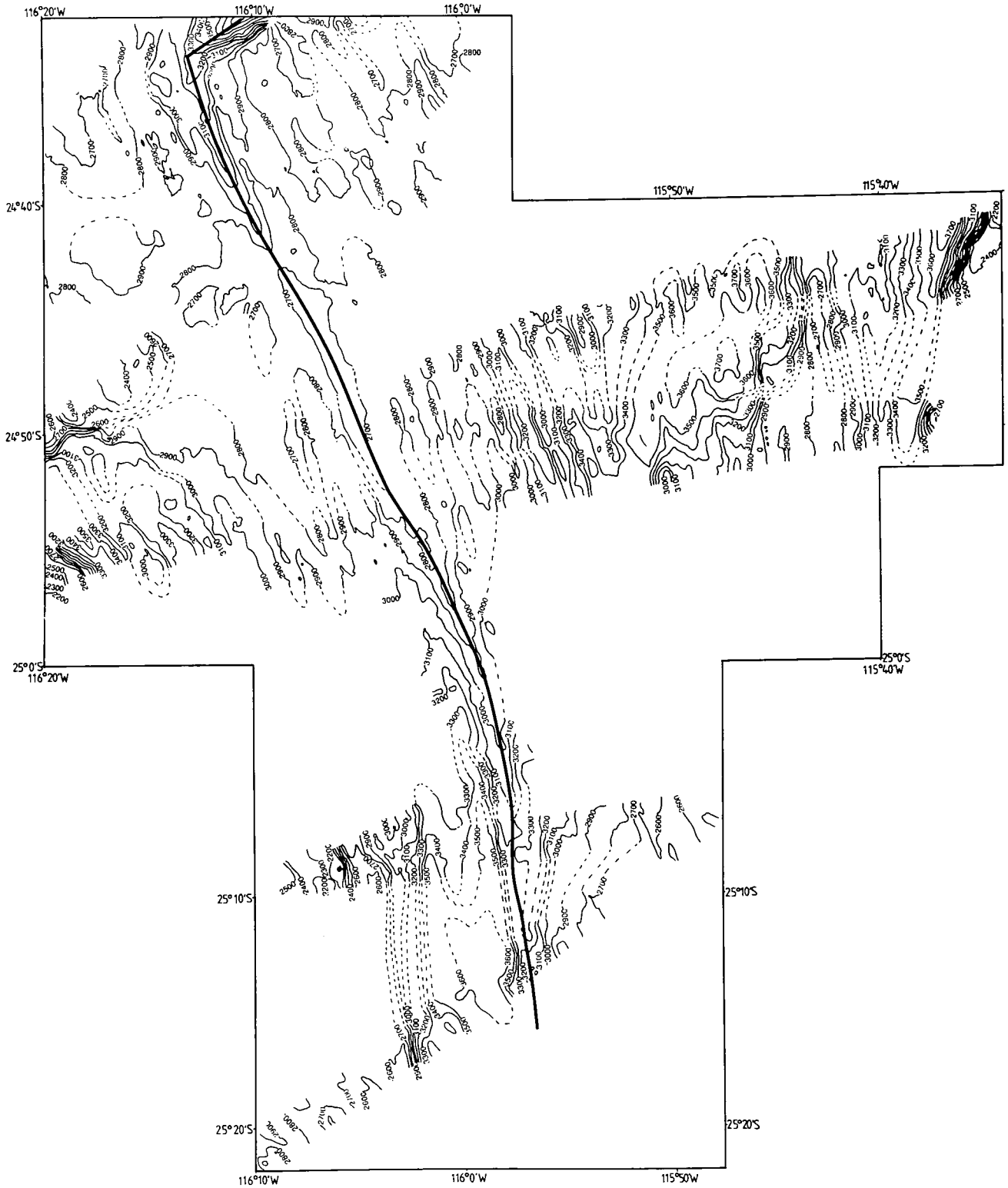

Figure 4.5 Seabeam bathymetric data of the propagator to the south of the Terevaka transform, which trends SSE at the RTI and then curves round to a more north-south trend near its southern tip.

becoming more N-S in its trend. The total length of this spreading centre is about 83km, with its southern tip at 25°16'S, 115°57'W. The GLORIA mosaic reveals two high-relief pseudofaults forming an asymmetric V-shape either side of the ridge, with angles of 35° and 40° with the spreading axis.These imply a propagation history of more than 1 Ma and a southward propagation rate slightly greater than the spreading rate.

4.2.2 Southwest Rift

The Southwest Rift of the Easter Microplate forms part of the West Rift, but differs in morphology and origin from that of the northern part of the West Rift and so is described separately here. GLORIA data of the Southwest Rift together with an interpretation are given in Fig. 4.6a,b.

The axis of the Southwest Rift is first identified on the GLORIA mosaic at 25°10'S, 116°25'W. The "tail" of this dying spreading axis seems to be curved round towards the propagator in the east, so that the configuration of the ridges is similar to an Overlapping Spreading Centre (OSC), with the fabric between the two ridges strongly rotated. The width of the overlap is about 44 km, and its length 54 km. The Southwest Rift continues in a southeasterly (135°) direction for a total of about 290 km until it breaks through the southern "initial rifting scarp" or IRS (see below) of the microplate at 26°46'S, 114°53'W. Francheteau et al. (1988) have proposed that the spreading axis may be segmented along its length, but the GLORIA and SeaMARC II data (see interpretation in Fig. 4.1) suggest that it is a continuous feature.

At 25°27'S, 116°14'W the axis is a narrow ridge of less than 2400 m depth which broadens progressively towards the southeast, forming a broad and robust neovolcanic zone, with a summit of 2200 m at 25°41'S, 116°04'W. The ridge has a smooth appearance, lacking in the usual ridge-parallel scarps near the axis. Schilling et al. (1985) found freshly frozen lava lakes at two locations on this broad axial ridge, which may imply extreme tension in this area giving way to rapid lava extrusion.

Further to the southeast the axis gradually narrows and deepens, and at 26°45'S, 114°53'W the GLORIA data (Figs. 4.6a,b) reveal the ridge actually breaking through the IRS. The spreading axis has an overall strike of 135°, and there is no evidence (either on the GLORIA data, or the French and German Seabeam data) to suggest that the spreading axis is offset left-laterally along its length (as suggested by Francheteau et al., 1988). It is not known how recently the axis has broken through the IRS, but if active rifting and magmatism is still taking place, then it must have occurred during the last 0.5 myr, since the width of the gap in the IRS is about 30 km (measured orthogonally to the strike of the rift axis), and full spreading rates at this latitude are about 60 mm/yr. The

Figure 4.6 (a) GLORIA image of the Southwest Rift, with line drawing interpretation in (b). Note: curvature of propagator and "tail" of Southwest Rift to form an overlapping spreading centre; the Southwest Rift continues in a southeasterly direction for a total of about 270 km before it breaks through the southern "initial rifting scarp" (see text) at 26°46'S, 114°53'W; the smooth appearance of the axis south of the propagator, lacking in the usual ridge-parallel scarps near the axis.

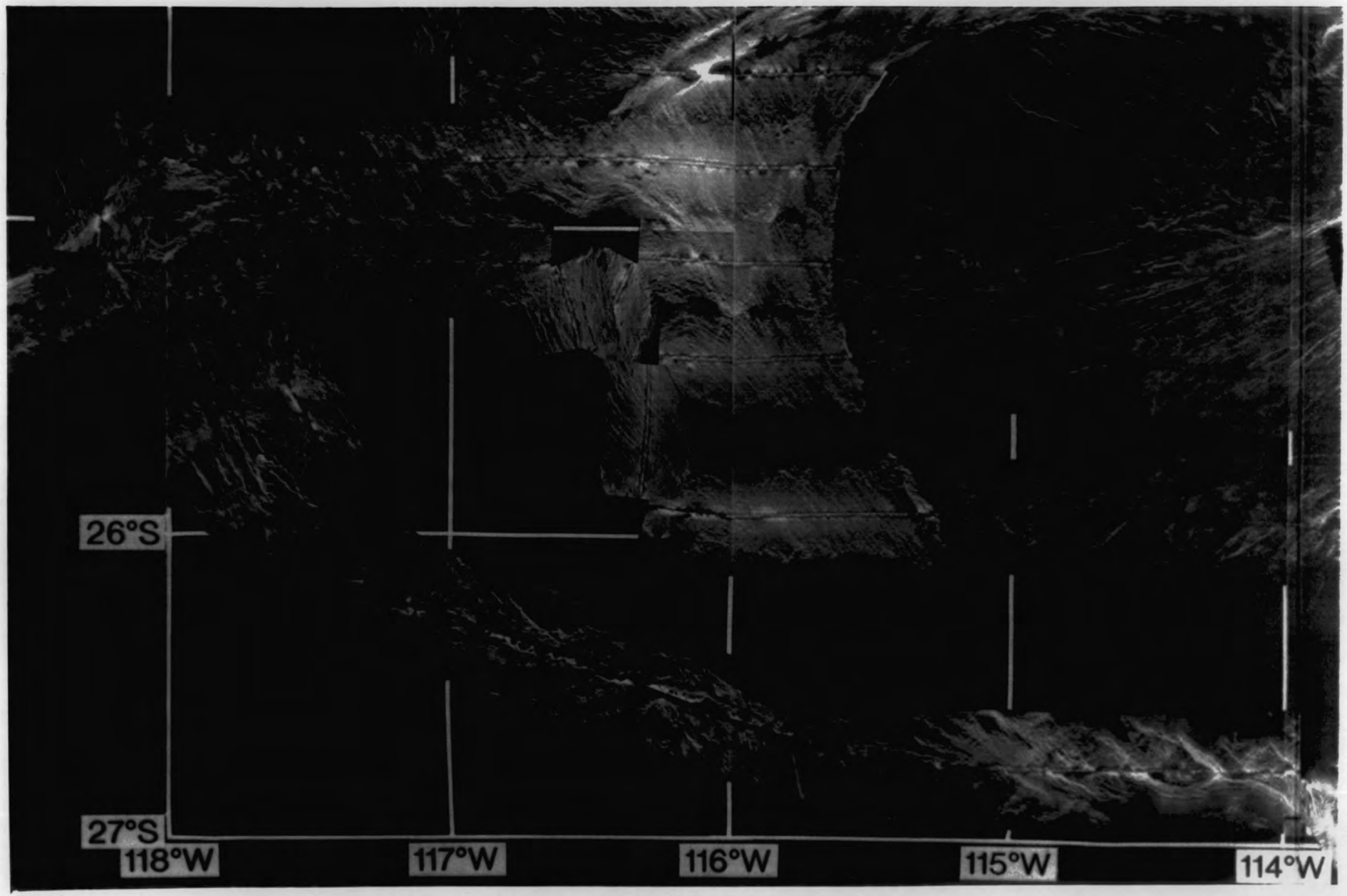

a

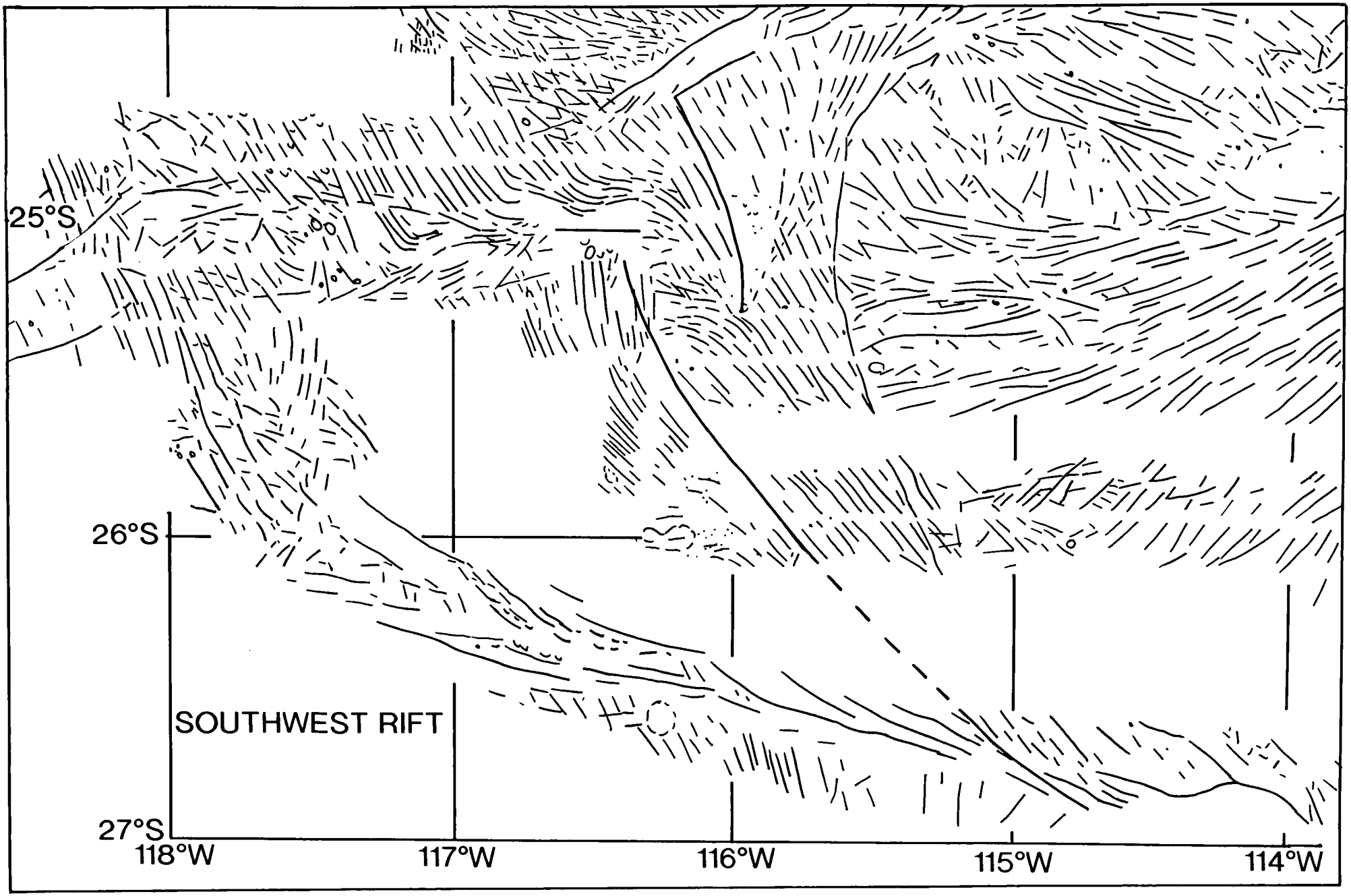

94

a

southernmost tip of the axis was not surveyed by GLORIA, but is thought to be around 26°55'S.

The "initial rifting scarp" (IRS) (see Fig. 4.1, and Fig. 4.7a,b) forms the outer pseudofault of the Southwest Rift (Hey et al., 1985), a diachronous feature that becomes younger to the southeast, and separates Pacific-Nazca spreading fabric to the south from Pacific-Easter lithosphere accreted at the Southwest Rift. The IRS is thought to mark the opening of the rift along a pre-existing sinistral offset transform fault or series of faults due to the clockwise rotation of the microplate, as proposed by Engeln and Stein (1984). The possible reasons for the current elevation of the IRS are discussed in section4.2.9. The active transform fault which is thought to have linked the northern and southern limbs of the EPR prior to the formation of the microplate would have been in the order of 200km long. The IRS was first imaged by GLORIA at around 25°50'S, 117°40'W (Fig. 4.7a,b) and followed along its length in a southeasterly direction until its convergence at 26°46'S, 114°13'W with another shallow ridge to the north (Fig. 4.6a,b). The shallowest part of the IRS is only 640m at 26°49'S, 114°28'W, some 2700 m above the surrounding seafloor to its south. It appears that the ridge is composed of a series of en echelon scarps with very short offsets between them giving a "scalloped" effect on the GLORIA sonograph.

A similar looking ridge is found to the north of the Southwest Rift, which is also imaged clearly on the GLORIA sonograph (Fig. 4.6a,b). This ridge shoals to 1490m at 26°40'S, 114°18.5'W. On the GLORIA mosaic these two ridges are seen to converge at 26°46'S, 114°13'W into one ridge, which continues to the southeast. This ridge becomes the extremely shallow (in one place only 980m depth) so-called "Orongo Fracture Zone" (Francheteau et al., 1988). Its extreme elevation suggests that transpressional strike-slip movement may be taking place along its length.

4.2.3 Southern Triple Junction

The Southern Triple Junction (STJ) region of the Easter Microplate (Fig. 4.1 and Fig. 4.8a,b) was imaged by GLORIA as far as 27°30'S, but a full understanding of this region has not yet been reached. It is possible that the present -day triple junction actually lies to the south of the area insonified by GLORIA (see below). There appears to be extensive magmatic activity in the region that has been imaged, and several actively spreading ridge segments exist, which overlap each other for much of their length to form OSCs. The triple junction itself may in fact be a region rather than a point.

The GLORIA data show that the whole area insonified around 27°S and further south is pitted with cones and volcanic edifices of varying sizes (see Fig. 4.8a,b). High backscattering, presumably recent, extensive lava flows have been imaged, which

Figure 4.7 (a) GLORIA image of the elongate ridges on the Pacific plate to the west of 118°W and the "initial rifting scarp", with line drawing interpretation in (b). The origin of the elongate ridges is not known. They appear to be pitted with recent volcanic cones and lava flows (smooth, high backscatter), and are near orthogonal to the spreading fabric that abuts them, suggesting they are remnant fracture zones that have become 'leaky'. The "initial rifting scarp" marks the opening of the Southwest Rift, probably along a pre-existing sinistral offset transform fault, or series of faults. It is complex in nature and consists of several high-relief scarps of varying local trend which generally curve round from a southeasterly trend in the west to a more easterly one near the Southwest Rift tip.

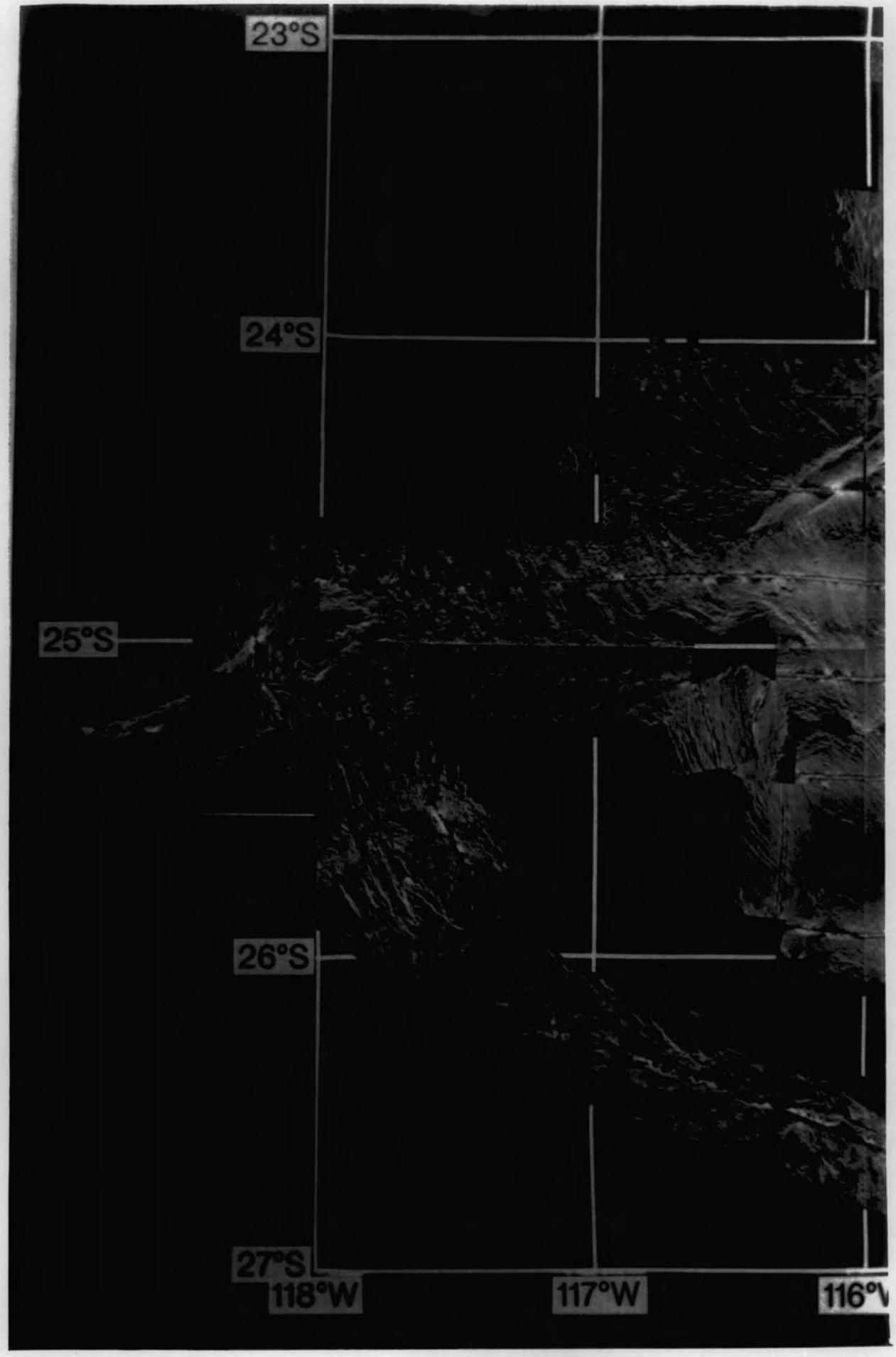

a

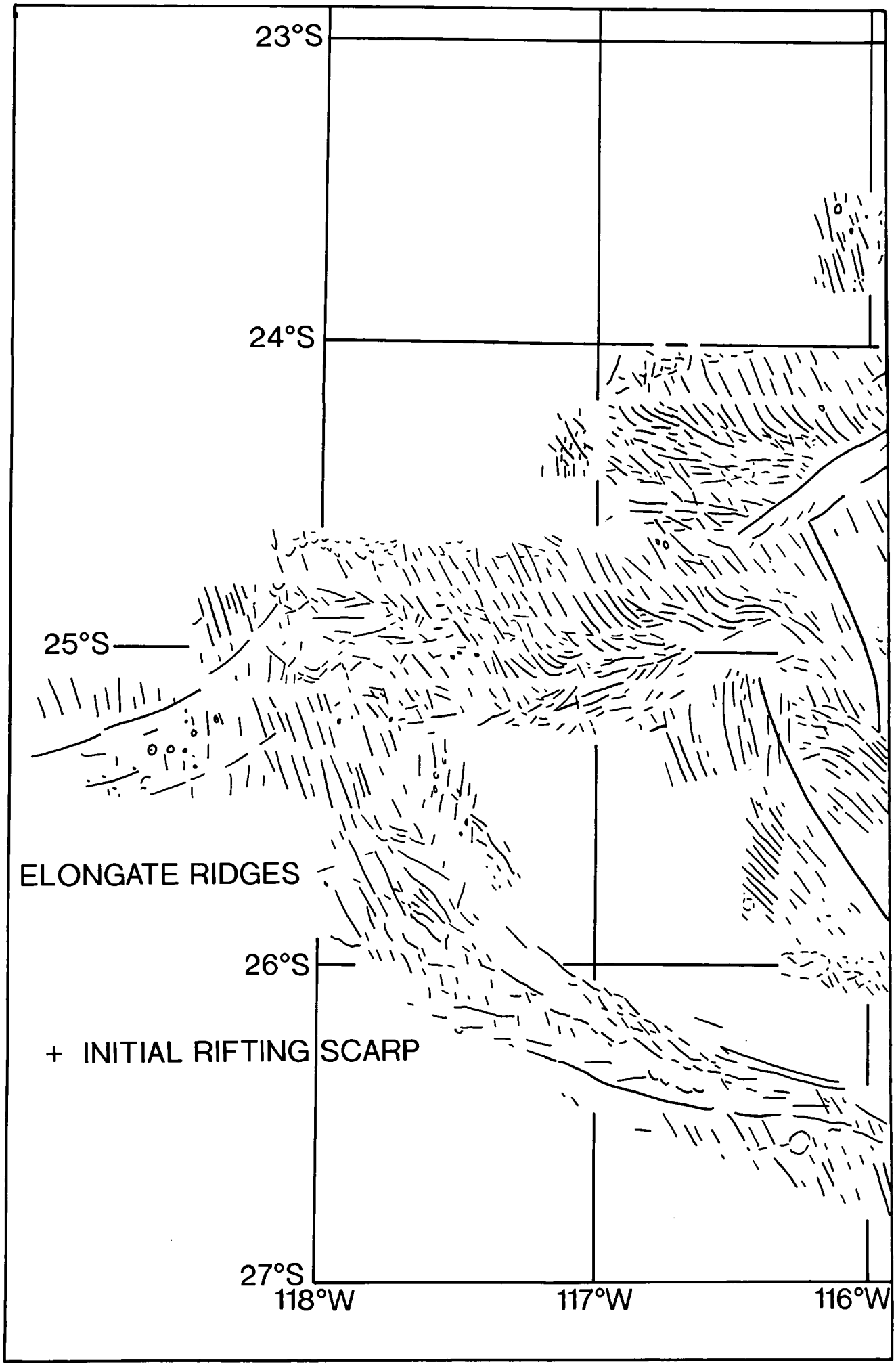
23°S
24°S
25°S
ELONGATE RIDGES
26°S
+ INITIAL RIFTING SCARP
27°S
118°W
117°W
116°W

b

Figure 4.8 (a) GLORIA image of the southern triple junction region, with line drawing interpretation in (b). Note: the whole area insonified around 27°S and further south contains a complex tectonic fabric with ridges and scarps of varying trends, but no evidence of any through-going transform fault as an eastward continuation of the Southwest Rift tip; the whole area is pitted with cones and volcanic edifices and high-backscattering lava flows, implying that much of the magmatism is off-axis; and the triple junction itself may actually lie to the south of the region insonified by GLORIA;

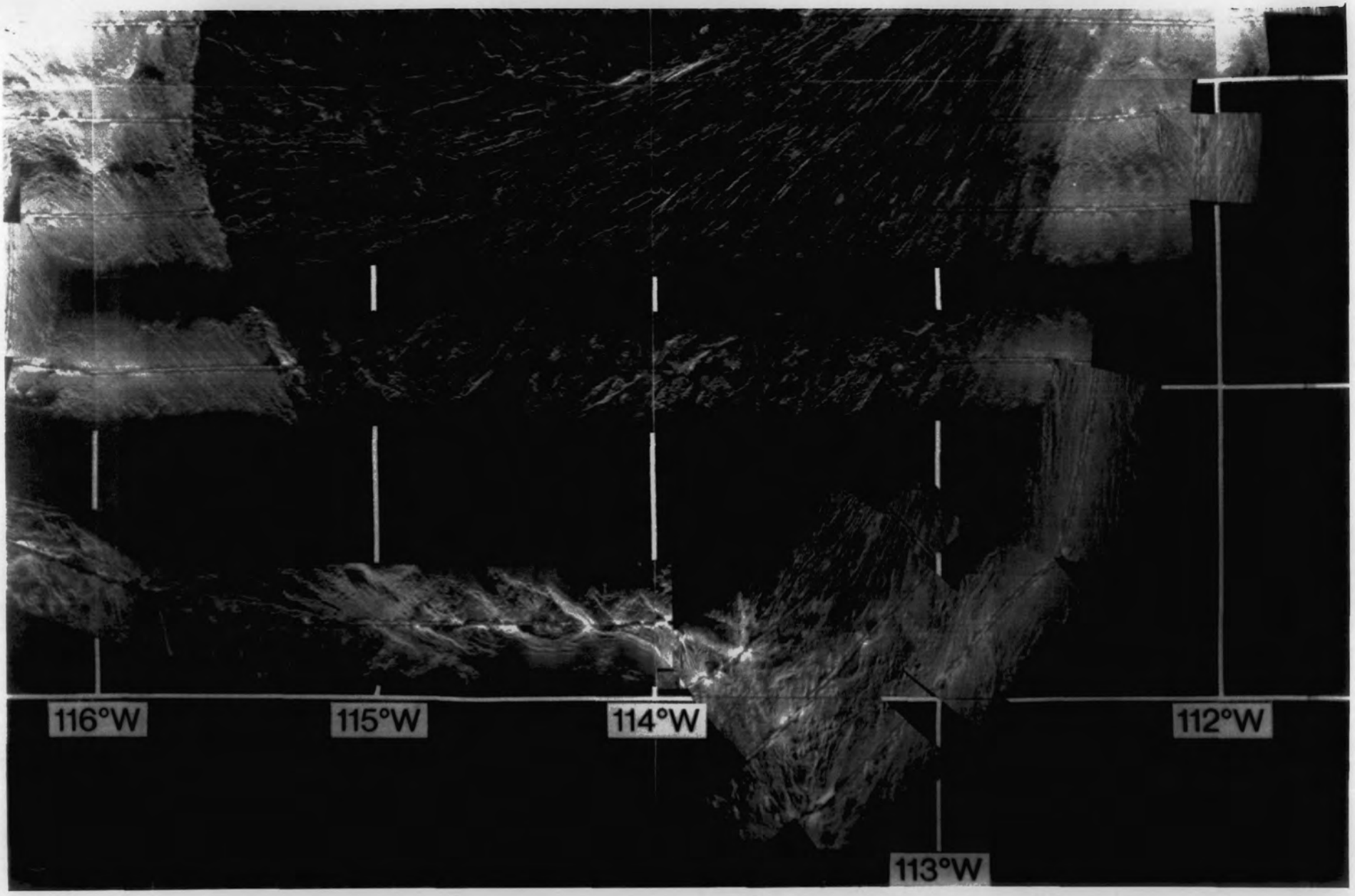

a

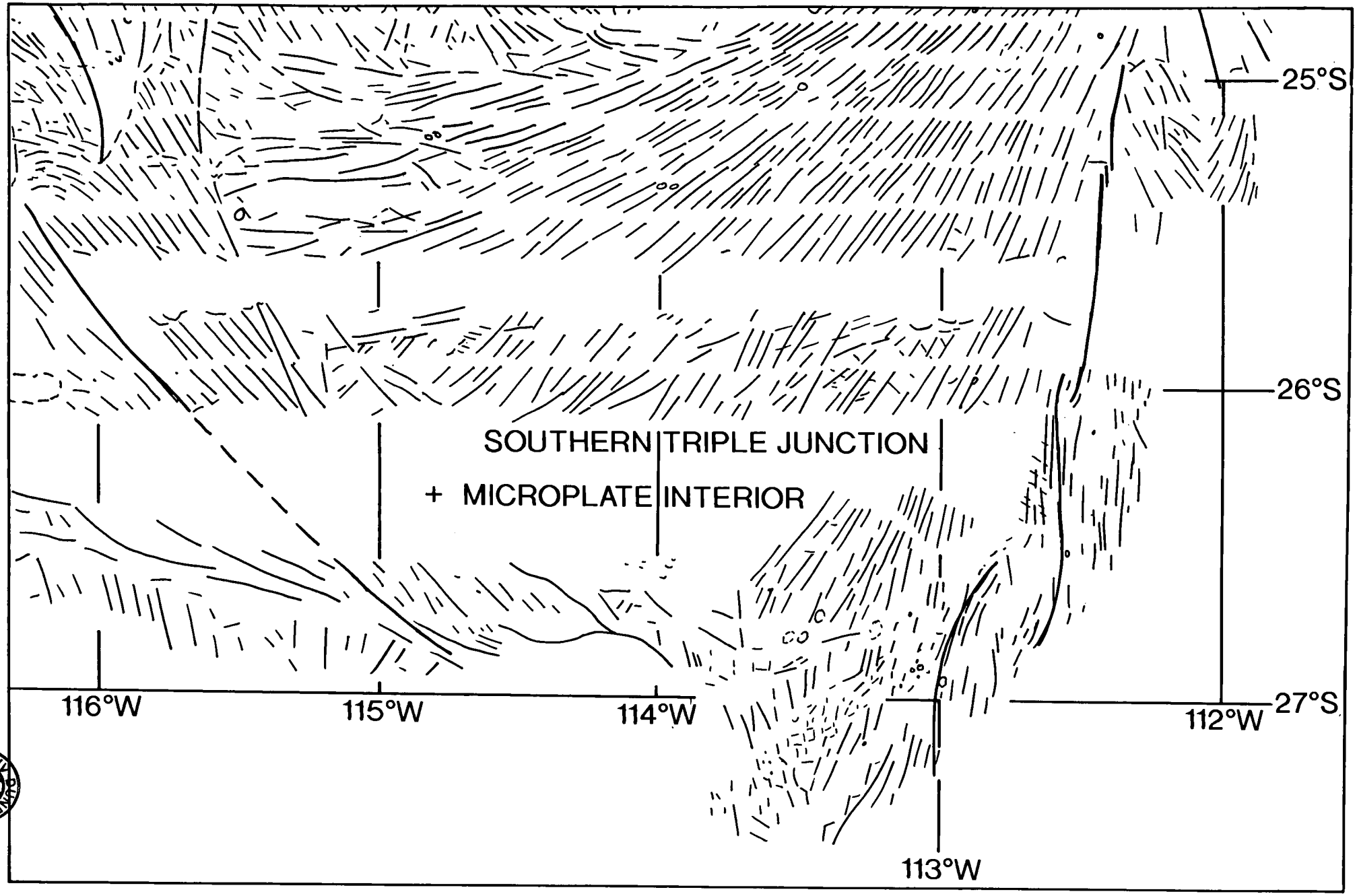
25°S
26°S
27°S
SOUTHERN TRIPLE JUNCTION
+ MICROPLATE INTERIOR
116°W
115°W
114°W
113°W
112°W

b

suggest that magmatic activity is not restricted to the spreading axes, and that off-axis volcanism is occurring.

A broad, shallow NW-SE trending ridge was imaged in the north by GLORIA (Fig. 4.1 and Fig. 4.8a,b) and was mapped along most of its length by Seabeam (labelled 'A' on Fig. 4.9). This ridge is shallower than 2000m in places and extends from around 26° 50'S in the north, as a southern continuation of the "Orongo Fracture Zone" of Francheteau et al. (1988). The southernmost crossing of this ridge was at 28°02'S, 113°08'W where it may begin to curve towards the east and deepen slightly as it approaches another ridge to the east (Fig. 4.9). The cause of the extreme elevation of this ridge is not known, but with the present Pacific-Easter Euler pole positioned at 27°40'S, 114°02'W (see section 5.4.2, Chapter 5) the northern part of this ridge forms an irregular small circle around the pole, so that strike-slip movement is predicted along this Pacific-Easter plate boundary, with increasing compression towards the south. However, there have been no recent compressional earthquake focal mechanisms in this area to confirm this prediction (see Chapter 5). Alternative explanations are that constructional volcanism is occurring, or that hydrothermal alteration of the rocks has led to serpentinisation of the upper mantle, with subsequent uplift (see discussion in section 4.2.9).

To the east, at 28°20'S, 112°54'W, another shallow, but slightly broader ridge (labelled 'B' in Fig. 4.9) is found. This extends from near 28°30'S in the south, northwards until around 27°30'S, 113°W. There is thus a large overlap between ridges A and B in this region, with an offset of about 30 km, and an overlap of around 60 km in a N-S direction. Between these two limbs and centred on 27°54'S, 113°04'W, lies what appears to be a large volcanic edifice of less than 1900 m depth, with a diameter of about 7 km (Fig. 4.9).

Naar & Hey (1991) suggest two possible theoretical locations for the southern triple junction, based on the idea of "equal spreading rates". They suggest that the triple junction may be found where the spreading rate about the Pacific-Nazca pole is equal to the spreading rate about the Easter-Nazca pole. Two hypothetical solutions are produced because of the overlap of ridges A and B, which puts the Southern Triple Junction of the Easter Microplate at around 28°S, 113°W. Here Easter-Nazca and Pacific-Nazca spreading rates are about 160 mm/yr, near the 'STJ' label on Fig. 4.9. However, as Naar & Hey (1991) also point out, Pacific-Easter plate motions in this region imply the triple junction cannot be ridge-ridge-ridge. Instead I interpret it to be ridge-ridge-fault, as transpressional strike-slip movement is predicted to occur along the Pacific-Easter plate boundary (see section 4.2.9).

Figure 4.9 Seabeam data in the region of the southern triple junction (STJ), which is interpreted to be at around 28°S, 113°W, within the region of overlap between the two spreading limbs labelled 'A' and 'B'. Note: ridge 'A' is only at 1700 m water depth at two places along its length and elsewhere remains very shallow; this ridge is linked to the Orongo fracture zone further to the north; and the large irregularly shaped feature at 27°55'S, 113°05'W which is interpreted to be a large seamount (an offset in the navigation of about 1 nm between different crossings of the seamount give it the irregular shape on the map).

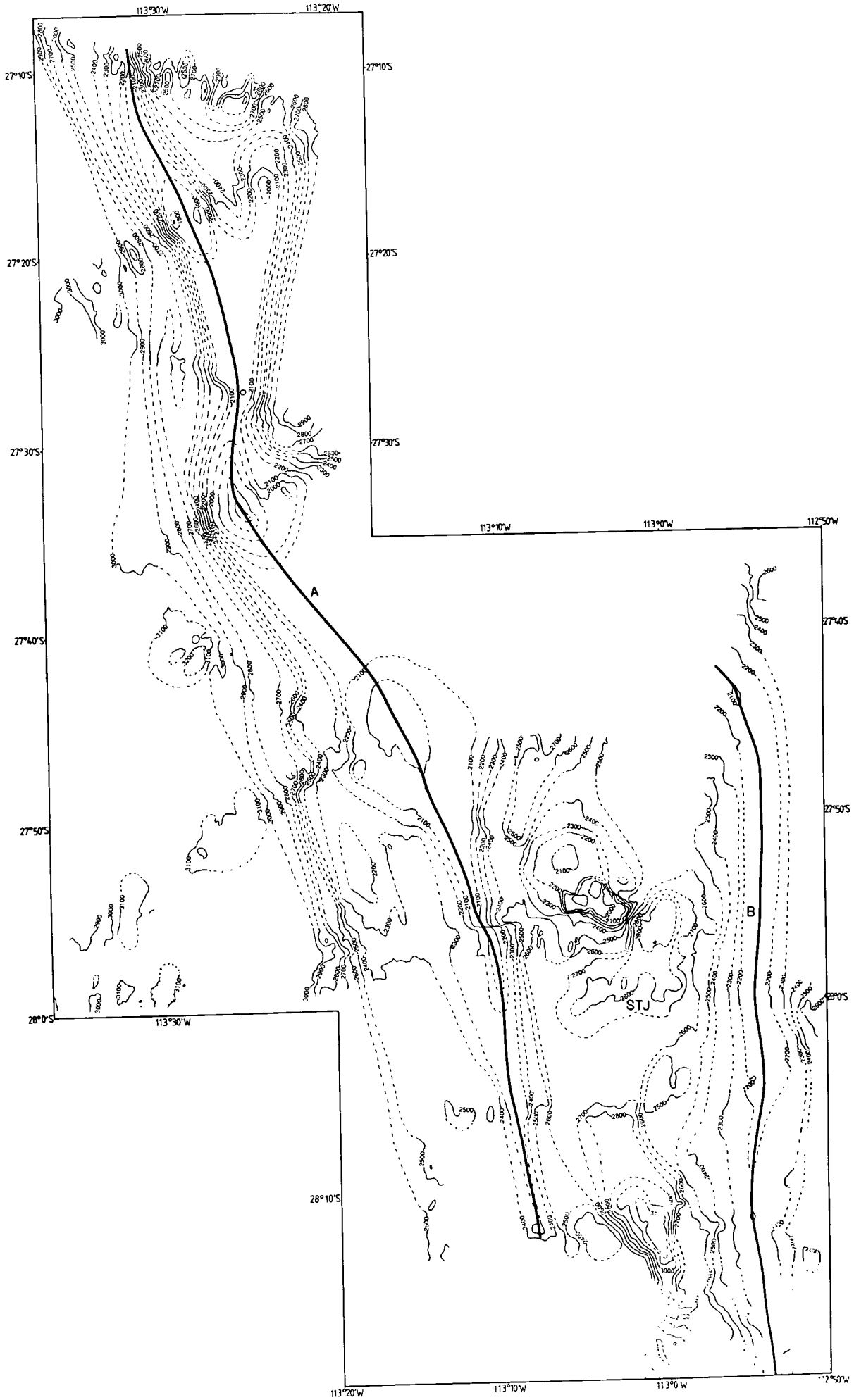
113°30'W
113°20'W
27°10'S
27°20'S
27°30'S
27°40'S
27°50'S
28°0'S
28°10'S
113°10'W
113°0'W
112°50'W
A
B
STJ

4.2.4 East Rift

On the East Rift of the microplate south of 27°S the Easter-Nazca plate boundary consists of several overlapping spreading centres, while north of 27°S three northward propagating rifts were recognised, all with dextral offset between them. North of these, the axis becomes a deep graben and probably passes through Pito Deep at 23°00'S, 111°56.5'W, with its maximum depth of 5890m.

Assuming that the ridge labelled 'A' in Fig. 4.1 and Fig.4.9 and described above is the Pacific-Easter plate boundary, then ridge B in Fig. 4.9, which overlaps with ridge A, may accommodate Easter-Nazca spreading at its northern end. At around 27°35'S, 112°57'W, this ridge is replaced by another ridge (labelled 'C' in Fig. 4.1) situated some 16 km to the west, so that a small overlap is formed. This ridge C has been imaged by GLORIA north of 27°30'S (Fig. 4.8a,b). It trends northward till around 26°50'S, where it starts to curve eastwards towards another spreading axis (D). The northernmost tip of ridge C is at 26°37'S, 112° 48'W.

Ridge D (Fig.4.1) can be seen on the GLORIA mosaic at 26°50'S (Fig. 4.8a,b and Fig. 4.10a,b), but may in fact begin further south than this. The ridge trends northwards, and is shallowest (2050 m) at 26°30'S (see Fig. 4.11), where there is a mantle $^{3}He/^{4}He$ anomaly (see section 4.3.5) and then gradually deepens to 2700 m at its northern limit at 25°58'S. At 26°14'S, the ridge appears to bifurcate, as outlined by the 2600 m contour, with the eastern limb being shorter and less prominent than its western counterpart. I suggest that the western limb has recently propagated to the outside (west) and north of the eastern limb, thus abandoning it, and increasing the north-south overlap (18 km), and east-west offset (10 km) between ridges D and E to the east (see Fig. 4.11). At some later stage, ridge E may retreat northwards, abandoning curved ridge tips to the southeast as it does, as is known to have occurred elsewhere along the EPR (Macdonald et al., 1988).

Ridge E is first located at 26°07'S, 112°32'W (Fig. 4.10a,b and Fig. 4.11). North of its curved overlap with ridge D, it continues along a northerly trend until 25°26'S, 112°29'W, where it appears to jump eastwards via a short en echelon ridge to 25°23'S, 112°27'W (Fig. 4.12). At 25°10'S, the spreading axis begins to curve round towards the east and its depth increases to form a graben as it nears its tip (24°57'S, 112°24'W) (Fig. 4.12 and Fig. 4.13). This spreading axis has been described in detail by Naar and Hey (1986) and shall be referred to here and elsewhere in this thesis as the "fast propagator". Previously the tip of this propagating axis was thought to be associated with a seamount located at 24°52'S, 112°26'W (Naar and Hey, 1986). However, on the GLORIA mosaic (Fig.

Figure 4.10 (a) GLORIA image of the southern end of the East Rift, with line drawing interpretation in (b). Note: large overlapping spreading centre (OSC) at 26°50'S, 112°50'W, between ridges 'C' and 'D' (see Fig. 4.1 also) and smaller OSC at 26°S, between ridges 'D' and 'E'; ridge 'E' is offset to the east by means of a small en echelon ridge at around 25°25'S, 112°30'S; and the tip of the "fast propagator" is at 24°57'S, 112°24'W, with oblique spreading fabric between it and the tail of the dying rift some 40 km to the east.

a

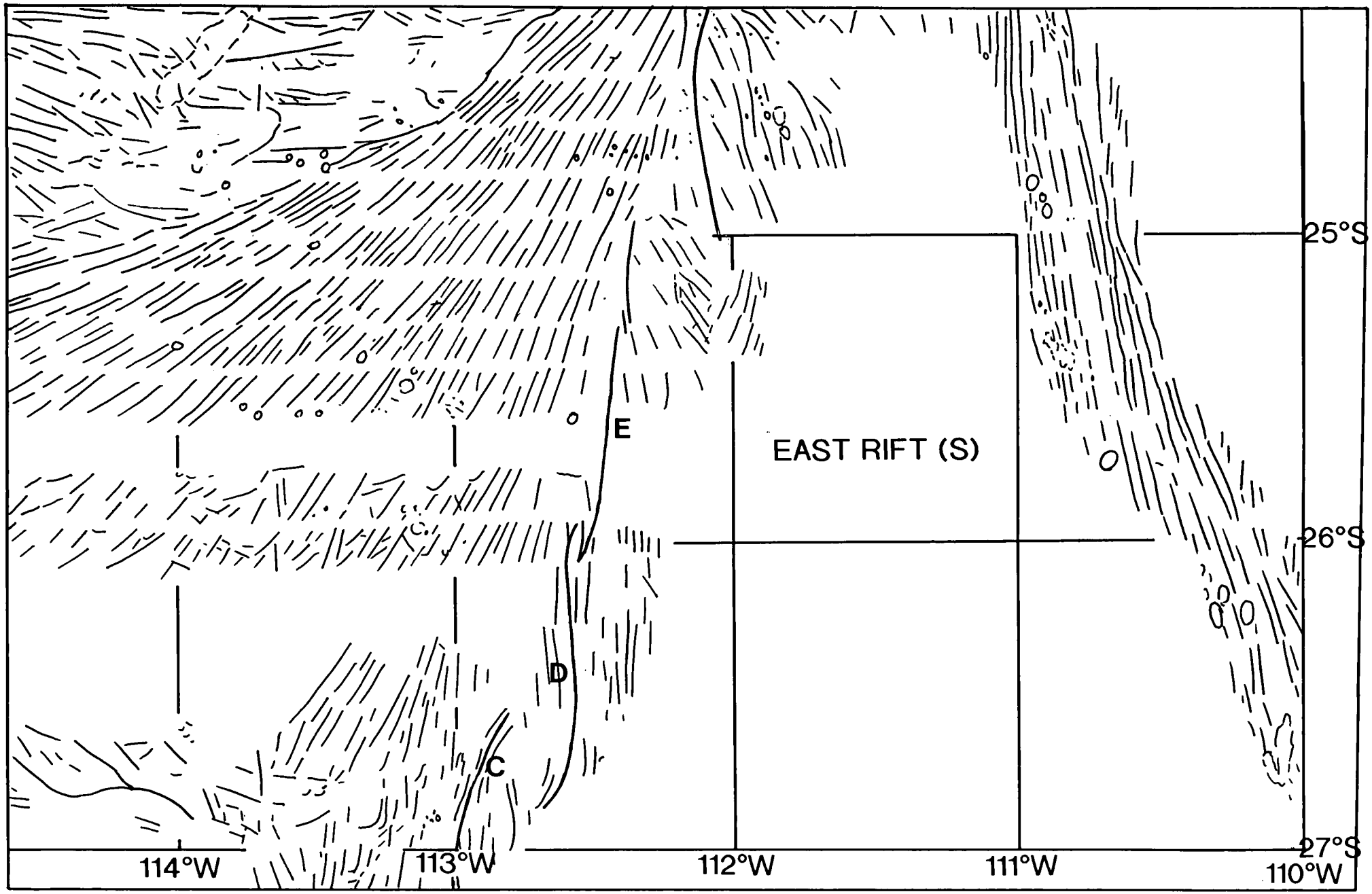

b

Figure 4.11 Seabeam bathymetric data at 26°S on the East Rift, showing the small overlapping spreading centre between ridges 'D' and 'E'. Note: the shallowest part of the East Rift is at 26°30'S (2050 m) which also coincides with the $^{3}He/^{4}He$ anomaly of Craig et al. (1984); Ridge 'D' appears to bifurcate at 26°14'S, as outlined by the 2600m contour, and the western limb is interpreted to have recently propagated to the outside (west) and north of the eastern limb.

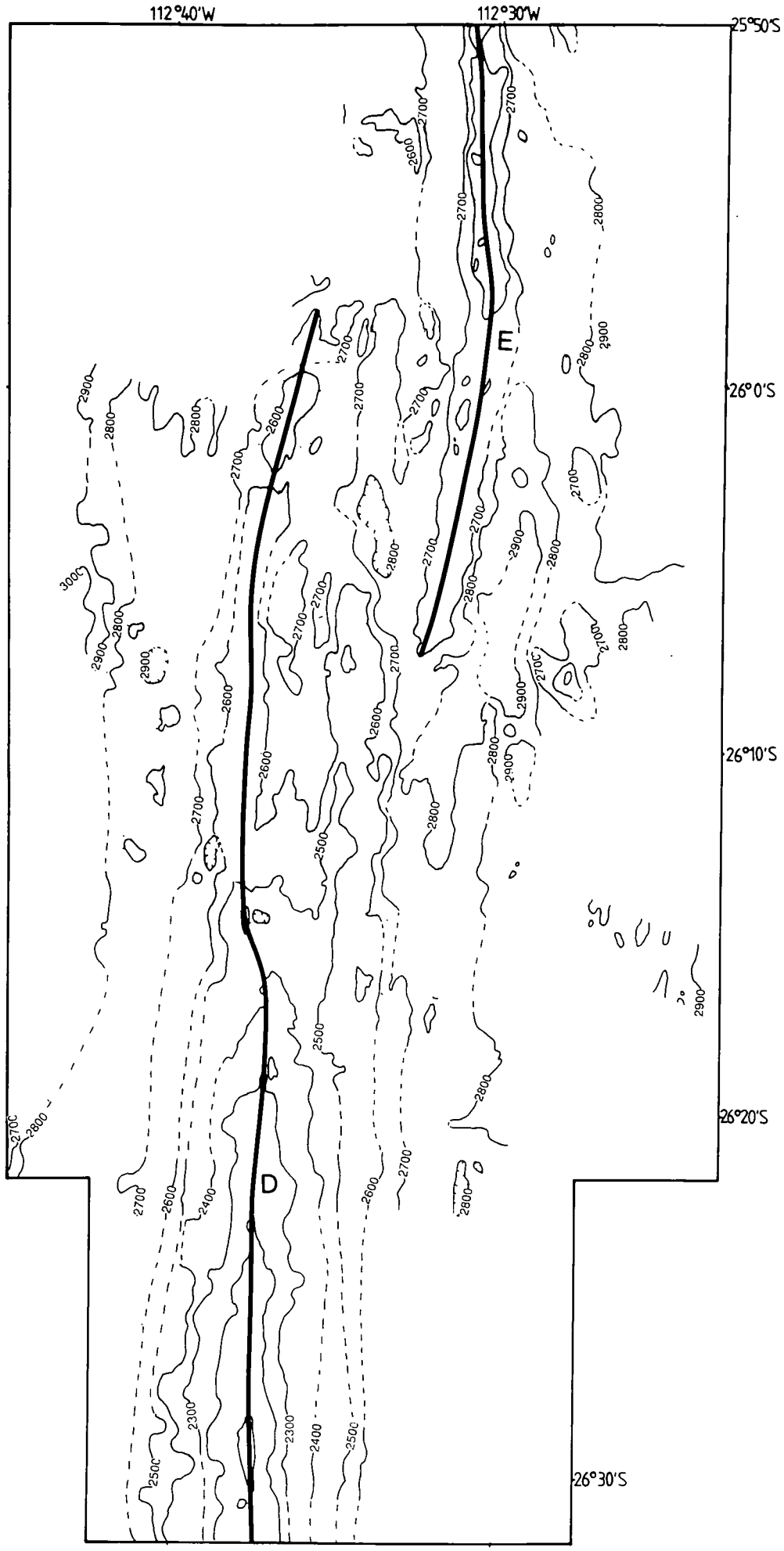
112°40'W
112°30'W
25°50'S
26°0'S
26°10'S
26°20'S
26°30'S
E
D

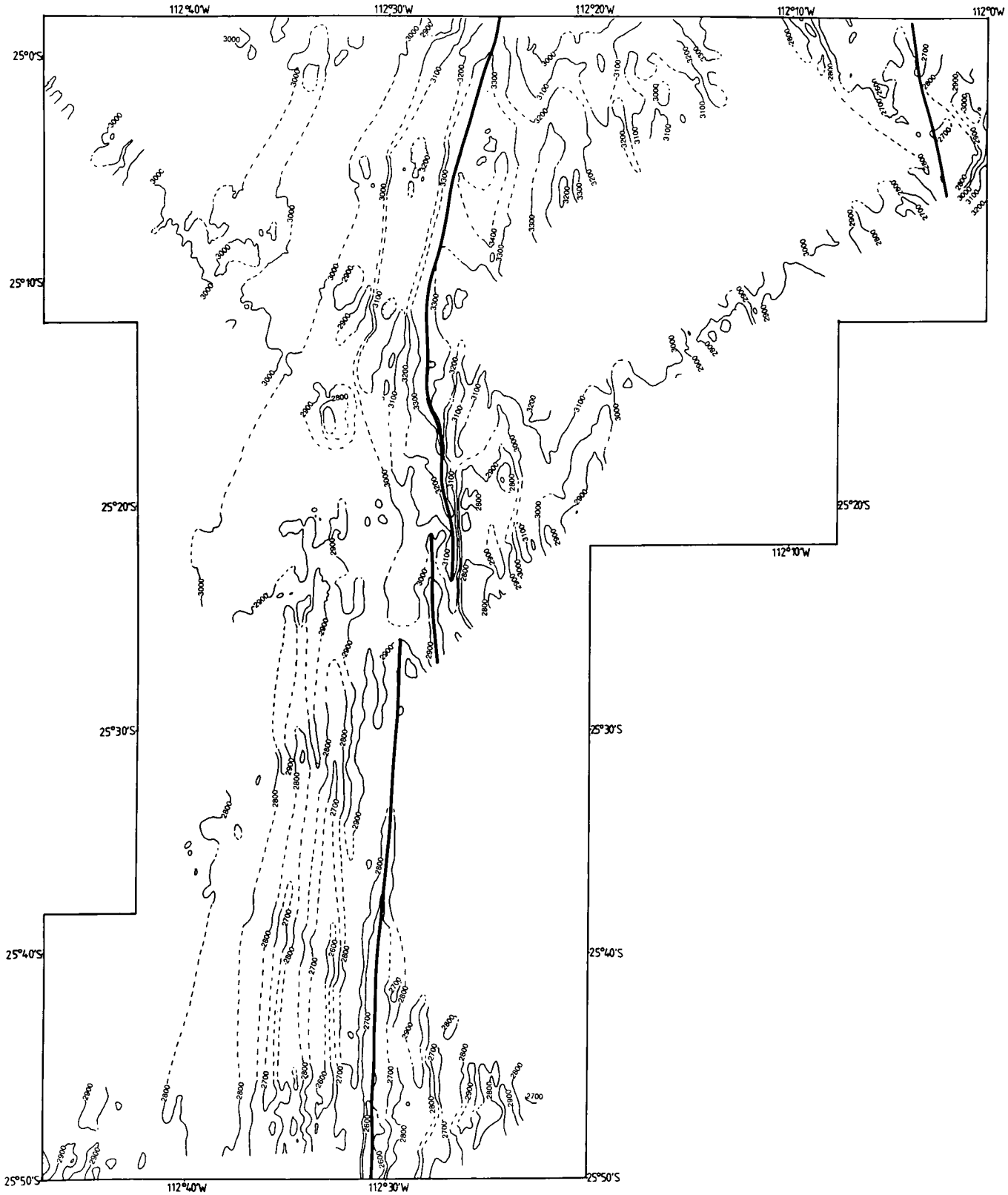

Figure 4.12 Seabeam bathymetric data showing the southernmost propagator (the "fast propagator") on the East Rift. Note: the offset of the axis to the east via a small en echelon ridge at 25°25'S, 112°30'S; oblique tectonic fabric to the east of the propagator which has been rotated in an anticlockwise sense due to rift propagation; and curvature of the propagator from a north-south trend to a NNE-SSW trend in the north.

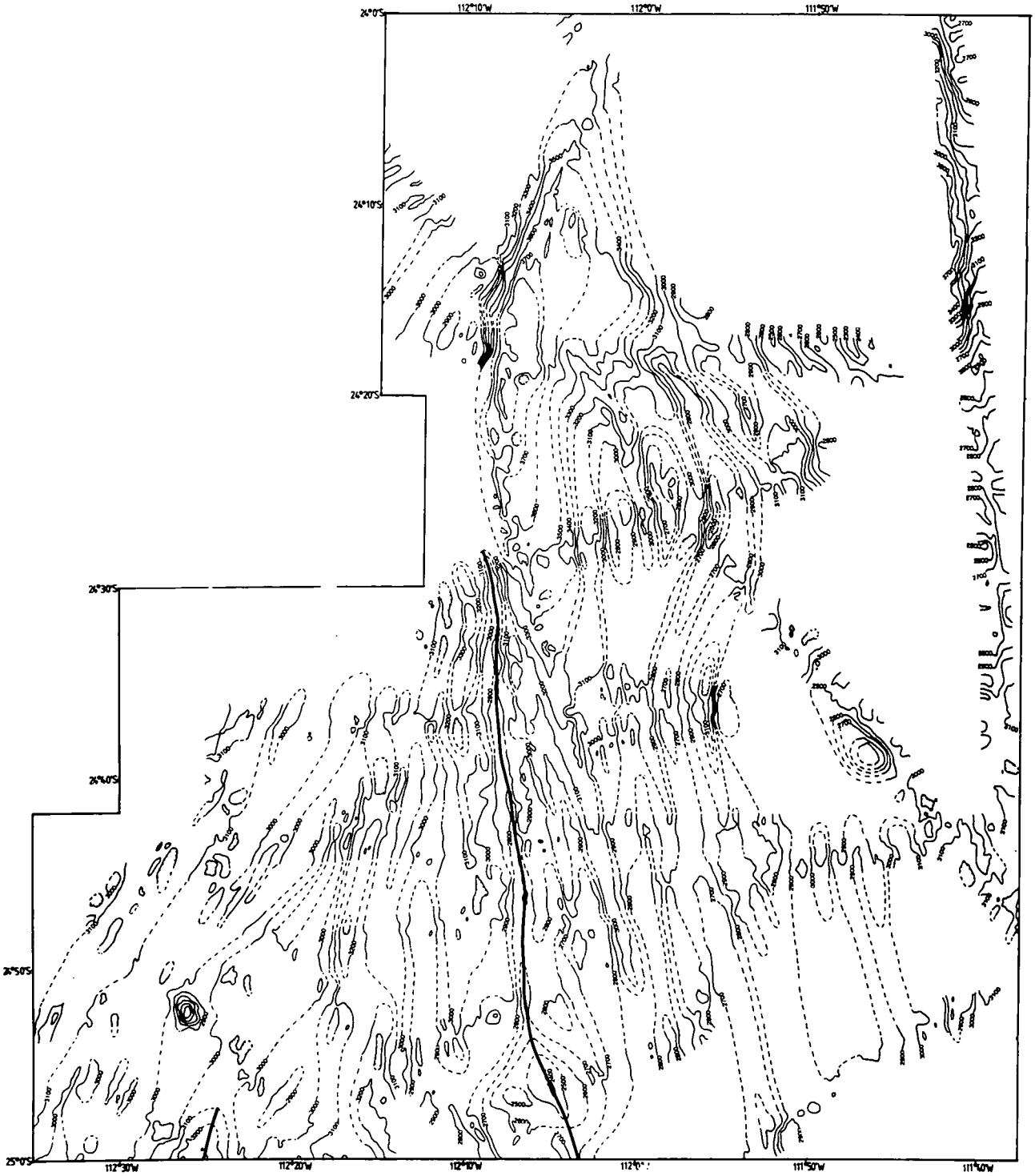

Figure 4.13 Seabeam bathymetric data in the region of the middle propagator on the East Rift. Note: the fanning of the tectonic fabric around the plate boundary (heavy line); dramatic deepening of the axis from a shallow ridge in the south to a deep graben (down to 3900 m depth) in the north; and curvature of the axis round to a NE-SW trend in the north (outlined by the 3600 m contour).

4.10a,b) it is apparent that this is not the case, as differences in reflectivity indicate that the seamount is located on older crust to the northwest of the propagating rift tip.

To the east of this propagator, the tail of the dying rift is first located at 25°06'S, 112°02'W, i.e. 40 km to the east (see Fig. 4.12 and Fig. 4.13). The overall trend of this ridge is 150° until 24°28'S, 112°09'W (Fig. 4.13). The GLORIA data shows that this ridge continues along a trend that is slightly east of north until around 24°S, with a few very small volcanic cones marking the neovolcanic zone (Fig. 14a,b). On the Seabeam data (Fig. 4.13), the northern part of this axis is not marked but is outlined by the 3600 m contour. The axis is a deep graben, which reaches depths in excess of 3900 m, in stark contrast to the shallow ridge to the south. However, the fanned distribution of tectonic fabric around this graben, associated with northward rift propagation (Fig. 4.14a,b), supports the idea that this is the site of the present day rift axis.

The next and probably the most northern magmatically active spreading segment on the East Rift extends from around 23°54'S, 111°46'W to around 23°46'S, 111°58'W. This short spreading axis is not very morphologically distinct, as it forms a slight ridge within a graben. It trends 330° (as revealed by the GLORIA mosaic, Fig. 4.14a,b) and lies within a complex area of high backscatter, but stands out as having higher backscatter than its surrounds. A series of small volcanic cones lie on or near the rift axis, and the CD35 ship's track which crosses it at 23°50'S, 111°55'W, shows that it has a small positive magnetic peak, sustaining the view that this is the neovolcanic zone. Unfortunately the one Seabeam crossing of this rift (Fig. 4.15) neither supports nor dismisses this interpretation.

Between this axis and the Pito Deep region to the north (Fig. 4.1), the structural lineaments revealed by GLORIA are even more complex (Fig. 4.14a,b). Some 25-30 km NE of the rift tip, the basement fabric is oriented roughly NE-SW, and must have undergone severe shearing due to rift propagation and reorganisation. There is no obvious location of a spreading axis north of here, either on the GLORIA mosaic or the Seabeam data (Fig. 4.15), although various ridges and troughs exist.

The Pito Deep area appears to be highly faulted and extends from around 23°35'S to 22°38'S in the north. Pito Deep itself is the deepest part of the rifted area (5890 m at 23°00'S, 111°56.5'W). This region has been extensively studied by Francheteau et al. (1988), Zukin (1990), Hey and Naar (1987), Naar et al. (1991) and Martinez et al. (1990) using SeaMARC II sidescan sonar and bathymetric data, as well as Seabeam data, and so it is mentioned only briefly here. The high relief (up to 3000 m) fault scarps which characterise the region appear as long sinuous features on the GLORIA mosaic (Fig. 4.14a,b) but little fine structural detail is observed between them. Francheteau et

Figure 4.14 (a) GLORIA image of the northern end of the East Rift, with line drawing interpretation in (b). Note: curvature round to the NE of the northern end of the middle propagator as in Fig. 4.13, with its tip near 24°S; probably the most northerly magmatic propagator on the East Rift extends from around 23°54'S, 111°46'W to around 23°46'S, 111°58'W forming a slight ridge within a graben; this short spreading segment is associated with several small volcanic cones; an area of complex oblique structures exists to the northeast, which is presumably associated with previous rift propagation events; the area to the north of 23°30'S is a highly complicated region of horsts and graben that appear sinuous on the GLORIA data and have formed due to rifting apart of pre-existing lithosphere of the Nazca plate; Pito Deep is at 23°S, 112°W but does not show up clearly on the GLORIA image.

23°
24°
25°

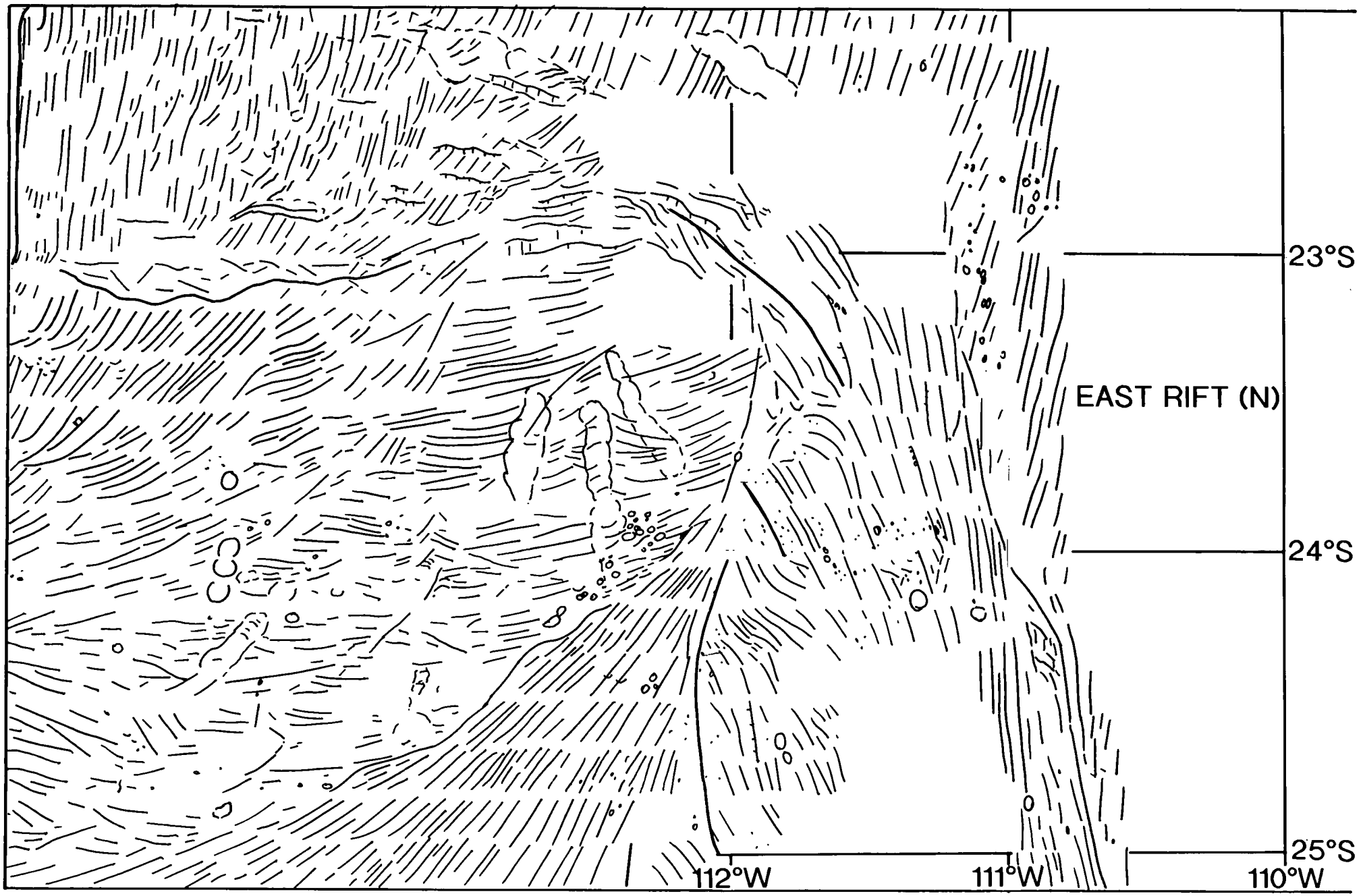

b

al.'s (1988) Seabeam survey of this region was the first to show that these prominent horsts and graben are rifting apart pre-existing abyssal hill fabric. This lithosphere was part of the Nazca plate that was accreted some 3 Ma ago at the East Pacific Rise. Recently processed SeaMARC II data (Naar et al., 1991) reveal even more dramatically how this is occurring. Martinez, et al. (1990) have suggested that large scale normal faulting and tilting of crustal blocks in the region has been able to accommodate significant amounts of upper lithospheric extension. Serpentinised peridotites (Schilling et al., 1985) and gabbros (Stoffers et al., 1990) retrieved from the area further support this idea. Recent local extrusion of lavas may have occurred at 23°20'S, 111°35'W (Naar et al., 1991) but elsewhere the activity is mainly tectonic. The plate boundary marked on Fig. 4.15 is fairly arbitrary as pervasive faulting seems to be occurring throughout the area.

4.2.5 Northern Boundary

The entire northern boundary of the Easter Microplate was imaged by GLORIA, from the Pito Deep area in the east, to the Northern Triple Junction in the west (Fig. 4.16a,b). Much of the boundary consists of a series of broad, high ridges that appear to have been caused by strong transpressional motion across them.

The boundary extends from 112°20'W (at the westernmost limit of the Pito rifting area) for about 250 km until the northern triple junction is reached at 114°32'W, and roughly follows 23°S latitude over its length (Fig. 4.16a,b and Fig. 4.17). It consists of several high relief faults striking almost east-west with steep scarps (30°-40°) to the south and shallow slopes to the north (7°). The seafloor to the south of the northern boundary is generally between 500 m and 1000 m lower than that to the north. The detailed morphology of this region has been determined by Francheteau et al. (1988) and Zukin (1990), but is briefly discussed here in conjunction with the GLORIA data.

West of Pito Deep, a series of ENE-WSW trending faults were imaged by GLORIA, between 112°20'W and 113°00'W (Fig. 4.16a,b). These faults lie obliquely to Nazca abyssal hill fabric to the north, and sub-parallel to similar fabric now incorporated into the microplate interior to the south. One of these faults has been defined as a "principal shear zone" by Francheteau et al. (1988). It is a 4-5km wide fault zone characterised by a narrow, continuous trough following the crest of a small ridge, and is located between 112°17'W and 112°40'W. This fault has been named the "Pito Fracture Zone" (Francheteau at al., 1988) and is thought to accommodate almost pure strike-slip movement. West of 112°50'W, the GLORIA mosaic reveals a prominent WSW trending feature, with an irregular, scalloped edge to the south, extending as far as 114°21'W (Fig.

Figure 4.15 Seabeam data to the south of Pito Deep, where a series of prominent horsts and graben have formed due to rifting apart of pre-existing Nazca plate lithosphere. Note the rapid elevation of the ridges and the deepening of the troughs, with reliefs of up to 3000 m. The exact location of the plate boundary is fairly arbitrary as pervasive faulting seems to be occurring throughout the region.

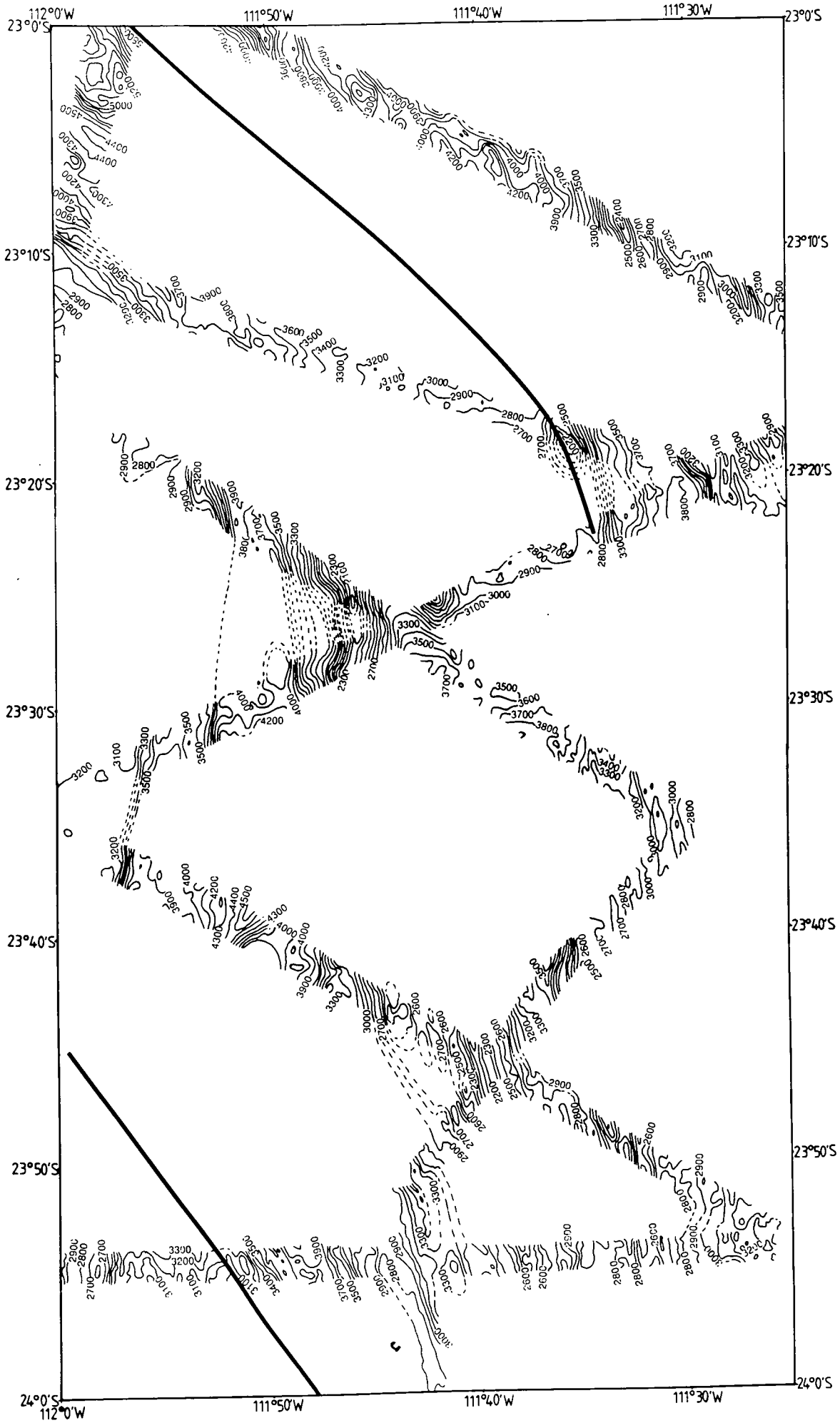
112°0'W
111°50'W
111°40'W
111°30'W
23°0'S
23°10'S
23°20'S
23°30'S
23°40'S
23°50'S
24°0'S

Figure 4.16 (a) GLORIA image of the northern boundary and the Nazca plate to the north, with line drawing interpretation in (b). Note: a series of ENE-WSW faults exist immediately to the west of Pito Deep, the largest of which may accommodate pure (dextral) strike-slip motion; to the west of 112°50'W the northern boundary forms a broad, prominent feature trending WSW with an irregular scalloped edge to the south which abruptly abuts the tectonic fabric of the microplate interior, while to the north it slopes away more gently; the northern triple junction is located at 23°03'S, 114°32'W; on the Nazca plate to the north of the microplate a series of high relief, asymmetrical ridges exist which form a discontinuous chain extending from around 22°S, just to the east of the EPR, in a southeasterly direction towards Pito Deep; much of the abyssal hill fabric within this region is no longer sub-parallel to the EPR and appears to have been rotated in a clockwise sense.

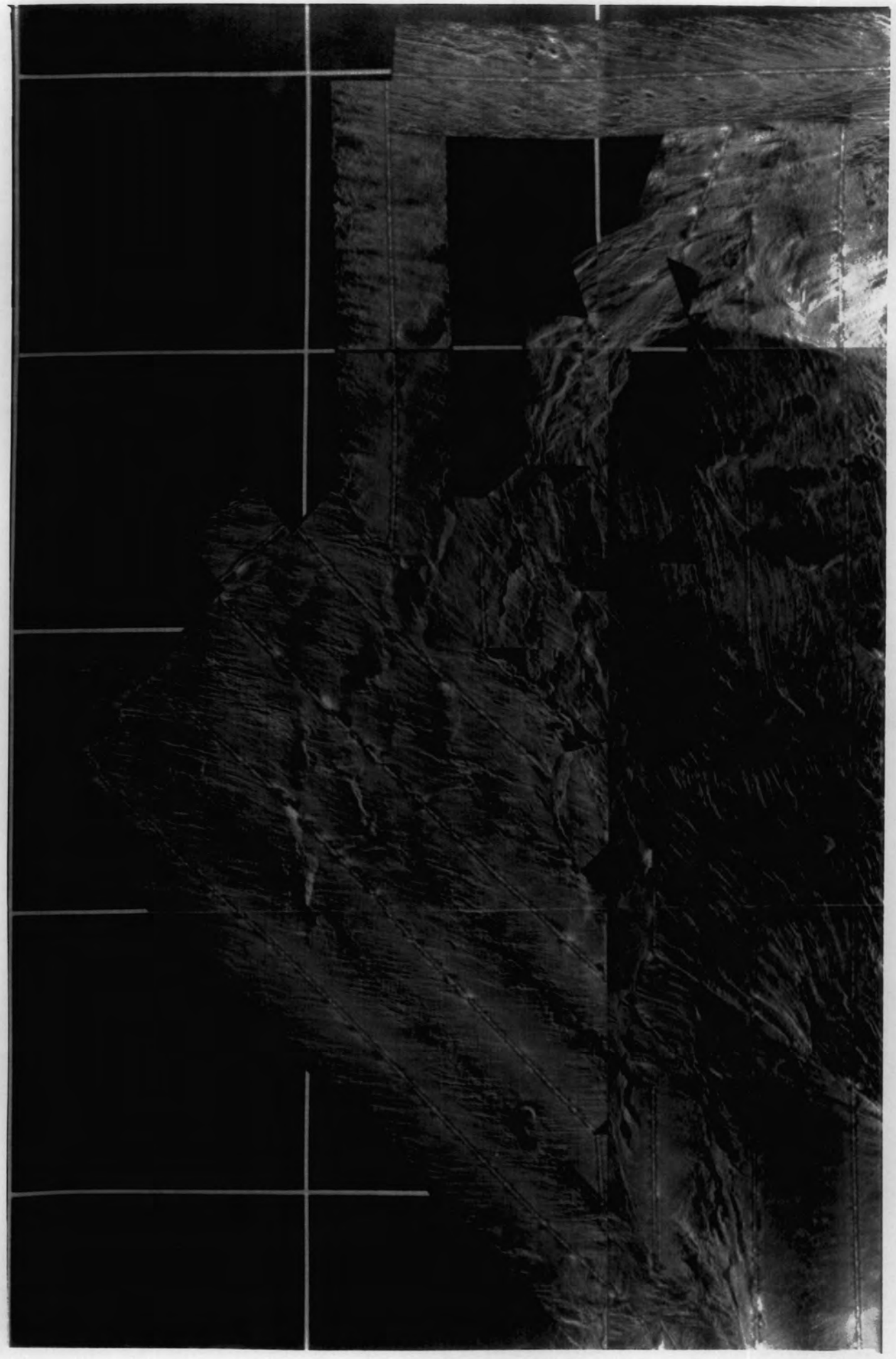

a

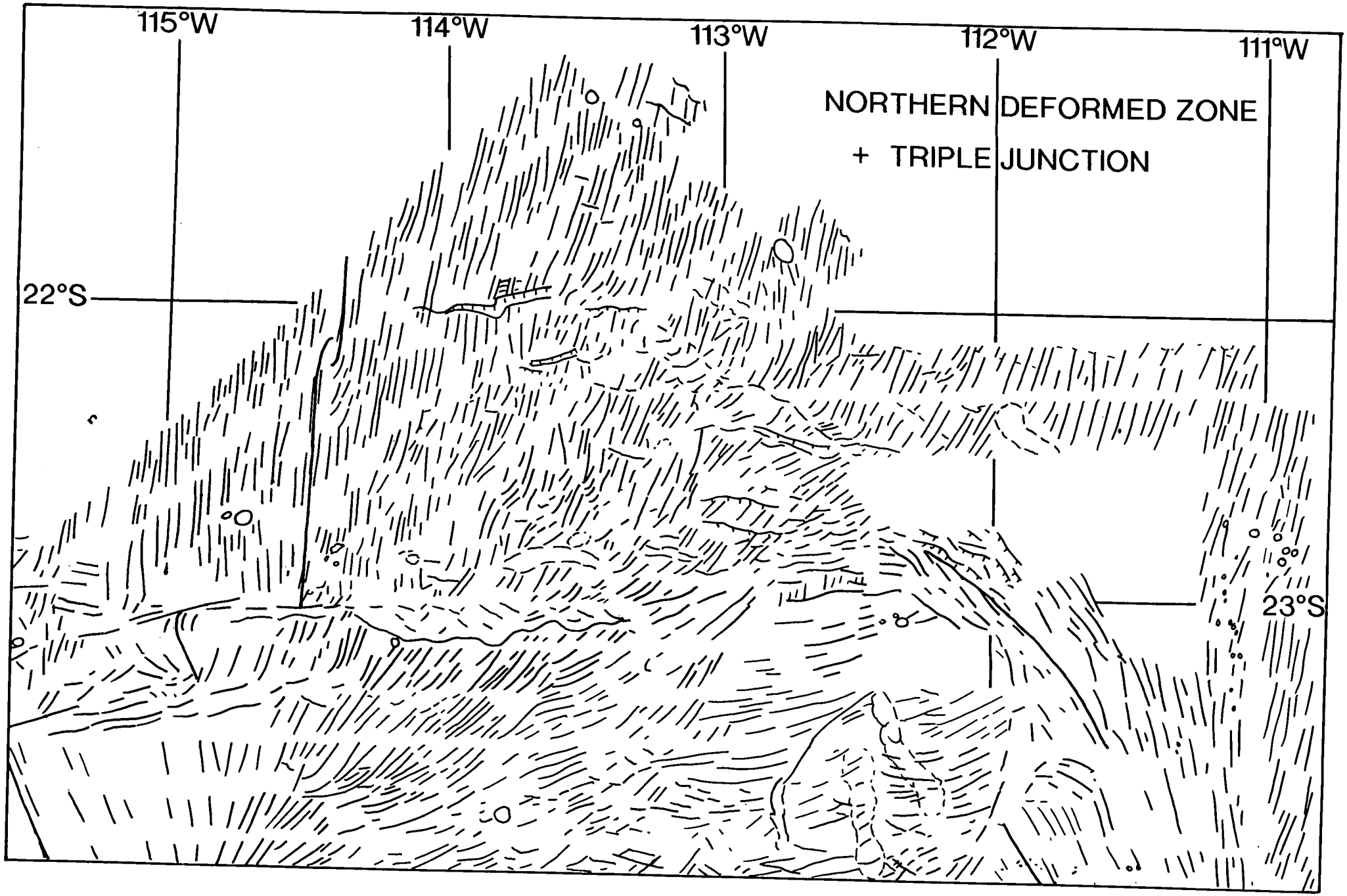
115°W
114°W
113°W
112°W
111°W
NORTHERN DEFORMED ZONE
+ TRIPLE JUNCTION
22°S
23°S

123

b

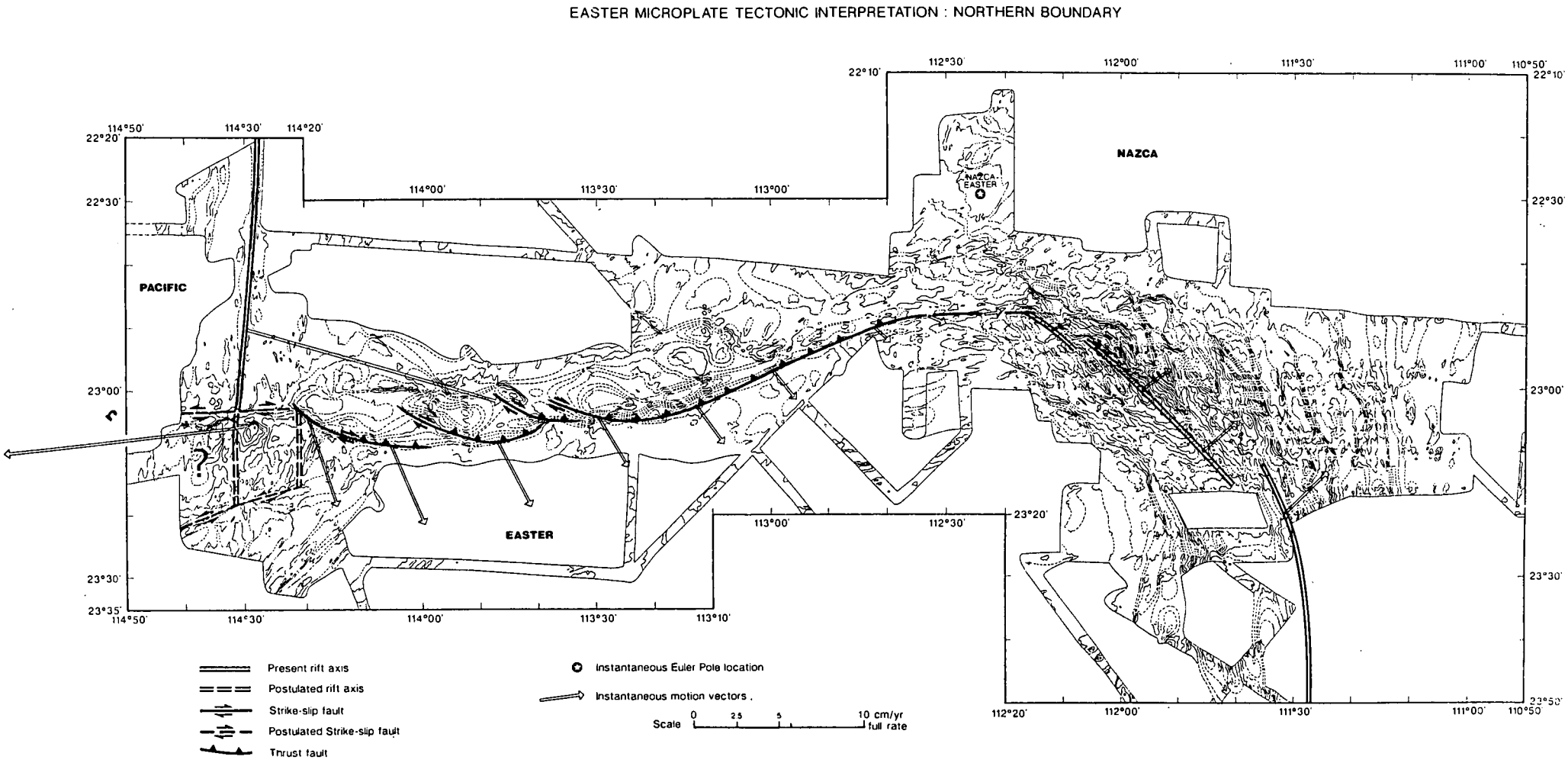

Figure 4.17 Hand-contoured Seabeam map of the northern boundary of the Easter Microplate based on data from several expeditions, with tectonic interpretation of plate motions along the boundary (from Zukin, 1990). Note: the extreme relief of the northern boundary with the steep scarps to the south and the shallow slopes to the north; the deeper seafloor to the south of the boundary than to the north; and the series of thrust faults that are proposed to exist along this boundary, separated by lateral ramps, which are required to accommodate the predicted convergence between the Nazca and Easter plates. (Instantaneous Euler pole is from Naar & Hey, 1989).

4.16a,b). This ridge abruptly abuts the tectonic fabric of the microplate interior, while sloping away more gently to the north. The western half of this feature is interpreted by Zukin (1990) to consist of a series of en echelon ridges (Fig. 4.17). Unfortunately these en echelon ridges are not obvious on the GLORIA mosaic (Fig. 4.16a,b), although there is a slight hint that they exist.

The present day Nazca-Easter Euler pole (Chapter 5, section 5.4.2) predicts that very little strike-slip movement is taking place between the Easter and Nazca plates along the northern boundary, but instead strong transpressional motion must be taking place. Fig. 4.17 shows Zukin's (1990) interpretation that these asymmetric ridges are actually thrust faults, whereby slightly younger material to the north has been overthrusted over the older material to the south. The significance of this is not discussed by Zukin (1990) and so is dealt with further in Chapter 7.

4.2.6 The Northern Triple Junction

The Northern Triple Junction (NTJ) is located at 23°03'S, 114°32'W (Fig. 4.1 and Fig. 4.16a,b). Here the almost north-south (002°) Pacific-Nazca spreading axis intersects the eastern end of the Anakena Transform (trending 088°) and the western end of the northern boundary. These latter two features appear as one continuous fault extending from 114°21'W (where the prominent Northern Boundary ridge stops) to 114°51'W (where the western fault strand of the Anakena Transform begins) (Fig. 4.16a,b). The length of the Nazca-Easter part of this fault (to the east of the NTJ) is 18 km, while the length of the Pacific-Easter part is 33 km. The seafloor south of this fault falls sharply away some 500m to the south to a depth of 3500 m (Francheteau et al., 1988) and a strong acoustic shadow is produced on the GLORIA mosaic. Naar and Hey (1991) point out that the plate motions in this region imply that the triple junction cannot be stable as a ridge-fault-fault type. However, the triple junction can be stable as a ridge-trench-fault system, whereby convergence is accommodated by some non-trench forming faulting mechanism along the Northern Boundary. The thrust faults to the east of 114°21'W seem to accommodate the convergence without actually forming a trench, although the lithosphere is certainly deeper to the south of the thrust faults, forming a trough, presumably due to downward flexure of the lithosphere as southward overthrusting of the Nazca plate to the north occurs. However, in the immediate vicinity of the triple junction itself, the morphology suggests that only strike-slip movement is taken up. This suggests that there is strain partitioning here, with one part of the plate boundary accommodating the strike-slip movement, and another the compressional motion.

4.2.7 East Pacific Rise and the Nazca Plate north of the Easter Microplate

The East Pacific Rise south of 21°50'S and the tectonic fabric of the Nazca plate to the east were imaged by GLORIA and are shown in Fig. 4.16a,b. German Seabeam data are available along the EPR south of 21°S, and also a broad zig-zag was mapped extending from Pito Deep in the southeast to just north of a small OSC in the northwest (Fig. 4.18)

At 22°10'S, 114°25'W a small overlapping spreading centre (OSC) is observed on the GLORIA mosaic (Fig. 4.1 and Fig. 4.16a,b). The north-south overlap between the two limbs is about 13 km, and the limbs are about 7 km apart in an east-west sense. Immediately to the southeast of the OSC a subtle series of curved faults can be seen, which are interpreted as being limbs that have been rafted off from earlier migrating OSCs in the region (Fig. 4.16b). These rafted older limbs suggest that the present OSC may have migrated directly northwards some 20 km in the last 1 myr, or may have migrated northwestwards, accommodating some of the marked asymmetry observed in the spreading rates (faster to the east) either side of the spreading axis.

Within the region imaged to the east of the EPR, some unusual east-west trending ridges are seen which disrupt otherwise fairly normal seafloor fabric. These features extend from around 22°0'S, 114°10'W, near the East Pacific Rise, in an overall southeasterly trend to near Pito Deep at 23°S, 112°W. The majority of these prominent ridges have consistently steep scarps to the south and shallow slopes to the north, as can be seen from the different backscatter strengths on the GLORIA mosaic (Fig. 4.16a,b) and from the Seabeam track through the area (Fig. 4.18). The asymmetry of some of these ridges seems to be less marked in the east of the area than in the west. The GLORIA data reveal that originally ridge-parallel spreading fabric is curved in a clockwise direction into the ends of these large ridges. Features such as these have not been observed elsewhere on oceanic lithosphere to date.

Spreading rate data and plate tectonic reconstructions of the region (Chapter 5 and Chapter 6) indicate that the whole area, between the OSC in the west and Pito Deep in the east, is undergoing dextral transpression, with a strong north-south compressional component and a much smaller east-west dextral shear component (due to faster spreading rates in the north than in the south). The most obvious explanation for these prominent ridges is that they are thrust faults which are able to accommodate tectonic shortening by the southward overthrusting of slightly younger lithosphere to the north over marginally older seafloor to the south, in a fashion similar to that occurring along the northern boundary. Slight dextral movement along these faults (which may be contemporaneous with the thrust faulting) is indicated by the curvature of originally ridge-

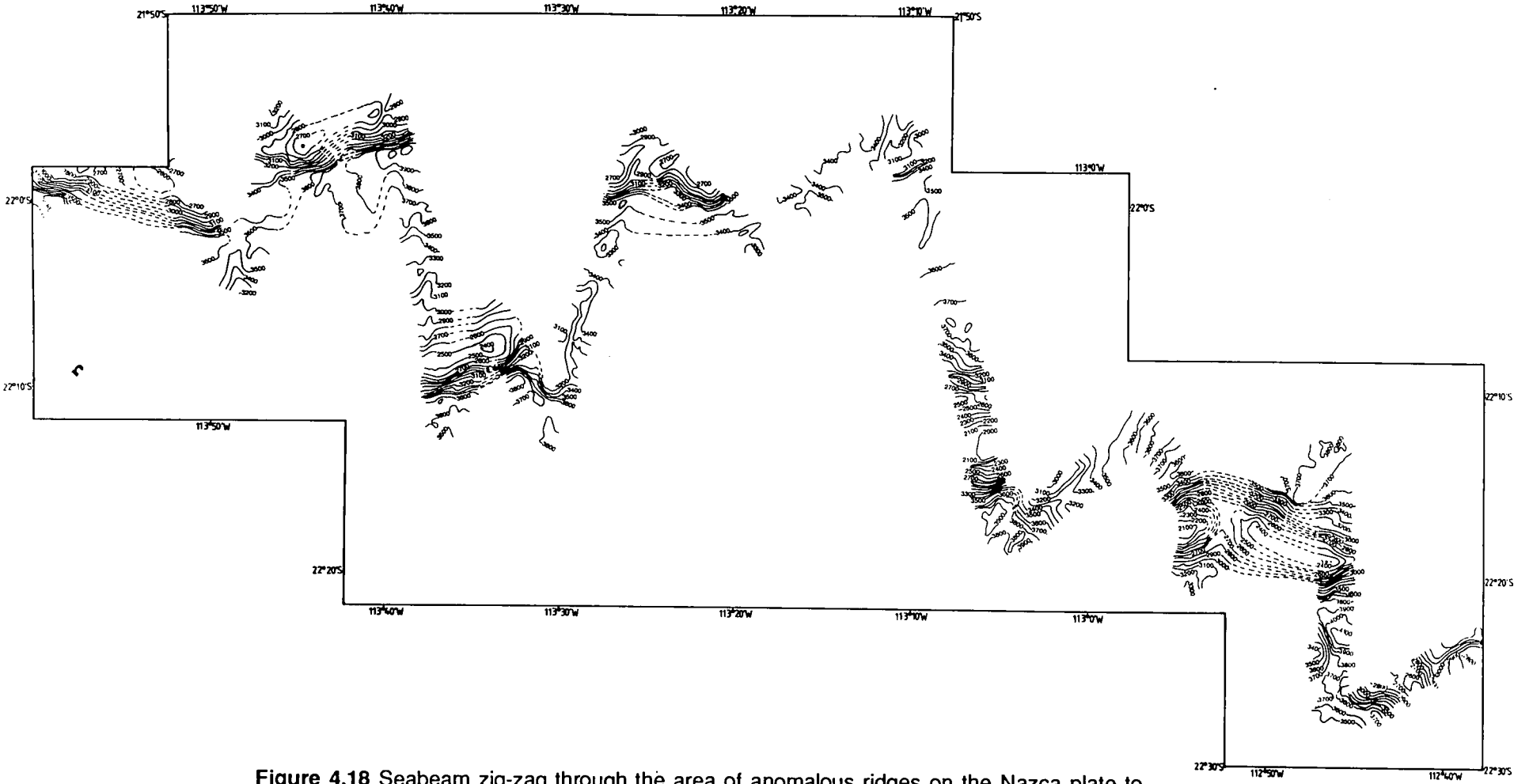

Figure 4.18 Seabeam zig-zag through the area of anomalous ridges on the Nazca plate to the north of the microplate. Note: the asymmetric nature of these ridges, with their steep slopes to the south (30-40°) and their gentle slopes to the north (7-10°); the relief of these ridges is over 1000 m in places.

parallel tectonic fabric into these faults, and also by what appears to be fabric that has been rotated in a clockwise direction elsewhere in the region. Between these thrust faults, earthquake focal mechanisms in the region (Chapter 5, section 5.5.4) suggest that sinistral anti-Riedel shear movement may presently be taking place along the NE-SW trending rotated abyssal hill fabric. The implications and significance of these faults is discussed fully more in Chapter 7.

4.2.8 The Microplate Interior

The microplate interior, revealed in its entirety for the first time by the GLORIA survey (Fig. 4.19a,b), consists of several domains of different origin, tectonic fabric and apparent ages. The poor backscattering and lack of fault scarps on the GLORIA data over the west of the interior implies greater sediment cover and hence greater age than the rest of the microplate, which has since accreted around this older domain. Fanning reflectors about the East and West Rifts of the microplate, due to rift propagation, changes in spreading rates and microplate rotation, have produced dramatic patterns in the microplate interior, with strong acoustic contrast between recently accreted and older crust (Fig. 4.19a,b).

The two most obvious features within the microplate interior are the two inner pseudofaults from the propagating northern tip of the East Rift and the southern tip of the Southwest Rift (Fig. 4.19a,b). The East Rift Inner Pseudofault (EIPF on Fig. 4.1) curves southwestwards from near the Pito Deep region, where there is an age contrast of around 2.5 Ma between the material either side of it, possibly to around 24°49'S, 115° 39'W, where there appears to be negligible age contrast either side of the pseudofault. Initial examination of foraminifera from the base of a 15 m piston core taken within the area to the north of this pseudofault (237P, see section 4.3.2 below) (M. Weissel, pers. comm.; Marchig et al., 1989), where 3.5 kHz records show sedimentary cover of up to 20 m, suggests that the crust may be at least 6 Ma old.

The inner pseudofault of the Southwest Rift (WIPF, Fig. 4.1) extends from 26°46'S, 114°13'W (Fig. 4.8a,b) northwestwards and northwards until around 24°20'S, 115°20'W (Fig. 4.19a,b), where the age contrast across the pseudofault is on the order of 4-5 myr as suggested by magnetic anomaly data (Fig. 2.7, Chapter 2). On the GLORIA mosaic there is a dramatic contrast in reflectivity due to differing sedimentation cover (Fig. 4.19a and Plate 1). North and east of here, the fabric formed at the West Rift has been gradually rotated clockwise from its presumed original NNW orientation (Fig. 6.7-Fig. 6.19, Chapter 6) in a clockwise sense over a period of nearly 4 Ma. The fabric at around 24°30'S, 114°30'W has now been rotated almost 120° away from its original orientation, producing the spectacular fanning effect seen on the GLORIA mosaic. In addition to the

Figure 4.19 (a) GLORIA image of the northern part of the microplate interior, with line drawing interpretation in (b). Note: fanning reflectors about the East and West Rifts which have produced dramatic patterns in the microplate interior, with strong acoustic contrast between recently accreted and older crust; the East and West Rift inner pseudofaults (see Fig. 4.1); the oldest part of the microplate interior at around 24°40'S, 115°20'W; several large, circular seamounts, especially at around 24°S, 113°46'W, where they form a north-south chain; several anomalous, asymmetric ridges, for example the three ridges near 23°30'S, 112°30'W, which trend roughly north-south and may be analogous to some of the ridges found on the Nazca plate to the northwest of Pito Deep.

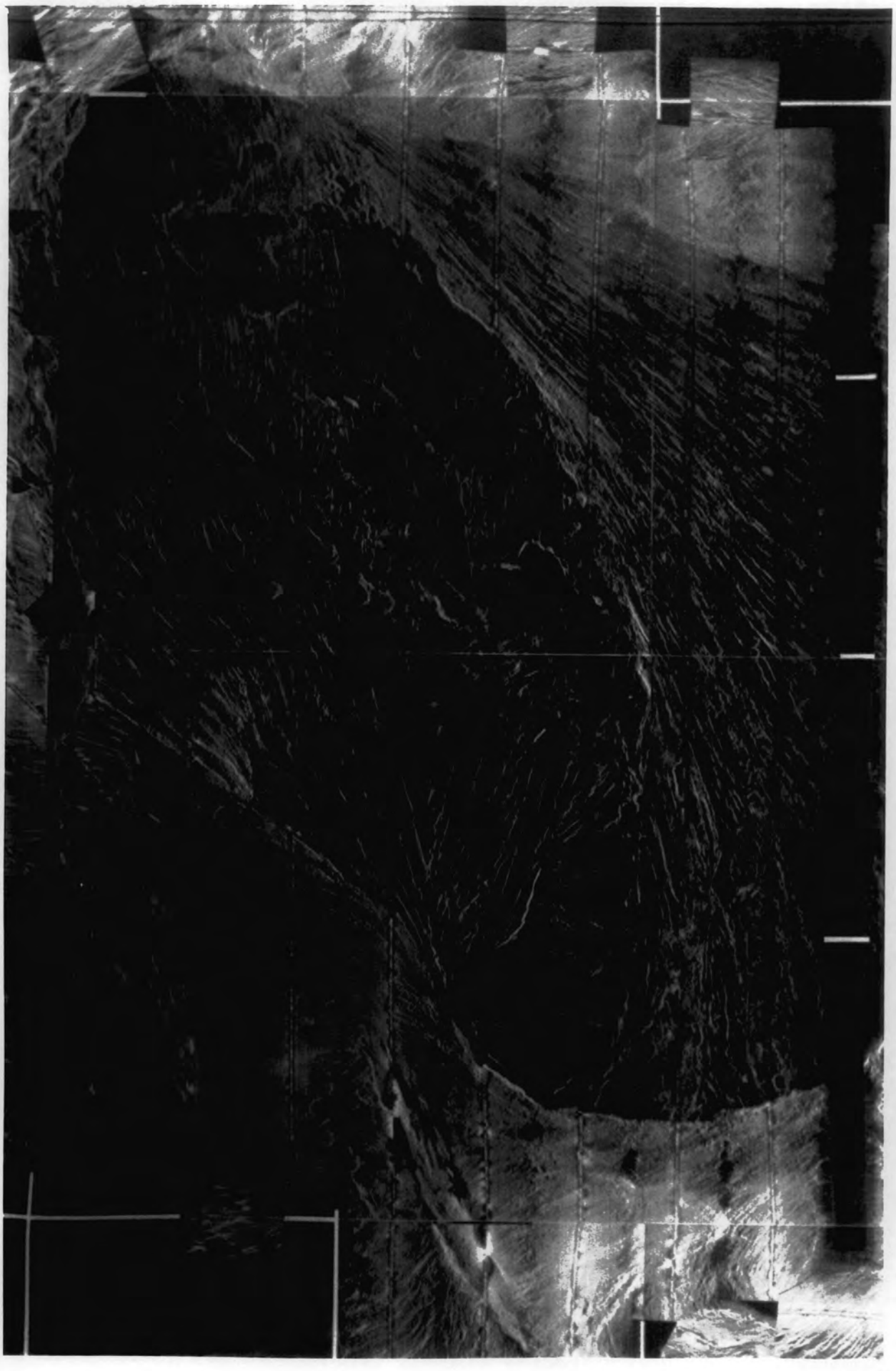

a

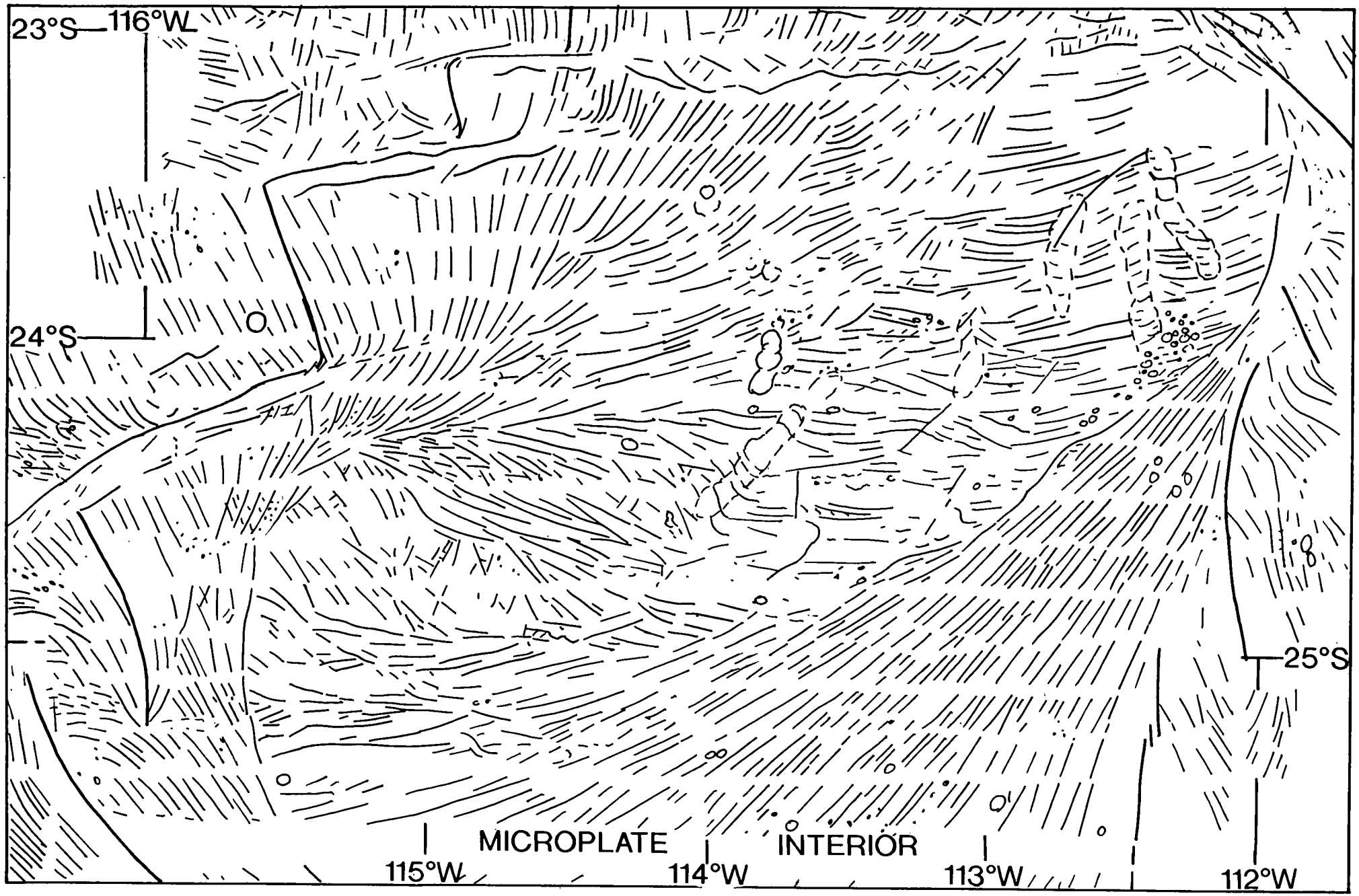

b

overall rotation of the microplate, small amounts of localised dextral shear may have occurred to the east of pre-existing transforms, where a fracture zone would normally be found, due to the slightly faster spreading rate immediately to the north of each transform zone (e.g. at around 23°40'S, 114°33'W, Fig. 4.19a,b). This would explain the localised areas of increased clockwise rotation of pre-existing ridge parallel abyssal hill fabric.

The material formed on the East Rift and lying on the interior of the microplate shows almost continuous fanning from the present site of lithosphere accretion westwards out to the major inner pseudofault (EIPF). Propagation along the East Rift today is to the west (inside) of the dying rift that is being replaced. This leaves the most prominent evidence for rift propagation (i.e. the sheared and rotated lithosphere that has been transferred from the Easter plate to the Nazca plate) on the Nazca plate, and not on the microplate interior (Fig. 4.10a,b and Fig. 4.14a,b). However, the GLORIA images of the pseudofaults of the most recent propagators along the East Rift (Plate 1 and Fig. 4.19a,b) are seen more clearly on the microplate side of the rifts than on the Nazca plate side. They separate younger, highly reflective seafloor from slightly older, less reflective seafloor. Subtle changes (< 10°) are seen in the orientation of spreading fabric either side of the pseudofaults.

Evidence for older episodes of East Rift propagation within the microplate interior are less obvious (Fig. 4.8a,b and Fig. 4.19a,b). The propagation events associated with the original northward growth of the East Rift (between about 5.25 Ma and just after 2.5 Ma, see section 6.3, Chapter 6) can be detected from subtle changes in spreading fabric to the southeast of the EIPF along most of its length. Magnetic anomaly interpretations (Fig. 2.7, Chapter 2) suggest that there was an anticlockwise spreading centre reorganisation between anomaly 2 and the start of anomaly 2A, which should be evident at around 26°S, and between, say, 113°20'W and 114°W on the GLORIA mosaic (Fig. 4.8a,b). The southernmost east-west ship's track which passes through this area reveals confused seafloor fabric of varying trend. This fabric, however, is not diagnostic of rift propagation, although presumably it has been caused by such a mechanism. Older, weaker spreading fabric presently trending around 050° appears to have been overwritten by younger, stronger fabric which now trends 025°.

Other notable features within the microplate interior include a series of large, circular seamounts, and several prominent ridges. Four or five large seamounts (of about 7 km in diameter) trend roughly north-south along 113°46'W at around 24°S (Fig. 4.19a,b). These seamounts are similar in size and appearance to the seamount situated to the west of the West Rift at 23°56'S, 115°37'W. No rock samples have been collected from these seamounts, and little is known about them. They may have formed at the ridge axis

(West Rift) at the same time as the lithosphere on which they are found, due to an excessive melting anomaly (or small mantle plume), or they may be true intraplate seamounts. Either way, it is impossible to say whether they were formed from the same magma source and whether or not this source was stationary or migrated laterally with time. If these seamounts were formed at the ridge axis from the same stationary source, they would have recorded the absolute motion of the Easter Microplate during the time of their formation (about 1 myr.) possibly during the period of, say, 3.8-4.8 Ma (estimated from Fig. 2.7, Chapter 2 and a plausible half spreading rate of 50 mm/yr). Other volcanic cones of much smaller diameter (< 4 km) can be observed scattered throughout the microplate interior.

Several anomalous ridges have been imaged by GLORIA within the microplate. Three such ridges exist to the southwest of the Pito Deep region, at around 23°30'S, 112°30'W. The westernmost ridge trends roughly 010°, the middle one north-south, and the easternmost one around 335°. The northern end of the eastern ridge (which curves into a more northerly trend) has also been imaged by Sea MARC II (Naar et al., in press), and clearly stands out on a colour relief map of the area. These ridges appear to be analogous to some of the ridges found on the Nazca plate to the northeast of Pito Deep (Fig. 4.16a,b), which occur within lithosphere of a younger age. Other ridges like these are found on even older lithosphere to the southwest, such as at around 24°10'S, 113°05'W (trending north-south), and around 24°20'S, 113°50'W (trending 040°). Some of these ridges may be constructional in nature (i.e. made up of chains of large seamounts and small volcanic cones) rather than tectonic in origin. However, their striking resemblance to the ridges on the Nazca plate to the north of the microplate (which are almost certainly tectonic in origin), and the fact that they are cross-cut by old abyssal hill fault scarps, suggests that the latter is the case. On the GLORIA mosaic, they look like buckled areas of the seafloor. The morphology of these features suggests that they are the result of compressional folding rather than faulting mechanisms. Similar looking ridges have also recently been imaged using GLORIA on the Juan Fernandez microplate, and have been identified as compressional in nature (Bird et al., 1991; Larson et al., submitted 1991).

4.2.9 Discussion

There is clear evidence of earlier episodes of rift propagation associated with the West Rift of the Easter Microplate during the last few million years. This is shown by the rotated abyssal hill lineations to the west of the microplate, where obliquely trending lineaments caused by the rift propagation events have both transposed and superimposed earlier near ridge-parallel trends. Rift propagation events in the past

appear to have been episodic, and where propagation has ceased for a sufficient length of time (>0.5 myr) a transform fault has formed. Although GLORIA data to the east of the East Rift are relatively scarce, there is no evidence to show that individual rift propagation events associated with it have been discontinuous and so a transform fault could not initiate.

The Anakena, Raraku and Terevaka transform faults presently situated along the West Rift are 41 km, 74 km and 103 km long respectively, and are longer in the south than in the north. All three of these transform faults consist of more than one through-going active fault strand ("Principal Transform Displacement Zone" or PTDZ), and are able to accommodate small changes (<10°) in relative plate motion. The Anakena and Raraku transforms show evidence for small clockwise changes in motion during the last 1 myr or so, presumably in response to the clockwise rotation of the microplate. The Terevaka transform appears to have rotated anticlockwise recently, which has resulted in the initiation of a north-south trending extensional relay basin between the east and west active fault strands. Anticlockwise rotation of the fracture zones is required to maintain the major Pacific-Nazca relative plate motion vectors constant either side of the microplate. Larger changes in orientation of the West Rift plate boundary are accommodated by rift propagation events.

The propagating rifts of the East Rift point towards the Nz-Ea pole as predicted, and as there is no evidence to show that rift propagation has ceased at any time, it is assumed to be a continuous process. The lengths of individual spreading segments remain roughly constant as they migrate northwards because the tail of each segment is continuously being replaced by the subsequent propagator as fast as the tip can propagate. Spreading centre reorientations on the East Rift are subtle, and it is not clear what provides the catalyst for the initiation of these individual rift propagation events. The tails of all the OSC limbs and propagators are roughly aligned along a trend of 016°, which is also the predicted (though not actual) trend of the East Pacific Rise in this region (using DeMets et al. (1990) pole, or others). The reason, or significance of this is not clear. Possibly this is because the initially rapid northern propagation of the East Rift has meant that it remained more or less under the influence of the Pa-Nz stress field. One possibility is that the main magmatic bodies associated with the East Rift are situated along this trend, while the rift segments propagate towards the Nz-Ea pole as a function of the relative plate motions. Propagation on the East Rift is continuous, and so no transforms can form to accommodate the sinistral shear between the offset ridge segments. "Bookshelf" faulting, involving the anticlockwise rotation of individual fault blocks, thus occurs within the migrating shear zones in a way originally described by

Kleinrock and Hey (1989). Many abandoned shear zones which have resulted from earlier rift propagation episodes should exist to the east of the East Rift. These would have to be fairly small in areal extent, as the magnetic anomaly data are relatively undisturbed. Only small discontinuous changes in spreading fabric orientation can be distinguished to the west of the East Rift, indicating that changes in ridge orientation achieved by propagation along the East Rift must have been subtle. Rift propagation at the northern end of the East Rift is more complex than at the southern end, as the difference between the spreading direction and the overall trend of the plate boundary is greatest. Areas of spreading fabric that are now highly oblique both to the local spreading direction and the overall trend of the East Rift are observed on the GLORIA data (at around 23°36'S, 111°45'W), having resulted from relatively slowly migrating shear zones.

Overlapping spreading centres (OSCs) associated with the Easter Microplate tend to occur in regions of faster spreading rates (>100 mm/yr.), which are subject to higher magmatic fluxes. At the southern end of the East Rift, the absence of decapitated rift segments and rafted-off limbs suggests the OSCs are ephemeral ridge axis discontinuities that migrate and evolve extremely rapidly, according to either changing stress regimes or magmatic processes.

Ridge segmentation and offset by (a) transform faults or (b) overlapping spreading centres provide the two extremes by which changes in plate motions around the Easter Microplate are accommodated, while rift propagation connects the two. The absence of any normal transform faults on the East Rift may indicate that the lithosphere is too thin and weak to sustain narrow well-defined strike-slip fault zones, while the abundance of OSCs south of 26°S on the East Rift and south of the microplate may suggest that the plate boundary is not strong enough to support even propagating rift systems with migrating shear zones. As similarly fast spreading rates and lengths of offsets are accommodated at the northern end of the West Rift by transform faults, I suggest that the occurrence of these OSCs is related to the presence of the Easter hotspot within the vicinity . The idea that the length of OSC overlap to the width of offset is usually a ratio on the order of 3:1 (e.g. Macdonald et al., 1988) is not supported by the OSCs found around the Easter Microplate, which vary in ratio from 0.9:1 to 1.9:1.

The anomalous morphology of the northern boundary of the microplate supports the idea proposed by Zukin (1990) that the predicted convergence between the Nazca and Easter plates is being accommodated by thrust faulting. The recently computed earthquake focal mechanism from the area (no. 30, Chapter 5) adds further weight to this view. Pure strike-slip movement only occurs at the eastern end of the boundary, and

possibly to the east of the northern triple junction, while along the remainder of the boundary, in order to accommodate the dextral transpression predicted, there is possibly strain partitioning between thrust faulting and strike-slip movement. Thrust faulting is also inferred to take place within the Nazca plate to the north of the microplate along a series of prominent east-west trending en echelon faults. These extend from around 22°S just east of the EPR to near the Pito Deep region. The thrust faulting on the Nazca plate does not occur immediately adjacent to the EPR. Instead it is offset by a short distance which corresponds to about 0.3 myr in age. Similarly, the thrust faulting along the northern boundary is offset by about 0.25 myr. This time increment may correspond to the period required for sufficient compressional stress to build up within the lithosphere before thrust faulting can take place, or for the lithosphere to grow strong enough to deform by brittle faulting. Further dextral transpression in the region to the north of the microplate is accommodated by pervasive bookshelf faulting, as shown by the rotated abyssal hill fabric and the occurrence of several earthquake mechanisms consistent with sinistral strike-slip movement along antithetic Riedel shears.

At the southern boundary, pure dextral strike-slip movement between the Pacific and Easter plates occurs along only a small part of the boundary (the so-called Orongo fracture zone). To the east of the convergence of two anomalously shallow ridges and the Southwest Rift tip, transtension is predicted by the instantaneous Pa-Ea pole, while further to the southeast along the ridge extending from the Orongo fracture zone, transpression must occur. The cause of the extreme elevation of the southern boundary (only 640m water depth at the shallowest part) is difficult to determine from the morphology alone. These ridges may be relicts of transverse ridges associated with a transform separating the Pacific and Nazca plates prior to the formation of the microplate (before 5.25 Ma), or the proposed transform that connected the southern end of the West Rift with the East Rift/EPR before the Southwest Rift opened up (i.e. before 2.5 Ma). Transform faults are sites of anomalous hydrothermal alteration processes, leading to serpentinisation of gabbros and peridotites. These serpentinised rocks are easily uplifted as the transverse ridges of fracture zones, that in the extreme case may form islands (such as the St. Peter and Paul islands associated with the St. Paul fracture zone). However, these extreme cases of uplift are generally only associated with large-offset fracture zones, and the offset here would not have been greater than 200 km. The shallow ridges of the southern boundary of the microplate may have been serpentinised and uplifted in a similar way, or may have formed purely due to tectonic convergence. Alternatively they may have formed from constructional volcanism associated with the Easter hotspot, although the GLORIA data do not indicate the presence of any small volcanic cones or fresh-looking lava flows.

The region of the southern triple junction remains poorly understood. A complex series of ridges exists that may be part of a relict Pacific-Nazca or Pacific-Easter transform that has been broken up and incorporated into the Easter Microplate.The whole region south of 27°S appears to be very magmatically active, since recent-looking lava flows and numerous small volcanic cones have been imaged by GLORIA. If the triple junction is taken as being at around 28°S, 113°W, then at a gross scale it may be viewed as a ridge-ridge-fault (R-R-F) system (the convergence along the Pacific-Easter fault is negligible) (Fig. 4.20a). However, this configuration is unstable, and must evolve into a F-F-R system. With continued spreading, the limbs of the southern EPR and the southern end of the East Rift become offset along a fault, which is in fact the sheared interior of the OSC (Fig. 4.20b). Through time, this rift offset will inevitably grow, unless the tips of the two limbs continuously reorganise themselves to prevent this.

Within the microplate interior, chains of seamounts and ridges have been imaged by GLORIA. The chains of seamounts may represent a period of excess magmatism on the East Pacific Rise and West Rift over 3 myr. ago, possibly as the fractionated remains of a magma chamber were extruded. I suggest that at least one of the ridges imaged, which dips steeply to the west and gently to the east, is analogous to the thrust faults found on the Nazca plate to the north of the microplate, and may have originally formed before being transferred to the microplate interior by propagation of the East Rift (i.e. well before 2.5 Ma). The other ridges are similar to the compressional folds recently imaged by GLORIA to the north of the Juan Fernandez microplate (Bird et al., 1991, Larson et al., in press) and I suggest they have formed in a similar manner.

4.3 Rock Samples

4.3.1 Introduction

In the following subsections the geochemistry of rock samples from three different published data sets is examined. An attempt is made to relate the geochemistry of these samples to their tectonic setting, both in terms of their proximity to the elusive Easter Hotspot, and their relation to ridge segmentation.

4.3.2 Data set

All the data (except sample 122D) have been collected on or near the present day spreading centres around the Easter Microplate, and their locations are shown in Fig. 4.21. The samples numbered 1D to 44D are dredge samples from Schilling et al. (1985), collected during the R/V Endeavor cruise EN-113. Of these samples, 18D is a

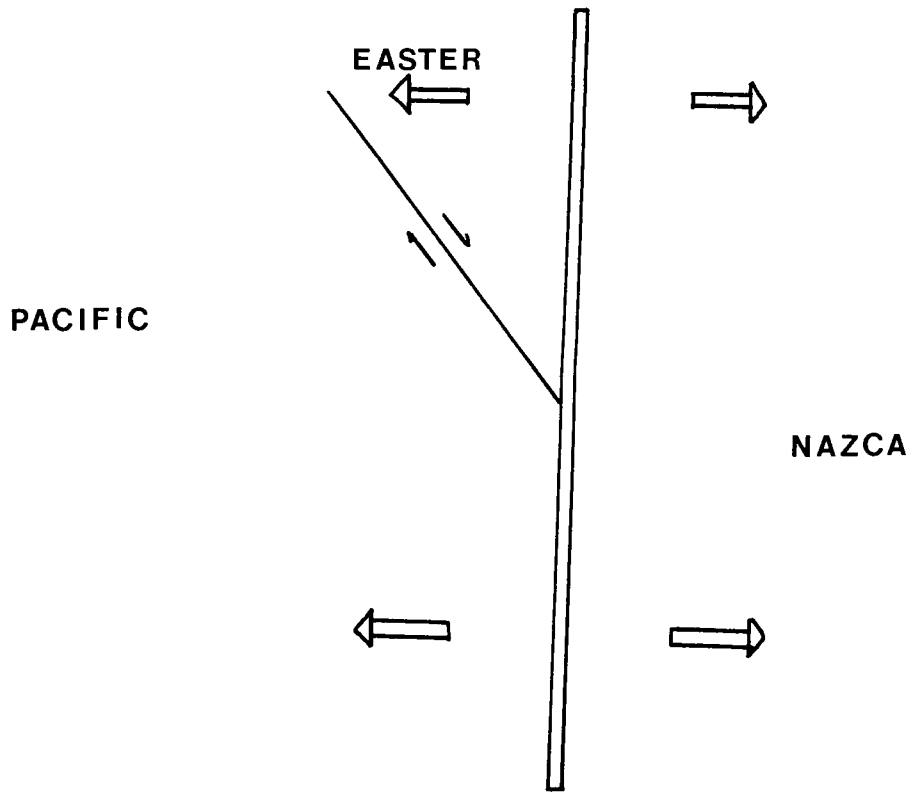

a

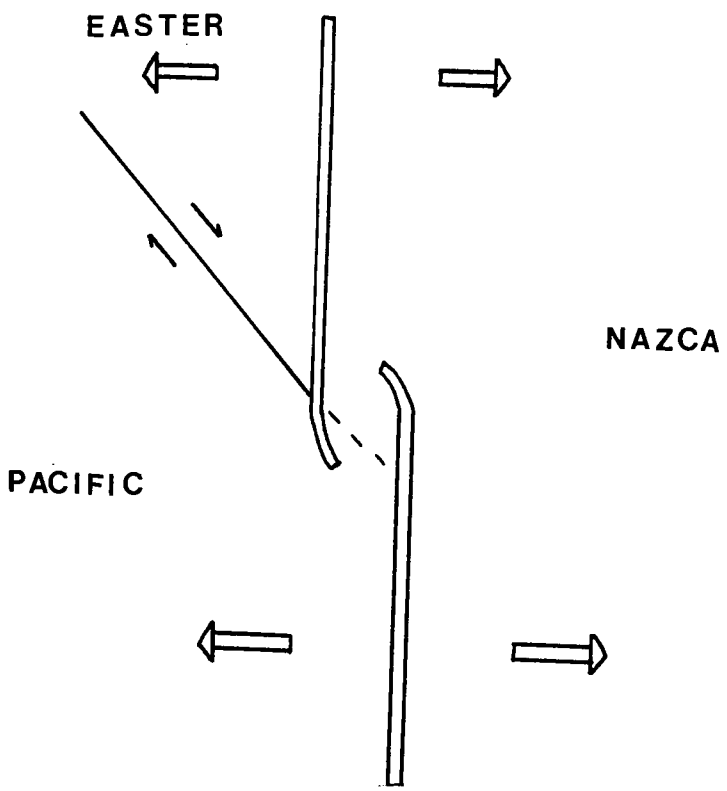

b

Figure 4.20 Schematic diagram indicating the behaviour of the southern triple junction. If the triple junction is taken as being at around 28°S, 113°W, then at a gross scale it may be viewed as a ridge-ridge-fault (R-R-F) system, which is intrinsically unstable (a). This has to evolve into a F-F-R system, with the limbs of the southern EPR and the southern end of the East Rift offset along a fault, which is in fact the sheared interior of an OSC (b). Through time, this rift offset will inevitably grow, unless the tips the two limbs of the OSC continuously reorganise themselves to prevent this.

Figure 4.21 Simplified tectonic interpretation of the Easter Microplate showing locations from which rock samples have been recovered. All the data have been collected on or near the present day plate boundaries (except for 122D). The samples numbered 1D to 44D are dredge samples from Schilling et al. (1985), collected during the R/V Endeavor cruise EN-113. Samples numbered 73D to 154F were collected during the Geometep 4 cruise SO40 (Marchig & Gundlach, 1987) and samples 215S to 268F were collected during leg 1 of the Geometep 5 cruise SO62. Sample numbers suffixed by "D" denote dredge samples; "G" denotes samples recovered using a grab mounted with a TV camera; "S" denotes glass fragments found in the crown of 5 m gravity cores; "F" denotes samples inadvertently recovered by the towed camera sledge OFOS (Ocean Floor Observation System).

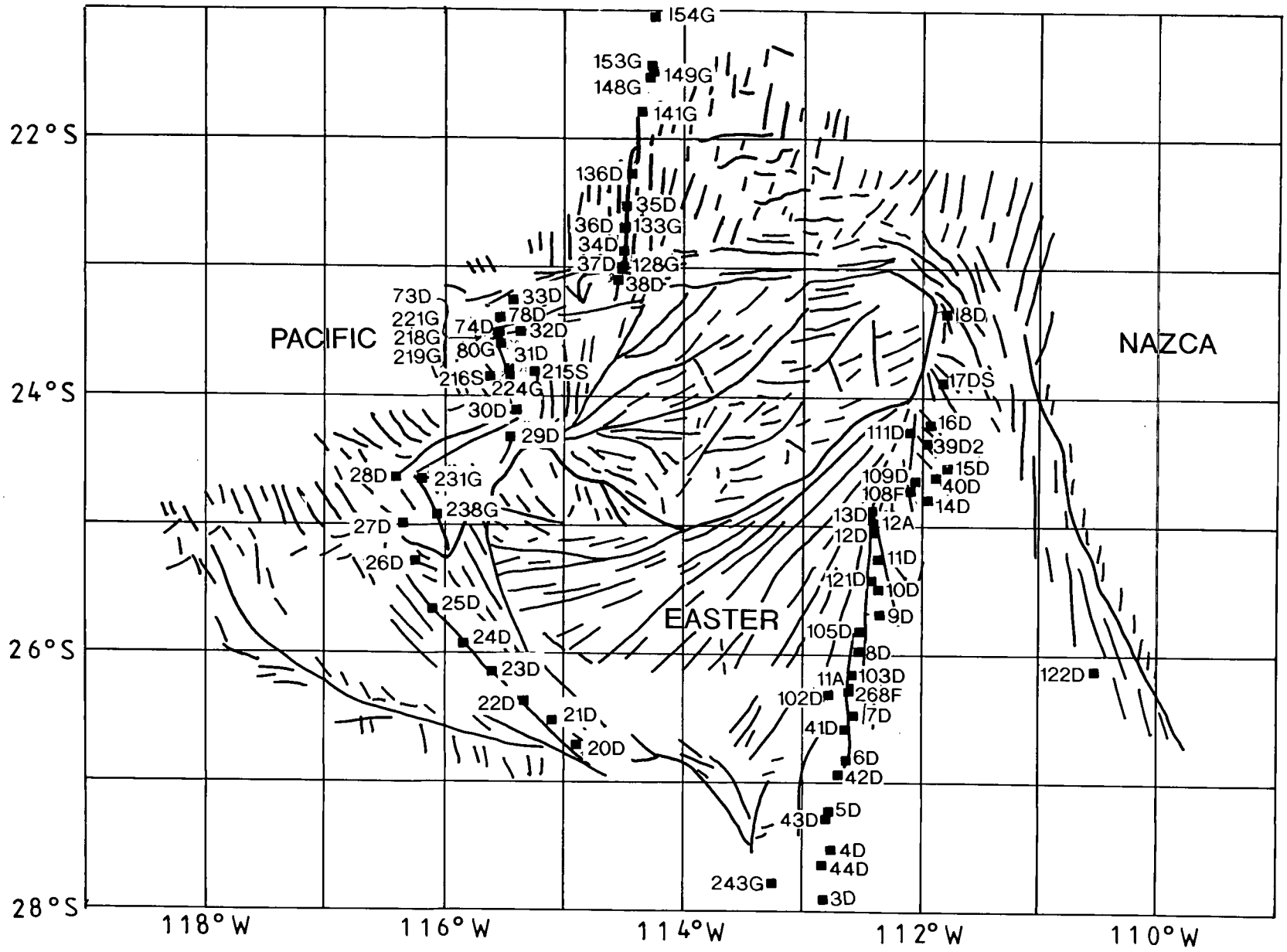
154G
153G
149G
148G
141G
136D
35D
36D
133G
34D
37D
128G
38D
73D
33D
221G
78D
74D
32D
218G
80G
31D
219G
216S
224G
215S
30D
29D
28D
231G
238G
27D
26D
25D
24D
23D
22D
21D
20D
PACIFIC
EASTER
NAZCA
18D
17DS
16D
111D
39D2
15D
109D
40D
108F
14D
13D
12A
12D
11D
121D
10D
9D
105D
8D
11A
103D
268F
102D
7D
41D
6D
42D
43D
5D
4D
44D
243G
3D
122D
22°S
24°S
26°S
28°S
118°W
116°W
114°W
112°W
110°W

serpentinised peridotite retrieved from near the Pito Deep region, and three samples (38D, 33D and 29D) are breccias, associated with the transforms of the West Rift (see Fig. 4.21). Samples numbered 73D to 154F were collected during Geometep 4 (cruise SO40) (Marchig & Gundlach, 1987) and samples 215S to 268F were collected during leg 1 of Geometep 5 (cruise SO62) (Marchig et al., 1989). Sample numbers suffixed by "D" denote dredge samples; "G" denotes samples recovered using a grab mounted with a TV camera; "S" denotes glass fragments found in the crown of 5m gravity sediment cores; "F" denotes samples inadvertently recovered by the towed camera sledge OFOS (Ocean Floor Observation System). Although the samples have been analysed by electron microprobes in different laboratories, the errors encountered by these laboratories using this method are sufficiently small (< 0.5%) to allow comparison of the data sets. Averages of the major element concentrations for each sample are given in Table 4.1. Also given are the concentrations of Cr and Co, Nb/Zr ratios, chondrite normalised La/Sm ratios and $^{87}Sr/^{86}Sr$ ratios where these have been obtained.

4.3.3 Major and minor element variations

I have calculated CIPW norms (Cross et al., 1903) for most of the samples and the results are given in Table 4.2. The program used for this was "CIPWNorm" written by D.R. Mason. Although Schilling et al. (1985) report five nepheline normative samples (undersaturated in SiO_2 and with higher Al_2O_3 and Na_2O concentrations) from around the Easter Microplate (13D, 31D, 28D, 26D and 4D, as indicated on Fig. 4.22), my calculations show that samples 31D and 4D are actually olivine normative tholeiites (saturated in SiO_2). The remainder (majority) of the basalts are either olivine or quartz normative tholeiites (oversaturated in SiO_2) and correspond to normal mid-ocean ridge basalts (MORBs). Those that are quartz normative are indicated by a "Q" on Fig. 4.21, and those that are highly quartz normative (> 2% quartz in the norm) are indicated by "hiQ".

The samples vary from basalts to ferrobasalts and basaltic andesites (with SiO_2 contents showing a typically narrow variation of between 47% and 53%, Fig. 4.23a). I calculated Mg numbers (Mg# = Mg^{2+} x 100/ (Mg^{2+} + Fe^{2+})) and used these to illustrate differentiation by fractional crystallisation from primitive to more evolved compositions. Samples with $FeO_{(T)}$ >12% and TiO_2 > 2% are classified as being "FeTi basalts" or "ferrobasalts" (Byerly et al., 1976; Natland, 1980), and are indicated here by "FeTi" in Fig. 4.22 and above the dividing line in Fig.4.23c,d).

The major oxides for the glasses have been plotted against Mg# in Fig. 4.23a-j, with the EPR, East Rift and West Rift plotted separately, and many samples labelled.

Table 4.1 Analysis of Easter Microplate Rocks

Sample no.	Latitude	Depth	SiO2	Al2O3	FeO(T)	MgO	CaO	Na2O	K2O	TiO2	P2O5	MnO	Total	Mg#	Cr	Co	(La/Sm)n	Nb/Zr	87Sr/86Sr
E.P.R.(N)																			
154G	21.04	-2871	51.50	15.00	9.38	7.55	12.50	2.73	0.08	1.26	0.10	0.18	100.55	58.92	300	39		0.037	
153G	21.43	-2767	51.10	14.50	10.50	6.82	11.34	2.85	0.10	1.72	0.16	0.19	99.45	53.65	193			0.031	
149G	21.48	-2777	51.10	14.10	11.07	7.19	11.37	2.80	0.08	1.75	0.15	0.20	100.05	53.65	197	40	0.50	0.033	
148G	21.49	-2765	51.00	14.30	10.82	7.30	11.38	2.70	0.07	1.72	0.14	0.19	100.71	54.59	251	42		0.025	
141G	21.80	-2900	51.20	13.50	12.57	6.72	10.73	2.63	0.08	2.04	0.16	0.22	100.18	48.79	124	49		0.030	
136D	22.26	-2914	50.80	15.10	10.03	7.84	11.66	2.73	0.10	1.61	0.15	0.17	100.79	58.21	329	40	0.52	0.036	
35D	22.53	-2912	50.13	15.69	10.53	8.19	11.48	2.54		1.55	0.07	0.18	101.53	58.09	310	42	0.51		0.70243
133G	22.67	-2910	50.70	14.70	11.01	6.95	11.16	2.75	0.09	1.94	0.18	0.19	99.94	52.94	221	46	0.52	0.028	
36D	22.68	-2950	50.55	14.72	10.31	7.45	11.83	2.84		1.59	0.11	0.16	100.71	56.29	266	40	0.57		0.70247
34D	22.90	-2975	51.17	15.15	9.21	8.38	12.42	2.40		1.21	0.04	0.16	101.17	61.85	344	39	0.44		0.70239
128G	22.99	-3003	50.90	15.35	9.09	8.56	12.41	2.34	0.07	1.15	0.09	0.16	99.86	62.66	385	42	0.38	0.037	
37D	23.00	-3035	50.68	14.11	11.81	6.80	11.27	2.85		1.96	0.10	0.20	101.09	50.64	180	44	0.51		0.70240
38D	23.08	-3125													191	45	0.35		0.70240
East Rift																			
18D	23.54	-3532													64	32	0.60		
170S	23.86	-3905	50.38	14.73	10.64	6.89	12.11	3.01	0.05	1.97	0.22	0.17	101.35	53.57	257	41	0.62		0.70239
16D	24.20	-2950	50.55	15.68	8.61	8.30	12.16	3.24	0.10	1.49	0.24	0.18	101.51	63.21	280	39	1.02		0.70251
111D	24.24	-3615	50.90	15.30	9.72	8.11	11.86	2.61	0.09	1.45	0.13	0.17	102.33	59.79	273	44		0.049	
39D-2	24.36	-2898													197	42	0.54		0.70254
15D	24.53	-2975	50.78	12.69	14.10	6.00	10.53	2.89	0.05	2.93	0.36	0.36	102.26	43.13	194	42	0.64		0.70262
40D	24.61	-2825	50.23	15.33	9.31	8.43	13.10	2.54		1.11	0.10	0.16	101.35	61.74	340	43	0.44		0.70280
109D	24.66	-3173	50.60	15.20	9.72	8.02	11.86	2.55	0.08	1.44	0.14	0.17	100.01	59.52	276	40	0.72	0.039	
108F	24.71	-2686	49.90	15.60	10.68	7.48	11.34	2.67	0.14	1.81	0.16	0.18	100.04	55.52	251	42		0.031	
14D	24.78	-2630	51.41	14.93	9.57	7.72	11.87	2.80	0.02	1.45	0.21	0.09	101.14	58.97	322	40	0.59		0.70266
13D	24.86	-2948	48.91	17.11	8.70	8.15	11.75	3.54		1.50	0.17	0.04	100.84	62.54	499	49	0.39		0.70249
12A	24.98	-3264	50.25	13.41	13.39	5.95	10.07	3.08	0.15	2.57	0.32	0.30	100.98	44.19	80	44	0.84		0.70261
12D	25.03	-3255	50.57	13.21	13.30	5.68	10.20	3.01	0.12	2.66	0.36	0.17	100.76	43.22	121	42	0.94		0.70278
11D	25.24	-3158													187	42	1.15		0.70278
121D	25.38	-3159	51.20	14.70	11.70	7.69	11.39	2.47	0.14	1.90	0.17	0.20	101.77	53.94	292			0.056	
10D	25.47	-2970	50.83	13.16	13.66	5.54	10.16	2.97	0.10	2.74	0.33	0.27	101.28	41.95	46	43	0.93		0.70270
9D	25.66	-2865	50.62	13.56	12.62	6.04	10.66	2.93	0.11	2.72	0.35	0.18	101.19	46.03	86	41	0.93		0.70271
105D	25.80	-2778	50.70	14.50	10.72	7.52	11.60	2.40	0.16	1.74	0.16	0.18	99.87	55.56	255	47	0.86	0.067	
8D	25.98	-2668	51.04	14.36	11.50	6.97	10.39	2.85	0.10	2.16	0.22	0.18	101.05	51.92	242	40	0.96		0.70268
122D(a)	26.10	-3003	50.50	13.45	12.98	6.02	10.36	2.72	0.40	1.97	0.18	0.20	99.17	45.25	92	44	0.72	0.051	
122D(b)	26.10	-3003	52.90	14.65	8.78	6.19	10.96	2.97	0.38	2.17	0.20	0.19	103.62	55.68	73	44		0.042	
103D	26.15	-2652	49.80	15.30	10.26	7.22	11.50	2.65	0.25	1.84	0.19	0.18	98.99	55.63	289	41	1.00	0.084	
268F	26.26	-2390	46.14	10.92	8.29	1.16	9.95						77.38	19.96					
11A	26.27	-2425	50.11	14.60	10.84	6.82	11.48	2.96	0.23	2.09	0.29	0.23	100.86	52.86	215	38	1.10		0.70285
102D	26.30	-2782	50.80	14.30	11.67	6.39	11.09	3.01	0.29	2.10	0.20	0.20	99.14	49.39	134	41	1.63	0.064	
7D	26.46	-2272	49.75	15.65	10.30	6.93	10.37	3.03	0.37	2.57	0.30	0.17	100.59	54.52	195	37	1.71		0.70285
41D	26.58	-2282	50.42	15.40	13.12	7.02	11.41	3.06	0.20	2.20	0.28	0.19	104.76	48.81	231	39	1.39		0.70285
6D	26.81	-2362	49.81	16.27	10.09	7.14	10.18	3.02	0.45	2.54	0.30	0.15	101.07	55.77	281	41	1.94		0.70299
42D	26.92	-2590	50.54	15.37	9.66	7.50	11.35	2.92	0.19	2.04	0.31	0.21	101.17	58.05	133	43	1.26		0.70281
5D	27.21	-2632	50.08	15.72	9.21	9.21	12.01	2.41		1.07	0.12	0.19	100.86	64.05	351	44	0.54		0.70261
43D	27.30	-2438	50.48	14.80	9.96	7.46	11.96	2.77	0.09	1.69	0.27	0.18	100.77	57.17	261	40	1.03		0.70269
4D	27.53	-2520	47.29	16.59	11.23	10.59	10.24	2.83		1.39	0.12	0.18	101.71	62.69	364	58	0.59		0.70321
44D	27.64	-2522	50.19	15.70	8.73	8.21	12.55	2.75	0.06	1.44	0.26	0.18	101.04	62.63	367	43	1.03		0.70269
243G	27.77	-1987	49.31	13.69	12.51	6.15	11.04	2.95	0.16	2.01	0.15	0.22	99.58	46.70	329	48		0.059	
3D	27.88	-2300	49.64	16.34	9.43	8.23	10.99	2.93	0.19	1.87	0.20	0.23	101.10	60.86	252	38	1.44		0.70278
West Rift																			
33D	23.25	-2815													148	40	0.62		0.70257
78D	23.37	-2463	48.70	16.90	8.59	6.70	10.22	3.34	0.89	2.20	0.44	0.22	99.16	58.16	189	34		0.164	
32D	23.48	-3270	50.56	14.24	11.22	7.36	11.62	2.64	0.02	1.95	0.16		101.02	53.89	288	40	0.69		0.70244
74D	23.48	-2595	50.70	13.70	12.68	6.37	10.75	2.92	0.21	2.19	0.21	0.20	101.34	47.24	118	45		0.046	
73D	23.51	-2630	51.20	14.10	11.75	7.05	11.39	2.69	0.15	1.90	0.17	0.18	101.89	51.67	192	40		0.050	
218G	23.53	-2615	50.20	14.30	11.26	6.95	11.20	2.85	0.19	1.83	0.19	0.22	100.44	52.38	396	41		0.058	
221G	23.53	-2620	50.10	14.50	11.08	7.01	11.20	2.79	0.26	1.85	0.20	0.20	100.42	52.99	359	42		0.055	
219G	23.54	-2615	50.40	14.20	11.35	6.75	11.00	2.88	0.25	1.89	0.22	0.20	100.40	51.45	343	42		0.058	
80G	23.57	-2581	50.20	14.60	11.01	7.20	11.28	2.79	0.19	1.84	0.18	0.14	100.66	53.82	238	43	0.85	0.059	
31D	23.77	-2660	50.51	14.70	10.75	7.78	11.77	2.67		1.45	0.08	0.19	101.10	56.33	250	43	0.65		0.70241
215S	23.80	-2940	50.40	12.90	14.05	4.79	8.82	3.52	0.42	2.64	0.60	0.26	99.96	37.79					
224G	23.83	-2660	50.40	14.80	9.55	8.22	12.50	2.25	0.05	1.15	0.09	0.18	100.25	60.53	558	43		0.076	
216S	23.84	-3040	49.40	14.40	11.62	7.05	10.40	3.05	0.29	2.09	0.25	0.25	100.09	51.95					
30D	24.11	-2800	50.34	15.11	10.34	7.25	11.28	3.09	0.01	1.93	0.28	0.19	100.97	55.54	245	44	0.35		0.70229
29D	24.31	-2692	49.79	15.01	10.42	7.70	11.71	2.98	0.04	1.60	0.30	0.20	100.91	56.84	174	53	0.71		0.70243
28D	24.64	-2740	49.31	16.43	9.01	8.55	12.31	3.02		1.32	0.02	0.19	101.16	62.84	317	45	0.40		0.70250
231G	24.64	-3008	50.00	15.10	9.28	8.32	12.70	2.37	0.05	1.12	0.05	0.17	100.19	61.50	541	47		0.082	
238G	24.91	-2960	50.10	14.17	11.02	7.28	11.82	2.24	0.07	1.29	0.07	0.20	99.49	54.07	364	48		0.067	
27D	24.99	-2060	50.53	14.78	9.84	7.76	12.44	2.64	0.07	1.54	0.09	0.16	100.95	58.43	363	43	1.10		0.70293
26D	25.28	-2052	47.90	17.96	9.51	9.92	11.36	2.79		0.82	0.01	0.17	101.50	65.02	352	54	0.43		0.70229
25D	25.66	-2240	50.60	14.57	10.69	7.43	11.72	2.99	0.04	1.65	0.17	0.15	101.20	55.33	231	42	0.83		0.70249
24D	25.90	-2212	50.36	14.50	10.90	7.28	11.67	2.96	0.07	1.73	0.17	0.24	101.09	54.34	142	42	0.96		0.70260
23D	26.13	-2606	50.42	14.60	10.94	7.28	11.90	2.92	0.05	1.77	0.15	0.24	101.49	54.25	175	43	0.88		0.70260
22D	26.35	-2788	50.60	13.75	12.49	6.56	10.83	2.91	0.08	2.21	0.19	0.26	101.27	48.35	117	43	0.95		0.70260
21D	26.52	-2705	50.93	13.94	11.52	6.88	11.44	2.84	0.06	1.73	0.18	0.30	101.10	51.56	195	39	0.86		0.70258
20D	26.70	-2918	49.88	14.71	10.47	7.46	12.35	3.04	0.08	1.76	0.19	0.22	101.33	55.94	245	43	1.09		0.70272

Table 4.2 CIPW norms

Samp	Q	Or	Ab	An	Ne	Dwo	Den	Dfs	Hen	Hfs	Fo	Fa	Mt	Il	Ap	Sum
E.P.R. (N)																
154G	0.00	0.47	23.10	28.44	0.00	13.75	8.44	4.52	9.96	5.33	0.70	0.41	3.04	2.39	0.23	100.79
153G	0.60	0.59	24.12	26.48	0.00	12.00	6.63	4.91	10.36	7.67	0.00	0.00	2.46	3.27	0.37	99.45
149G	0.46	0.47	23.69	25.67	0.00	12.43	6.96	4.96	10.95	7.80	0.00	0.00	2.99	3.32	0.35	100.05
148G	0.43	0.41	22.85	26.69	0.00	12.05	6.73	4.84	11.45	8.24	0.00	0.00	3.44	3.27	0.32	100.71
141G	2.71	0.47	22.25	24.79	0.00	11.44	6.09	4.99	10.65	8.71	0.00	0.00	3.83	3.87	0.37	100.18
136D	0.00	0.59	23.10	28.65	0.00	11.78	6.79	4.45	9.50	6.23	2.27	1.64	2.38	3.06	0.35	100.79
35D	0.00	0.00	21.49	31.41	0.00	10.47	6.24	3.70	11.06	6.56	2.17	1.42	3.90	2.94	0.16	101.53
133G	0.57	0.53	23.27	27.50	0.00	11.14	6.18	4.53	11.13	8.16	0.00	0.00	2.81	3.68	0.42	99.94
36D	0.00	0.00	24.03	27.42	0.00	12.76	7.42	4.74	9.09	5.80	1.44	1.01	3.74	3.02	0.25	100.71
34D	0.00	0.00	20.31	30.56	0.00	12.86	7.94	4.17	12.63	6.63	0.21	0.12	3.33	2.30	0.09	101.16
128G	0.00	0.41	19.80	31.17	0.00	12.44	7.80	3.88	12.36	6.16	0.81	0.45	2.17	2.18	0.21	99.86
37D	0.39	0.00	24.12	25.71	0.00	12.34	6.66	5.26	10.28	8.11	0.00	0.00	4.28	3.72	0.23	101.09
East Rift																
17D	0.00	0.30	25.47	26.53	0.00	13.41	7.63	5.20	6.65	4.53	2.02	1.51	3.86	3.74	0.51	101.35
16D	0.00	0.59	27.42	27.95	0.00	12.87	8.19	3.85	2.14	1.01	7.25	3.76	3.12	2.83	0.56	101.51
111D	0.00	0.53	22.08	29.77	0.00	11.78	6.84	4.39	9.84	6.31	2.47	1.74	3.52	2.75	0.30	102.33
15D	2.49	0.30	24.45	21.51	0.00	11.85	5.77	5.87	9.17	9.33	0.00	0.00	5.12	5.56	0.83	102.26
40D	0.00	0.00	21.49	30.43	0.00	14.16	8.69	4.66	5.88	3.16	4.50	2.66	3.38	2.11	0.23	101.35
109D	0.00	0.47	21.58	29.79	0.00	11.75	7.12	3.98	11.64	6.50	0.85	0.52	2.75	2.73	0.32	100.01
108F	0.00	0.83	22.59	30.17	0.00	10.46	6.18	3.76	10.36	6.30	1.46	0.98	3.15	3.44	0.37	100.04
14D	0.07	0.12	23.69	28.11	0.00	12.28	7.41	4.21	11.82	6.72	0.00	0.00	3.47	2.75	0.49	101.13
13D	0.00	0.00	0.00	30.80	16.23	11.02	7.01	3.30	0.00	0.00	9.31	4.83	3.16	2.85	0.39	88.89
12A	1.03	0.89	26.06	22.32	0.00	10.67	5.25	5.21	9.57	9.50	0.00	0.00	4.86	4.88	0.74	100.98
12D	2.46	0.71	25.47	22.18	0.00	10.89	5.33	5.35	8.81	8.85	0.00	0.00	4.83	5.05	0.83	100.76
121D	0.55	0.83	20.90	28.61	0.00	11.18	6.29	4.43	12.86	9.06	0.00	0.00	3.06	3.61	0.39	101.77
10D	2.97	0.59	25.13	22.28	0.00	10.84	5.17	5.52	8.63	9.22	0.00	0.00	4.96	5.20	0.76	101.28
9D	2.14	0.65	24.79	23.52	0.00	11.30	5.86	5.14	9.18	8.05	0.00	0.00	4.58	5.17	0.81	101.20
105D	0.86	0.95	20.31	28.32	0.00	11.77	6.73	4.52	12.00	8.07	0.00	0.00	2.57	3.30	0.37	99.77
8D	1.51	0.59	24.12	26.09	0.00	10.03	5.59	4.04	11.77	8.52	0.00	0.00	4.18	4.10	0.51	101.05
122D(a)	4.48	2.36	23.02	23.31	0.00	11.24	6.81	3.81	8.18	4.58	0.00	0.00	7.24	3.74	0.42	99.17
122D(b)	1.29	2.25	25.13	25.52	0.00	11.50	5.77	5.49	9.65	9.18	0.00	0.00	3.26	4.12	0.46	103.62
103D	0.00	1.48	22.42	29.11	0.00	11.15	6.48	4.14	9.47	6.04	1.43	1.00	2.33	3.49	0.44	98.99
268F	23.19	0.00	0.00	29.80	0.00	8.17	2.09	6.54	0.80	2.52	0.00	0.00	3.00	3.02	0.00	79.12
11A	0.00	1.36	25.05	25.87	0.00	12.19	6.87	4.81	7.83	5.48	1.60	1.23	3.93	3.97	0.67	100.86
102D	0.93	1.71	25.47	24.65	0.00	12.13	6.97	4.62	8.94	5.92	0.00	0.00	3.33	3.99	0.46	99.14
7D	0.00	2.19	25.64	28.01	0.00	8.97	5.34	3.17	9.58	5.68	1.64	1.07	3.74	4.88	0.70	100.59
41D	0.00	1.18	25.89	27.69	0.00	11.31	5.95	5.02	5.14	4.34	4.48	4.17	4.76	4.18	0.65	104.76
6D	0.00	2.66	25.55	29.51	0.00	7.95	4.82	2.70	9.42	5.27	2.49	1.54	3.65	4.82	0.70	101.07
42D	0.00	1.12	24.71	28.27	0.00	10.86	6.61	3.65	10.02	5.52	1.44	0.87	3.51	3.87	0.72	101.17
5D	0.00	0.00	20.39	32.08	0.00	11.16	7.03	3.44	10.05	4.92	4.11	2.22	3.33	2.03	0.28	101.03
43D	0.00	0.53	23.44	27.68	0.00	12.48	7.38	4.47	9.74	5.90	1.03	0.69	3.57	3.21	0.63	100.74
4D	0.00	0.00	23.95	32.56	0.00	7.29	4.53	2.32	0.36	0.18	15.06	8.48	4.07	2.64	0.28	101.71
44D	0.00	0.35	23.27	30.32	0.00	12.63	7.96	3.88	6.54	3.19	4.17	2.24	3.16	2.73	0.60	101.04
243G	2.08	0.00	17.18	21.58	0.00	14.21	7.76	5.94	10.67	8.18	0.00	0.00	4.52	3.95	0.00	96.07
3D	0.00	1.12	24.79	30.87	0.00	9.33	5.83	2.93	6.81	3.42	5.51	3.05	3.42	3.55	0.46	101.10
West Rift																
78D	0.00	5.26	28.26	28.49	0.00	8.07	5.01	2.58	0.83	0.43	7.60	4.31	3.12	4.18	1.02	99.16
32D	0.16	0.12	22.34	26.95	0.00	12.38	6.94	4.95	11.39	8.12	0.00	0.00	3.16	3.70	0.37	100.58
74D	0.62	1.24	24.71	23.65	0.00	11.82	6.08	5.44	9.79	8.75	0.00	0.00	4.60	4.16	0.49	101.35
73D	0.82	0.89	22.76	25.96	0.00	12.29	6.73	5.12	10.83	8.23	0.00	0.00	4.26	3.61	0.39	101.89
218G	0.00	1.12	24.12	25.66	0.00	11.97	6.60	4.91	9.42	7.01	0.90	0.74	4.09	3.48	0.44	100.46
221G	0.00	1.54	23.61	26.27	0.00	11.68	6.53	4.69	9.46	6.80	1.03	0.81	4.02	3.51	0.46	100.41
219G	0.00	1.48	24.37	25.08	0.00	11.71	6.40	4.90	10.16	7.77	0.18	0.15	4.12	3.59	0.51	100.42
80G	0.00	1.12	23.61	26.75	0.00	11.70	6.64	4.57	9.71	6.69	1.12	0.85	3.99	3.49	0.42	100.66
31D	0.00	0.00	22.59	28.13	0.00	12.42	7.15	4.70	10.01	6.58	1.55	1.12	3.90	2.75	0.19	101.09
215S	1.48	2.48	29.79	18.16	0.00	9.05	3.90	5.15	8.03	10.59	0.00	0.00	4.57	5.01	1.39	99.60
224G	0.00	0.30	19.04	30.14	0.00	13.06	7.89	4.46	12.16	6.88	0.29	0.18	3.47	2.18	0.21	100.26
216S	0.00	1.71	25.81	24.74	0.00	10.53	5.82	4.31	7.44	5.50	3.01	2.46	4.22	3.97	0.58	100.10
30D	0.00	0.06	26.15	27.33	0.00	11.19	6.54	4.12	8.70	5.49	1.98	1.37	3.76	3.67	0.65	101.01
29D	0.00	0.24	25.22	27.46	0.00	11.97	7.00	4.40	6.04	3.79	4.30	2.98	3.78	3.04	0.70	100.92
28D	0.00	0.00	0.00	31.27	13.84	12.39	7.77	3.85	0.00	0.00	9.48	5.18	3.26	2.51	0.05	89.60
231G	0.00	0.30	20.05	30.42	0.00	13.47	8.24	4.46	8.70	4.71	2.65	1.58	3.36	2.13	0.12	100.19
238G	0.43	0.00	17.60	25.64	0.00	14.44	8.23	5.59	11.30	7.68	0.00	0.00	3.97	2.51	0.00	97.39
27D	0.00	0.41	22.34	28.27	0.00	13.72	8.21	4.79	8.56	4.99	1.79	1.15	3.57	2.92	0.21	100.93
26D	0.00	0.00	0.00	36.48	12.79	8.27	5.22	2.54	0.00	0.00	13.66	7.33	3.45	1.56	0.02	91.32
25D	0.00	0.24	25.30	26.22	0.00	12.87	7.39	4.90	7.59	5.03	2.47	1.80	3.87	3.13	0.39	101.20
24D	0.00	0.41	25.05	26.07	0.00	12.82	7.25	5.03	7.38	5.12	2.45	1.87	3.96	3.29	0.39	101.09
23D	0.00	0.30	24.71	26.58	0.00	13.14	7.44	5.15	7.18	4.97	2.46	1.88	3.97	3.36	0.35	101.49
22D	0.75	0.47	24.62	24.22	0.00	11.60	6.06	5.20	10.28	8.81	0.00	0.00	4.52	4.20	0.44	101.17
21D	0.33	0.35	24.03	25.11	0.00	12.72	6.87	5.42	10.27	8.11	0.00	0.00	4.18	3.29	0.42	101.10
20D	0.00	0.47	25.72	26.26	0.00	14.10	8.19	5.25	3.01	1.93	5.17	3.65	3.80	3.34	0.44	101.33

Figure 4.22 Simplified tectonic interpretation of the Easter Microplate showing the distribution of anomalous rock samples. "Perid." indicates peridotites; "Brec." indicates "Breccia"; "Q" indicates samples which are quartz normative; "hiQ" indicates those that are highly quartz normative (> 2% quartz in the norm); "Ne" indicates those that are nepheline normative; "FeTi" indicates those that are classed as "FeTi basalts", with $FeO_{(T)}$ >12% and TiO_2 >2%; "K" indicates those that have high amounts of K_2O >0.1 wt.%; "(La/Sm)n" indicates those that have a chondrite normalised La/Sm ratio of >1.

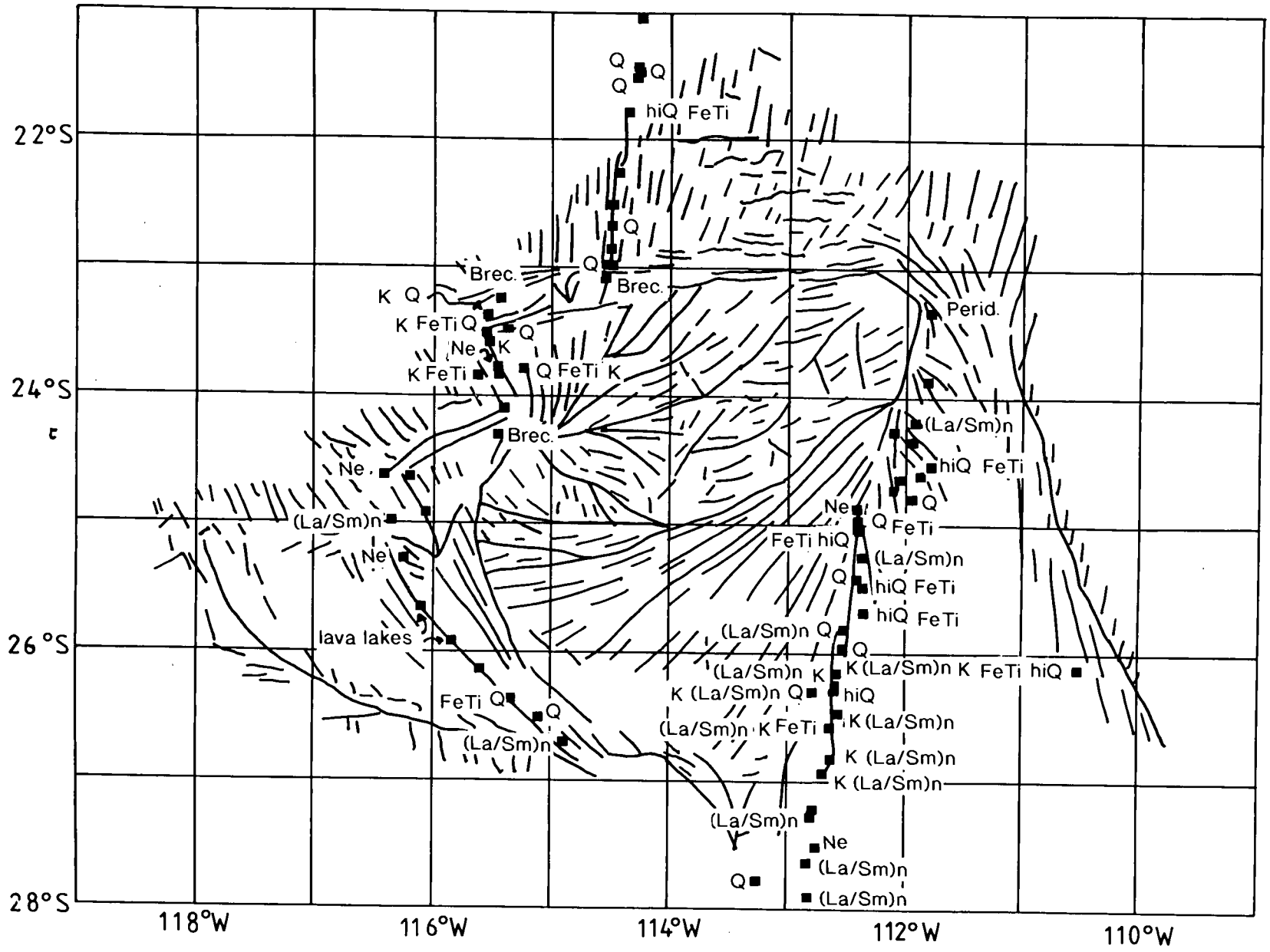
22°S
24°S
26°S
28°S
118°W
116°W
114°W
112°W
110°W
Q
Q
Q
hiQ FeTi
Q
Brec.
Brec.
K Q
K FeTi Q
Q
Ne
K
K FeTi
Q FeTi K
Brec.
Perid.
(La/Sm)n
hiQ FeTi
Q
Ne
Q FeTi
FeTi hiQ
(La/Sm)n
Q
hiQ FeTi
hiQ FeTi
Ne
(La/Sm)n
Ne
lava lakes
(La/Sm)n Q
Q
(La/Sm)n K
K (La/Sm)n K FeTi hiQ
K (La/Sm)n Q
hiQ
FeTi Q
Q
(La/Sm)n K FeTi
K (La/Sm)n
(La/Sm)n
K (La/Sm)n
K (La/Sm)n
(La/Sm)n
Ne
Q
(La/Sm)n
(La/Sm)n

Figure 4.23 (a) - (h) Plots of major oxides against Mg# to illustrate differentiation by fractional crystallisation from primitive to more evolved systems (with decrease in Mg#). See text for detailed description of trends. (i)-(j) Plots of two transitional trace elements (Cr and Co) against Mg#. (k) plot of $FeO_{(T)}/MgO$ versus latitude to illustrate the regions of increased fractionation along the microplate boundaries. Ratios of less than 1.75 are common for normal MORB, while ferrobasalts have values greater than this. (l) Plot of K_2O versus latitude to see the distribution of those samples with values >0.1 wt %, which may be indicative of hotspot activity. Two groups are found, one at the northern end of the West Rift, and the other at the southern end of the East Rift, both of which may be related to high amounts of hydrothermal activity in these areas, rather than hotspot activity. (m) The depth at which each sample was recovered is plotted against latitude for comparison with (k), (l), (n), (o) and (p). (n) chondrite normalised La/Sm ratios are plotted against latitude to illustrate the distribution of those with values >1 which may be influenced by hotspot activity. (o)and (p) $^{87}Sr/^{86}Sr$ and Nb/Zr ratios are plotted against latitude and are found to increase southeastwards along the West and Southwest Rifts as well as southwards along the East Rift, indicating a possible increase in influence of a mantle plume.

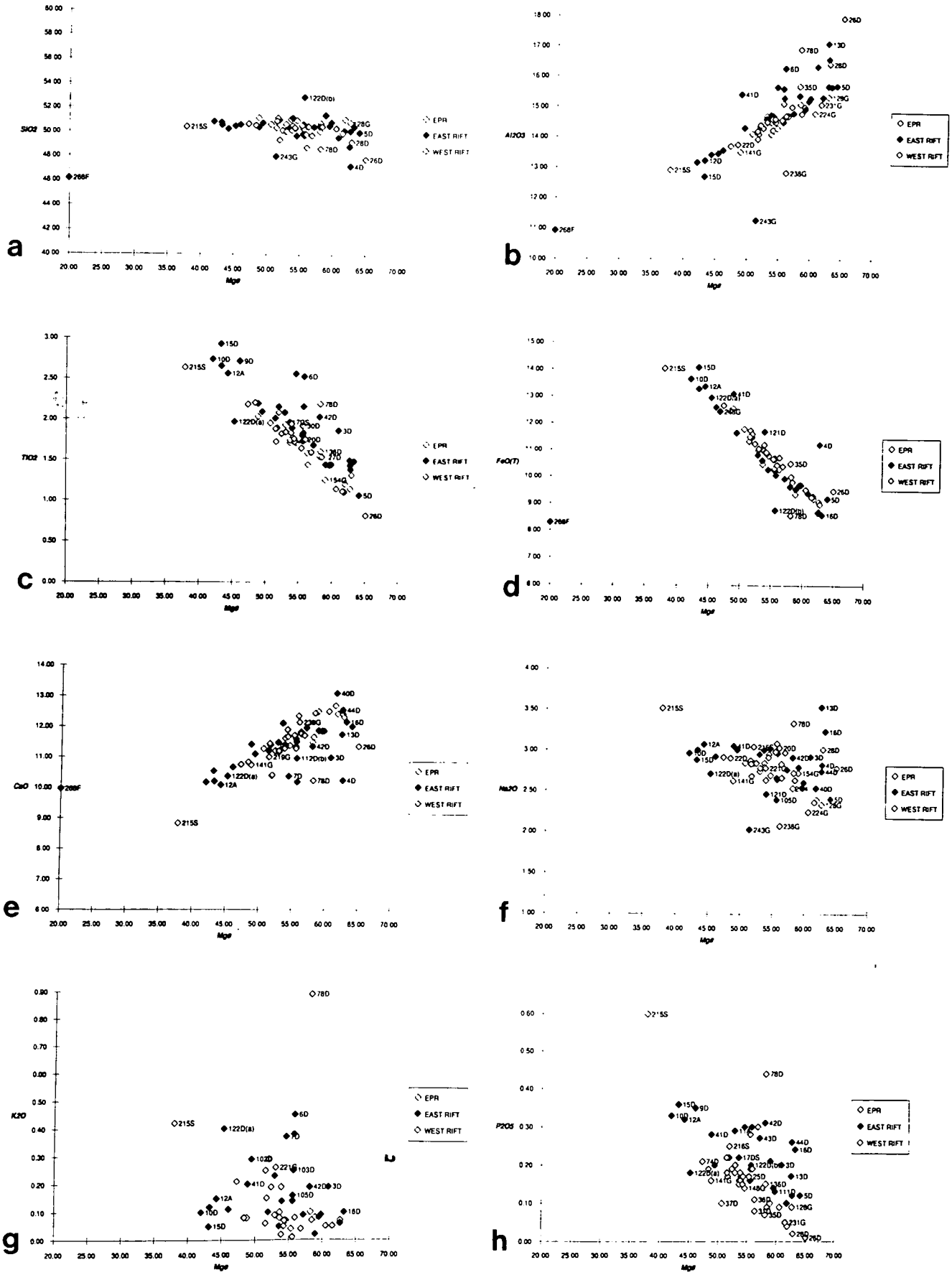
a
b
c
d
e
f
g
h
EPR
EAST RIFT
WEST RIFT
Mgo
SiO2
Al2O3
TiO2
FeO(T)
CaO
Na2O
K2O
P2O5

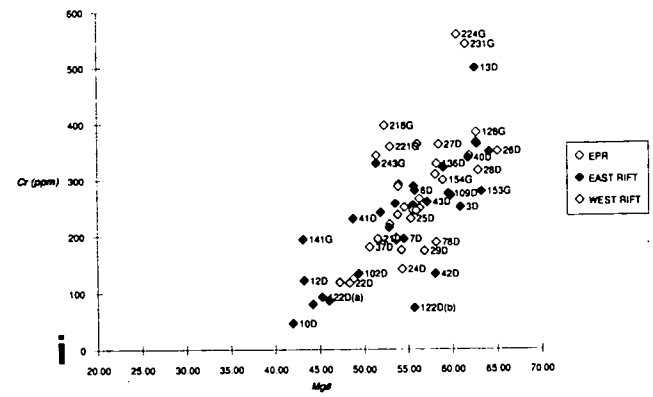
Cr (ppm)
MgO
EPR
EAST RIFT
WEST RIFT

i

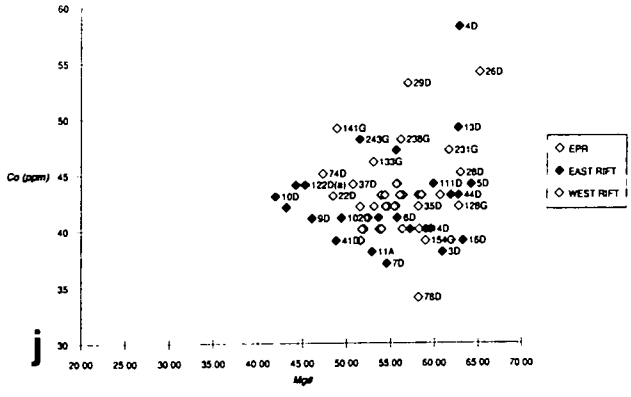
Co (ppm)
MgO
EPR
EAST RIFT
WEST RIFT

j

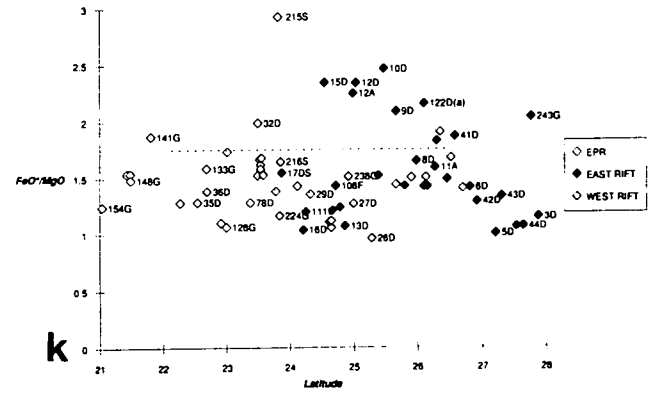
FeO*/MgO
Latitude
EPR
EAST RIFT
WEST RIFT

k

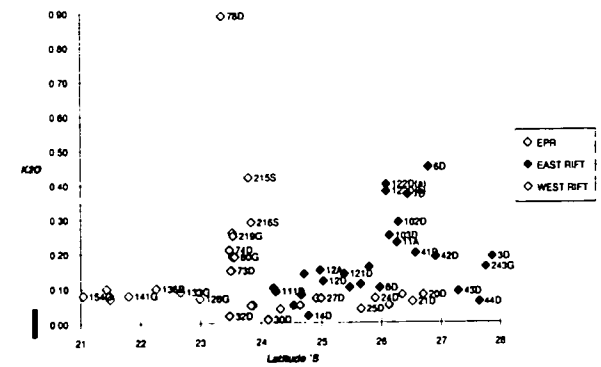
K2O
Latitude 'S
EPR
EAST RIFT
WEST RIFT

l

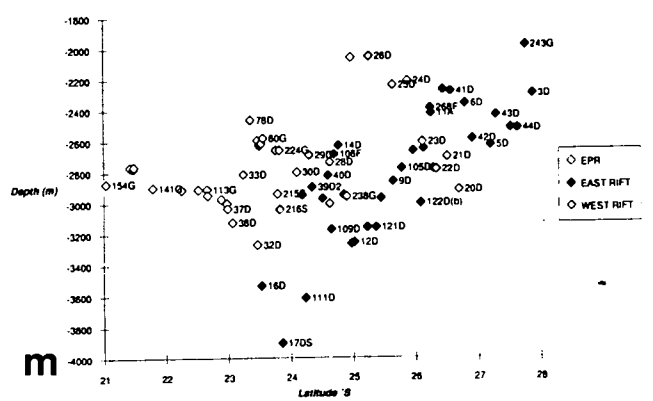
Depth (m)
Latitude 'S
EPR
EAST RIFT
WEST RIFT

m

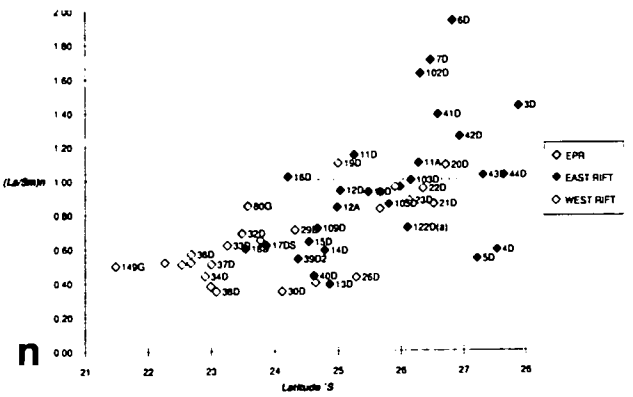
(La/Sm)n
Latitude 'S
EPR
EAST RIFT
WEST RIFT

n

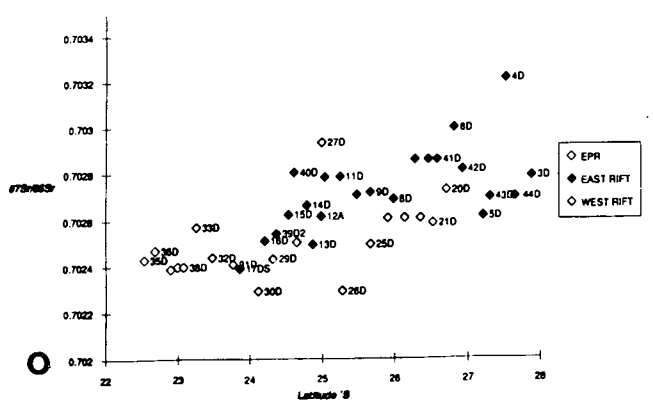
87Sr/86Sr
Latitude 'S
EPR
EAST RIFT
WEST RIFT

o

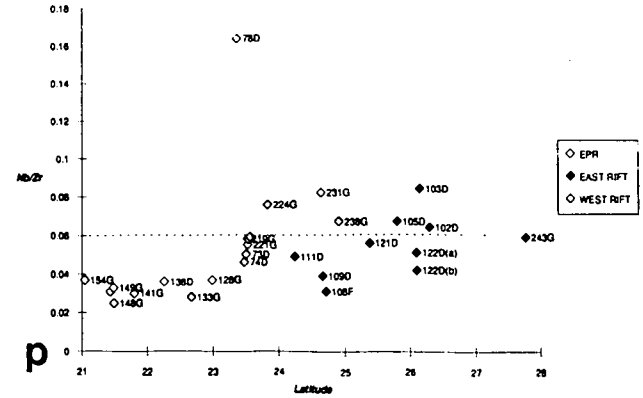
Nb/Zr
Latitude
EPR
EAST RIFT
WEST RIFT

p

Although Mg# varies between 65 and 38, the SiO_2 concentrations show no increase with decreasing Mg# and instead remain more or less constant at around 50% (Fig. 4.23a). The concentrations of TiO_2, $FeO_{(T)}$, and P_2O_5 increase as expected for a basalt-ferrobasalt-basaltic andesite series (Fig. 4.23c,d,h). Al_2O_3 and CaO both decrease with decreasing Mg# which may indicate the crystallisation of plagioclase phenocrysts (Fig. 4.23b,e) and although K_2O and Na_2O show a vague overall increase in concentration with fractionation as expected, there is a broad scatter of the data (especially around Mg# 55-60), which may be partly due to seawater alteration (Fig. 4.23g).

The trace elements of Cr and Co have also been plotted against Mg# in Fig. 4.23i,j. Cr shows a characteristic decrease with progressive fractionation, which is due to the simultaneous crystallisation of olivine- and Cr-rich spinel, and possibly Cr-rich clinopyroxene. However, although a similar decrease in Co is expected as it partitions into olivine during fractional crystallisation (Wilson, 1989), this is not readily seen (Fig. 4.23j).

In Fig. 4.23k-p, data are plotted against latitude. As with Fig. 4.23a-j, the EPR, East Rift and West Rift are plotted separately and many of the samples are labelled. A plot of $FeO_{(T)}/MgO$ against latitude is given in Fig. 4.23k to illustrate the regions of increased fractionation along the microplate boundaries. Ratios of less than 1.75 are common for normal MORB, while ferrobasalts have values greater than this (Byerly, 1980).

The element K_2O increases in concentration with increased fractionation because it is an incompatible element. If the K_2O content varies for a given Mg#, some other explanation is needed, and it could be either the composition of the magma source rock or the degree of partial melting that produced the magma. Normal MORB usually has very low concentrations (< 0.1 wt. %) at a given Mg#, while more enriched MORB (in this case, basalts that may have been influenced by the presence of the so-called Easter Hotspot) contain higher concentrations than this at a given Mg#.

4.3.4 Geochemical correlations with ridge segmentation

Studies of rock samples from the Galapagos Spreading Centre and elsewhere have led to the development of a widely accepted model for the evolution of basalts behind propagating ridge tips and possibly at fracture zones (Christie & Sinton, 1981; 1986; Sinton et al., 1983). Immediately behind the propagating rift tip, relatively unfractionated basalts are erupted. As distance from the rift tip increases, the degree of fractionation increases and FeTi basalts are erupted, followed by a wide range of basaltic and siliceous lavas, which reach a maximum differentiation between 20-50 km away. Beyond this peak, the amount of differentiation gradually decreases, so that at about 100-150 km

away, the magmatism has reached the normal steady state conditions found at typical ridge segments. The explanation given for this is that near the tip of the propagator, magma supply rate is small, and as the spreading centre propagates into colder, pre-existing crust, cooling rates are high. Initially this leads to no magma being erupted, but a slight increase in the magma supply results in eruption of unfractionated lavas with little or no residence in the crust. With increasing distance behind the tip, the magma supply rate increases, while the rate of cooling decreases. Where there is a delicate balance between these two parameters, extreme fractionation will occur. Then as supply rate increases further, the composition of the magma is buffered, so that extreme fractionation cannot occur, and hence a steady-state is reached.

Schilling et al. (1985) have reported an increase in $FeO_{(t)}$ and $FeO_{(t)}/MgO$ towards the tip of the 25°S northward propagating segment on the East Rift, and also a more subdued increase in the south at the tip of the propagating Southwest Rift. A closer examination of all the data available from around the Easter Microplate (Figs. 4.22a-j) does not immediately reveal the systematic three-phase evolution of rock types described above that are believed to be associated with rift propagation. The occurrence of FeTi basalts, at first sight, seems to be almost random. One sample (141G) is from north of a small OSC on the EPR; three are from the north end of the West Rift (74D, 215S and 216S); one is from about 60 km behind the tip of the Southwest Rift (22D); six are found between 24.5°S and 26.5°S on the East Rift (15D, 12A, 12D, 10D, 9D, 41D); and another was found just to the west of the East Rift outer pseudofault (122D) (Fig. 4.22). Of the twelve examples of FeTi basalts, only two are not associated with quartz-normative rocks, while half of them are associated with highly quartz-normative rocks (> 2% quartz in the norm) (Fig. 4.22). Those that occur at the northern end of the West Rift may be associated with the Raraku and Terevaka transforms, since rift propagation has not occurred there for at least 1 myr. (see Chapter 6).

If the length of spreading segments around the Easter Microplate is considered, the longest segment is 290 km (the Southwest Rift) while the remainder of the segments vary between 35 and 110 km. Along the East Rift, strongly fractionated rocks occur up to 80 km behind the rift tip, which is slightly further away than is found at the Galapagos Spreading Centre. Since both the East and West Rifts are evolving rapidly, it is possible that steady-state magmatic conditions are never reached. Continuous spreading centre reorganisation in response to the rapid rotation of the microplate may ensure that the presence of normal, large, well-mixed magma chambers is never established. The exception to this may be along the Southwest Rift, where a quartz-normative, FeTi basalt sample was collected from about 60 km behind the slow-spreading propagating rift tip (sample 22D), while other samples collected from further behind the rift tip (samples 26D

- 23D) show no sign of extensive fractionation (sample 26D is in fact nepheline-normative) (Fig. 4.22) and suggest the presence of a normal, well-mixed magma chamber at this end of the rift. The occurrence of lava lakes at 25D and 24D (Schilling et. al., 1984) may be further evidence for a rapid magma supply rate in response to increasingly faster spreading rates away from the rift tip. The northernmost samples from the East Rift, which are taken from deep axial rift graben, show no sign of extensive fractionation, and this may be because cooling rates are consistently high, as the ridges frequently reorganise themselves, and yet magma supply rates remain low. Therefore the critical balance between cooling rate and magma supply rate that is needed for extreme fractionation to take place is never reached.

Schilling et al. (1985) suggested that the nepheline-normative sample 13D, found just to the north of the 25°S propagator (Fig. 4.21, Fig. 4.22), may represent the first melt associated with rift propagation, which has resulted from lower degrees of partial melting at greater depth. At the propagating rift tip (or in this case, it seems, slightly ahead of the rift tip) where the spreading rate is slow (or nonexistent), melt may have segregated from depth and been erupted without significant mixing or residence time in the magma chamber. Sample 4D occurs just to the northwest of the tip of a small OSC at the southern end of the East Rift (Fig. 4.21, and see section 4.5, Chapter 4) and may either represent off-axis, ridge-flank magmatism, or perhaps the first melt associated with the northern propagation of the eastern limb of this small OSC. If this is the case, then both 13D and 4D appear to have erupted ahead of the rift tip, rather than slightly behind it as suggested by Christie and Sinton (1981).

The three nepheline-normative samples located on the West Rift, however, do not appear to be associated with rift propagation. Sample 31D was found in the middle of the spreading segment between the Raraku and Terevaka transforms, at a fairly normal depth of 2660 m. It occurs immediately adjacent to an olivine-normative sample (224G), and samples retrieved off-axis to the east and west of it (215S and 216S) are both FeTi basalts (Fig. 4.22). Sample 28D is located to the west of the present-day western ridge-transform intersection of the Terevaka transform (Fig. 4.21). The rock sample recovered is a pillow basalt with a thick glass rind and Mn staining due to hydrothermal alteration (Schilling et al., 1984). This sample may have been erupted shortly after the short spreading segment south of the Terevaka transform first started to propagate south, when cooling rates were high, and magma supply rates still low. Small amounts of partial melting at high pressure would allow relatively primitive, alkalic basalts to be extruded. Sample 26D is situated between the southward propagating rift tip and the overlapping tail of the Southwest Rift (Fig. 4.21) at a shallow depth of only 2052 m. Both very fresh and glassy pillow basalts as well as partly altered ones were recovered from this site

(Schilling et al., 1984). The partly altered samples were probably formed at the axis of the Southwest Rift before the propagator grew southwards to overlap with it. The recent glassy, nepheline-normative samples, however, have formed off-axis either since or during the most recent southward propagation episode within the region of shear between the two spreading centres. Presumably a small, ephemeral magma chamber has formed here between the two rifts, subject to the same fast cooling rates and low magma replenishment rates as at the other nepheline-normative sites, enabling the formation of this relatively unusual type of basalt.

4.3.5 Geochemical implications for hotspot - ridge interaction

Various geochemical and radiogenic isotope data have drawn attention to the fact that a plume or Easter Hotspot may be influencing the lavas erupted around the microplate boundaries. Craig et al. (1984) first observed a strong, plume-like $^{3}He/^{4}He$ anomaly at 26.5°S on the East Rift (the shallowest point along the East Rift), which suggests the influence of a nearby "high ^{3}He" Easter hotspot, similar to the Austral, Society, Samoan, Hawaiian, Reunion and Icelandic hotspots. Poreda et al. (submitted, 1991) examine this $^{3}He/^{4}He$ data in more detail, and look at the correlation between helium anomalies and other radiogenic isotope anomalies within the region. Macdougall and Tanzer (1984) note elevated $^{87}Sr/^{86}Sr$ values and lower $^{143}Nd/^{144}Nd$ and $^{230}Th/^{232}Th$ values at this latitude, compared to elsewhere along the EPR, which suggest the influence of a mantle plume. The $(La/Sm)_n$ data published by Schilling et al. (1985) were found to increase towards the south along the East and West Rifts, with a more pronounced increase along the East Rift and a maximum at around 26.5°S. Pb isotope data are described in detail by Hanan and Schilling (1989), and are found to covary with the $(La/Sm)_n$ data published by Schilling et al. (1985). Sr isotopes and REEs were also found to covary linearly with the Pb isotope data (Fontignie & Schilling, 1991), providing even more support for the idea that abnormal mantle material underlies this part of the plate boundary.

In Fig. 4.23m, the depth at which each sample was recovered is plotted against the latitude, for comparison with Figs. 4.23k-l and Fig. 4.23n-p. Generally there is an overall decrease in depth along the East and West Rifts that accompanies the presumed increasing proximity to the Easter Hotspot. In Fig. 4.23o, $^{87}Sr/^{86}Sr$ is plotted against latitude to illustrate deviation away from a normal N-type MORB. The overall increase in $^{87}Sr/^{86}Sr$ towards the south can be seen, and although this increase is less apparent in the data from the West Rift, there is a marked increase in the ratio along the Southwest Rift (samples 26D to 20D) as it approaches the EPR.

The incompatible trace elements Nb and Zr tend to be preferentially concentrated in E-type MORB that is associated with oceanic islands and hotspots, rather than N-type MORB. The ratio of Zr/Nb can be a useful discriminator between these two types of MORB, with high ratios (> 30) being associated with N-type MORB and lower ratios (around 10) being associated with E-type MORB (Wilson, 1989). The inverse of this ratio (Nb/Zr) has been plotted against the latitude in Fig. 4.23p. Here I have marked 0.06 (the inverse of 17) as the cut-off between basalts that show evidence that may indicate the involvement of the plume or hotspot, and those that are normal MORB. There appears to be an overall gentle increase in the Nb/Zr ratio with increasing latitude.

Rare earth element (REE) data have been published for many of the Easter Microplate samples (Marchig et al., 1987; Fontignie & Schilling, 1991). Typical N-type MORB is strongly depleted in light REEs compared to the heavier elements, while enriched (E-type) MORB shows varying degrees of light REE enrichment. A ratio of chondrite-normalised $(La/Sm)_n$ (i.e. light REE to medium REE) can be used to distinguish between these two types. N-type MORB generally has $(La/Sm)_n < 1$ and E-type MORB has $(La/Sm)_n > 1$ (Schilling et al., 1985). High $(La/Sm)_n$ ratios may result from shallow depth fractional crystallisation and from smaller degrees of partial melting as well as from the influence of an enriched mantle source (such as the Easter hotspot). Schilling et al. (1985) suggested that since the high $(La/Sm)_n$ ratios along the East Rift do not appear to be related, for example, to the high $FeO_{(T)}/MgO$ ratios or to nepheline-normative basalts, they could not have resulted from fractional crystallisation or low degrees of partial melting at depth. Thus the $(La/Sm)_n$ ratios of the East Rift were considered to be mantle-derived and related to the influence of a hotspot located east of the microplate. I have plotted $(La/Sm)_n$ against Mg# (not shown here) and have found no correlation between the two, suggesting that high $(La/Sm)_n$ ratios have not resulted from fractionation.

I have calculated $(La/Sm)_n$ ratios from the REE data published for the Geometep 4 samples (Marchig et al., 1987) and combined these with the published values for the EN-113 samples (Schilling et al., 1985) in order to try and distinguish between basalts that have been influenced by the Easter hotspot and those that are just normal MORB. Fig. 4.23n shows an overall general increase in $(La/Sm)_n$ from north to south, although there is considerable scatter in the data. A closer examination of the data reveals that $(La/Sm)_n$ values along the EPR hover around 0.5, and in fact decrease towards the northern boundary of the Easter Microplate, thus showing no sign of being influenced by a mantle plume. Of the samples collected from the West and Southwest Rifts, only two samples have $(La/Sm)_n$ ratios of greater than 1. These are 27D, and 20D, the former lying just to the west of the short propagator (at about 25°S), and the latter almost at the tip of the propagating Southwest Rift (Fig. 4.21). Schilling et al. (1985) suggest that the slight

overall increase in $(La/Sm)_n$ southeastwards along the West and Southwest Rifts may be explained by decreasing distance from the East Rift and the said Easter hotspot. Whether or not a hotspot situated to the east of the East Rift might be able to influence basalts erupted on a ridge to the west of the East Rift is not apparent. Schilling et al.'s (1985) migrating ridge-sink hotspot source model explains preferential non-radial flow of plume material towards a migrating ridge axis, but it is not evident whether the channel(s) connecting the hotspot and migrating ridge could continue beyond the East Rift to influence basalts erupted along the West and Southwest Rifts' axes. If this can and does occur, it is easy to see why the sample 20D has a high $(La/Sm)_n$ value, being nearest to the supposed plume, but there is no obvious reason to explain why sample 27D should have such a high value. Alternatively, these two high $(La/Sm)_n$ ratios may have resulted from the low degrees of partial melting associated with the tips of propagating rifts (i.e. the short propagator and the tip of the Southwest Rift), although similar increases in $^{87}Sr/^{86}Sr$ and Nb/Zr ratios southeastwards along the West and southwest rifts suggest that the plume does in fact affect the source of these basalts.

The majority of the $(La/Sm)_n$ data available are from the East Rift (Fig. 4.23n). Although these data do show an overall increase towards the south, there is considerable scatter in the data. Of the 29 ratios obtained, 12 of these have $(La/Sm)_n > 1$, and may represent binary mixing of a normal magmatic source and an enriched hotspot source. Six of these high $(La/Sm)_n$ samples occur between 26°S and 27°S, with three more occurring further north, and three further south (Fig. 4.22). If these high $(La/Sm)_n$ values are indeed indicative of the effect of the Easter hotspot, then it is seems that the greatest influence exerted by the hotspot is centred around 26.5°S on the East Rift, as originally observed by Craig et al. (1984) and Macdougall and Tanzer (1984).

The highest K_2O concentrations around the Easter Microplate spreading axes are not related to the highest $(La/Sm)_n$ ratios (Fig. 4.22). Fig. 4.23l shows that there are two peaks of high K_2O concentrations, one at around 23.5°S on the West Rift (i.e. between the Raraku and Terevaka transforms), and the other at around 26.5°S on the East Rift. These two regions are both sites of high amounts of hydrothermal vent activity (Marchig & Gundlach et al., 1987; Marchig et al., 1989). Although the high K_2O concentrations (> 0.1 wt. %) on the East Rift may be due to mixing of normal MORB and an enriched MORB, it is unlikely that those at the northern end of the West Rift are. The most likely explanation is that these high values have resulted from hydrothermal seawater alteration of the basalts.

Schilling et al. (1985), Hanan and Schilling (1989) and Schilling (1990) maintain that the present site of the hotspot is beneath Sala y Gomez island. This hypothesis is based

on the idea that the anomalous elevation of a ridge associated with a hotspot, together with the width of the geochemical anomaly, can be used to predict the distance of a hotspot from the ridge. However, the empirical relationship that they use to predict this has been developed from slow-spreading areas of the Atlantic and Pacific oceans, and does not seem to be applicable here. The eroded appearance of Sala y Gomez island does not immediately suggest that this is the site of a hotspot. Instead, the current opinion of other workers is now generally leaning towards the idea that the Ahu Volcanic Field (Hagen et al., 1990) may represent the present day location of the Easter hotspot. This site of recent voluminous extrusive activity, at around 111°W, lies directly between the anomalously shallow part of the East Rift (26.5°S, 112.6°W) and Easter Island (27.1°S, 109.4°W), and these three locations are near-parallel to the Nazca absolute plate motion along a trend of 118° (Naar & Hey, 1989).

CHAPTER 5
INTERPRETATION OF MAGNETIC DATA AND THE CALCULATION OF PLATE MOTIONS

5.1 Introduction

In this chapter, magnetic anomaly profiles are modelled along the East Pacific Rise, and the East, West and Southwest Rifts of the Easter Microplate. Spreading rates are measured for the interval from the present to the Brunhes/Matuyama reversal (0.72 Ma, timescale of Harland et al., 1990) along all of these plate boundaries. Together with transform fault and seismic-slip vector azimuths, these data are inverted using the Minster and Jordan (1978) algorithm to obtain three-plate closure and best fit Euler vectors for Nazca, Pacific and Easter plate motions. Earthquake seismicity and focal mechanisms from the Easter Microplate region are then examined in the light of known and predicted plate motions.

5.2 Identification of Magnetic Anomalies

5.2.1 Modelling the Magnetic Anomalies

In Chapter 2 (section 2.3.2) the compilation of the magnetic anomaly data set and its presentation in both profile and contoured form is described. Also a general overview of the magnetic anomalies identified is given. In this chapter attention is focussed more on the use of the magnetic anomalies to provide information on spreading rates, which are then used to calculate the Euler poles used in the reconstructions carried out in Chapter 6. As so much hinges on the correct identification of the magnetic anomalies (the inferred history of the Easter Microplate) it is important that these identifications be as well constrained as possible.

Models of the magnetic anomalies that best imitate the observed profiles have been produced using the program MAGIC (written by R.C. Searle, using the method of Vacquier (1972) pp. 163-168). Eight magnetic models were calculated, one for the East Pacific Rise (where the magnetic anomalies are most readily identified), two for the West Rift, two for the Southwest Rift, and three for the East Rift. As described in Chapter 2, the parameters that remained constant for all of the models are as follows:

Average strength of the present field=34500 nT;

Declination of present field=15°E;
Separation between adjacent field-points=1 km;
Depth of field-points in km=0 km;
Intensity of magnetisation (modulus) for seafloor older than Brunhes=10 A/m;
Depth to top of magnetised bodies=3 km;
Depth to bottom of magnetised bodies=5 km;

Also, the magnetisation of the seafloor formed during the last 100,000 years is 2.5 times that of the other bodies, and the magnetisation of the rest of the Brunhes is twice that of the other bodies. The timescale used is that of Harland et al. (1990).

The other parameters used to calculate the anomaly models are shown in Table 5.1. Parameters such as the present- and palaeo-strikes, and the present dip and palaeo latitude were measured or estimated in order to calculate the "skewness" of the magnetic anomalies (Schouten & McCamy, 1972) within the program MAGIC. The "skewness" (θ) of the anomalies is given by the equation:

$$\theta = 180 - I_R' - I_F'$$

where I_R' and I_F' are the inclination of the remanent field and the total field, respectively, in the plane perpendicular to the anomaly strike, which in turn are given by the equations:

$I_R' = \tan^{-1}(\tan j / \sin \delta)$ where j is the palaeo-dip and δ is the palaeostrike

and $I_F' = \tan^{-1}(\tan i / \sin(\alpha + d)$ where i is the present dip, α is the present strike and d is the declination.

The spreading rates are calculated by measuring the distance between anomaly picks in km, and dividing this by the time interval represented by the picks. The model profiles are projected onto east-west lines to give the "adjusted rates" given in Table 5.1. The present strike of the magnetic bodies is measured in degrees from true north, where clockwise is positive. The palaeostrike is the estimated strike of the bodies when they were formed. The present dip (inclination) is given by: dip=$\tan^{-1}(2\tan\theta)$, where θ is the latitude in degrees and north is positive, i.e. geocentric dipole assumption. The palaeo-latitude is the estimated latitude of the bodies at the time of their formation.

For each time interval given in Table 5.1, the predicted magnetic model was calculated using the appropriate spreading rate, and present- and palaeo-strikes. The resulting models were pasted together to produce the continuous profiles shown in Fig. 5.1. The lower part of each profile indicates the normally magnetised blocks, filled in black and labelled with the relevant anomaly number. The upper part of each model is the resulting field anomaly in nT calculated using the parameters given. The positive part of the anomaly is coloured black, and the vertical scale is shown to the left of each profile

TABLE 5.1 Magnetic Anomaly Model Parameters

Profile No.	Time Interval (myr)	Distance (km)	Projected Rate* (km/myr)	Present Strike/*	Paleo-Strike/*	Present Dip	Paleo-Latitude
1	5.08 - 3.87	65.6	53.81	006	006	-37.5	-21
	3.87 - 3.03	65.6	77.50	"	"	"	"
E.P.R.	3.03 - 2.45	44.1	75.29	"	"	"	"
	2.45 - 1.77	37.9	55.43	"	"	"	"
	1.77 - 0.94	56.4	67.90	"	"	"	"
	0.94 - 0.72	17.4	79.04	"	"	"	"
	0.72 - 0	50.2	69.68	"	"	"	"
	0 - 0.72	60.5	83.40	"	"	"	"
	0.72 - 0.94	19.5	79.76	"	"	"	"
	0.94 - 1.77	70.7	83.00	"	"	"	"
	1.77 - 2.45	78.9	115.75	"	"	"	"
	2.45 - 3.03	45.1	75.77	"	"	"	"
	3.03 - 3.40	31.8	83.39	"	"	"	"
2	3.40 - 2.45	40	39.31	-020	-020	-41.7	-24
	2.45 - 2.09	79	198.88	-016	"	"	"
West Rift	2.09 - 1.65	31	87.80	-016	"	"	"
	1.65 - 0.94	37	48.40	-018	"	"	"
	0.94 - 0.72	18	76.88	-012	"	"	"
	0.72 -0	42	58.33	-010	"	"	"
	0.72 - 0.94	13	55.53	000	"	"	"
	0.94 - 1.77	30	34.00	026	"	"	"
3	0.94 - 1.77	40	42.90	011	-020	-41	-23.5
	1.77 - 2.45	14	18.34	042	"	"	"
West Rift	2.45 - 3.40	66	60.76	056	"	"	"
4	2.45 - 1.77	43	54.76	-042	-030	-44	-25.75
	1.77 - 0.72	10	8.25	-050	-040	"	"
S.W. Rift	0.72 - 0	35	42.92	-040	-040	"	"
	0 - 0.72	30	36.79	-039	-040	"	"
	0.72 - 1.77	30	25.23	-039	-040	"	"
5	1.77 - 0.72	16	15.24	-050	-040	-44.6	26.25
S.W. Rift	0.72 - 0.72	34	23.61	-040	"	"	"
6	4.79 - 4.26	22	41.51	060	000	-43	-25
	4.26 - 4.12	19	126.67	062	"	"	"
East Rift	4.12 - 3.99	34	261.53	058	"	"	"
	3.99 - 3.87	18	150.00	055	"	"	"
	3.87 - 3.40	21	44.68	050	"	"	"
	3.40 - 3.17	34	147.83	048	"	"	"
	2.45 - 2.09	39	108.33	035	"	"	"
	2.09 - 1.65	12	27.27	035	"	"	"
	1.65 - 0.94	11	15.70	023	"	"	"
	0.94 - 0.72	14	63.64	028	"	"	"
	0.72 - 0.72**	44	30.55	000	"	"	"
	0.72⇔0.72**	10	6.94	000	"	"	"

	0.72 - 0.72**	26	18.06	-003	"	"	"
	0.72 - 0.94	11	50.06	-003	"	"	"
	0.94 - 1.77	43	51.81	-003	000	-43	-25
	1.77 - 2.45	22	32.35	-002	"	"	"
	2.45 - 3.40	42	44.20	-015	"	"	"
7	3.17 - 2.45	46	63.65	037	000	-45	-26.5
	2.45 - 1.77	44	64.55	037	"	"	"
East Rift	1.77 - 0.94	18	21.60	033	"	"	"
	0.94 - 0.72	10	45.21	026	"	"	"
	0.72 - 0	38	52.65	022	"	"	"
	0 - 0.72	48	66.30	005	"	"	"
	0.72 - 0.94	18	81.37	010	"	"	"
	0.94 - 1.77	88	105.00	005	"	"	"
	1.77 - 2.45	34	49.38	-012	"	"	"
	2.45 - 3.40	41	42.63	-011	"	"	"
8	3.40 - 3.17	35	152.17	044	000	-42.3	-24.5
	2.45 - 1.77	27	39.98	039	"	"	"
East Rift	1.77 - 0.72	16	15.24	034	"	"	"
	0.72 - 0.72	40	27.78	-013	"	"	"
	0.72 - 1.77	45	42.86	-022	"	"	"
	1.77 - 2.45	27	39.71	-003	"	"	"
	2.45 - 3.40	27	28.42	-008	"	"	"

* Rate projected onto east-west lines
** Double Brunhes anomaly

(from -1000 nT to 1000 nT). Fig. 5.1 uses spreading rates chosen to give the best match all along the profiles. The magnetic anomaly profiles in Fig. 5.2 are the same as those in Fig. 2.7 of Chapter 2, but instead of the colour overlay showing the interpretations of the magnetic anomalies, the modelled anomalies of Fig. 5.1 may be overlain and directly compared with the observed anomalies.

5.2.2 Magnetic Anomalies of the East Pacific Rise

Profile 1 (Fig. 5.1) models a magnetic anomaly profile that crosses the East Pacific Rise at 21°18'S, using the parameters given in Table 5.1. The model matches the observed anomalies (Fig. 5.2) exceedingly well, out to the end of anomaly 3 to the west of the EPR, and out to the end of anomaly 2A to the east. The average half-spreading rate to the west of the EPR is 68 mm/yr and to the east it is 87 mm/yr. For each time interval the spreading rates are consistently faster to the east than to the west, which suggests that either the spreading itself is asymmetric or that overall accretion is asymmetric due to ridge jumps or rift propagation, with the jumps being as frequent as the field reversals themselves. Between 1.77 - 2.45 Ma, a half-spreading rate of 116 mm/yr is required to match the magnetic anomaly peaks to the east of the EPR. This particularly high rate may be due to strongly asymmetric accretion due to ridge jumps or rift propagation. The average full spreading rate is 158 mm/yr, which is consistent with rates predicted by the NUVEL-1 plate motion model (DeMets et al., 1990).

Further models have not been produced for other magnetic anomaly profiles along the EPR, since Naar and Hey (1989) have recently published a total of 24 models for the EPR north and south of the Easter Microplate and DeMets et al., (1990) have also published further magnetic anomaly models. Naar and Hey's (1989) models concentrated on matching the Brunhes/Matuyama reversals either side of the EPR, to aid their spreading rate calculations for this time interval. DeMets et al.'s (1990) models attempted to match the rates between the central peaks of Anomaly 2A for their global 12-plate closure model, with little attention being paid to the more recent reversals. Despite these different approaches, my measured spreading rates are comparable with both Naar and Hey's (1989) and DeMets et al.'s (1990) rates. Nowhere along the EPR are the anomaly peaks difficult to identify, and so instead attention has been focussed on modelling the much more complex anomalies of the East and West Rifts of the Easter Microplate.

5.2.3 Magnetic Anomalies of the West Rift

Two models were compiled for the magnetic anomalies of the West Rift, one of a profile crossing the axis at 23°50'S (Profile 2), and the other further north at 23°30'S

Figure 5.1 Synthetic magnetic anomaly models computed using the parameters listed in Table 5.1 and projected onto the east-west tracks shown. These profiles can be overlain on top of the observed magnetic anomalies in Fig. 5.2 for comparison. For each time interval given in Table 5.1, the predicted magnetic model was calculated using the appropriate spreading rate, and present- and palaeo-strikes. The resulting models were pasted together to produce these continuous profiles. The lower part of each model indicates the normally magnetised blocks, filled in black and labelled with the relevant anomaly number. The upper part of each model is the resulting field anomaly in nT, calculated using the parameters given. The positive part of the anomaly is coloured black, and the vertical scale is shown to the left of each profile (from -1000 nT to +1000 nT).

Figure 5.2 Magnetic anomaly profiles plotted along the ships' tracks, as in Fig. 2.5, Chapter 2, with positive to the north and negative to the south. Positive anomalies are shaded black. Although the ships' tracks are not shown their location is implicit from the black and white colouring of the anomalies.

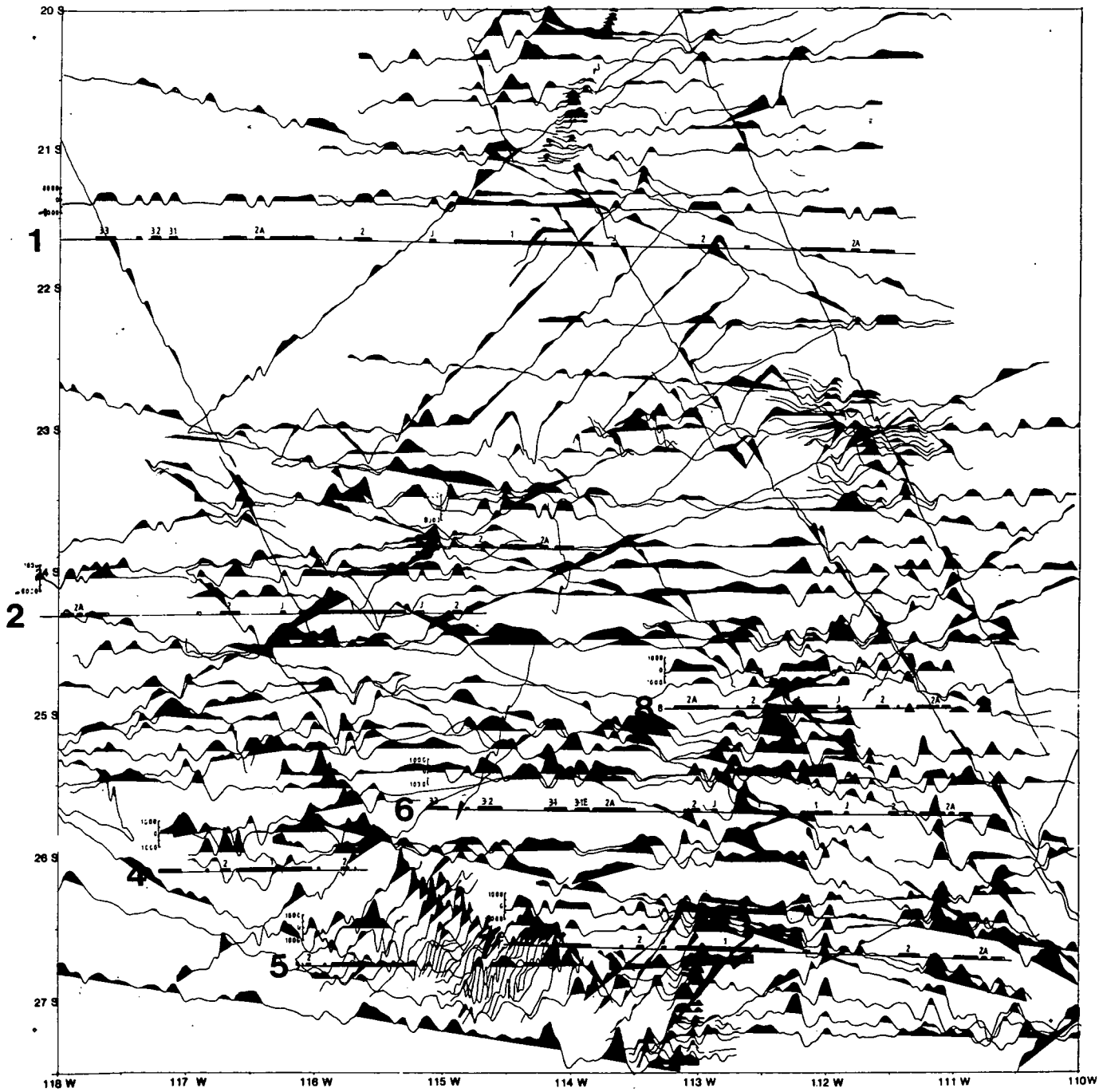
20 S
21 S
22 S
23 S
24 S
25 S
26 S
27 S
118 W
117 W
116 W
115 W
114 W
113 W
112 W
111 W
110W
1
2
4
5
6
8

(Profile 3). The GLORIA data that exist to the west of the West Rift reveal a complex history of reorganisation of tectonic fabric (possibly through ridge propagation), and there are few long profiles of magnetic anomalies that can be readily modelled. To the east of the West Rift, the GLORIA data indicate that the tectonic fabric of the microplate interior has been strongly rotated. Thus although the magnetic anomalies have been modelled as though it is the spreading rates that have changed dramatically in the last few million years, most of the anomalous rates used to model the anomaly peaks are likely to be the result of ridge jumps, rift propagation and rotation of tectonic fabric. The calculated model of profile 2 fits well with the observed anomalies. The large amount of crust between the anomalies 2 or 2r-1 and the start of anomaly 2A suggests there has been a rift jump between these anomalies, which appears to be matched by a distinct shortage of fabric of a similar age to the east of the West Rift (see Fig. 2.7, Chapter 2), although not modelled here. The observed skewness of the peaks is matched by that predicted by the model.

Profile 3 models anomalies 2 and 2A to the east of the West Rift. Anomalies older than 2A are not readily picked out, since not only has the seafloor been strongly rotated, but also the lineament pattern is sub-parallel to the magnetic profile orientation. However, these anomalies may be identified with a certain degree of confidence from the magnetic contour map in Fig. 2.10 (Chapter 2) and by a tentative comparison between GLORIA sidescan sonar reflectivity from areas thought to be of a similar age. No attempt has been made to model these older anomalies here. Profile 3, however, fits the observed magnetic anomaly peaks of 2 and 2A well.

5.2.4 Magnetic Anomalies of the Southwest Rift

Because of its NW-SE trend, the central Brunhes anomaly all the way along the Southwest Rift has a strongly negative skew, with a deep negative trough to the west of the central anomaly and high positive peak on the eastern side. The Jaramillo anomaly can barely be picked out on either side of the Brunhes, but anomaly 2 can be seen. No anomalies older than anomaly 2 are found on the eastern side of the Southwest Rift, but to the west there is plenty of crust that is assumed to be older than anomaly 2. Prior to anomaly 2 (1.88 Ma) it appears that all the lithosphere formed at the Southwest Rift was rafted off (presumably by rift propagation) from the microplate to the Pacific plate on the outside of the spreading ridge, leaving no remains of its existence on the microplate. Whether this happened as a series of discreet propagation events, or as one major event just before anomaly 2 was formed, is not clear, since the presumed older lithosphere does not have any instantly recognisable magnetic anomalies associated with it.

In Profiles 4 and 5, I have only attempted to produce models out to anomaly 2. The strongly negative skewness of the Brunhes and other anomalies is extremely well matched by the models, and although the rates used to match the Brunhes are considerably faster than those used for the interval between the Brunhes and anomaly 2 (Table 5.1), the fit is good, suggesting that the spreading rate along the Southwest Rift has significantly increased since the start of the Brunhes.

5.2.5 Magnetic Models of the East Rift

Three synthetic models of the magnetic anomalies along the East Rift have been produced. Although the East Rift extends as far north as 23°S, the northern end of the East Rift is complicated by the fact that the Pito Deep region (see Chapter 4) is undergoing amagmatic extension of pre-existing Nazca plate lithosphere (Francheteau et al., 1988; Naar & Hey, 1986; Naar et al., in press; Martinez et al., in press). The resulting complex magnetic signature has not been modelled since it would provide no further information on Nazca-Easter spreading rates.

Profile 6 is the longest synthetic model produced for the East Rift, and it extends from almost the end of anomaly 3 in the west to the end of anomaly 2A in the east. The lithosphere accreted at the East Rift is fanned about the nearby Nazca-Easter Euler pole, and so in order to model each magnetic anomaly wiggle, the present strike of the magnetic bodies must be changed each time. For all of the models associated with the East Rift, the palaeostrike has been set at 000°, the supposed overall trend of the East Rift. However, if the rift was broken up into smaller spreading segments, separated by small non-transform offsets, as is the case today, these smaller spreading segments would probably trend slightly west of north (i.e. toward the Nz-Ea pole).

At around 25°S, a fast rift propagator is known to be replacing a dying ridge situated some 45 km further to the east (Naar & Hey, 1986; Chapter 4, section 4.5, this thesis). Both the presently active propagator and the dying ridge have a central Brunhes anomaly associated with them, which I have modelled in Profile 6. (In Table 5.1, three values for 0.72W - 0.72E are given, which correspond to the two positive central anomalies separated by a small negative interval, which when summed together, give an average half rate of 56 mm/yr.) All of the modelled anomalies to the east of the East Rift agree extremely well with the observed magnetic anomalies. However, to the west of the East Rift, the evolution seems to be more complex.

The interval between the Jaramillo anomaly and anomaly 2 to the west of the East Rift is fairly small, presumably due to the rift propagation episode referred to above. Anomalies 2A and 3 are not easily recognised, due to apparent rift propagation events as

well as the obliquity of the anomalies to the east-west ship's tracks. At the southern end of the East Rift, both major peaks of anomaly 2A are present (see profile 7, Fig. 5.1 and the observed anomalies in Fig. 5.2). However, moving further northward, the youngest peak gradually disappears, presumably due to an anticlockwise change in orientation of the rift by propagation just after this time (2.45 Ma). Thus on profiles 6 and 8, Fig. 5.1, only the oldest peak of 2A is shown (seeFig. 5.2 and Fig. 2.5, Chapter 2). The "other half" of the vanished peak should be somewhere to the east of the present day spreading axis if this is the case, but it has not been found.

To the west of what is believed to be anomaly 2A, the basement fabric formed at the East Rift becomes increasingly further rotated in a clockwise direction. Several positive magnetic anomaly peaks exist, but none of them appear to represent the familiar peaks of anomaly 3. However, the east-west ships' tracks through these profiles are within 30° of the structural lineations seen on the GLORIA image, and so any magnetic anomalies viewed from this oblique angle will appear elongate and unfamiliar. I have attempted to model the anomaly 3 peaks and the results are acceptable. Although the spreading rates for 4.26 - 3.87 Ma which were used to model the peaks appear very high (see Table 5.1), the average spreading rate for the whole of anomaly 3 as measured along the ship's track (from 4.79 - 3.87 Ma) is 101 mm/yr half rate. If this is then projected normal to the trend of the spreading fabric (i.e. normal to 060°), the rate is halved (cos60°=0.5), giving 50.5 mm/yr half rate, which is compatible with more recent rates at this latitude.

Further south, Profile 7 attempts to model an observed magnetic anomaly profile that crosses the East Rift at 26°30'S. The model goes out to the oldest portion of anomaly 2A on both sides of the present day spreading axis, and at this latitude, all of the anomaly 2A peaks to the west of the axis are recognised. The model matches the observed anomalies extremely well, giving an average half spreading rate of 58.59 mm/yr.

At 24°30'S, Profile 8 models the magnetic anomalies out to the end of 2A on either side of the East Rift. Presently the spreading axis is propagating to the inside (west) of another spreading segment to the north, while at its southern end it is being replaced by the fast propagator referred to above (Naar & Hey, 1986; Chapter 4, section 4.5). The central Brunhes anomaly narrows towards the tip of the propagator, and at this latitude is fairly narrow. Again, as for Profile 6, only one of the anomaly 2A peaks is present to the west of the spreading axis. The average half rate is 31.91 mm/yr, and the model agrees well with the observed data.

5.3 Data used to Calculate the Nazca-Pacific, Pacific-Easter and Nazca-Easter Instantaneous Euler Poles

5.3.1 Nazca-Pacific Data

A total of 57 data were used to calculate the motion between the Nazca (Nz) and Pacific (Pa) plates (see Table 5.2). Of these, 24 were rate data (ra), 6 were transform fault data (tf) and 27 were seismic-slip data (sv). The first four rate data (north of 15°S) were taken from the NUVEL-1 data set (DeMets at al., 1990), since I did not have NGDC data (World Data Center, Boulder, Colorado) from this region. South of 15°S, NGDC data were available, and I have measured all the rate data from plots of the original magnetic data in order that there be some consistency with the rates obtained for the Pacific-Easter and Nazca-Easter plate boundaries. All the magnetic anomalies along this portion of the East Pacific Rise (EPR) are easily recognised, and have been exhaustively modelled by Naar and Hey (1989) and DeMets et al. (1990), thus no further attempts were made to model these anomalies, except for one profile which crosses the axis at 21°18'S. Although, as mentioned in the previous section (5.2), spreading rates between 21°S and 23°S decrease southwards, instead of increasing as expected with distance from the pole, I have nevertheless included two rate data from this region, as they are given small "importances" (a measure of the information contribution of each datum to the model (Minster et al., 1974), which depends on its assigned uncertainty and how much it duplicates information contributed by other data). Thus these two extra data do not significantly alter the location of the Nz-Pa Euler pole. Spreading rates were calculated for the interval 0-0.72Ma, i.e. from the present back to the Brunhes/Matuyama reversal (timescale of Harland et al. (1990)), the youngest easily recognisable reversal boundary.

The uncertainties (equivalent to the standard deviation) assigned to the first four rate data of the NUVEL-1 data set were retained. The other uncertainties were allotted along the following guidelines: The maximum uncertainty given is 2.0 cm/yr (i.e. 20 mm/yr), where the anomaly pick is poorly constrained and other factors such as navigational errors are thought to be high. The minimum uncertainty given is 0.4 cm/yr (i.e. 4 mm/yr), where the edge of the Brunhes/Matuyama reversal is located with extreme confidence, and navigational errors are thought to be minimal. A reasonably good magnetic anomaly pick would be given an uncertainty of 1.0 cm/yr, while more confidently measured rates would be given uncertainties of 0.6 - 0.7 cm/yr.

The Nz-Pa transform data are the same as those used by Naar and Hey (1989), and the uncertainties they assigned to them are retained. That is, for the three transform azimuths measured from the GLORIA survey of the Quebrada, Discovery and Gofar

TABLE 5.2 Three Plate Closure Model and Data

ID	Plate	Plate	Type	Lat. N	Lon. E	Datum	S.D.	Pred.	Wt. Resid.	Imp.	Reference
1	nz	pa	ra	-7.00	-107.00	13.00	2.00	14.50	-0.75	0.04	NGDC Many profiles 6-8°S
2	nz	pa	ra	-10.50	-110.20	15.00	1.50	14.91	0.06	0.04	NGDC Many profiles 8-13°S
3	nz	pa	ra	-12.00	-111.20	14.00	1.40	15.06	-0.75	0.03	NGDC Chain 100 11
4	nz	pa	ra	-12.60	-111.00	15.00	0.60	15.10	-0.16	0.16	NGDC Rispo 2
5	nz	pa	ra	-16.00	-112.95	15.30	0.40	15.37	-0.16	0.18	NGDC POL7302
6	nz	pa	ra	-17.00	-113.11	15.00	0.50	15.43	-0.85	0.10	NGDC V1905
7	nz	pa	ra	-17.17	-113.15	15.40	1.00	15.44	-0.04	0.02	NGDC C1306
8	nz	pa	ra	-17.41	-113.20	16.60	1.50	15.45	0.77	0.01	NGDC C1306
9	nz	pa	ra	-17.59	-113.25	16.20	1.00	15.46	0.74	0.02	NGDC C1306
10	nz	pa	ra	-17.84	-113.29	15.90	1.00	15.47	0.43	0.02	NGDC C1306
11	nz	pa	ra	-18.00	-113.32	15.60	0.80	15.48	0.15	0.03	NGDC C1306
12	nz	pa	ra	-18.19	-113.36	15.30	0.50	15.49	-0.38	0.08	NGDC POL7302
13	nz	pa	ra	-18.45	-113.39	15.20	0.40	15.50	-0.76	0.12	NGDC POL7302
14	nz	pa	ra	-19.00	-113.49	15.90	0.70	15.53	0.52	0.04	NGDC POL7302
15	nz	pa	ra	-19.16	-113.50	15.70	0.70	15.54	0.23	0.04	NGDC POL7302
16	nz	pa	ra	-19.50	-113.07	15.50	0.60	15.56	-0.10	0.05	NGDC POL7302
17	nz	pa	ra	-20.20	-113.75	15.60	0.60	15.59	0.02	0.05	NGDC Several profiles
18	nz	pa	ra	-20.87	-113.81	15.60	0.60	15.61	-0.02	0.05	NGDC Several profiles
19	nz	pa	ra	-21.14	-114.03	14.90	0.60	15.63	-1.21	0.05	NGDC C1714
20	nz	pa	ra	-21.34	-114.25	14.90	0.60	15.63	-1.22	0.05	NGDC POL 7302
21	nz	pa	ra	-29.88	-111.74	15.70	0.50	15.77	-0.14	0.28	NGDC PASC03WT
22	nz	pa	ra	-30.49	-111.80	16.10	0.60	15.77	0.55	0.21	NGDC POL7303
23	nz	pa	ra	-31.02	-111.91	16.30	0.70	15.77	0.76	0.17	NGDC YAQ7304
24	nz	pa	ra	-31.30	-111.96	16.40	1.00	15.77	0.63	0.09	NGDC YAQ7304
25	nz	pa	tf	-3.70	-103.20	*102.00	4.00	101.61	0.10	0.18	Searle (1983), Quebrada, GLORIA
26	nz	pa	tf	-4.00	-104.00	102.00	4.00	102.04	-0.01	0.18	Searle (1983), Discovery, GLORIA
27	nz	pa	tf	-4.60	-105.50	102.00	4.00	102.81	-0.20	0.18	Searle (1983), Gofar, GLORIA
28	nz	pa	tf	-6.25	-107.25	104.00	8.00	103.58	0.05	0.04	Lonsdale (1983), Yaquina, Seabeam
29	nz	pa	tf	-9.00	-109.30	102.00	5.00	104.39	-0.48	0.11	Wilkes, SeaMARC II (MW8710)

30	nz	pa	tf	-13.50	-111.50	106.00	5.00	105.13	0.17	0.11	Garrett, SeaMARC II (MW8710)
31	nz	pa	sv	-2.37	-102.48	*115.00	20.00	101.34	0.68	0.01	Dziewonski et al. (1984c), 1.11.84
32	nz	pa	sv	-3.71	-102.51	93.00	20.00	101.22	-0.41	0.01	CMT , Quebrada, 9.21.85
33	nz	pa	sv	-3.91	-103.97	95.00	20.00	102.03	-0.35	0.01	CMT, Discovery, 3.01.81
34	nz	pa	sv	-3.97	-104.07	96.00	20.00	102.08	-0.30	0.01	CMT, Discovery, 2.06.80
35	nz	pa	sv	-4.06	-104.37	91.00	20.00	102.24	-0.56	0.01	CMT, Discovery, 1.16.86
36	nz	pa	sv	-4.45	-104.82	94.00	15.00	102.45	-0.56	0.01	CMT, Gofar, 3.22.96
37	nz	pa	sv	-4.36	-104.88	98.00	20.00	102.49	-0.22	0.01	CMT, Gofar, 5.15.84
38	nz	pa	sv	-4.59	-105.51	97.00	20.00	102.81	-0.29	0.01	CMT, Gofar, 10.10.84
39	nz	pa	sv	-4.60	-105.80	103.00	15.00	102.97	0.00	0.01	Anderson & Sclater (1972), Gofar
40	nz	pa	sv	-4.53	-105.87	97.00	20.00	103.02	-0.30	0.01	CMT, Gofar, 8.28.84
41	nz	pa	sv	-4.40	105.90	105.00	20.00	103.05	0.10	0.01	Anderson et al., (1974), Gofar
42	nz	pa	sv	-4.50	-106.00	104.00	15.00	103.09	0.06	0.01	Anderson & Sclater (1972), Gofar
43	nz	pa	sv	-4.86	-105.92	95.00	20.00	103.01	-0.40	0.01	CMT, Gofar, 10.08.80
44	nz	pa	sv	-4.65	-106.05	99.00	15.00	103.10	-0.27	0.01	CMT, Gofar, 3.01.84
45	nz	pa	sv	-4.56	-106.17	95.00	15.00	103.18	-0.55	0.01	CMT, Gofar, 9.12.78
46	nz	pa	sv	-8.97	-108.34	92.00	20.00	103.90	-0.59	0.01	CMT, Wilkes, 7.30.80
47	nz	pa	sv	-8.98	-108.54	120.00	20.00	104.00	0.80	0.01	CMT, Wilkes, 5.08.79
48	nz	pa	sv	-9.07	-109.07	100.00	20.00	104.27	-0.21	0.01	CMT, Wilkes, 5.13.86
49	nz	pa	sv	-8.90	-109.47	101.00	20.00	104.49	-0.17	0.01	CMT, Wilkes, 8.21.86
50	nz	pa	sv	-13.37	-111.34	100.00	20.00	105.06	-0.25	0.01	CMT, Garrett, 6.13.78
51	nz	pa	sv	-13.30	-111.50	105.00	10.00	105.15	-0.01	0.03	Anderson & Sclater (1972), Garrett
52	nz	pa	sv	-13.22	-112.15	104.00	20.00	105.48	-0.07	0.01	CMT, Garrett, 7.08.79
53	nz	pa	sv	-13.34	-111.59	100.00	20.00	105.19	-0.26	0.01	CMT, Garrett, 1.07.86
54	nz	pa	sv	-28.70	-112.70	118.00	20.00	105.14	0.64	0.01	Anderson et al. (1974)
55	nz	pa	sv	-28.78	-112.65	117.00	20.00	105.12	0.09	0.01	CMT, 8.21.83
56	nz	pa	sv	-29.01	-112.60	98.00	15.00	105.09	-0.47	0.01	CMT, 9.12.82
57	nz	pa	sv	-29.39	-112.30	108.00	20.00	104.94	0.15	0.01	CMT, 7.15.77
58	pa	ea	ra	-23.60	-15.56	11.10	1.50	12.72	-1.08	0.21	NGDC Several profiles
59	pa	ea	ra	-23.88	-115.42	11.20	1.50	11.82	-0.41	0.17	NGDC Several profiles
60	pa	ea	ra	-24.65	116.20	9.10	1.50	10.65	-1.03	0.13	NGDC Several profiles
61	pa	ea	ra	-24.87	-116.09	8.80	1.50	9.95	-0.77	0.11	NGDC Several profiles

62	pa	ea	ra	-25.57	-116.16	8.70	1.50	8.42	0.19	0.08	NGDC Several profiles
63	pa	ea	ra	-25.73	-116.01	8.30	1.50	7.80	0.33	0.07	NGDC Several profiles
64	pa	ea	ra	-25.87	-115.89	8.10	1.50	7.29	0.54	0.06	NGDC Several profiles
65	pa	ea	ra	-26.08	-115.71	7.70	1.50	6.51	0.79	0.05	NGDC Several profiles
66	pa	ea	ra	-26.28	-115.49	6.80	1.50	5.69	0.74	0.05	NGDC Several profiles
67	pa	ea	ra	-26.44	-115.21	5.90	1.50	4.85	0.70	0.05	NGDC Several profiles
68	pa	ea	tf	-23.03	-114.75	*88.00	10.00	82.12	0.59	0.04	Searle et al. (1989) GLORIA
69	pa	ea	tf	-23.40	-115.24	75.00	10.00	75.91	-0.09	0.04	Searle et al. (1989) GLORIA
70	pa	ea	tf	-24.18	-115.51	69.00	10.00	69.50	-0.05	0.05	Searle et al. (1989) GLORIA
71	pa	ea	tf	-24.54	-116.19	60.00	10.00	58.85	0.12	0.05	Searle et al. (1989) GLORIA
72	pa	ea	tf	-25.88	-115.85	48.00	10.00	48.56	-0.06	0.12	Searle et al. (1989) GLORIA
73	pa	ea	sv	-24.70	-116.19	*56.00	20.00	57.52	-0.08	0.01	CMT
74	pa	ea	sv	-26.51	-114.11	77.00	20.00	86.16	-0.46	0.15	Engeln & Stein (1984)
75	pa	ea	sv	-26.67	-113.96	-71.00	20.00	-87.08	0.80	0.21	Engeln & Stein (1984)
76	pa	ea	sv	-26.87	-113.58	-72.00	20.00	-65.02	-0.35	0.34	Engeln & Stein (1984)
77	na	ea	ra	-25.25	-112.36	5.10	3.00	7.96	-0.95	0.01	NGDC Several profiles
78	na	ea	ra	-25.40	-112.32	6.10	2.00	8.41	-1.15	0.02	NGDC Several profiles
79	na	ea	ra	-25.49	-112.32	6.80	1.50	8.67	-1.25	0.03	NGDC Several profiles
80	na	ea	ra	-25.68	-112.32	8.70	0.80	9.23	-0.67	0.08	NGDC Several profiles
81	na	ea	ra	-25.78	-112.49	8.30	1.50	9.52	-0.81	0.02	NGDC Several profiles
82	na	ea	ra	-25.89	-112.49	9.10	0.80	9.85	-0.93	0.07	NGDC Several profiles
83	na	ea	ra	-26.03	-112.51	10.10	0.40	10.26	-0.40	0.26	NGDC Several profiles
84	na	ea	ra	-26.30	-112.62	11.40	1.00	11.07	0.33	0.04	NGDC Several profiles
85	na	ea	ra	-26.34	-112.62	11.60	0.70	11.18	0.59	0.09	NGDC Several profiles
86	na	ea	ra	-26.38	-112.62	11.70	0.70	11.30	0.57	0.09	NGDC Several profiles
87	na	ea	ra	-26.53	-112.62	12.10	0.50	11.74	0.71	0.21	NGDC Several profiles
88	na	ea	ra	-26.69	-112.63	12.70	1.00	12.22	0.48	0.06	NGDC Several profiles
89	na	ea	ra	-27.22	-112.73	14.50	1.00	13.79	0.71	0.12	NGDC Several profiles

* Azimuths in degrees from north, positive clockwise, negative anticlockwise.

transforms, as the azimuths of the transforms could be confidently measured, uncertainties of 4.0° were given; for the azimuths determined from SeaMARC II data of the Wilkes and Garrett transforms, uncertainties of 5.0° were given; and for Seabeam data from the Yaquina transform (Lonsdale, 1983), an uncertainty of 8.0° was given.

All the Nz-Pa seismic-slip vectors used here are taken from the NUVEL-1 data set. The majority of the seismic-slip data are taken from published CMT (Centroid Moment Tensor) solutions (Dziewonski et al., 1981; Dziewonski and Woodhouse, 1983). Three additional data are from Anderson and Sclater (1972), and two are from Anderson et al. (1974). Four seismic-slip vectors are from south of the Easter Microplate. It is has recently been shown that no transform fault exists here (Klaus et al., 1991); however, these data do not deviate significantly from the predicted azimuths, so should have little influence on the results. The assigned uncertainty for each slip vector is 20°, except for those given a lower uncertainty by DeMets et al. (1990).

5.3.2 Pacific-Easter Data

Ten rate data were obtained for the West Rift of the Easter Microplate, from magnetic anomalies of the NGDC data set, as described in section 5.2. Two or three adjacent profiles were used to calculate each rate. The uncertainties for each datum were set at 1.5 cm/yr, due to the obliquity of the magnetic stripes, and the apparent rotation of the spreading fabric to the east of the present axis, and hence the uncertainty that correct rates had been obtained.

The five transform fault data were all measured from the GLORIA data set, from which azimuths are usually accurate to within a few degrees. The uncertainties assigned to the data were 10°, instead of the more usual 4° (DeMets et al., 1990) for GLORIA transform fault data, in order that the data were not given too high importance levels.

Three seismic slip data from the West Rift were taken from Engeln and Stein (1984) and the fourth slip vector was taken from published CMT solutions (Dziewonski et al., 1981; Dziewonski and Woodhouse, 1983). Uncertainties of 20° were assigned to each datum.

5.3.3 Nazca-Easter Data

Only rate data were used to describe Na-Ea plate motions along the East Rift, as no transform faults exist, and the seismic-slip vectors available do not represent strike-slip movement along the present plate boundary. No data were used to describe Nazca-Easter motion along the northern boundary of the microplate, because of its complex

nature, and the uncertainty that pure strike-slip movement is occurring. Thirteen rate data were used, and were assigned uncertainties ranging from 3.0 cm/yr for the northernmost datum, where narrowing of the Brunhes anomaly (see section 5.2) has resulted from rift propagation rather than closeness to the Na-Ea Euler pole, to 0.4 cm/yr for the most confidently determined rate.

5.4 Calculation of Euler Poles

5.4.1 Calculation of a Finite Pacific-Easter Rotation Pole

Initial efforts to calculate the location of the Pacific-Easter (Pa-Ea) rotation pole using the conventional Minster and Jordan (1978) algorithm, with three-plate closure of the Pacific, Nazca and Easter plates, proved to be unsuccessful, due to the lack of a reasonable starting Euler vector. Attempts to close the West and Southwest Rifts back in time around the resulting Euler pole led to a large mismatch of basement fabric lineations and magnetic isochron lineations, especially along the Southwest Rift. In order to try and understand the evolution of the West Rift, I decided to try and calculate a more reasonable Pacific-Easter finite rotation pole using the method of Patriat (1985). The program used (FITPOL, written by Ph. Patriat of IPG, Paris) is based on an original method by McKenzie and Sclater (1971), but has been significantly improved upon (see Patriat (1985) for a detailed description of the method).

Before running the program, magnetic anomaly picks are made either side of the spreading axis in question, so that two sets of isochrons are obtained for one particular anomaly. Magnetic anomaly picks are designated to be either "fixed" or "mobile" points, or to be "fixed" for one calculation, and then "mobile" for the next. Ideally, two "fixed" points are needed to bracket every "mobile" point. One line of isochrons is then rotated about a given trial pole towards the second line of isochrons, until the "mobile" points coincide with the "fixed" points. The best rotation angle required to do this is found, and a search is then made for a better trial pole. The search is done on a circle of given radius around the present pole to find the direction of a better pole. This next pole is then used in the same way as the initial trial pole, to find the best rotation angle and the best direction for the next trial pole. This process is repeated several times, varying the search radius until the most suitable pole is found (i.e. the one producing the smallest errors when superimposing the magnetic isochrons).

In this case, picks were made at the Brunhes/Matuyama reversal (0.72Ma) either side of the West and Southwest Rifts (Table 5.3). This Pacific-Easter plate boundary was divided into sections (A1, B1-5, see Table 5.3) containing associated "fixed" and "mobile"

TABLE 5.3 WEST RIFT DATA

	WEST		*EAST*	
Section	*Latitude*	*Longitude*	*Latitude*	*Longitude*
A1	23.72°S	115.05°W	23.86°S	115.85°W
	23.78°S	115.02°W	23.87°S	115.84°W
	23.84°S	115.00°W	23.98°S	115.78°W
B1	25.75°S	116.41°W	25.42°S	115.95°W
			25.52°S	115.88°W
B2	26.16°S	115.93°W	25.85°S	115.61°W
			25.93°S	115.54°W
B3	26.35°S	115.66°W	26.14°S	115.32°W
B4	26.52°S	115.38°W	26.34°S	115.09°W
	26.54°S	115.33°W		
B5	26.82°S	115.79°W	26.75°S	114.72°W

TABLE 5.4 ROTATION POLES

	Lat. N	Long. E	deg./my.	Red. Chi-squared	M & J Ellipse σ_{max}	σ_{min}	*Az.(°)*
Three plate							
Nz-Pa	50.43	-89.50	1.445				
Pa-Ea	-27.68	-114.04	15.192		0.38	0.18	39.81
Nz-Ea	-22.55	-112.45	15.207	0.367	0.19	0.15	147.57
Best Fit Pole							
Nz-Pa	53.02	-88.51	1.435	0.294	5.08	1.44	19.70
Pa-Ea	-28.25	-113.88	12.623	0.304	0.59	0.22	171.15
Nz-Ea	-22.71	-112.27	15.899	0.539	0.30	0.09	143.65
Nuvel-1 Best Fit							
Nz-Pa	53.8	-88.2	1.42		8.20	2.60	19
Closure							
Nz-Pa	55.6	-90.1	1.42		1.8	0.9	-1

points. For the points given in Table 5.3, the best pole for Pacific-Easter plate motion since 0.72Ma was found to be:

Lat.	Lon.	Angle
27.57°S	114.12°W	10.8° (i.e. 15°/myr.)

This pole produces a good fit when attempting to rotate the Pacific and Easter plates back in time along the West and Southwest Rifts, and allows the plates to slide along the Anakena, Raraku and Terevaka transform faults and their fracture zone traces.

5.4.2 Calculation of Nazca-Pacific-Easter Three-Plate Closure Euler Poles

The three plate closure model was derived using the more conventional iterative, weighted, least-squares method employed by DeMets et al. (1990) for their NUVEL-1 model. This model has been modified slightly from the Minster & Jordan (1978) method to include Chase's (1978) fitting functions, which fit the spreading rate measured perpendicular to the ridge rather than asssuming the direction of plate motion is known before it is solved for. This method also runs faster due to formulation in cartesian coordinates. The algorithm repeatedly tries to minimize the squared residuals (data minus synthetic values) by adjusting the trial Euler vectors as described by Minster et al. (1974) and Minster and Jordan (1978). The choice of correct starting vectors can be critical in an attempt to obtain correct Euler poles by this method. Using the same data set (i.e. rates, transform azimuths and slip vector azimuths), with different starting Euler vectors or varying uncertainties, can lead to widely varying positions of the final Euler poles calculated.

Two trial Euler vectors are required for the three-plate calculation. The starting pole used for Nz-Ea motion was Naar & Hey's (1989) NAZ-EAS 3P pole (i.e. 22.49°S, 112.41°W, 14.99°/myr.). Using Naar and Hey's (1989) PAC-EAS 3P pole as the starting Pa-Ea pole led to the resulting Euler vector lying too far south, i.e. none of the magnetic isochrons or spreading fabric as seen on the GLORIA images matched up when rotated about the resulting pole (see section 5.4.1). Instead, the Pa-Ea pole obtained using Patriat's (1985) method (section 5.4.1) was used.

The resulting Euler vectors are given in Table 5.4, and the predicted rates and azimuths are shown alongside the measured values in Table 5.2. The weighted residuals (data minus the predicted values, divided by the standard deviation) and the importances are also given in Table 5.2. The importances measure the information contribution of each datum to the model (Minster et al., 1974). The total data importance equals the number of independent model parameters, which is 6 for the three-plate model.

5.4.3 Calculation of Best Fit Nazca-Pacific, Pacific-Easter and Nazca-Easter Euler Poles

The best fitting Euler poles for the three separate plate pairs were also found using the Minster and Jordan (1978) algorithm. The Pa-Ea and Nz-Ea starting vectors used for these calculations were the same as those used for the three-plate model, and the starting vector for the Nz-Pa plate pair is that produced by DeMets et al. (1990) from the 12-plate NUVEL-1 model. All the data (i.e. rates, transform azimuths and seismic-slip vector azimuths) are identical to those used for the three-plate model. The resulting Euler vectors are shown in Table 5.4.

5.4.4 Results

The inversion results for both the three-plate model and the three individual plate pairs seem reasonable. The locations of the Nz-Ea and Pa-Ea three plate model poles are indicated in Fig. 5.3 by solid stars, while the best fit poles are shown as open stars. Naar and Hey's (1989) 3P poles are shown by the small open triangles adjacent to the stars. Despite using more data than Naar and Hey (1989), the resulting Euler vectors from the three-plate model are remarkably similar. The Nz-Ea pole is very slightly closer to the tip of the East Rift, and also the Pa-Ea pole is also slightly closer to the tip of the Southwest Rift. Schouten et al.'s (1990) model (see section 1.5, Chapter 1 and section 6.5.1, Chapter 6 for full discussion) predicts that the Nz-Ea and Pa-Ea poles should lie actually at the present tips of their respective spreading axes. However, despite using a largely different data set than Naar and Hey (1989), the resulting Euler poles remain noticeably similar to theirs, and both sets lie some distance from the rift tips.

The Nz-Ea best fit pole lies southeast of its three-plate counterpart, and is closer to the tip of the East Rift (Fig. 5.3). It also appears to lie closer to the point where, according to my interpretation of the GLORIA mosaic (see section 4.8, Chapter 4), extensional normal faults give way to compressional faulting mechanisms. Thus this best fit pole seems to represent the motion between the Nazca and Easter plates better. The Pa-Ea best fit pole, however, lies some distance south of its three-plate model counterpart, and clearly does not describe the plate separation direction of the Pacific and Easter plates (Fig. 5.3). The Pa-Ea pole calculated using Ph. Patriat's FITPOL program is shown as a small open circle to the northwest of the Pa-Ea three-plate pole. The open circle, solid star and the open triangle form a line of northwest-southeast trend of possible locations of the Pa-Ea Euler pole. The FITPOL pole lies the closest to the southeast tip of the Southwest Rift, and most closely describes the motion between the Pacific and Easter

Figure 5.3 Simplified tectonic interpretation of the Easter Microplate. The locations of the Nz-Ea and Pa-Ea three-plate closure Euler poles are indicated by the solid stars; the best fit poles are indicated by the open stars; Naar & Hey's (1989) 3P poles are shown by the small open triangles adjacent to the stars; the Pa-Ea finite rotation pole calculated using Ph. Patriat's FITPOL program is shown as a small open circle to the northwest of the Pa-Ea three-plate pole; the 2-sigma (95%) error ellipses for the Pa-Ea and Nz-Ea three-plate closure Euler poles are illustrated. In addition, the location of 39 published earthquake focal mechanisms are shown. Those numbered 1-14 are from Engeln & Stein (1984) and the remaining 25 (earthquakes 15-39) were obtained from the hundreds of Centroid Moment Tensor earthquake mechanisms published each quarter (Dziewonski et al., 1981; Dziewonski and Woodhouse, 1983).

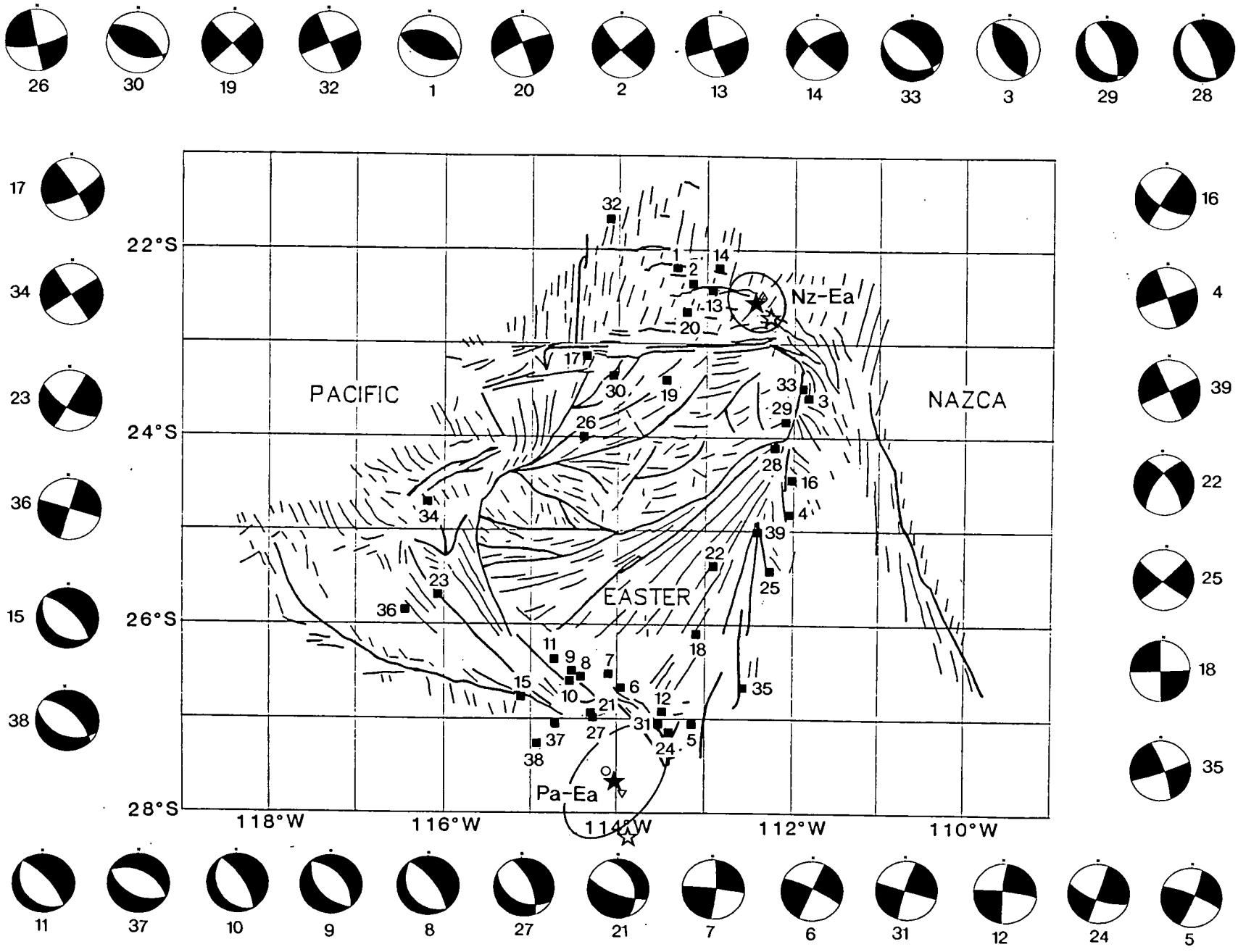
26
30
19
32
1
20
2
13
14
33
3
29
28
17
34
23
36
15
38
16
4
39
22
25
18
35
11
37
10
9
8
27
21
7
6
31
12
24
5
PACIFIC
NAZCA
EASTER
Nz-Ea
Pa-Ea
22°S
24°S
26°S
28°S
118°W
116°W
114°W
112°W
110°W

plates, in that when the magnetic isochrons and lineaments interpreted from the GLORIA mosaic are rotated around it, they produce the most convincing match .

The three plate model Nz-Pa pole and the best fit Nz-Pa pole calculated here are given in Table 5.4, along with the NUVEL-1 best-fitting and closure fitting Euler vectors. The two best fit vectors are almost identical in both position and angular rotation rates. However, the latitudes of the three-plate closure pole and the NUVEL-1 12-plate closure pole differ by over 5°. My three-plate pole does, however, lie within the NUVEL-1 error ellipse given in Table 5.4, and is therefore considered acceptable.

The one sigma error ellipses for the Pa-Ea and Nz-Ea poles are given in Table 5.4. and the two sigma (95% confidence) ellipses fro the three-plate model are illustrated on Fig. 5.3.

The weighted residuals (units are in cm/yr) for the three plate model, as listed in Table 5.2, are plotted against latitude in Figs. 5.4a-f. For the Nz-Pa plate boundary, the weighted residuals of the spreading rates (Fig. 5.4a) and transform azimuths (Fig. 5.4b) are roughly evenly distributed. However, the weighted residuals of the seismic slip vector azimuths (Fig. 5.4c) tend to be negative, as a result of the predicted azimuths of the slip vectors being almost consistently a few degrees more clockwise than the actual values. This in turn implies that either the longitude of the Nz-Pa pole (which is controlled mainly by the transform azimuths) is wrong or that the seismic slip vector azimuths do not correctly describe Nz-Pa plate motion.

The plot of weighted residuals for the spreading rates along the Pa-Ea and Nz-Ea plate boundaries (Fig. 5.4d) shows that the predicted spreading rates for both plate boundaries are too fast in the north, and too slow in the south. For the Pa-Ea plate boundary this implies that the three-plate model Euler pole is too close to the tip of the Southwest Rift. The position of the Pa-Ea best fit pole produces predicted spreading rates which agree more closely with the measured rates, however, as mentioned above, it does not describe the direction of plate separation well. Since so much importance is assigned to the rate data compared to the transform azimuths, and since there are invariably more rate data than transform azimuth data, it is inevitable that the best fit pole will better represent the rate of plate separation rather than the direction. The predicted spreading rates along the Nz-Ea plate boundary are also consistently too fast in the north, and too slow in the south (Fig. 5.4d), which implies that the three-plate closure Euler pole is too far from the tip of the East Rift. Again, the best fit Nz-Ea Euler pole predicts spreading rates which are much more compatible with the measured rates. No transform azimuth or seismic slip vector azimuth data are used for the East Rift, and so

Figure 5.4 (a) - (f) The weighted rate, transform and seismic slip residuals for the Nz-Pa, Nz-Ea and Pa-Ea plate pairs for the three plate model, as listed in Table 5.2, are plotted against latitude. The weighted residuals are equal to the observed datum minus the predicted datum, all divided by the standard deviation (or assigned uncertainty).

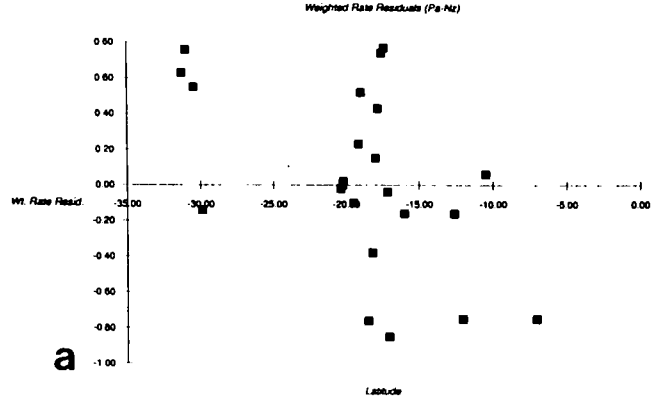
Weighted Rate Residuals (Pa-Nz)
Wt. Rate Resid.
Latitude

a

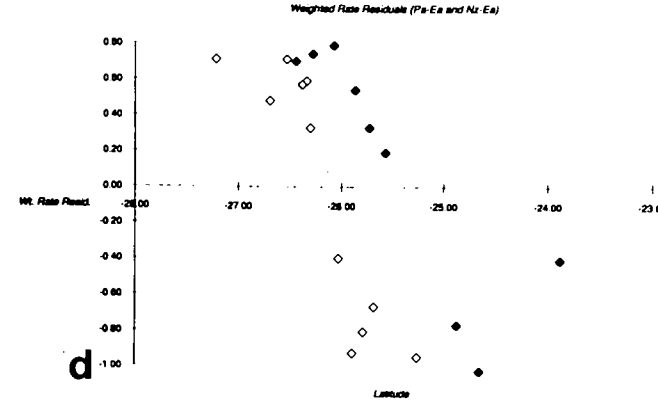
Weighted Rate Residuals (Pa-Ea and Nz-Ea)
Wt. Rate Resid.
Latitude

d

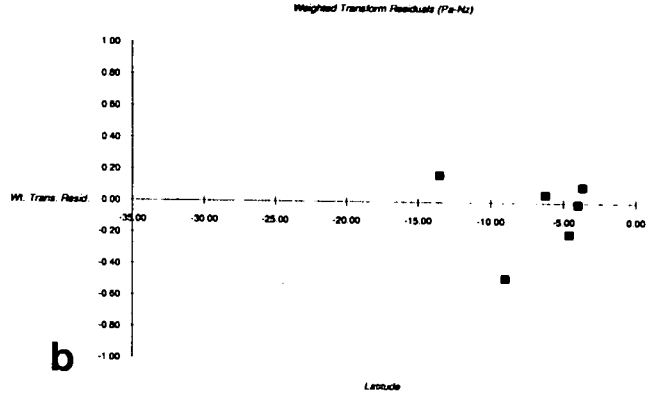
Weighted Transform Residuals (Pa-Nz)
Wt. Trans. Resid.
Latitude

b

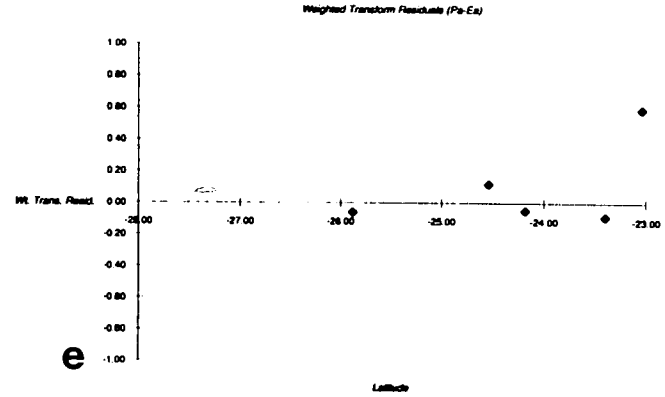
Weighted Transform Residuals (Pa-Ea)
Wt. Trans. Resid.
Latitude

e

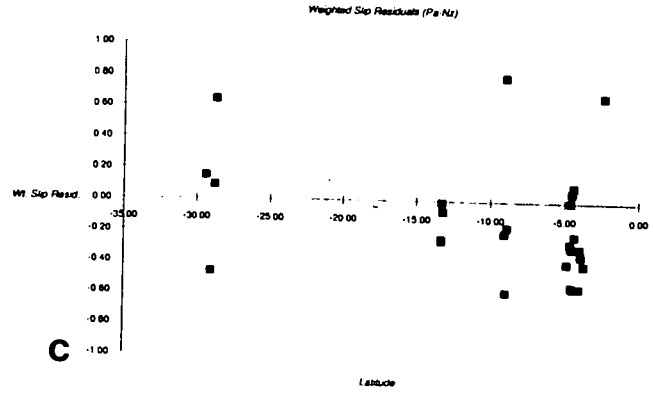
Weighted Slip Residuals (Pa-Nz)
Wt. Slip Resid.
Latitude

c

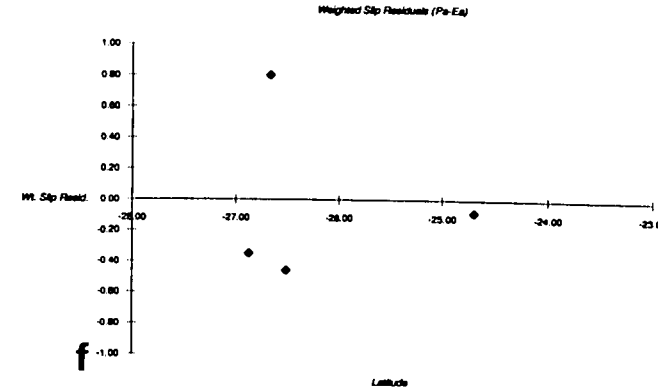
Weighted Slip Residuals (Pa-Ea)
Wt. Slip Resid.
Latitude

f

there is little to constrain the longitude of the best fit Euler pole. However, the longitude given seems to describe the direction of plate separation sufficiently well.

The weighted residuals of the few transform azimuth and seismic slip vector azimuth data that there are for the West Rift (Fig. 5.4e-f) do not show any marked skewness, implying that the longitude of the Pa-Ea three-plate closure pole is reasonable.

All the values of reduced chi-squared* calculated are much less than one (see Table 5.4), which suggests that the uncertainties assigned to the data are too conservative. However, in other recent plate motion models (e.g. Engeln and Stein, 1984; Naar and Hey, 1989; DeMets et al., 1990) the values of reduced chi-squared have also been much less than one, and usually less than 0.5. Thus, unless the standard method of assigning uncertainties is changed, little significance should be attached to the low values of reduced chi-squared.

It is difficult to constrain more tightly the absolute positions of the Pa-Ea and Nz-Ea Euler poles. The addition of more rate and azimuth data into the Pa-Ea data set would not necessarily produce better results, although letting the transform azimuth data assume more importance might better constrain the longitudinal position of the best fit pole. More decipherable magnetic anomaly profiles at the northern end of the East Rift, allowing additional rate data to be added to the Nz-Ea data set, might help to bring the position of the Nz-Ea closure pole closer to the rift tip. However, the longitude of the three-plate closure Euler pole will always be controlled by the position of the other two poles, since the direction of plate separation is not indicated by any pure strike-slip transform faults. The positions of the Pa-Ea and Nz-Ea three-plate closure model Euler poles appear to be a compromise in order to satisfy plate closure conditions. With so few data, it is difficult to establish statistically whether the differences between the best fit and closure models are significant at any level, and therefore whether this has resulted from the existence of a non-rigid microplate.

---

* Chi-squared is the sum of squared weighted residuals (i.e. the residuals divided by their corresponding standard errors), and reduced chi-squared is chi-squared divided by the number of degrees of freedom, N - 3p, where N is the number of data and p is the number of independant variables (=89 - 6 = 83 for this three-plate model).

5.5 Earthquake Seismicity, Focal Mechanisms and Recent Nazca-Pacific-Easter Plate Motions

5.5.1 Seismicity and the Easter Microplate

The existence of the Easter and Juan Fernandez microplates was first deduced from ring-like patterns of earthquake seismicity in the region (Herron, 1972a; Forsyth, 1972) (see section 1.4, Chapter 1). Fig. 5.5 shows the seismicity of the Easter Microplate region since 1912. The data up until 1970 were obtained from the data base of the Global Seismology Unit, British Geological Survey, Keyworth. Nearly all of these earthquakes are from the PDE (Preliminary Determination of Epicentres) data set. The epicentre locations prior to 1960 are distinguished from those after this date, as the locations of the former are only accurate to the nearest half a degree latitude and longitude. The locations of earthquakes reported by the International Seismological Centre since 1971 are also shown. These form the majority of the data, and presumably are the most accurately located epicentres. The epicentres form a diffuse ring about the present-day microplate boundary. A greater proportion of them are associated with the West Rift of the microplate (mostly on the transforms), the propagating tip of the Southwest Rift, and the Southern Triple Junction. Several epicentres are associated with the northern part of the East Rift, and the deformed wedge of Nazca plate lithosphere to the north of the Easter Microplate (see Chapter 7, section 7.2.3 for further discussion). South of the microplate there is considerable earthquake activity associated with the complex plate configuration and the many overlapping spreading centres of the area. Herron (1972a, 1972b) and other authors have suggested that one or more transform faults must exist south of the Easter Microplate, based mainly on the earthquake activity patterns (and the offset of the few magnetic anomalies available). However, recently obtained SeaMARC II data (Hey et al., 1987) has revealed that although the EPR is offset some 90 km at 29°S, no transform fault exists (Klaus et al., 1991), thus the earthquakes may represent the secondary types of faulting associated with ridge overlap and rift propagation (see Searle and Hey, 1983; Kleinrock and Hey, 1989).

Fig. 5.3 shows the location of 39 published earthquake focal mechanisms listed in Table 5.5. Of these, earthquakes 1-14 are from Engeln and Stein (1984), and the remaining 25 (earthquakes 15-39) were obtained from the hundreds of CMT (Centroid Moment Tensor) earthquake mechanisms published each quarter (Dziewonski et al., 1981; Dziewonski and Woodhouse, 1983). Fifteen of these earthquake mechanisms are associated with the southern tip of the Southwest Rift and the Southern Triple Junction region, eleven are from the East Rift, six from the deformed Nazca plate to the north of

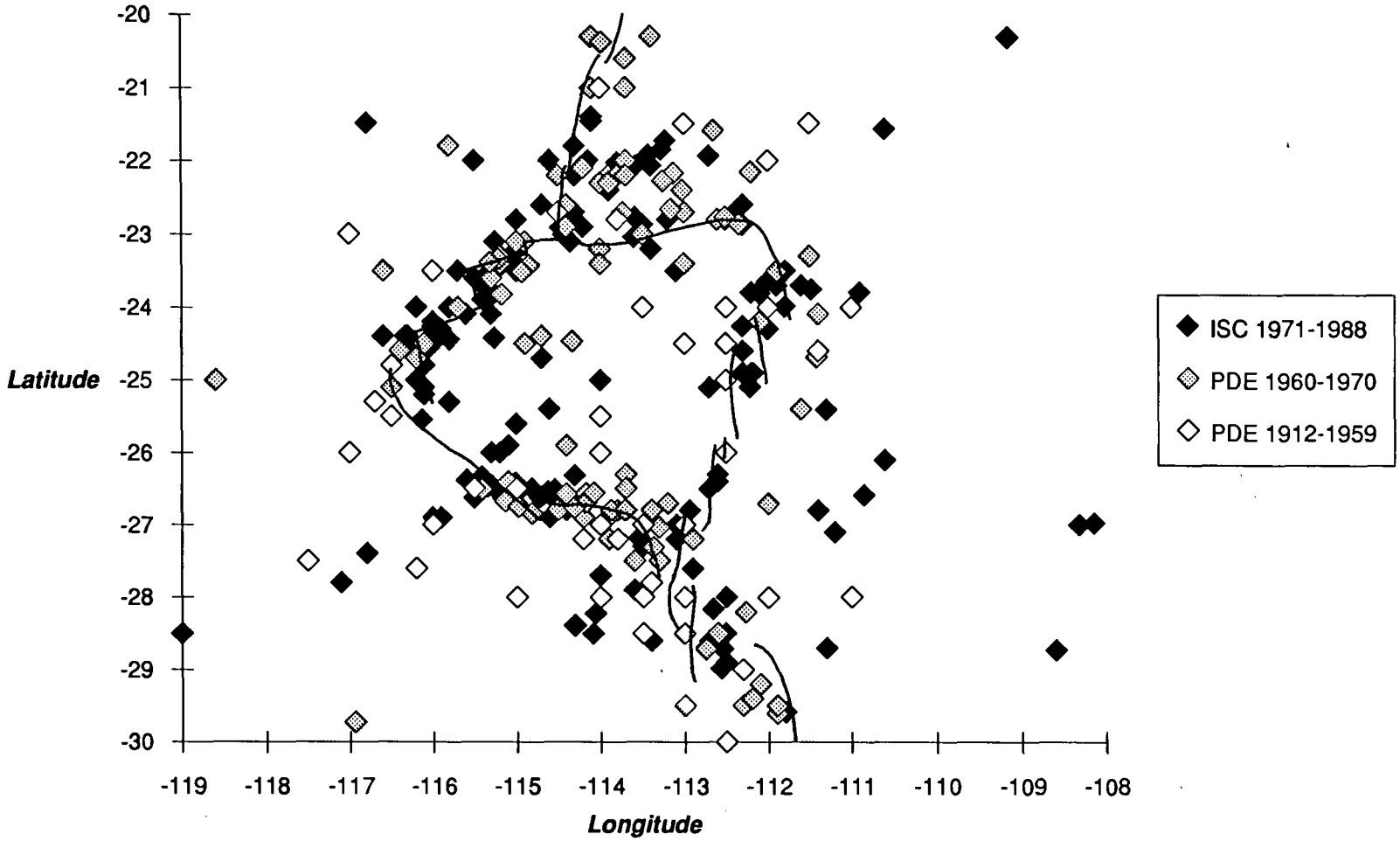

Figure 5.5 The seismicity of the Easter Microplate region since 1912. The data up until 1970 were obtained from the data base of the Global Seismology Unit, British Geological Survey, Keyworth. Nearly all of these earthquakes are from the PDE (Preliminary Determination of Epicentres) data set. The epicentre locations prior to 1960 are distinguished from those after this date, as the locations of the former are only accurate to the nearest half of a degree latitude and longitude. The locations of the earthquakes reported by the International Seismological Center are also shown. These form the majority of the data, and presumably are the most accurately located epicentres.

TABLE 5.5 EARTHQUAKE FOCAL MECHANISMS

	Year	Event No.	Lat.	Lon.	Plane 1			Plane 2			Mo
					Strike	Dip	Slip	Strike	Dip	Slip	
1	1974	6 - 22	-22.19	-113.36	294	40	90				
2	1968	8 - 09	-22.35	-113.15	140	78	182				
3	1973	5 - 13	-23.56	-111.82	330	35	90				
4	1974	12 - 16	-24.81	-112.07	70	89	360				
5	1970	7 - 31	-27.04	-113.14	20	79	12				
6	1969	4 - 22	-26.67	-113.96	203	88	170				
7	1969	4 - 22	-26.51	-114.11	7	78	6				
8	1964	6 - 06	-26.54	-114.42	324	65	270				
9	1974	7 - 25	-26.47	-114.52	320	45	270				
10	1978	2 - 26	-26.60	-114.56	330	67	270				
11	1976	9 - 14	-26.37	-114.73	320	67	270				
12	1963	3 - 07	-26.94	-113.49	280	82	188				
13	1965	11 - 03	-22.41	-113.94	65	85	165				
14	1965	11 - 06	-22.17	-113.86	52	60	166				
15	1978	78	-26.78	-115.12	127	26	-98	315	64	-86	1.3
16	1979	177	-24.45	-112.02	121	58	175	213	85	32	1.6
17	1980	31	-23.13	-114.35	63	66	9	329	81	156	2.7
18	1980	349	-26.09	-113.09	175	90	180	265	90	0	1.3
19	1980	456	-23.39	-113.45	312	90	180	42	90	0	2
20	1981	218	-22.66	-113.23	246	76	-6	338	84	-166	7.8
21	1981	340	-26.94	-114.31	340	34	-46	111	67	-115	1
22	1984(b)	14	-25.38	-112.91	221	58	-31	329	64	-144	1.37
23	1984(c)	140	-25.69	-116.07	123	62	-177	31	88	-28	3.85
24	1985(c)	50	-27.13	-113.40	110	64	-178	19	88	-26	1.04
25	1985(d)	83	-25.40	-112.28	134	82	-177	43	87	-8	2.69
26	1986(b)	92	-23.98	-114.40	78	72	-1	168	89	-162	6.4
27	1986(c)	09	-26.97	-114.28	123	35	-124	343	61	-38	3.8
28	1986(d)	08	-24.11	-112.22	149	18	-96	335	72	-88	1.8
29	1986(d)	09	-23.81	-112.09	138	30	-108	338	61	-80	2.2
30	1987(d)	53	-23.34	-114.05	109	41	79	303	50	99	5.9
31	1988(b)	75	-27.04	-113.52	200	83	4	109	86	173	1.7
32	1988(c)	28	-21.67	-114.11	157	90	180	247	90	0	6.5
33	1988(c)	64	-23.47	-111.88	111	27	-112	316	65	-79	1
34	1988(c)	92	-24.70	-116.19	146	90	180	236	90	0	2.5
35	1988(c)	160	-26.66	-112.58	343	78	174	74	84	13	1.7
36	1990(a)	105	-25.84	-116.44	290	90	-180	20	90	0	3.5
37	1990(a)	113	-27.05	-114.72	297	45	-90	117	45	-90	0.9
38	1990(a)	114	-27.24	-114.91	117	36	-108	318	56	-78	1.5
39	1990(b)	65	-25	-112.42	156	90	-180	246	90	0	2.9

check S. V's + table 5.2.

the microplate, four from the microplate interior, and three from the West and Southwest Rifts. These are discussed below in terms of their plate tectonic setting.

5.5.2 Southwest Rift tip and the Southern Triple Junction

The earthquakes associated with the southern tip of the Southwest Rift (15, 38, 11, 37, 10, 9, 8 and 27) all show normal faulting mechanisms. The magnitudes (M_s) of these earthquakes vary between 5.0 and 6.1, and the nodal planes all strike roughly northwest-southeast, along the trend of the Southwest Rift tip. Normal faulting earthquakes are not generally detected at fast spreading ridges, and are more commonly associated with the slower-spreading Mid-Atlantic Ridge. However, spreading rates at the southern end of the Southwest Rift are comparable with Atlantic rates, and so this region forms one of the most seismically active regions of the Easter Microplate boundary. Engeln and Stein (1984) note that their body-wave modelling of earthquakes 8, 10 and 11 indicated that all events occurred less than 7 km below the seafloor.

Going eastwards from the Southwest Rift tip, the earthquakes gradually adopt pure strike-slip mechanisms. The magnitudes of these earthquakes vary between 5.8 and 6.1. Earthquakes 21, 6 and 7 may have resulted from dextral strike-slip in a WNW-ESE direction between the Pacific and Easter plates, along the so-called Orongo Fracture Zone (Francheteau et al., 1988). However, the origin of earthquakes 31, 12, 24 and 5 is less clear. They may indicate that the Orongo Fracture Zone extends ESE, even though no such feature is detected from the GLORIA data (see section 4.2.4, Chapter 4), or alternatively, they may have resulted from sinistral strike-slip movement along originally ridge-parallel normal faults formed at the East Rift, which are undergoing bookshelf faulting (see Kleinrock and Hey, 1989) as the lithosphere is rotated away from the spreading axis. If the latter is the case, it would imply that the microplate is not behaving entirely rigidly, especially at the triple junction.

5.5.3 East Rift

Seven of the earthquakes in the region of the East Rift show strike-slip faulting mechanisms, despite the fact that the East Rift is undergoing extension. It seems likely that earthquakes 16, 4, 39, 25 and 35 have resulted from dextral strike-slip of pre-existing normal faults along roughly northwest-southeast trends. This would occur as a result of anticlockwise rotation of fabric to the east of the spreading axis as rift propagation takes place. Earthquake 22 may have occurred due to sinistral strike-slip movement of originally ridge-parallel normal faults as the microplate lithosphere is rotated in a clockwise direction away from the spreading axis. Earthquake 18 is the only true enigma,

although this mechanism does not appear to be too well constrained, as neither sinistral strike-slip along an east-west fault, nor dextral strike-slip along a north-south fault is compatible with the known structures as imaged by GLORIA.

Three normal faults (earthquakes 33, 29 and 28) are associated with the East Rift. Although all three of these appear to lie to the west of the present-day plate boundary (see Fig. 5.3), this may be due the lack of seismological stations to the west of the Easter Microplate region. All three earthquakes have nodal planes striking NNW-SSE, parallel to the northern segments of the East Rift plate boundary and, as for the Southwest Rift tip, they occur in a region of slow spreading.

Earthquake 3 (from Engeln and Stein, 1984) is shown as having a pure thrust fault mechanism, as nearly all the first motions are compressional. Compressional faulting at the northern end of the East Rift may occur in response to tectonic extension (ridge push) within the region, as the lithosphere is torn apart, although other examples of this occurring elsewhere in the ocean basin are not known.

5.5.4 Nazca plate north of the Easter Microplate

Six earthquake mechanisms are shown from a seismically active region to the north of the Easter Microplate. Of these, earthquakes 32, 20, 2, 13 and 14 all have strike-slip mechanisms with a slight NNE-SSW thrusting component and earthquake 1 indicates a thrust faulting mechanism. The tectonics of this anomalous region of the Nazca plate are discussed in full in Chapter 7, but are mentioned here briefly too. The region is thought to be subject to dextral shear due to a decrease in the EPR spreading rate south of about 21°S. Convergence on the order of 50 mm/yr is predicted between the Nazca and Easter plates along the northern boundary of the microplate by the present location and angular velocity of the Nz-Ea Euler pole, as given in Table 5.4. It is thought that the northern boundary is unable to accommodate all of this shortening, and so the Nazca plate to the north is also undergoing compression in an overall north-south sense. Thus the whole region is predicted to be under dextral transpression. The strike-slip earthquake mechanisms are thought to represent sinistral shear along roughly northeast-southwest trending pre-existing normal faults. This bookshelf faulting (with movement along antithetic Riedel shears) is able to accommodate much of the predicted dextral transpression. The thrust fault mechanism of earthquake 1 is thought to have resulted from southward overthrusting of oceanic crust , producing the anomalous ridges seen on the GLORIA mosaic (see section 4.8, Chapter 4, and section 7.2.1, Chapter 7). The magnitudes of all the earthquakes of this area range from 5.4 to 5.9.

5.5.5 Northwest Microplate Interior

Four earthquake mechanisms have been published from the norhtwest microplate interior. These are earthquakes 17, 26, 30 and 19 located east of the northern end of the West Rift. The basement lineations imaged by GLORIA (see section 4.9, Chapter 4), indicate that the three earthquakes with strike-slip mechanisms (earthquakes 17, 26 and 19) may have resulted from sinistral strike-slip faulting along roughly northeast-southwest oriented planes, as no structural fabric is found matching the orthogonal nodal planes. If this is the case, then the obvious explanation for this faulting mechanism is, again, bookshelf faulting along the originally ridge-parallel normal faults in order to accommodate the clockwise rotation of the microplate.

Earthquake 30, however, remains an enigma, as there are no structures with the required trend at the given position. If, however, the earthquake actually occurred some 30 km north of its position as given by ISC, then it may represent the thrust faulting that is predicted to occur along the northern boundary of the microplate, between the Nazca and Easter plates. As described in section 4.6, Chapter 4, the northern boundary of the microplate, as imaged by GLORIA and mapped by Seabeam (Francheteau et al., 1988) consists of a series of broad, high relief ridges with a roughly east-west trend overall. These ridges have a steep slope to the south, and a gentle slope to the north. The present position of the Nz-Ea Euler pole, as given in Table 5.4, implies that closure on the order of 50 mm/yr is occurring at the western end of the northern boundary. If earthquake 30 did occur further north than the location given by ISC, this would be the first piece of major evidence to support the idea (first suggested by Zukin, 1990) that thrust faults exist along the northern boundary (as is also indicated by the GLORIA data). Thus the anomalously prominent northern boundary may have occurred through overthrusting of Nazca plate lithosphere over Easter Microplate lithosphere.

5.5.6 Central West and Southwest Rifts

Earthquakes 34, 23 and 36 all have strike-slip faulting mechanisms. Of these earthquake 34 is associated with sinistral strike-slip movement along the Terevaka transform. The other two earthquakes have focal mechanisms which may reflect dextral strike-slip faulting along pre-existing ridge-parallel normal faults, which would imply that the Pacific plate adjacent to the West and Southwest Rifts is not behaving rigidly. If rift propagation was taking place near these earthquakes, there would be a ready explanation for this strike-slip faulting. However, the earthquakes lie to the north and south of the propagator that extends away from the Terevaka transform, and so there is

no reasonable explanation for the deformation of the Pacific plate that the earthquakes imply.

5.6 Conclusions

The magnetic anomaly profiles have been successfully modelled using the 2-D program MAGIC. Anomalous spreading rates highlighted by these models are attributed to rift propagation events that have relocated the spreading axis some distance east or west of its former location. Spreading rates along the East Pacific Rise are generally faster to the east than the west, so that the EPR appears to be continually migrating westwards.

Both three-plate closure fitting and best fit poles have been calculated for Nz-Pa, Pa-Ea and Nz-Ea plate motions. There is most difference between the Pa-Ea three-plate and best fit poles, as the spreading rates along the West and Southwest Rifts do not decrease greatly enough southwards to allow the best fit pole to lie close to the southem tip of the Southwest Rift. The differences between the two types of Euler poles are not sufficient, however, to conclude that the Easter Microplate is not behaving rigidly.

Most of the seismicity is concentrated at the microplate boundaries, and all of them are seismically active. Earthquakes have also occurred on the Pacific and Nazca plates surrounding the Easter Microplate, as well as the microplate interior. There is considerable activity on the Nazca plate just to the north of the microplate, and it is thought that this area is under dextral transpression, with a strong north-south compressional component.

The earthquake focal mechanisms reveal that much of the seismicity adjacent to the East and West Rifts is due to strike-slip faulting along pre-existing normal fault blocks that formed shortly after the lithosphere was accreted. Strike-slip events are also found within the microplate interior. These suggest that not only is the microplate not behaving entirely rigidly, but also parts of the Nazca and Pacific plates immediately adjacent to the microplate are also deforming.

Normal faulting events are restricted to the northern end of the East Rift and the southern end of the Southwest Rift, where full spreading rates are less than 50mm/yr. The focal mechanisms confirm predictions that thrust faulting is taking place along the northern boundary of the microplate as well as on the deforming Nazca plate just to the north, and support my interpretation of the GLORIA images that the prominent ridges that make up the northern boundary, as well as those to the north, have formed by southward overthrusting of the lithosphere to the north over that to the south.

In conclusion, although the Euler poles calculated do not predict that the Easter Microplate is deforming internally, earthquake mechanisms suggest that the fast rotation of the microplate (about 15°/myr) cannot be accommodated by an entirely rigid process. Small amounts of shear along pre-existing normal fault blocks are required. The relatively fast convergence predicted along the northern boundary by the Nz-Ea Euler vector is accommodated by thrust faulting within the Nazca plate to the north. Additional convergence is also allowed by the clockwise rotation of fault blocks within the Easter Microplate and the Nazca plate to the north.

CHAPTER 6
RECONSTRUCTION OF THE EASTER MICROPLATE

6.1 Introduction

In this Chapter, the three-plate Euler poles calculated in Chapter 5 are used to reconstruct the history of the Easter Microplate, from the present day back to the time of its initiation at around 5.25 Ma. Three digital data sets are used in the reconstructions which involve rotation of the data around Euler poles as if the plates were rigid. These data sets are digitised magnetic isochrons, digitised lineaments interpreted from the GLORIA data and the digitally processed GLORIA data itself. Use of all three data sets provides strong structural control on the reconstructions, particularly on the evolution of the East and West Rifts.

6.2 Methods of Reconstruction Used

In order to understand the kinematic evolution of the Easter Microplate, and reconstruct a geological history of the region, several methods may be employed. Recent reconstructions of the microplate by Naar and Hey (1991) involved "closing" the microplate in a series of steps using the Pacific-Nazca magnetic anomalies north and south of the microplate and the NUVEL-1 plate motion model. After each step, the Easter microplate was rotated rigidly to match the Nazca and Pacific anomalies. This method relies on reliable matching of magnetic anomalies to the north and south of the microplate, as well as having confidence in the interpretation of anomalies to the east and west where data are relatively scarce (see Chapter 2, Fig. 2.6). The unidentified magnetic lineations within the microplate interior were inferred by trying to match the sparse data to the west of the microplate.

Attempts to improve on Naar and Hey's method have been made in the reconstructions described below. By combining the tectonic fabric information from the GLORIA data and the magnetic data from the microplate itself and the surrounding area, stronger control can be exerted over the reconstructions despite the complex history of the region. Euler vectors used in the reconstructions for Pacific-Easter and Nazca-Easter motion were calculated by inversion of data from the East Pacific Rise, East Rift and West Rift as described in sections 5.3 and 5.4, Chapter 5. Magnetic anomalies were interpreted by comparison with computed models (section 5.2, Chapter 5), and the

resulting present-day configuration is shown in Fig. 6.1. Initial attempts to "close" the microplate (not shown here) were made using scissors and paste. Matching pairs of isochrons in this way allows a direct feel for the rigidity of the plates, and clearly highlights the gaps and overlaps that form during the reconstructions (resulting either from incorrectly interpreted magnetic anomalies, or from non-rigid stretching or compression of the lithosphere). Three methods of reconstruction have been employed for the studies described here. All the methods involve rotation of digital data around Euler poles as if the plates were rigid, using a computer program ROTATE adapted from Saunders et al. (1983). The three different data types used here are digitised magnetic isochrons, digitised lineaments interpreted from the GLORIA data (Fig. 6.2), and finally the digitally processed GLORIA data itself (Fig. 6.3) (as described in Chapter 3).

Rotation of the magnetic isochrons and removal of anomalies younger than the stage of rotation provides the age constraints on the reconstructions (see Figs. 6.6a-6.18a). After each rotation back in time the earlier spreading axes of the East and West Rifts are positioned between the youngest pair of remaining isochrons. These axes are divided into segments which are allowed to point to their relative Euler pole, where possible, based on the assumption that orthogonal spreading occurs in preference to oblique spreading. The division of the spreading axes into segments (especially on the East Rift) is controlled by discontinuities in the magnetic isochrons interpreted, where these have been found, but otherwise is a schematic representation of a possible previous plate configuration.

The digitised GLORIA interpretation (Fig. 6.2) is used to provide detailed structural control on the orientation of earlier spreading axes and transform faults (Figs. 6.6b-6.18b). Substantial mismatches in the orientation of fault scarps after each rotation (i.e. the normal faults formed at the spreading axes, assumed to be orthogonal to the spreading direction) indicate either an incorrect reconstruction, or that shearing of the lithosphere has occurred at a later stage, as commonly occurs between propagating and dying rifts (e.g. Searle & Hey, 1983; Hey et al., 1986; Kleinrock & Hey, 1989). However, small variations in the trends of mid-oceanic ridge fault scarps after rotation are not considered important. The reconstructions made using these data provide confidence in the interpretation of non-ridge-parallel fabric, found mainly on the Pacific plate to the west of the West Rift. Lineaments suspected to be relicts of fracture zones may be interpreted as such with confidence if after closure they are found to provide unambiguous sites for earlier transform faults. Also oblique lineaments thought to have resulted from shearing during rift propagation may match tips of older ridges after reconstruction. Unfortunately, the majority of GLORIA data available are from the interior of the Easter Microplate. If additional data were to be obtained to the west of the West Rift on the Pacific plate, and

Figure 6.1 Digitised present day configuration of magnetic isochrons based on interpretations discussed in Chapters 2 and 5. Ages are given in millions of years according to the Harland et al. (1990) timescale.

Present
5.08
3.40
2.45
3.87
1.77
0.72
0.94
3.03
3.40
2.45
1.77
0.94
0.72
3.87
5.08
3.40
2.45
1.77
0.94
0.72
3.03
2.45
3.40
1.77
0.72
0.94
0.72
1.77
2.45
3.03
3.40
3.87
3.03
2.45
3.40
3.87
1.77
0.72
1.77
0.72
1.77

A

Figure 6.2 Digitised interpretation of tectonic lineaments based on GLORIA and SeaMARC II sidescan sonar data. This is used to provide detailed structural control on the orientation of earlier spreading axes and transform faults during the rotations carried out in Figs. 6.6b-6.18b.

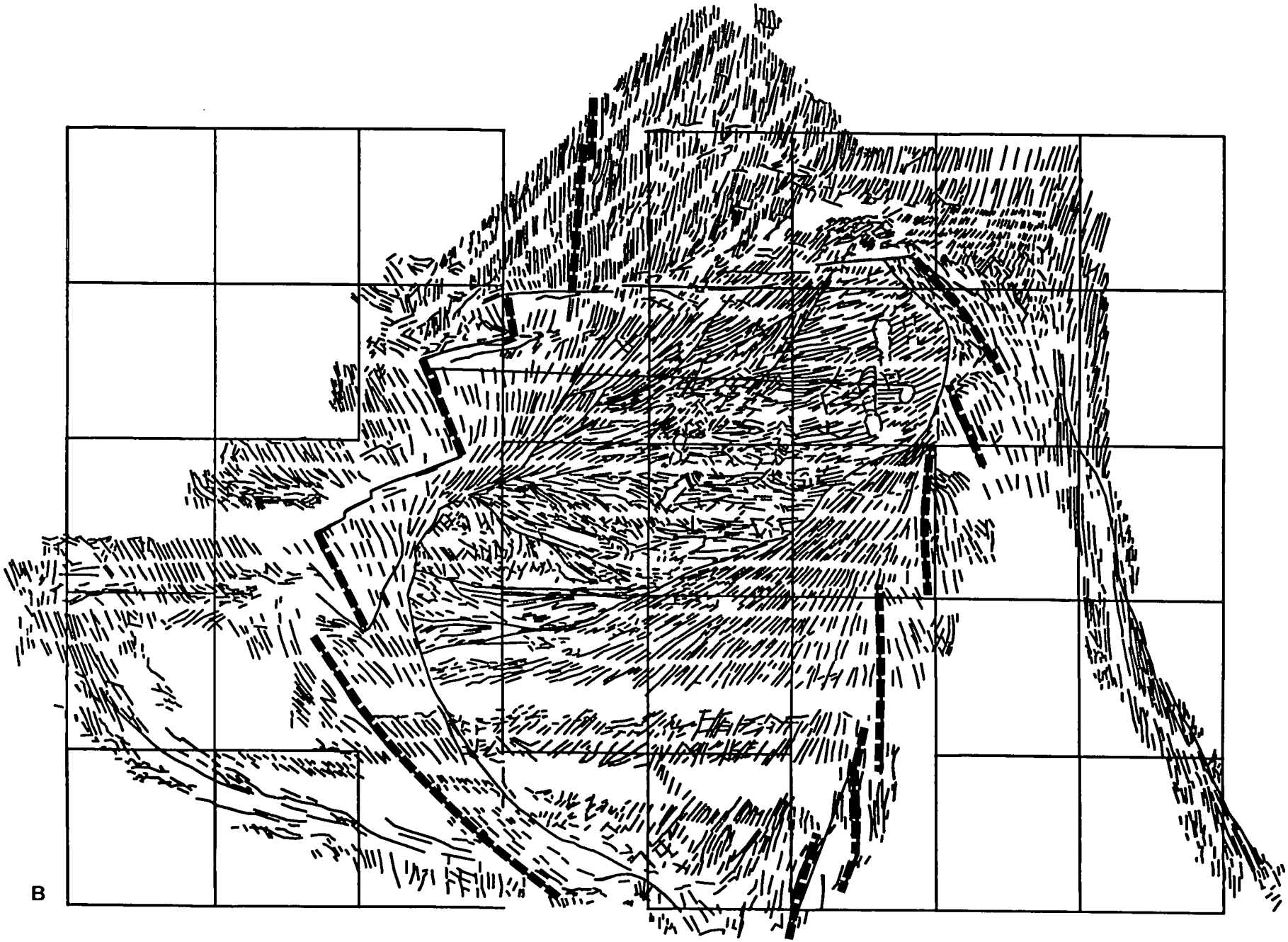

B

Figure 6.3 Digitally processed GLORIA mosaic, as described in Chapter 3, which has been subsampled by a factor of 10 to reduce the number of data points, so that one side of each pixel corresponds to 500 m. The mosaic was digitally cut along the present plate boundaries to form separate files corresponding to the Pacific, Nazca and Easter plates, which were then used in the rotations shown in Figs. 6.6c-6.18c.

PRESENT

between the East Rift and the major outer pseudofault on the Nazca plate, further constraints on ridge jumps and reorientations of the East and West Rifts could be made.

The digitally processed GLORIA mosaic (Fig. 6.3) was also used in the reconstructions (Figs. 6.6c-6.18c). The image used for the purpose of the reconstructions has been subsampled by a factor of 10 to reduce the number of data points, so that the side of each pixel corresponds to 500 m. The mosaic was digitally cut along present plate boundaries, to form separate files corresponding to the Pacific, Nazca and Easter plates. These three digital mosaics of the plates were used in the rotations, using the same ROTATE program as above, but converted for use within the MIPs (Mini Image Processing) system. The isochrons in Fig. 6.1 were digitised, and the data interpolated to produce a contour map of ages over the Easter Microplate region. This image was then digitally overlain on the GLORIA mosaic to produce Fig. 6.4. A colour spectrum gives a qualitative indication of the age of the seafloor, whereby younger, recently formed crust is denoted by warm red colours, while older material is indicated by colder blue colours. Interpolated age data used to create Fig. 6.4 were also used in the reconstructions. Specific age intervals were displayed as different bands of colour on top of the rotated GLORIA images, so that fabric formed later than the rotation age could be removed.

The advantage of displaying the digital sonograph data in its rotated form for the various time increments is that not only can individual sets of faults be matched up, as is the case for the digitised interpretation, but also areas of different backscatter intensity can be correlated across pre-existing spreading axes. Any marked differences in backscatter of juxtaposed domains may indicate errors in the reconstruction. For instance, within the microplate interior, between 23°S and 24°S and 112°W and 114°30'W, where magnetic data are difficult to interpret, a qualitative "eyeball" examination of the backscatter (see Fig. 6.3 and Plate 1) and basement fabric reveals two domains of similar age. The western domain trends roughly northeast-southwest, while the eastern one trends approximately east-west. The variation in backscatter across the western domain from northwest to southeast is similar to the variation across the eastern domain from north to south. The two domains are inferred to have formed at the same time at different spreading axes. Reconstruction of the data back in time (see below) does indeed reveal that the western domain formed at the northern end of the West Rift, while the eastern domain formed at the southern end of the East Pacific Rise during the same time period (around anomaly 2A time).

Throughout the reconstructions, the Pacific plate has been held fixed, while the Nazca and Easter plates have been rotated relative to it. For the first reconstruction, back to 0.25 Ma (Fig. 6.7a-c), the instantaneous Euler poles calculated in the previous chapter

Figure 6.4 GLORIA image digitally overlain by a contour map of ages. This was derived by treating digitised magnetic isochrons as if they were spot heights on a topographic surface and interpolating between them. A colour spectrum gives a qualitative indication of the age of the seafloor, with younger, recently formed crust represented by warm red colours, while older material is indicated by colder blue colours. These interpolated age data were also used in the reconstructions.

EASTER MICROPLATE
100 Km
110
112
114
116

were used. The Pacific-Easter (Pa-Ea) pole (the first named plate always moves with respect to the second) was subtracted from the Nazca-Easter (Nz-Ea) pole, to obtain the instantaneous Nazca-Pacific (Nz-Pa) pole used for this time interval, as given in Table 6.1. For this reconstruction the Nazca plate was thus rotated by 0.35° in a clockwise direction about the Nz-Pa pole, while the Easter plate was rotated by 3.7° in an anticlockwise direction about the Ea-Pa pole (the inverse of the Pa-Ea pole). The new positions of the Nazca and Easter plate data were saved to be used in the next reconstruction.

The instantaneous Nz-Ea pole was rotated in the same way as the Nazca plate around the Nz-Pa pole to its new position, for use in the next reconstruction. Meanwhile, and for all the other reconstructions, the Pa-Ea pole remains fixed at its original position on the Pacific plate. The Pa-Ea pole is again subtracted from the new Nz-Ea pole, to give a new Nz-Pa pole, which is used to rotate the Nazca plate from 0.25-0.5 Ma. So for the second reconstruction, the Easter plate is rotated around the same Ea-Pa pole as before, while the Nazca plate is rotated about the new Nz-Pa pole. This procedure is repeated for each of the reconstructions (i.e. the Ea-Pa pole is held fixed, while the Nz-Ea pole is rotated with the Nazca plate) and then the new Nz-Pa pole is found. For all the reconstructions, the same rotation rates were used, i.e. 14.8°/myr for the Pa-Ea pole, and 14.9°/myr for the Nz-Ea pole, as calculated in the previous chapter. Although Schouten et al.'s (1991) model predicts that the rotation rates should be faster for an older and smaller microplate, using the constant rates produces a good match for the magnetic isochrons back in time, and closes the two major pseudofaults associated with the East Rift well. Thus to prevent complicating the model unnecessarily, the rates are not changed. Obviously, the smaller the time increment between Nz-Ea poles calculated, the more accurate the reconstruction. For time increments of 0.5 Ma, a mismatch is produced between the Nazca and Easter plates (as shown by the magnetic isochrons and GLORIA data, though not shown here) as they are rotated relative to the Pacific plate. For time increments of 0.25 Ma, as used here, the error is negligible and within the errors of the data. For each of the magnetics figures (Figs. 6.6a-6.18a and Fig. 6.19a-h), the position of the Nz-Ea pole used for that reconstruction is shown. Although the Easter Microplate appears to have formed around 5.25 Ma ago (see below), not enough GLORIA or magnetic data are available on the Pacific and Nazca plates to allow reliable reconstructions back this far. Attempts to do so for the period of 3.0-5.0 Ma are shown in Figs. 6.19a-h, using only the magnetic data.

One of the most rigid controls for the evolution of the East Rift is the matching of the major inner and outer pseudofaults back in time. Similarities in the inflexions of the curves of the two pseudofaults either side of the East Rift are assumed to have resulted from

changes in propagation rate and/or spreading rate of the Rift during its evolution. Thus much of the history of the East Rift can be inferred from the shapes of the curves. During the reconstructions, where the two pseudofaults no longer match each other, the reconstructions are likely to be incorrect.

6.3 A Brief History of the Easter Microplate

This section summarises the microplate's history based on the reconstructions presented here. A more detailed description follows in section 6.4. A schematic history of the Easter Microplate is shown in Fig. 6.5. By rotating the magnetic isochrons repeatedly in the manner described above, eventually the two major pseudofaults of the East Rift disappear at 5.25 Ma. As the onset of propagation of the East Rift has traditionally been taken as the start of the formation of the microplate (e.g. Handschumacher et al., 1981; Engeln & Stein, 1984; Naar & Hey, 1991) this age of 5.25 Ma is herein taken as the time of initiation of the microplate, the implications for which are discussed below. Certainly incorrect magnetic anomaly interpretations and calculations of the Euler poles could lead to different proposed dates for the onset of East Rift opening, as could extending the outer (eastern) pseudofault to the southeast of Easter Island. Handschumacher et al. (1981) suggested that the microplate formed at 3.2 Ma, and Naar and Hey (1991) have recently offered 4.5 Ma as the starting date. Both these studies are based on magnetic anomaly determinations, and clearly show that the more data available, the better the interpretation. For the purpose of this study at least, 5.25 Ma will be taken as the start of the evolution of the Easter Microplate, and dates between 5.25 Ma and the present will be accepted as real.

Figure 6.5 shows that northward propagation of the East Rift continues until just after 2.5 Ma, when its tip reaches its northern limit at around 23°S. While this propagation takes place, the West Rift (formerly the East Pacific Rise) continually readjusts to accommodate a dual spreading ridge system (Engeln & Stein, 1984), by breaking into smaller segments, separated by transform faults, which rotate in an anticlockwise direction. From 2.25 Ma to the present, the East Rift continues spreading at the same angular rate but does not grow in length. During this same period, the West Rift continues to adjust, and the Southwest Rift begins to open up. Engeln and Stein (1984) presumed that this opening should occur along a pre-existing left-stepping transform fault or series of faults, based on their models (see Chapter 1).The possible existence of such a transform is discussed in Chapter 8. Initially the microplate grows not only in its north-south dimension as the East Rift propagates, but also the offset between the East and West Rifts gradually increases, though the propagation rate generally exceeds the half-

Figure 6.5 A schematic history of the Easter Microplate since 5 Ma based on the reconstructions described in the text. The East Rift of the Easter Microplate is initiated just after 5.25 Ma, and continues northward propagation until just after 2.5 Ma, when its tip reaches its northern limit at around 23°S. While this propagation takes place, the West Rift (formerly the East Pacific Rise) continually adjusts to the new spreading regime by breaking into smaller segments, separated by transform faults, which rotate in an anticlockwise direction. For some reason the East Rift ceases northward propagation at just after 2.5 Ma, and so the East Rift continues spreading at the same rate, but does not grow in length. During this time, the West Rift continues to readjust, and the Southwest Rift begins to open up, probably along a pre-existing left-stepping transform or series of transform faults.

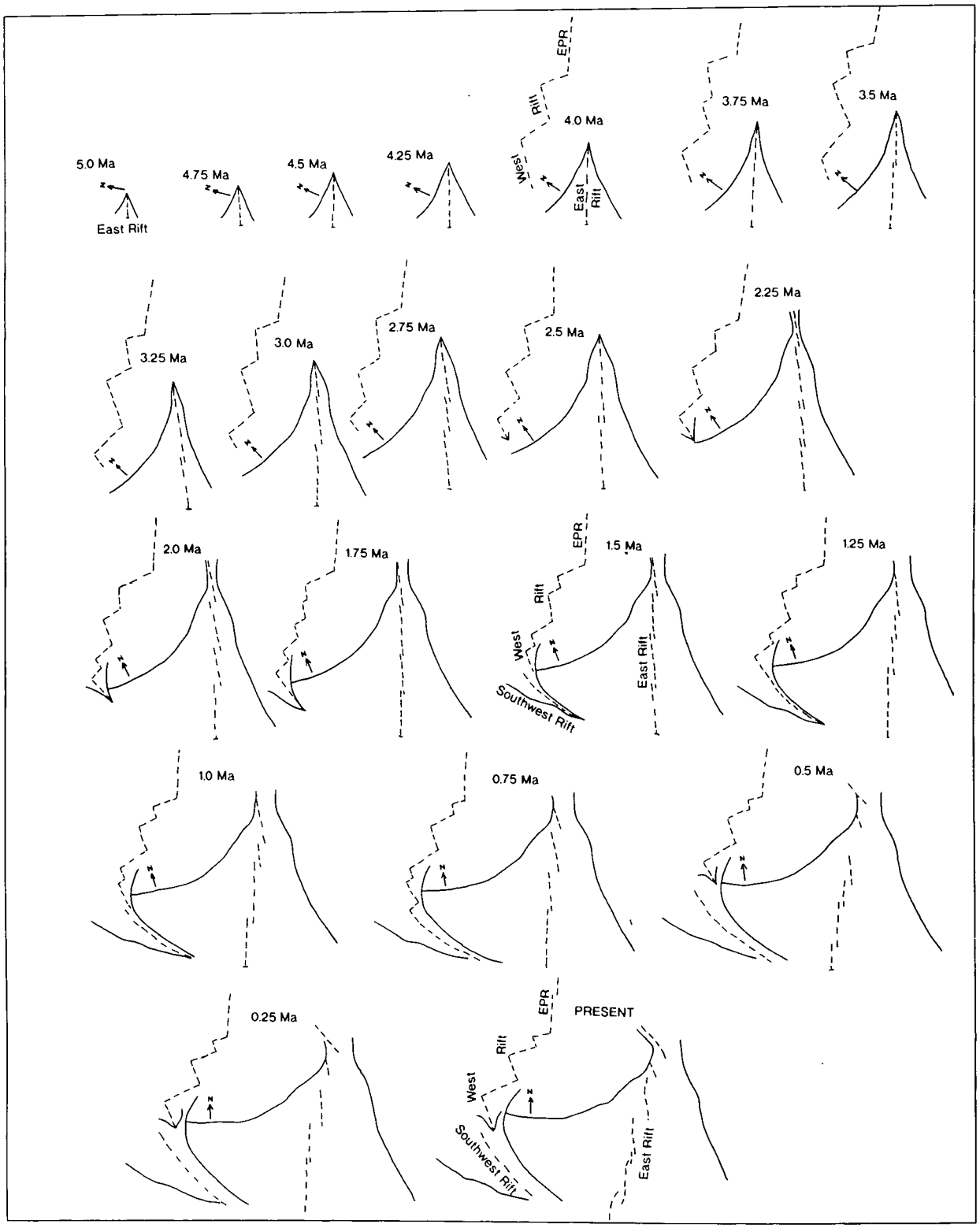
5.0 Ma
East Rift
4.75 Ma
4.5 Ma
4.25 Ma
EPR
Rift
West
4.0 Ma
East Rift
3.75 Ma
3.5 Ma
3.25 Ma
3.0 Ma
2.75 Ma
2.5 Ma
2.25 Ma
2.0 Ma
1.75 Ma
EPR
Rift
West
1.5 Ma
East Rift
Southwest Rift
1.25 Ma
1.0 Ma
0.75 Ma
0.5 Ma
0.25 Ma
EPR
PRESENT
Rift
West
Southwest Rift
East Rift

spreading rate. As the East Rift ceases propagation, the east-west offset continues to grow, though at a more subdued rate.

6.4 A detailed Chronicle of the Easter Microplate

0.0-0.25 Ma. The first rotation back in time (Fig. 6.7a-c) reveals little noticeable change in the tectonic configuration. Movement along the transform faults on the West Rift allows active part of the transforms themselves to migrate slightly southwestwards along their small circles around the Pa-Ea pole, while the spreading segments between them have moved westwards. The spreading segments on the East Rift also move westwards. Overlapping segments within the East Rift are shown as straight lines for convenience, whereas in all probability they would have been as sinuous as the present-day axes. The most notable change is the gap that has opened up along the northern boundary of the Easter Microplate (coloured black in Fig. 6.7b), which represents the total compression predicted between the Easter and Nazca plates along this boundary (a maximum of 14 km in 0.25 myr near the Northern Triple Junction). The mechanisms by which such a large amount of shortening may take place without the formation of a subduction zone in such young crust are discussed in full in the next chapter. However, for now, it may be said that a large part of this shortening during the last 1 Ma appears to have been taken up in the Nazca plate to the north of the boundary, by both block rotations and thrust faulting. As the reconstructions proceed back in time, and the Nz-Ea pole moves ever closer to the new location of the Northern Triple Junction, the maximum rate of convergence that is predicted along the northern boundary will decrease, back to a time when no compression is predicted.

0.25-0.5 Ma. From 0.25-0.5 Ma (Fig. 6.8a-c), again there is little noticeable change. The Southwest Rift has closed slightly, and the southern tip of the axis is shown pointing in a less southerly direction. The gap along the northern boundary has opened further. On the lower diagram (Fig. 6.8b) the cumulative amount of gap formed since the present is shaded, while on the upper diagram (Fig. 6.8a) the stippled area within the gap shows the amount the gap has increased (i.e. the amount of compression that has taken place) since the last reconstruction.

0.5-0.75 Ma. The Brunhes/Matuyama reversal isochron (0.73 Ma) has disappeared (Fig. 6.9a-c) and the spreading axes are located between the Jaramillo anomalies (0.94 Ma). The spreading segment that was replaced by the southward propagator has been added to the West Rift, between the propagator to the south of the Terevaka transform (see Chapter 2, Fig. 2.1), and the Southwest Rift. Note that the propagator is shorter, and its tip is adjacent to rotated fabric to the west (near 24.9°S, 116.4°W), as expected due to

Figure 6.6 (a) - (b) The digitised magnetic isochrons and digitised structural lineaments in their present-day configuration prior to the reconstructions.

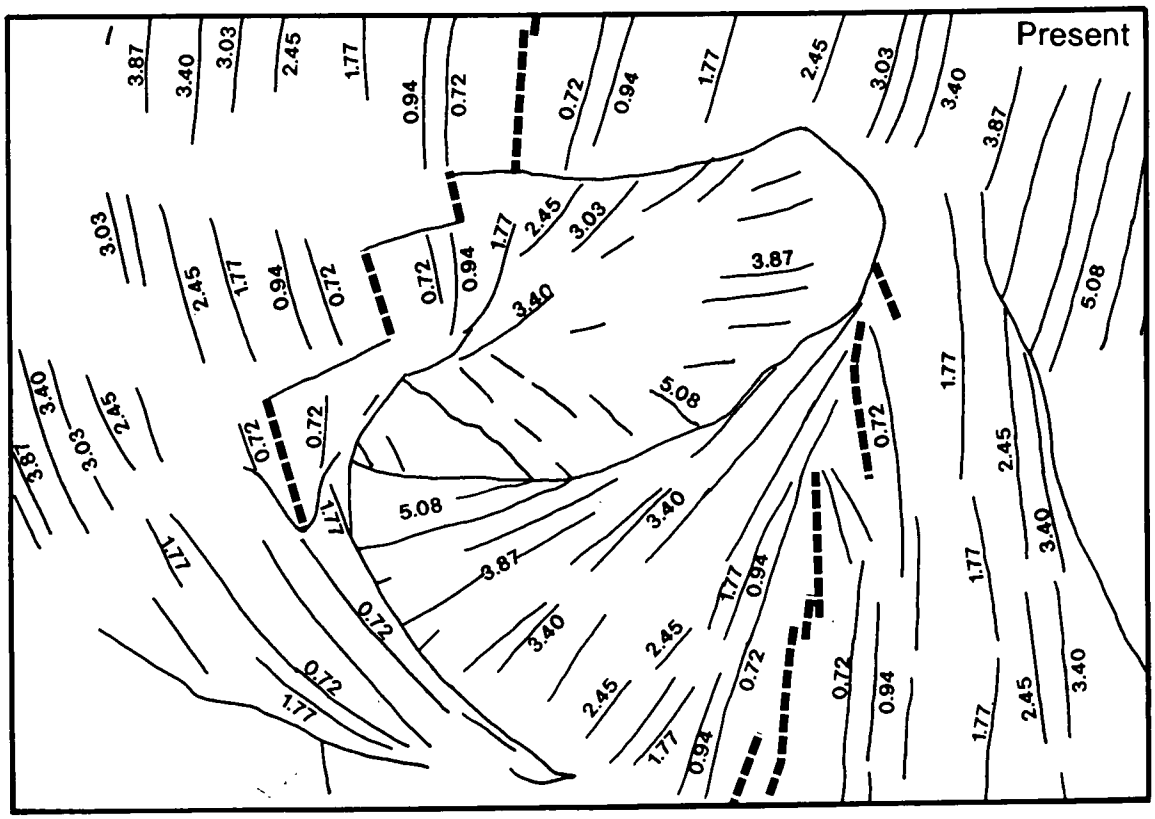

A

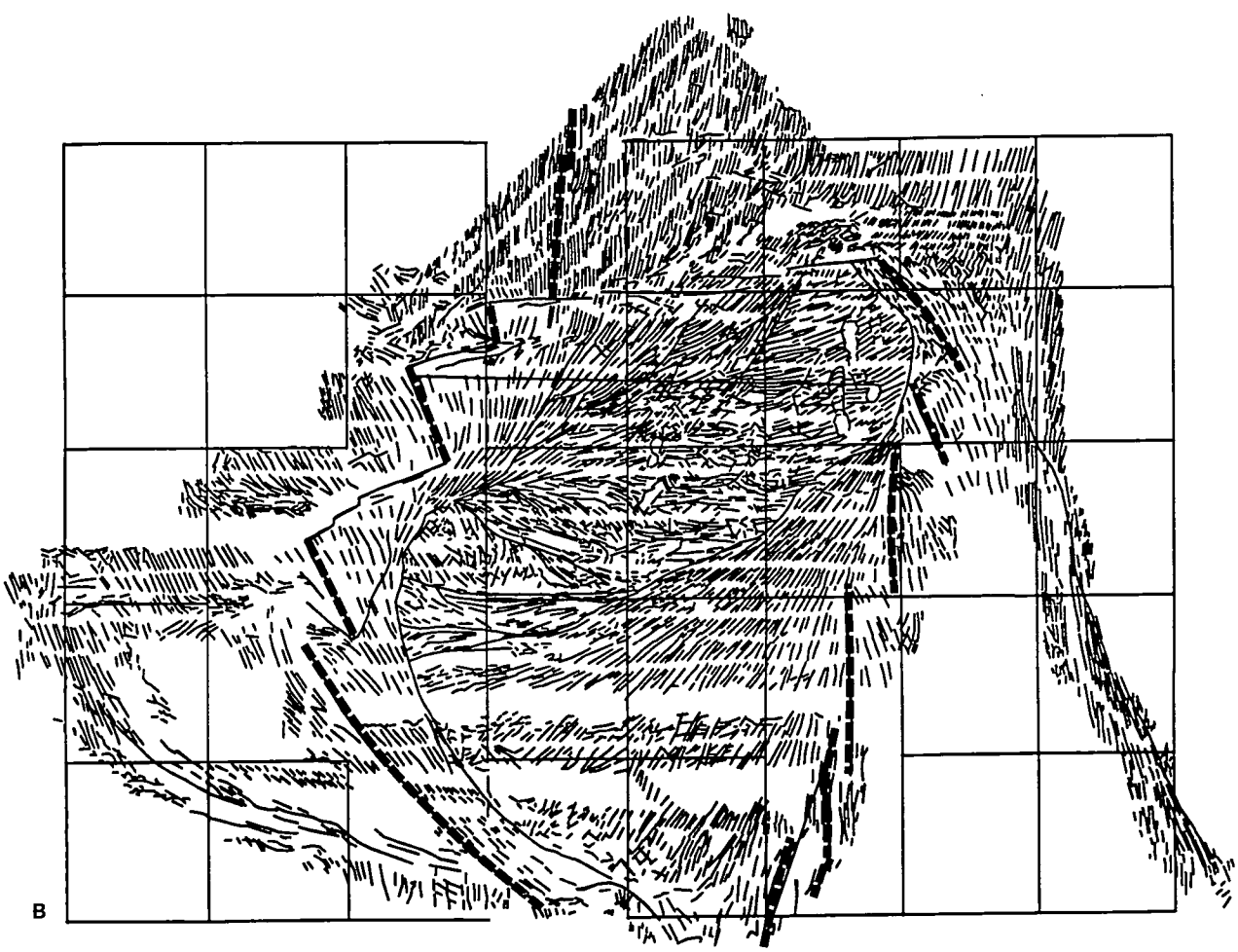

B

Figure 6.7 (a) - (c) The Easter Microplate at 0.25 Ma. During the reconstructions, the Pacific plate is held fixed, while the Nazca and Easter plates move relative to it. A gap has started to open up along the northern boundary, which indicates that shortening has taken place here. This is stippled in (a) and filled in black in (b). Overlapping segments are shown as straight lines for convenience, although they would undoubtedly have been as sinuous as those today. As the reconstructions proceed back in time, the Nz-Ea and Pa-Ea poles remain fixed with respect to the Nazca and Pacific plates, so that the Nz-Ea pole (indicated by the star) moves progressively closer to the East Pacific Rise.

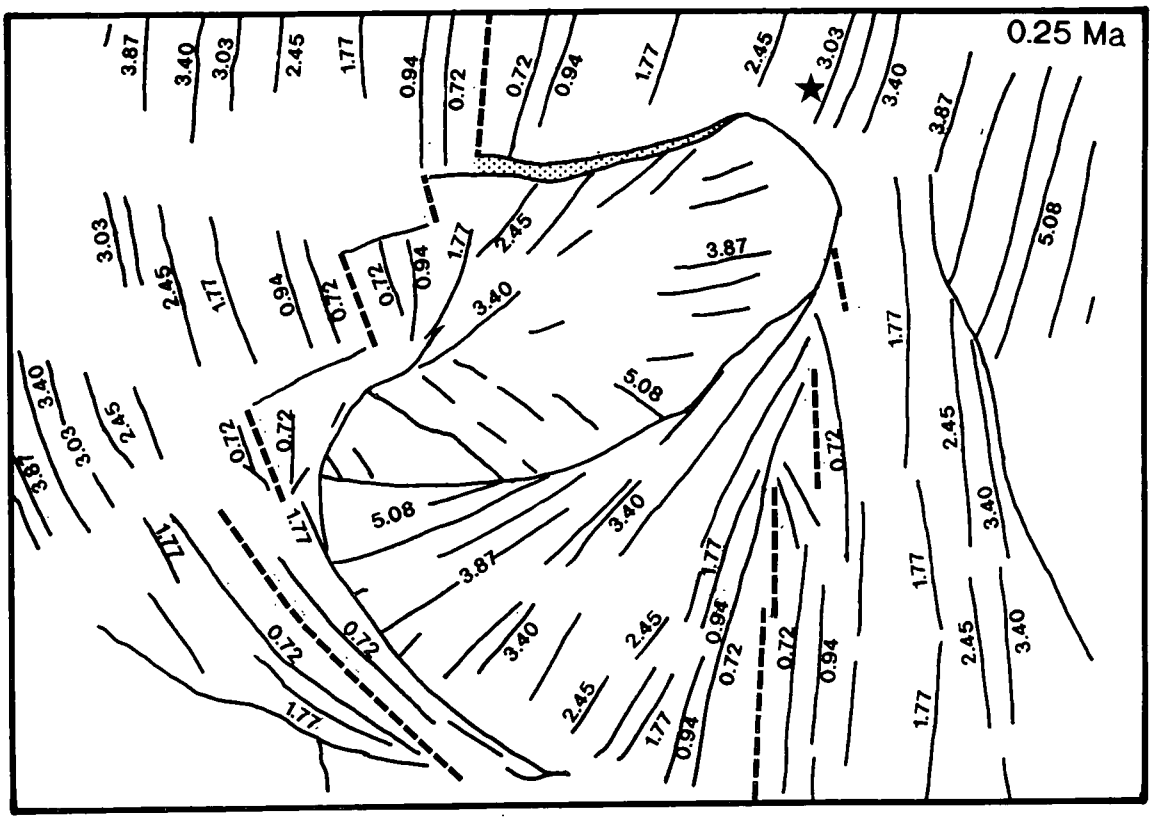

A

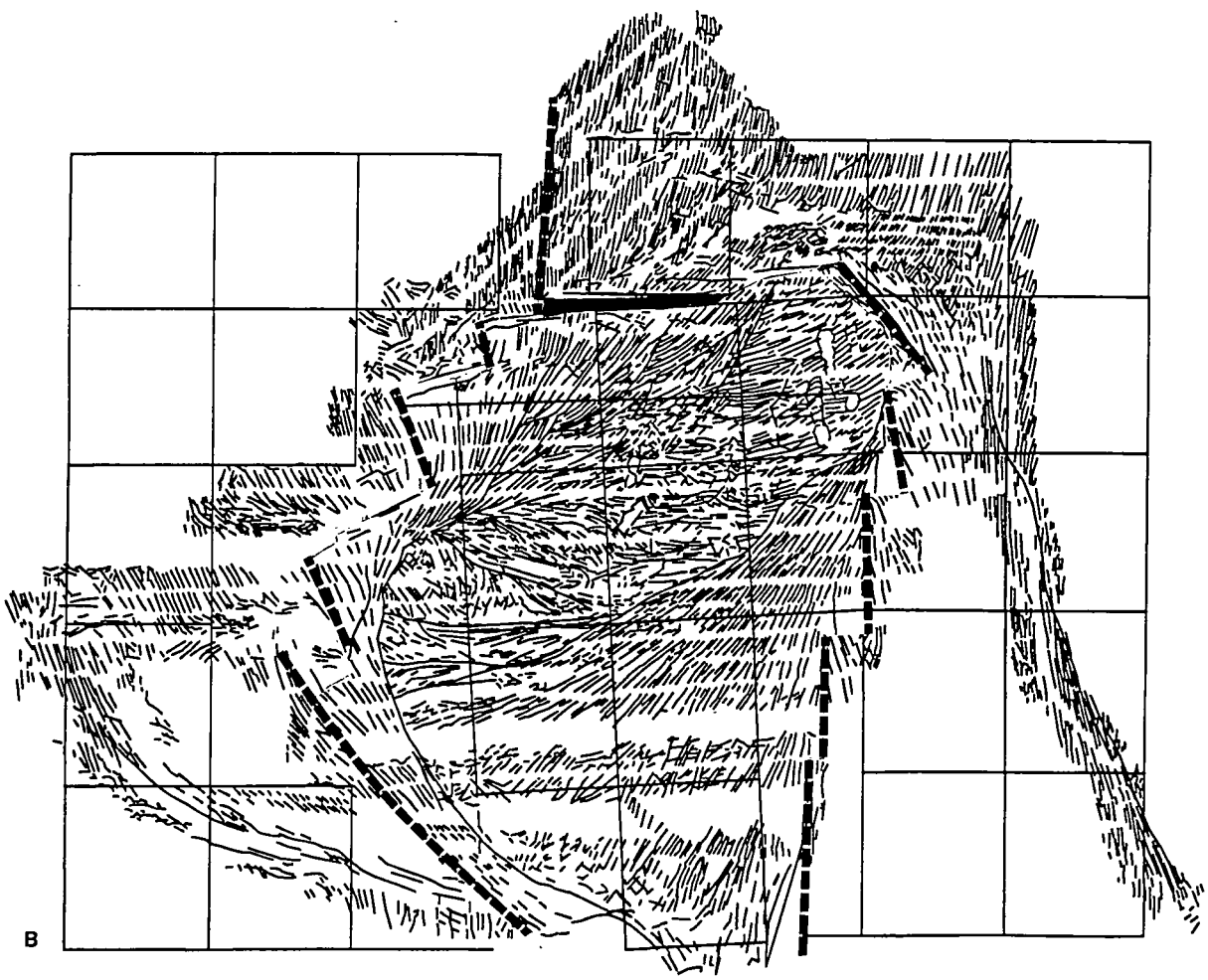

B

0.25Ma

c

Figure 6.8 (a) - (c) The Easter Microplate at 0.5 Ma. In (a), the stippled area within the increasing gap along the northern boundary shows the amount by which the gap has increased in the last 0.25 myr, while in (b) and (c) the cumulative amount is shown (in black).

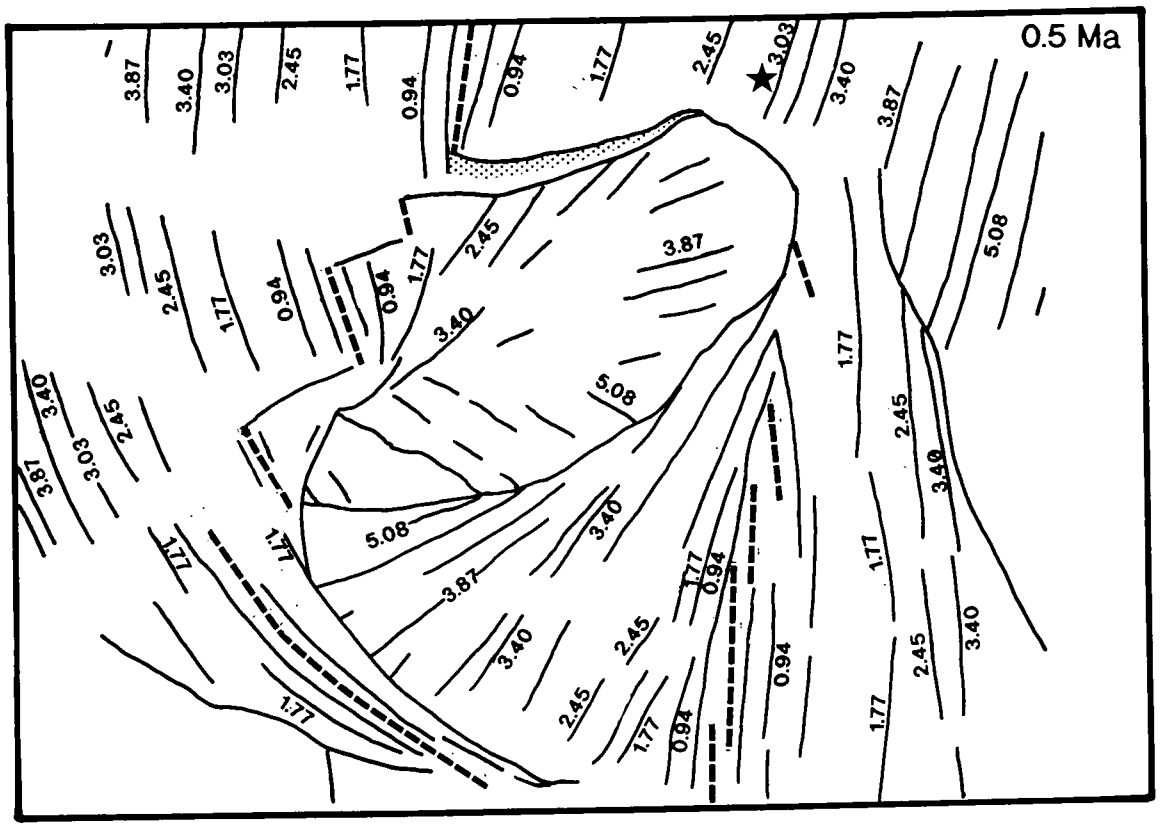
0.5 Ma
3.87
3.40
3.03
2.45
1.77
0.94
5.08
A

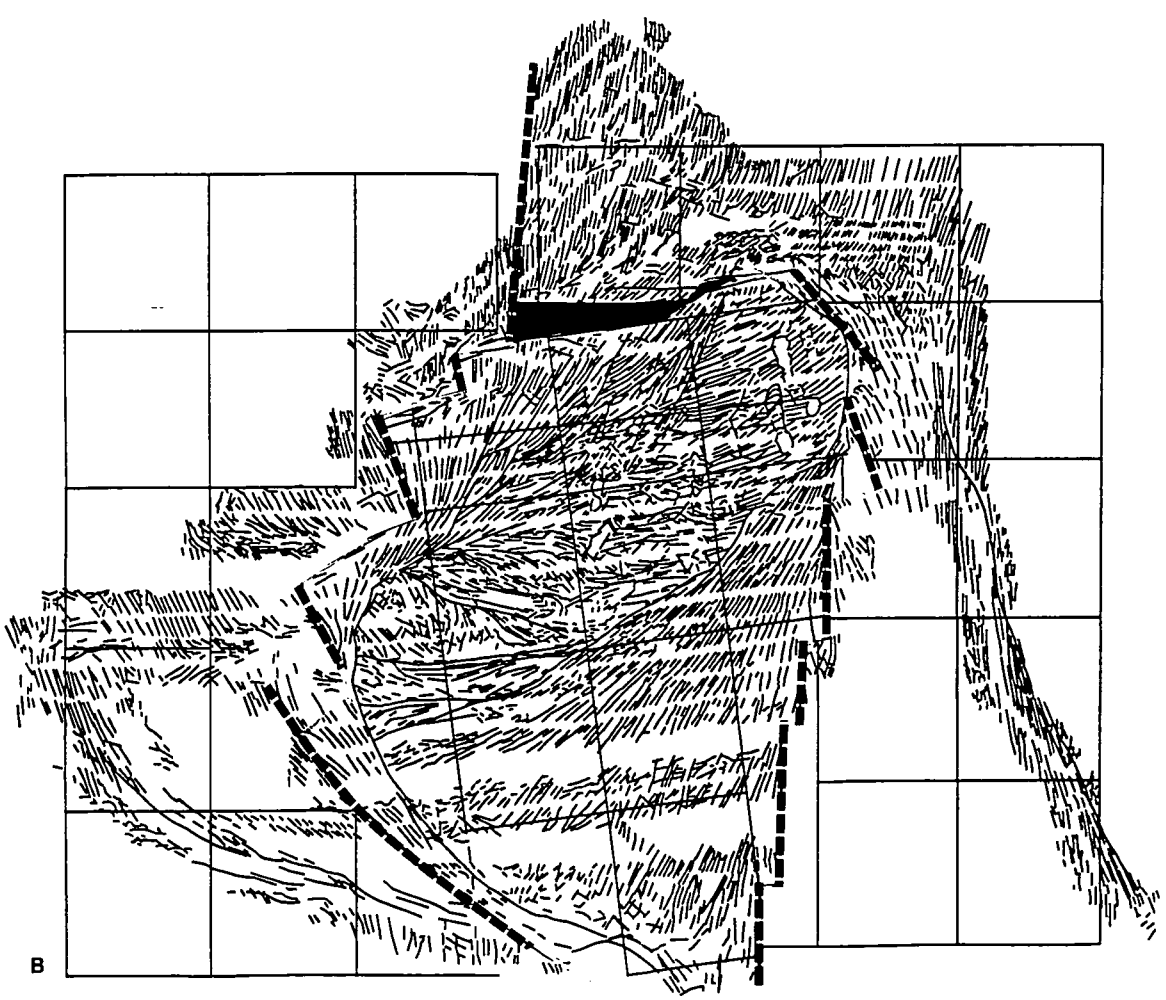
B

0.5Ma

c

Figures 6.9 - 6.18 (a) - (c) Reconstructions back in time from 0.75 Ma to 3.0 Ma, at time increments of 0.25 myr using the same conventions as for Fig. 6.7 and Fig. 6.8.

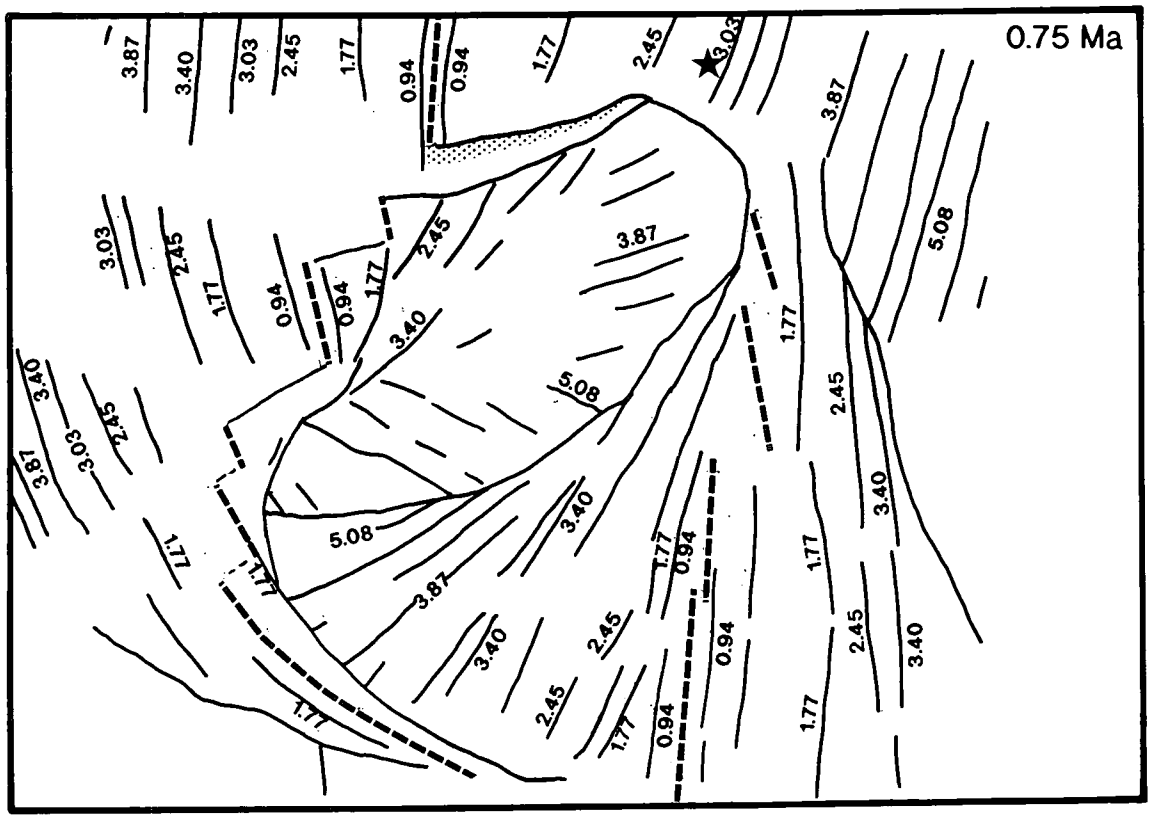

A

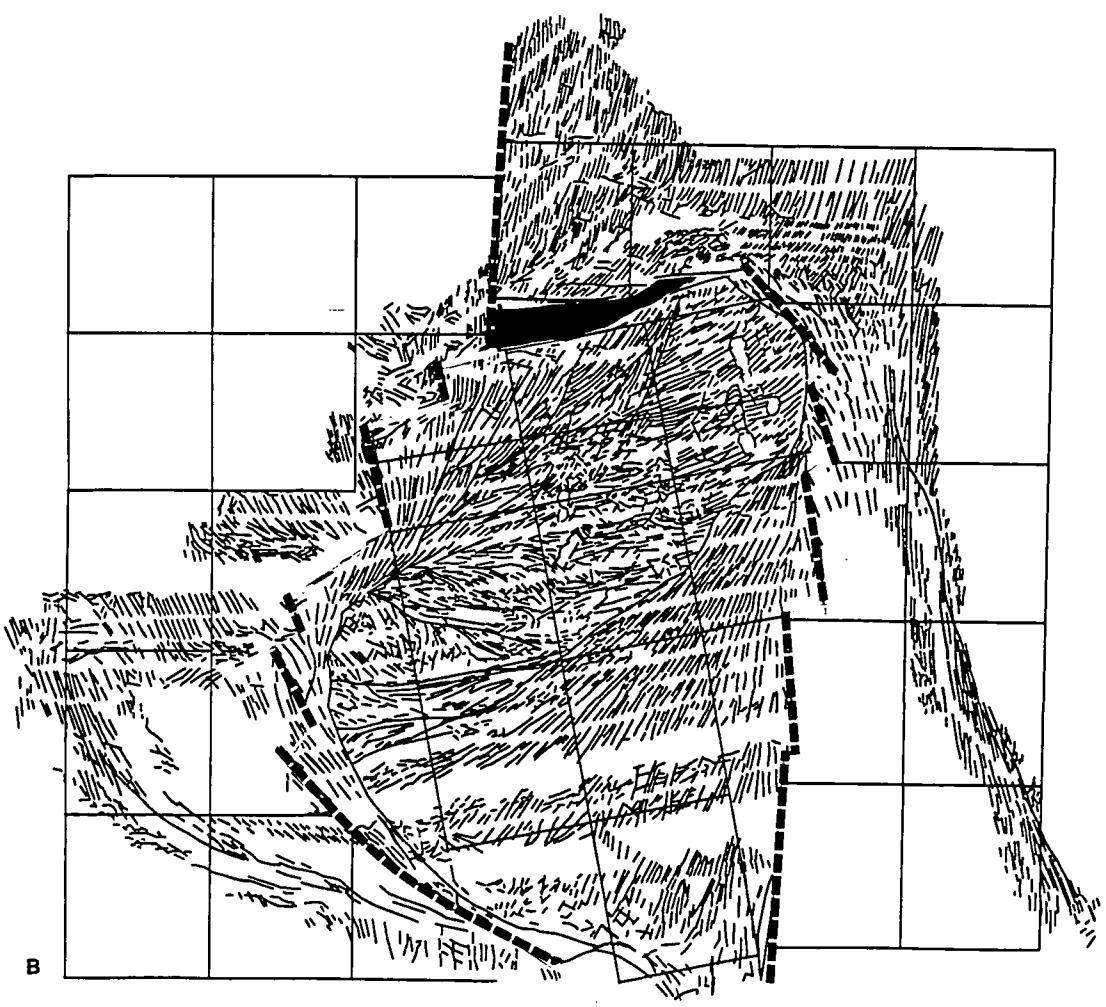

B

EASTER MICROPLATE
100 Km
110
114
116
0.75Ma
C

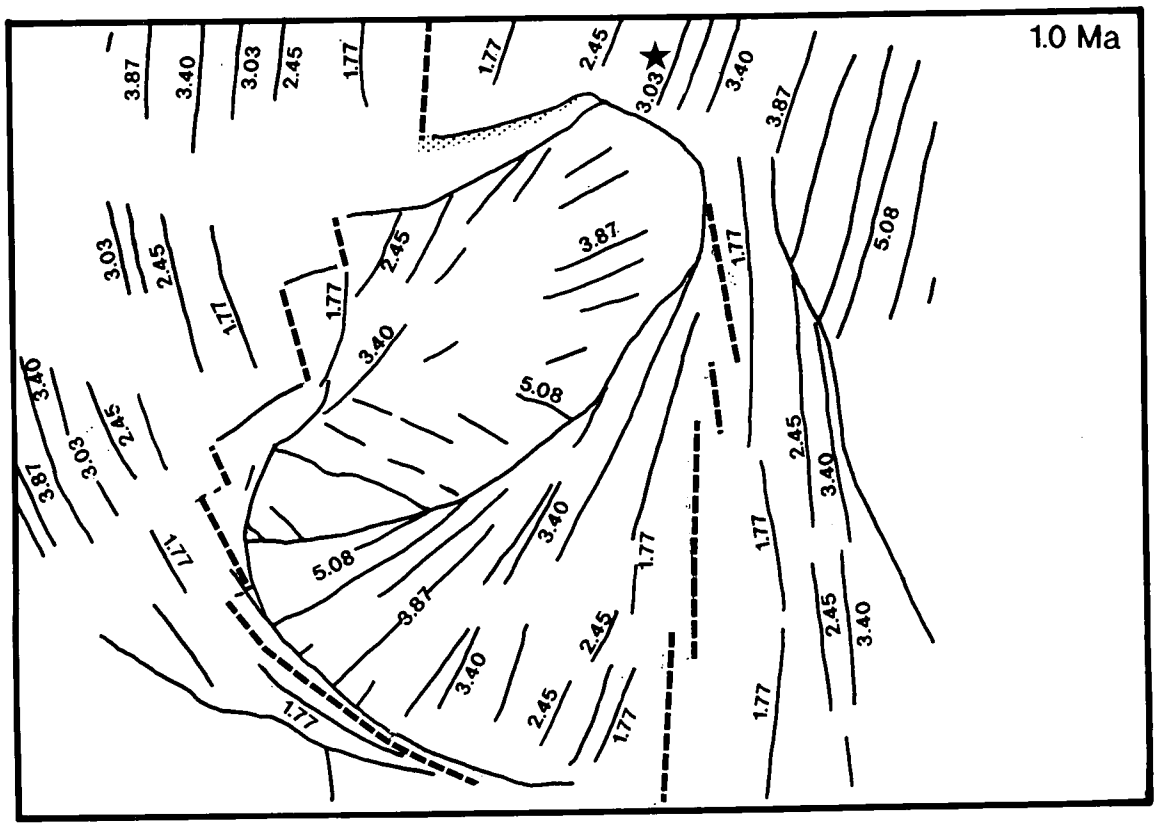

A

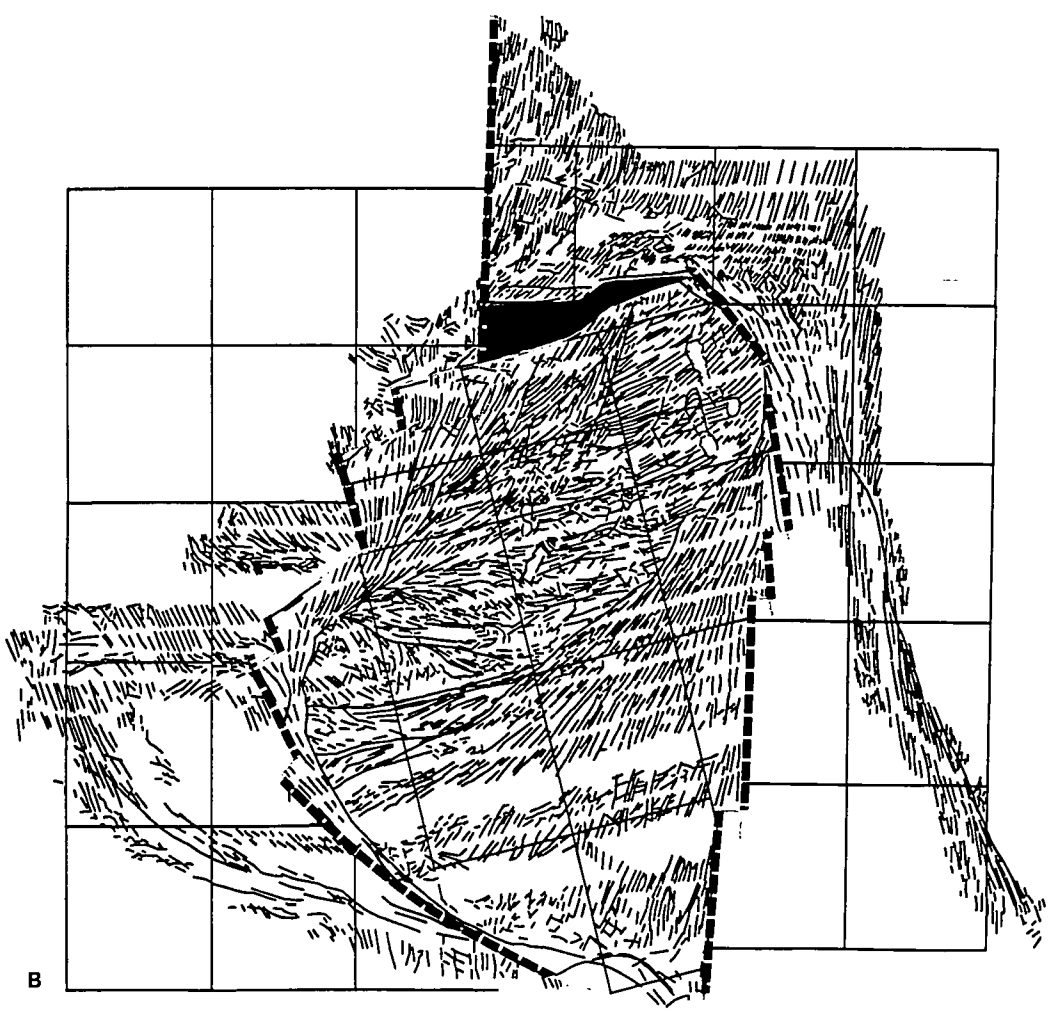

B

1.0Ma

c

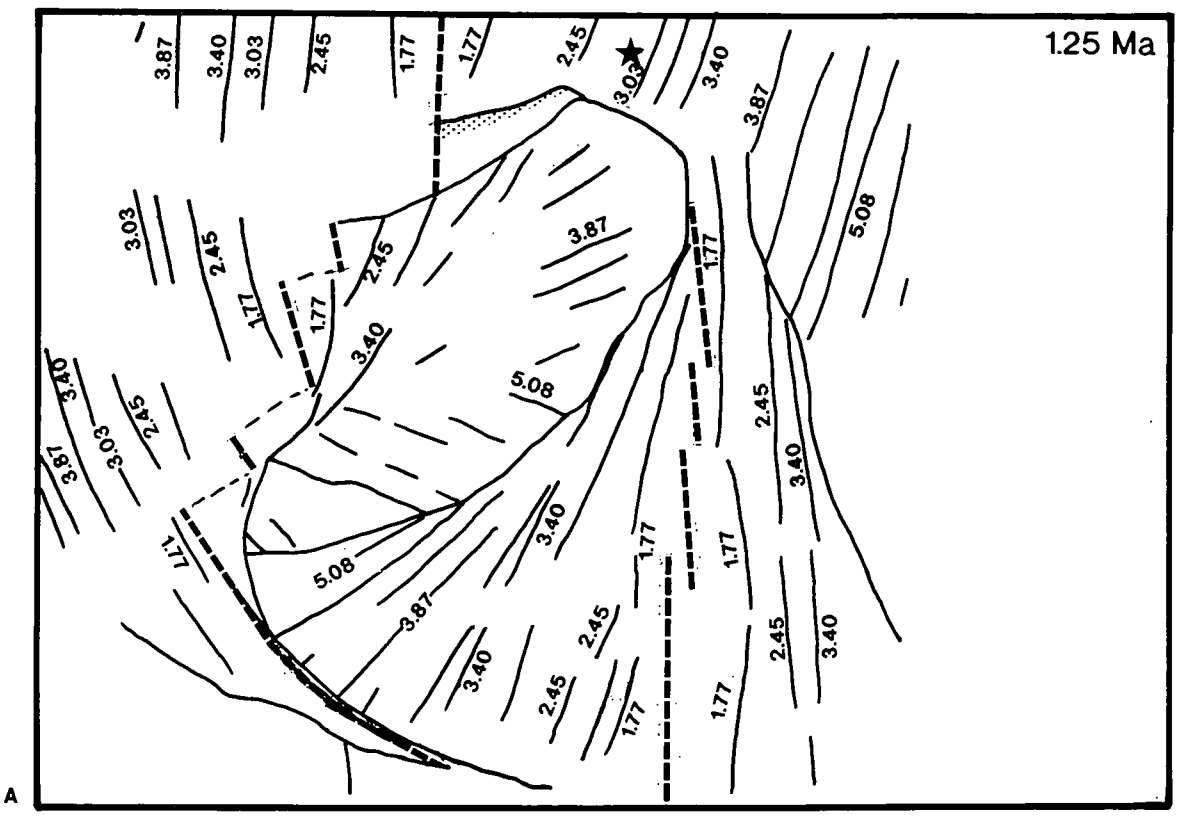

A

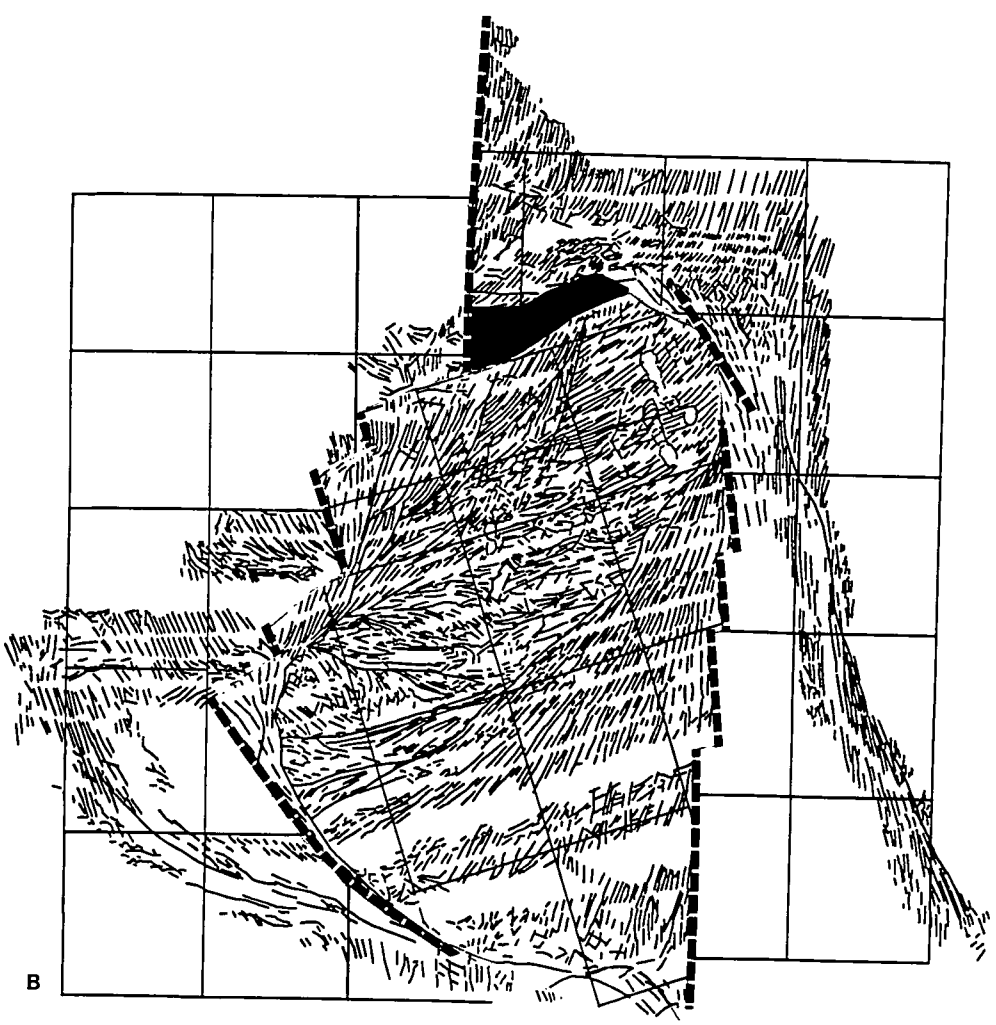

B

1.25Ma

c

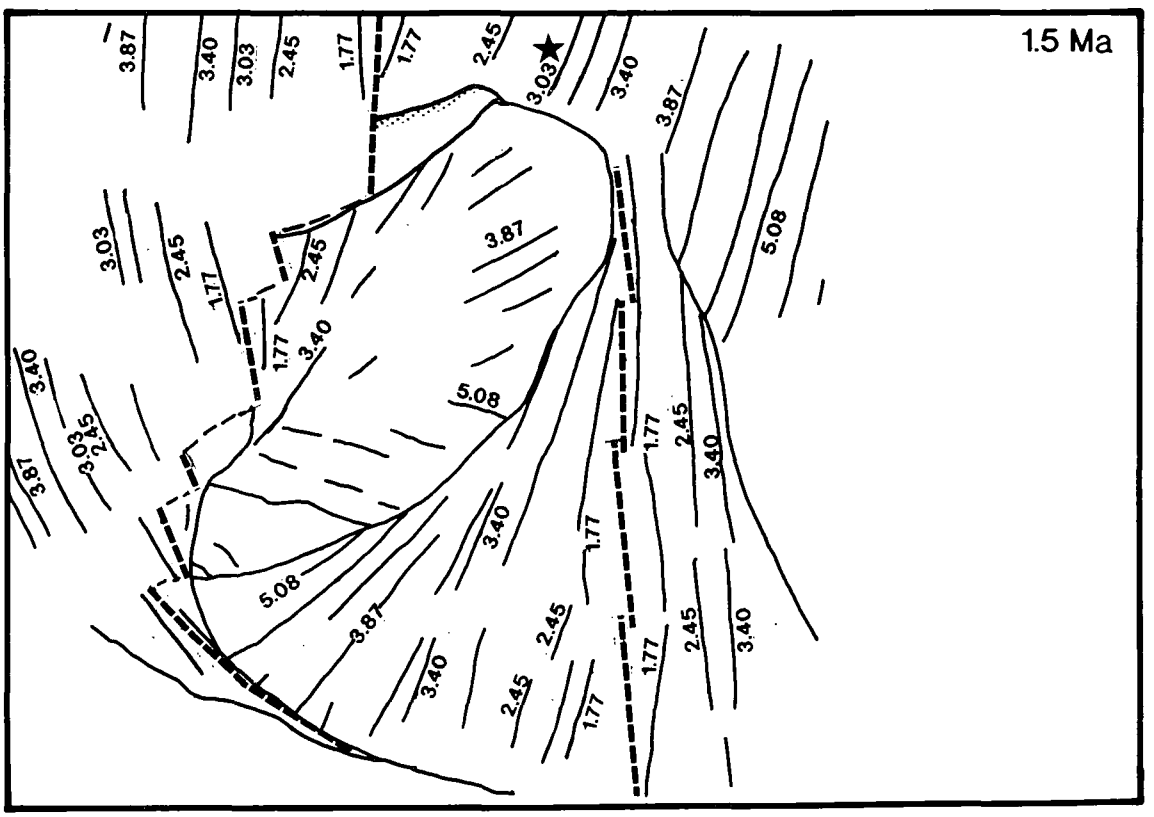

A

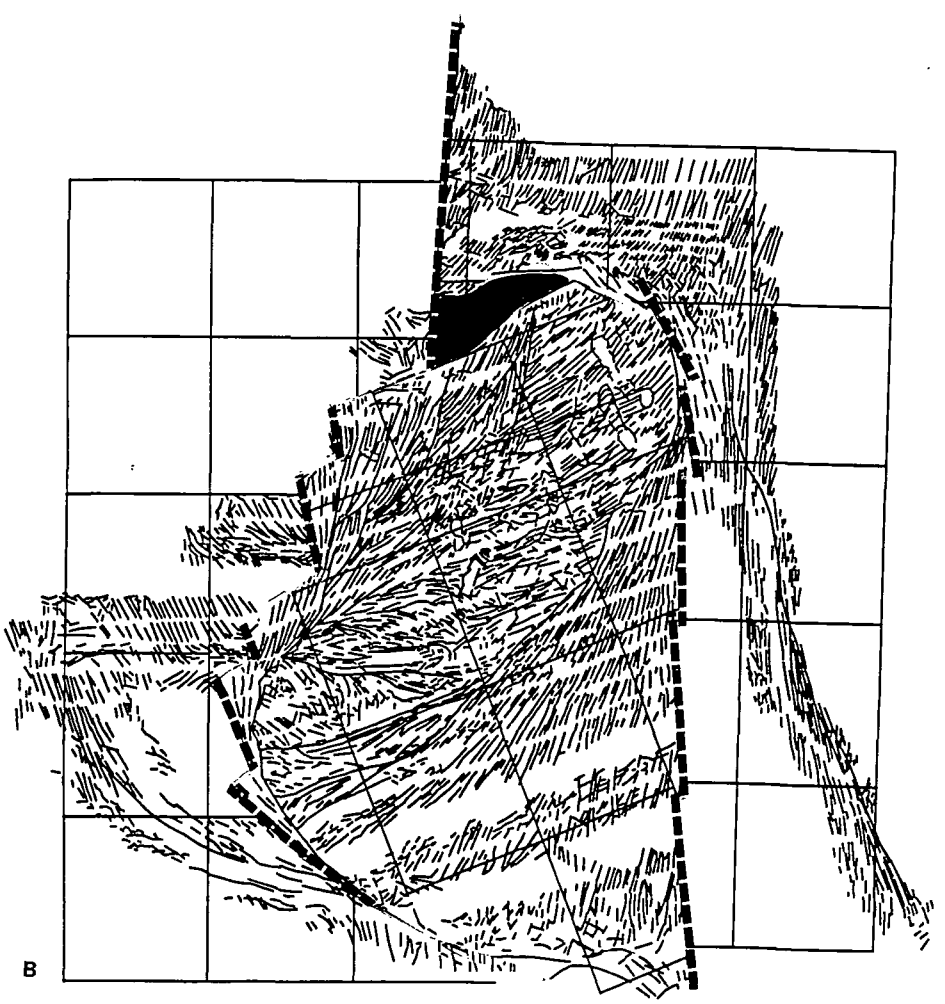

B

EASTER MICROPLATE
100 Km
N
E
110
114
116
1.5Ma
C

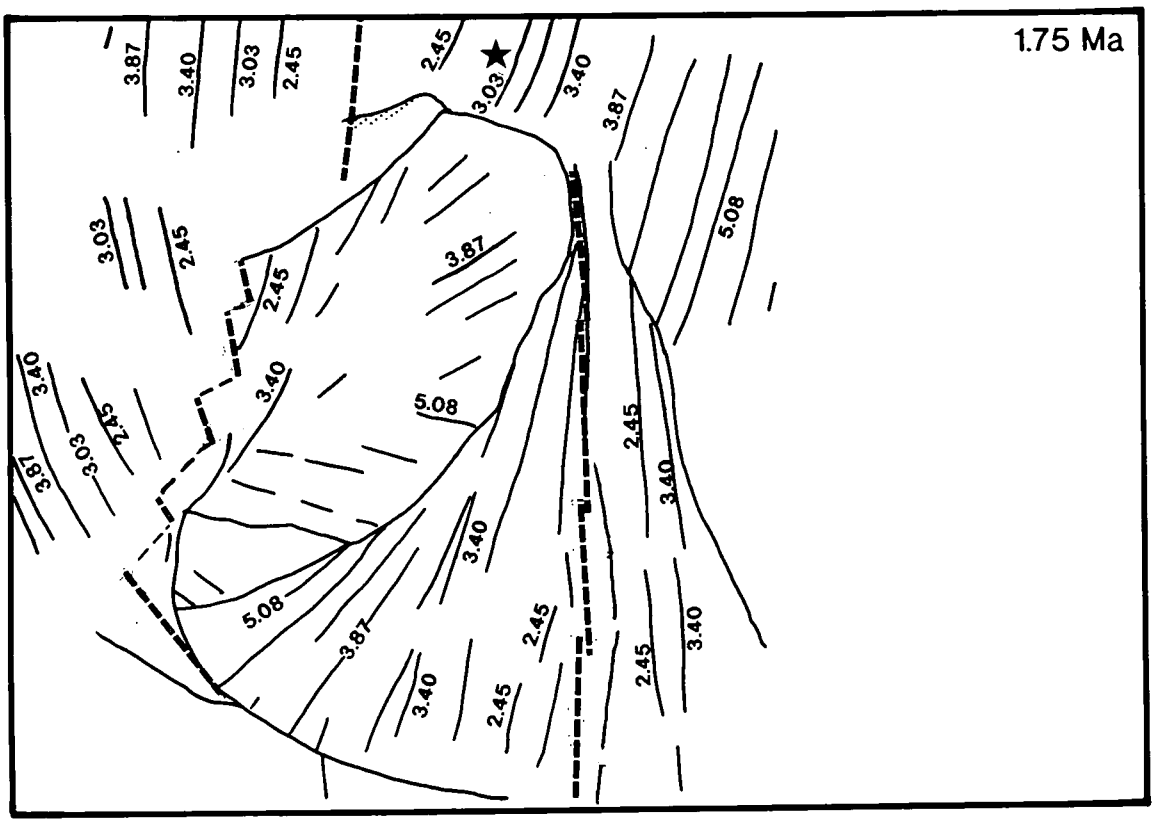

A

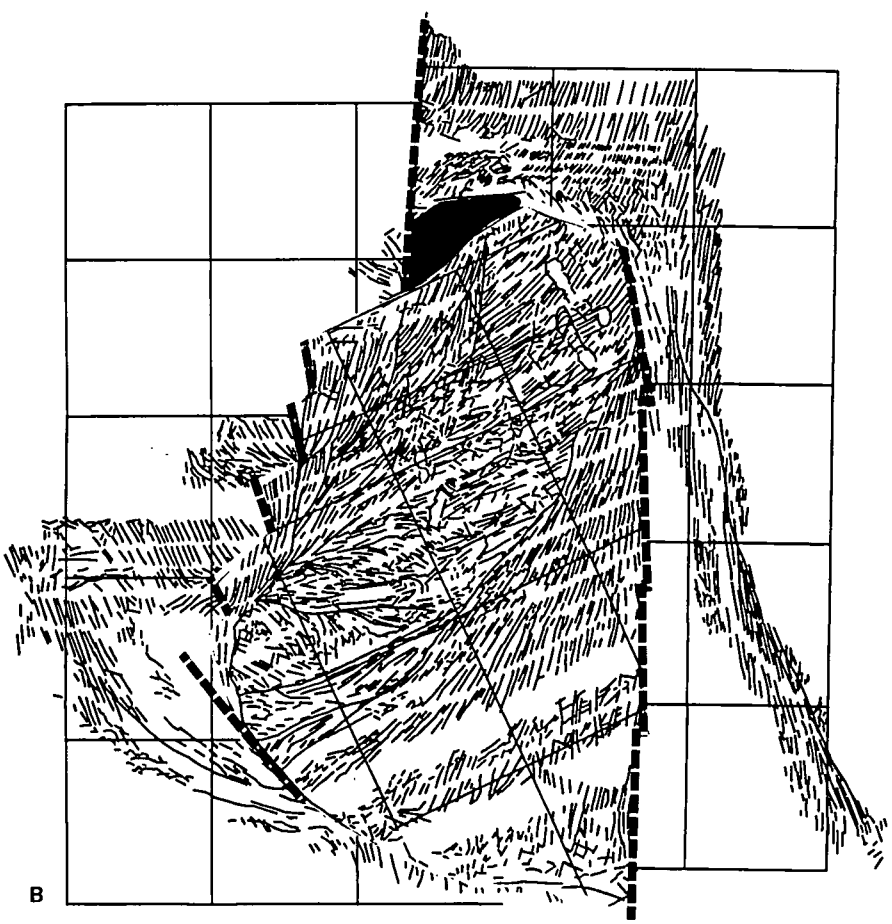

B

1.75Ma

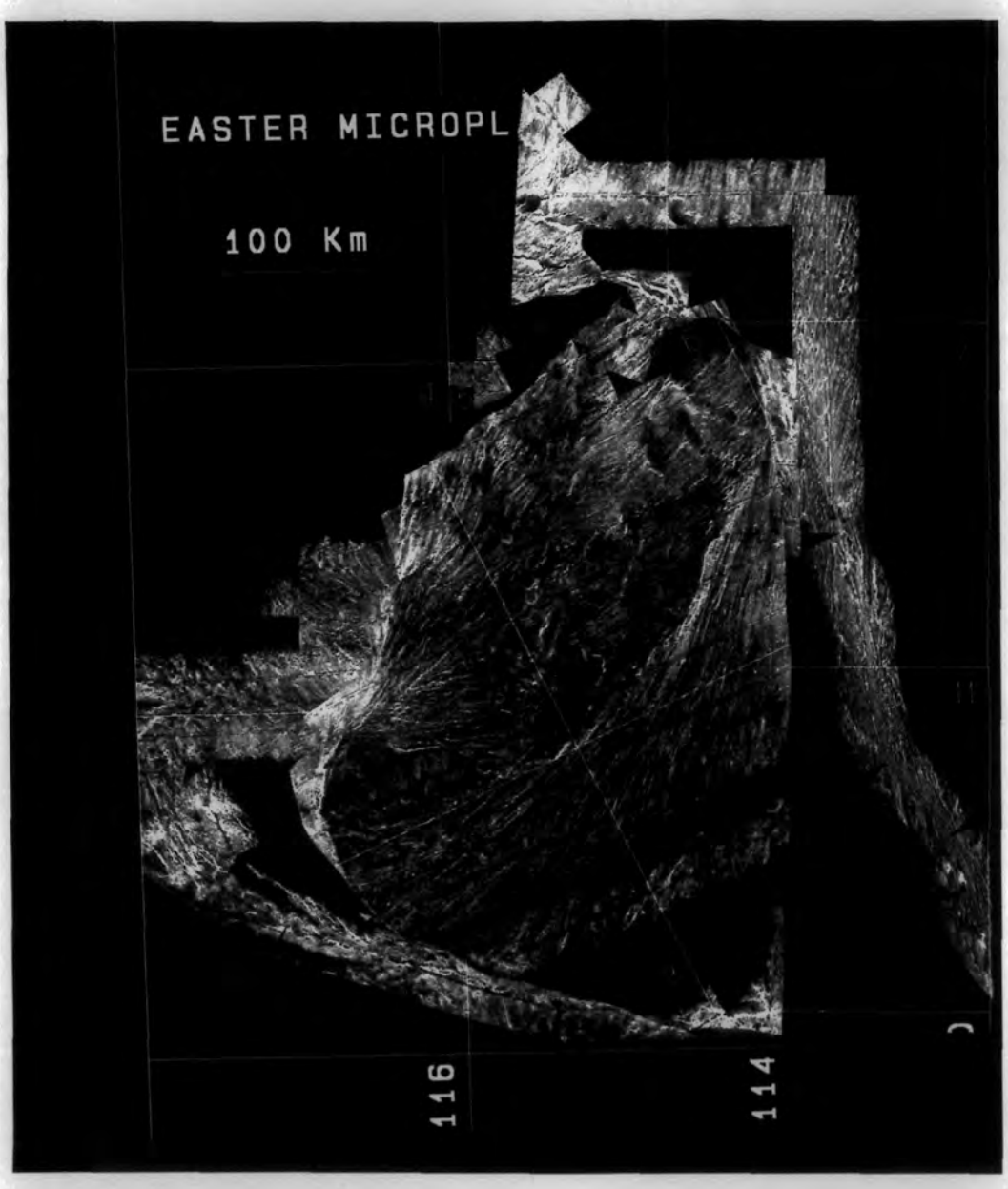

C

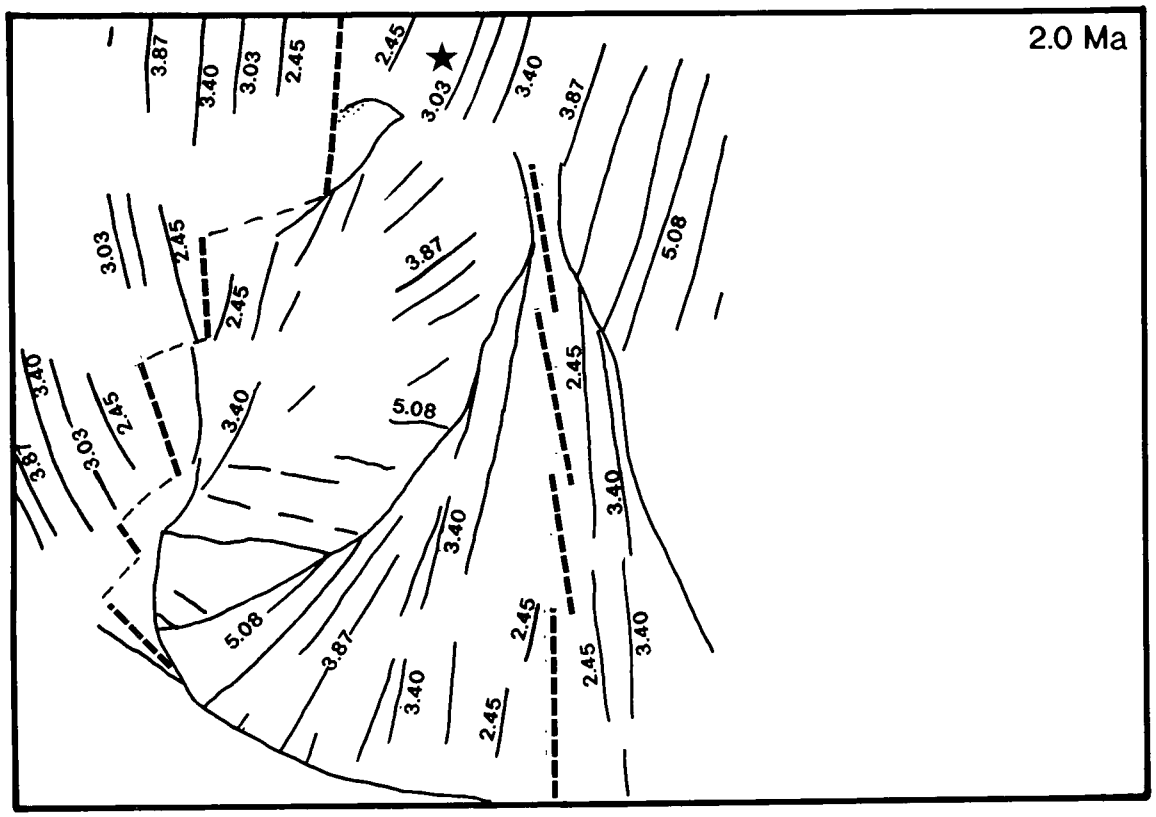

A

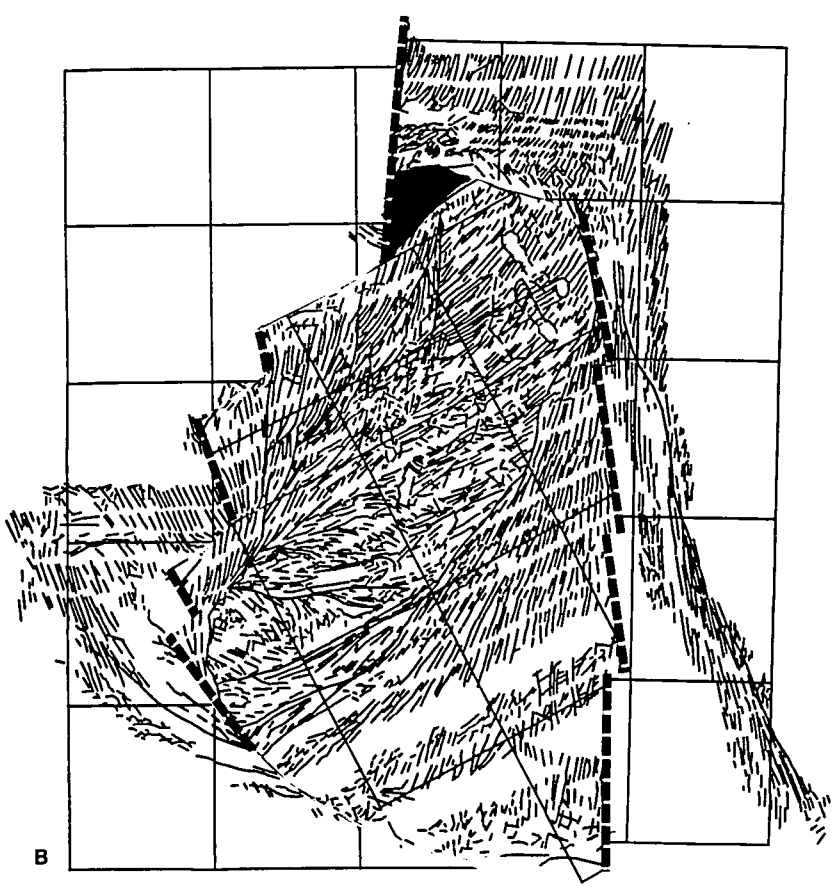

B

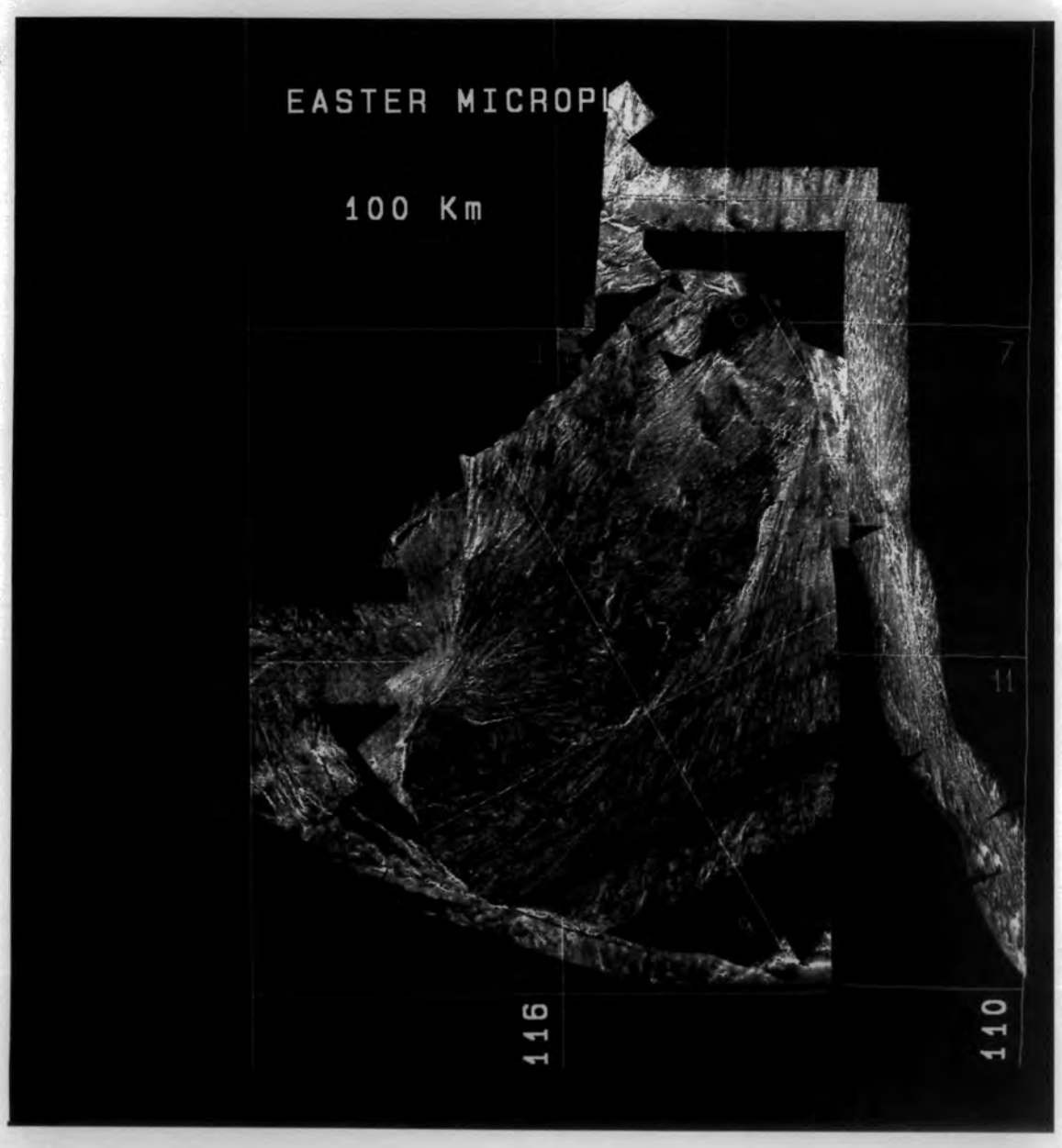
2.0Ma
EASTER MICROPL
100 Km
116
110
C

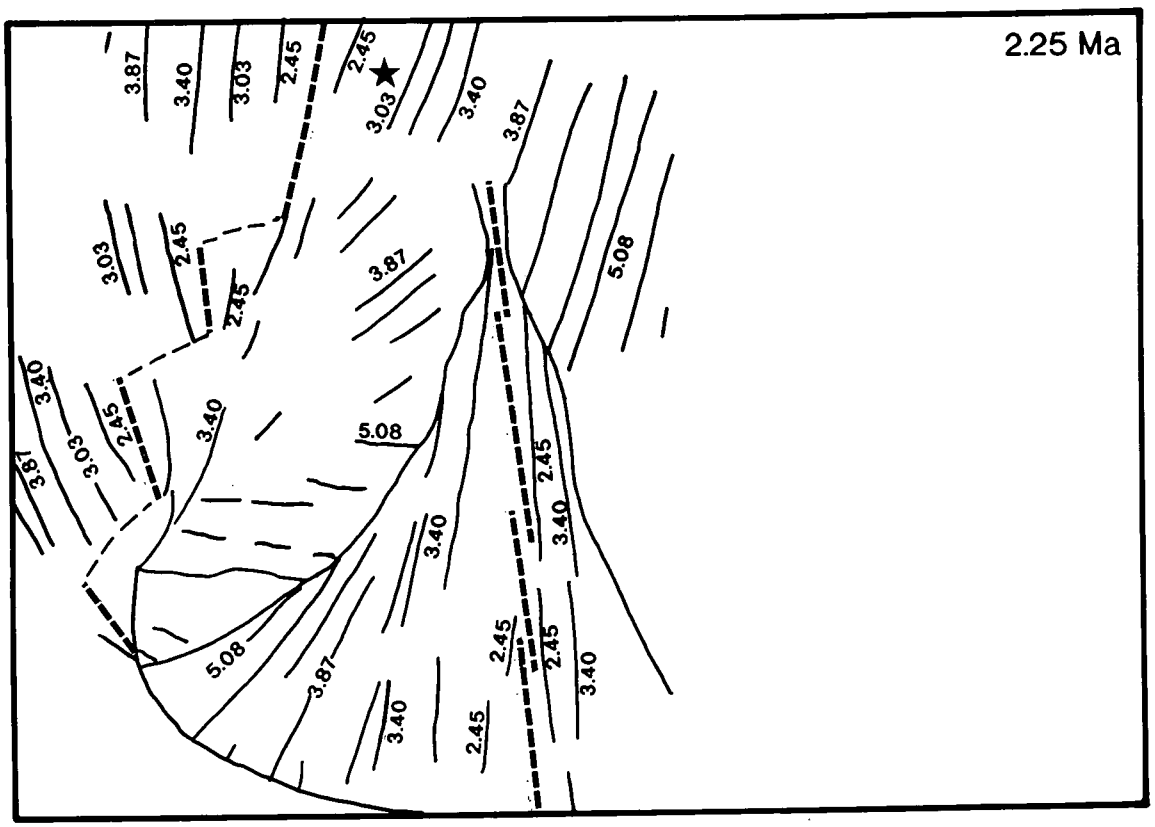
2.25 Ma
3.87
3.40
3.03
2.45
2.45
3.03
3.40
3.87
3.03
2.45
2.45
3.87
5.08
3.40
3.40
2.45
3.03
2.45
3.40
5.08
3.81
2.45
3.40
5.08
3.87
3.40
2.45
2.45
2.45
3.40
3.40
2.45

A

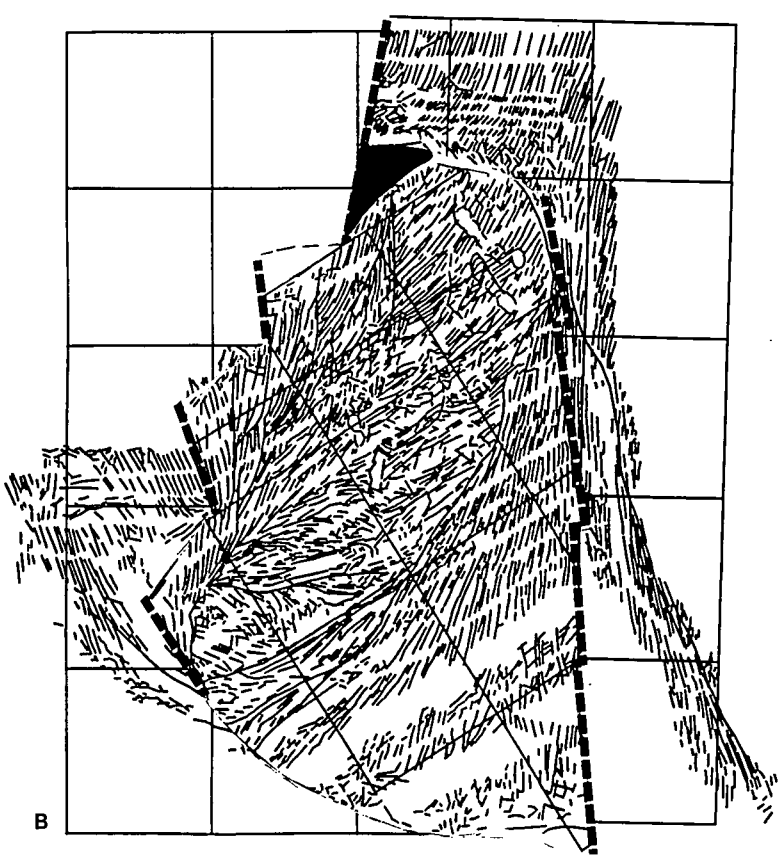

B

2.25Ma

C

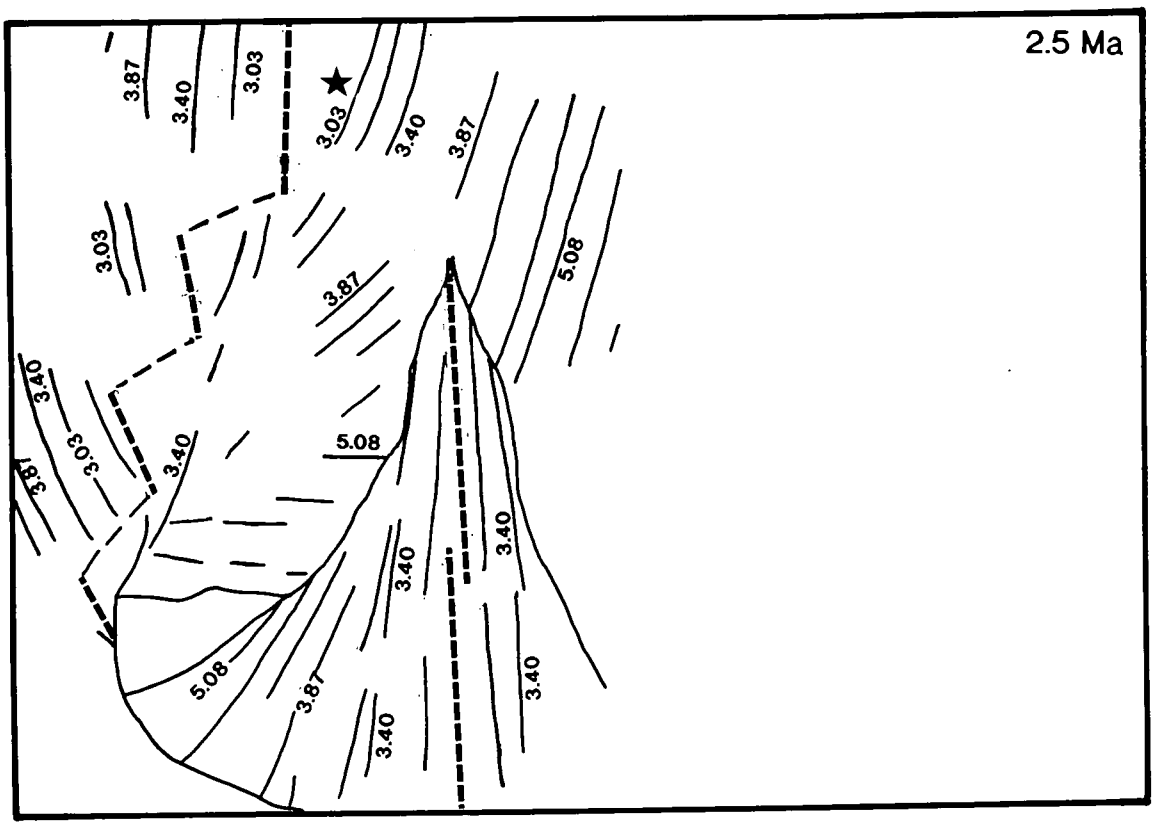
2.5 Ma
3.87
3.40
3.03
3.03
3.40
3.87
3.03
3.87
5.08
3.40
3.03
3.40
5.08
3.40
3.40
3.40
5.08
3.87
3.40

A

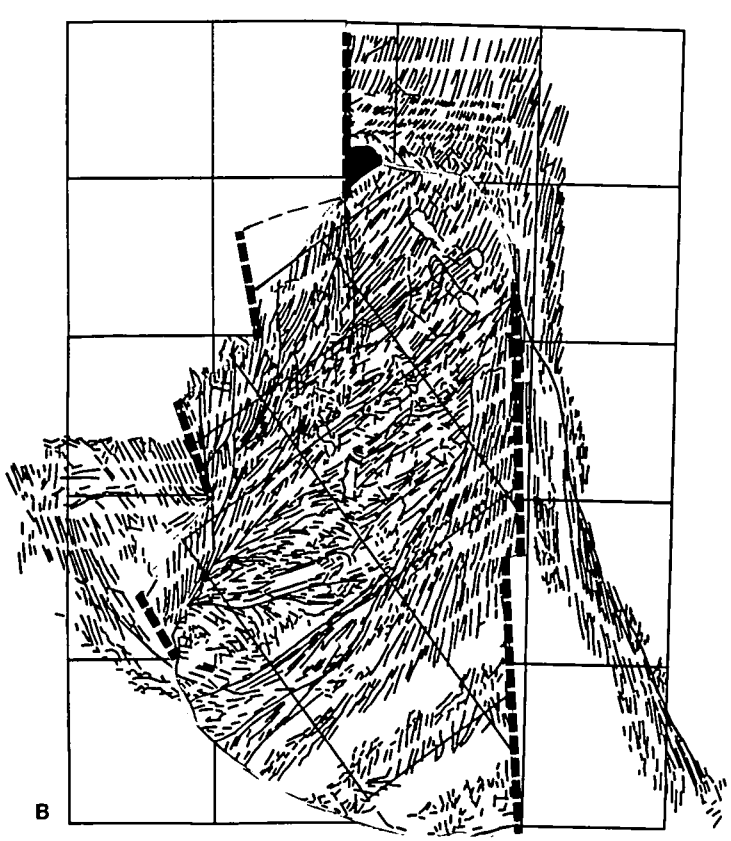

B

2.5Ma

c

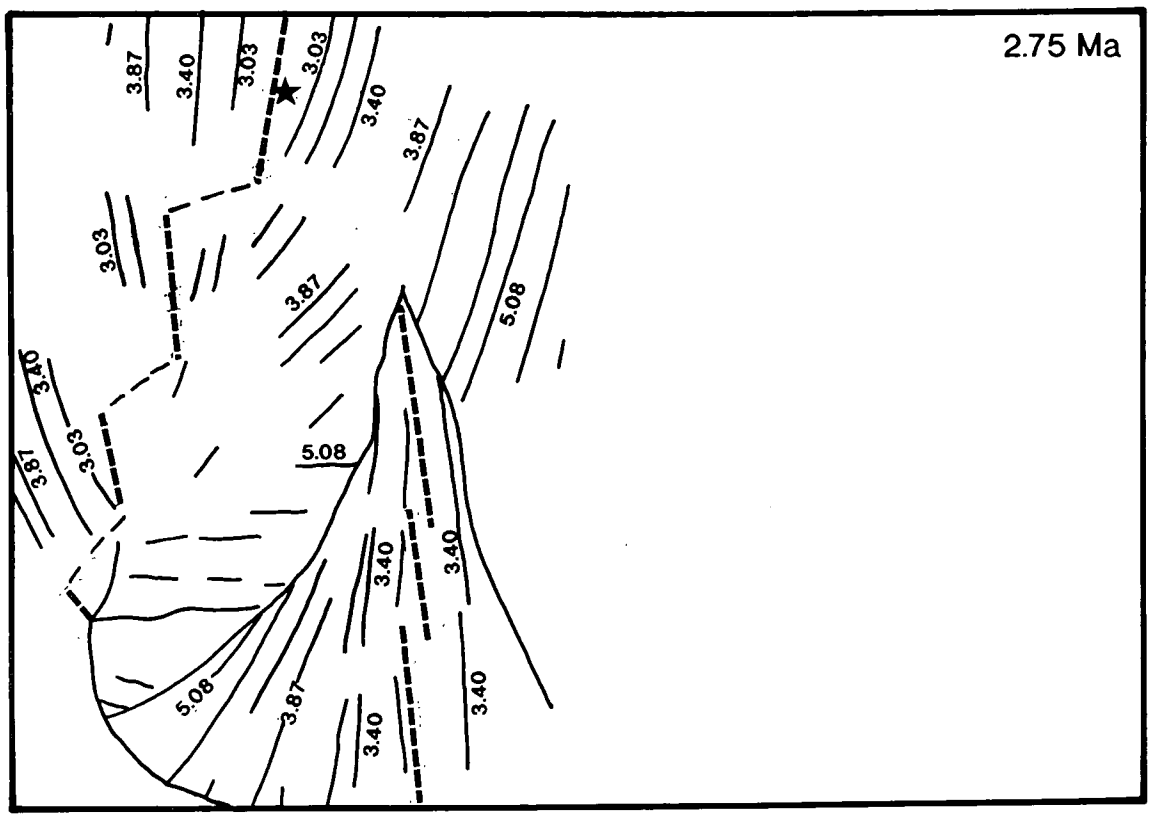
2.75 Ma
3.87
3.40
3.03
3.03
3.40
3.87
3.03
3.87
5.08
3.40
3.03
3.87
5.08
3.40
3.40
5.08
3.87
3.40
3.40

A

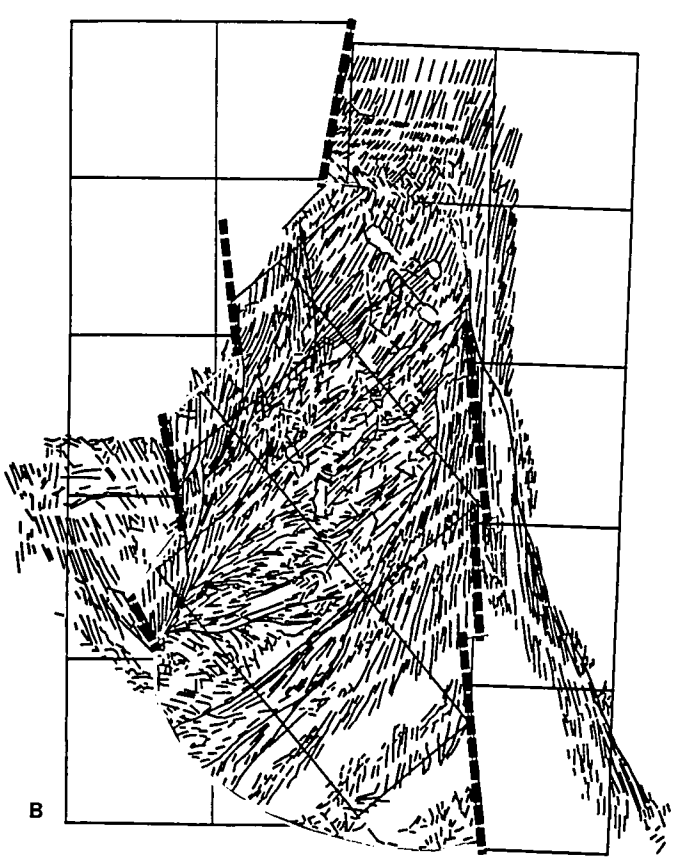

B

2.75Ma

c

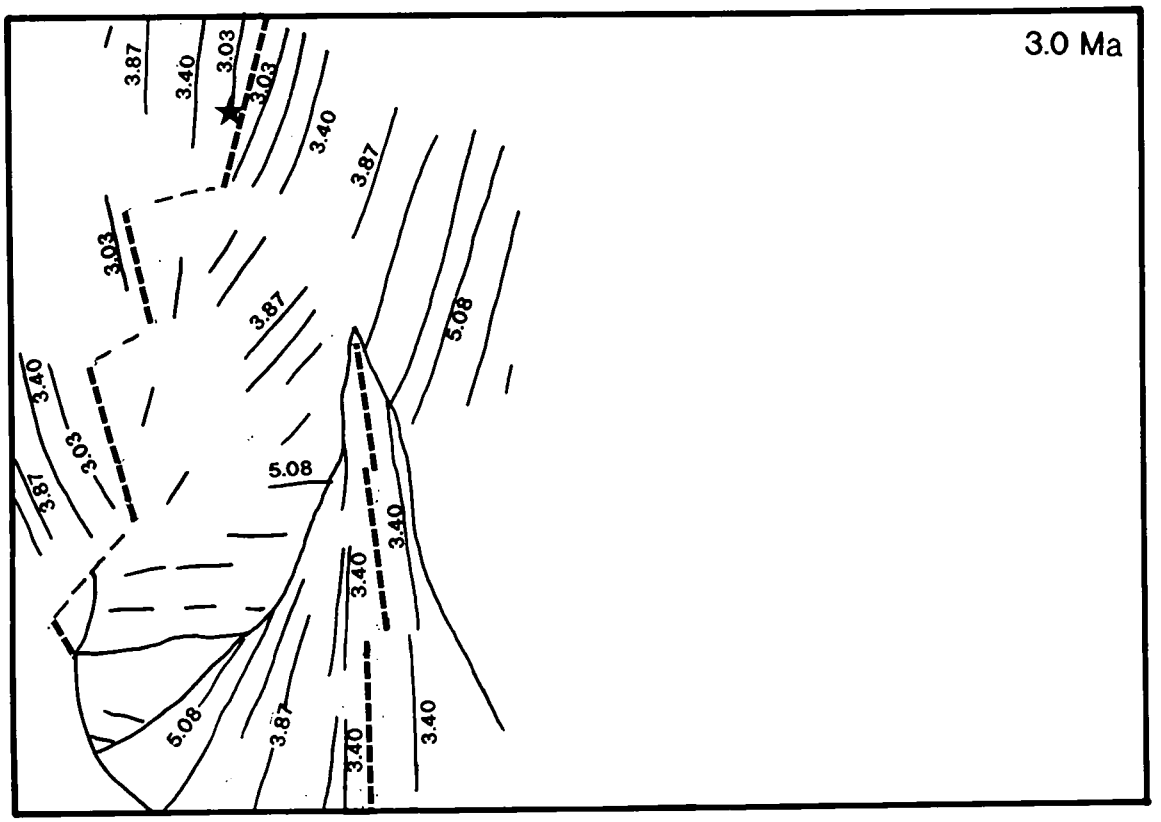
3.0 Ma
3.87
3.40
3.03
3.03
3.40
3.87
3.03
3.87
5.08
3.40
3.03
3.87
5.08
3.40
3.40
3.40
5.08
3.87
3.40
3.40

A

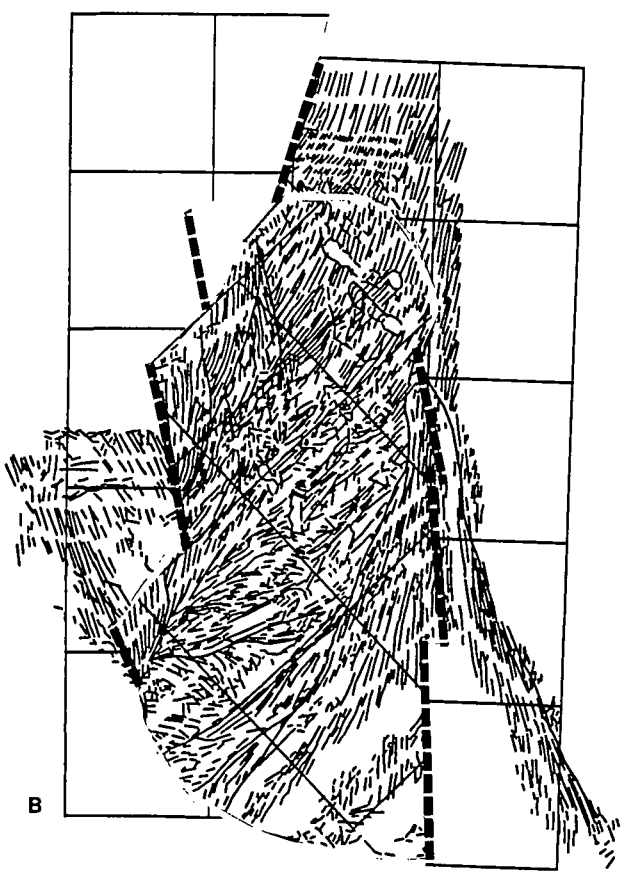

B

3.0Ma

C

its southward propagation. Both the propagator and the pre-existing segment (doomed rift) are assumed to be propagating southwards, away from the Terevaka transform, and towards the Pa-Ea pole. It seems likely that these small propagators, and others in the past, have allowed the Southwest Rift to accrete in an asymmetric manner over time, i.e. by transferring fabric formed on the Easter plate to the Pacific plate. Evidence for the existence of a series of propagators should be found in the tectonic fabric to the west of the present-day Southwest Rift, but unfortunately there is no GLORIA swath in this region. This type of transfer is also observed on the East Rift (Hey at al., 1985; Searle et al., 1989; Naar & Hey, 1989). Again the gap along the northern boundary has increased by the amount shown in Fig. 6.9a.

0.75-1.0 Ma. The Jaramillo anomaly (0.94 Ma) has now disappeared (Fig. 6.10a-c), and there is little control on the positioning of the spreading axes. The microplate interior has been rotated some 15° in an anticlockwise direction since the present-day, and the two major pseudofaults of the East Rift still appear to match each other. The maximum amount of shortening predicted along the northern boundary at 1.0 Ma for a 0.25 myr period is 7 km, i.e. half the amount at the present-day.

1.0-1.25 Ma The Southwest Rift tip has closed up, and started to retreat northwestwards (Fig. 6.11a-c). Presumably as it retreats back in time, the left-stepping transform between the Pacific and Easter plates grows. Near 25°S on the West Rift, the additional short spreading centre previously mentioned, and seen if Fig. 6.9 and Fig. 6.10, is no longer shown. Lineaments trending roughly northeast-southwest near 25°S, 117°W are believed to be remains of a fracture zone, and so a transform fault is drawn in Fig. 6.11 linking the by now very short propagator with the Southwest Rift.

*1.25-1.5 Ma.*Extension of pre-existing Nazca lithosphere appears to be small, and the small amount of dextral strike-slip movement between the Nazca and Easter plates (Fig. 6.12a-c) is taken up in the Pito Deep region (Chapter 2, Fig. 2.1). In the absence of any through-going transform fault traces or fracture zones, this movement is likely to be accommodated by block rotation or "bookshelf" faulting in the manner described by Kleinrock and Hey (1989) for the 95.5°W propagator, as the material is transferred from the Nazca to the Easter plate. Near 24.5°S, 116°W, to the west of the tip of one of the spreading segments on the West Rift, is another area of oblique lineaments, which indicate that the southward propagation of this segment ceased at around this time.

1.5-1.75 Ma. The West Rift has now been further sub-divided to allow a new segment to exist to the west of the southward propagating segment mentioned above (Fig. 6.13a-c). This new segment is connected to the southward propagator by either a rigid transform, which may have been slightly obscured in the propagation process, or by a

rotated shear zone, as found south of the Terevaka transform or on the East Rift. The model suggests that to the west of these segments more northeast-southwest trending lineaments exist, indicative of an earlier short-offset transform fault. The tip of the Southwest Rift has retreated further. At 1.75 Ma, anomaly 2 should just have started to form (1.67-1.87). The "picks" used here are 1.77 Ma (i.e. the centre of the anomaly), but on the East Rift the anomaly is still clearly seen, which may indicate that an older subchron (such as 2r-1 at 2.02 Ma) has been picked instead, or that the Ea-Nz Euler vector is wrong.

1.75-2.0 Ma. At 2.0 Ma, the southward propagator referred to above has not yet formed, and so the West and Southwest Rifts consist of four spreading segments again (Fig. 6.14a-c). The Southwest Rift has retreated still further, but unfortunately there is no GLORIA data from the Pacific plate to the south which might shed light on the proposed pre-existing transform fault (Engeln & Stein, 1984) that is supposed to have opened up. The north end of the East Rift is beginning to close up into a thin bottle-neck shape.

2.0-2.25 Ma. The maximum predicted total closure now between the Nazca and Easter plates along the northern boundary is approximately 4 km in 0.25 myr, and so the gap produced during the reconstructions is no longer shown in the upper magnetics diagrams (Fig. 6.15a-c). The West and Southwest Rifts are drawn as having only three segments in the absence of any data indicating a need for further segmentation. The East Rift major pseudofaults continue to remain a well-matched pair. At this time, the total rotation of the interior of the microplate since 0.0 Ma is about 33°. Spreading fabric originally formed on the Nazca plate, and then transferred to the microplate interior, is now beginning to match up with the concurrently formed fabric that has remained on the Nazca plate.

2.25-2.5 Ma. The tip of the East Rift has now started to retreat southwards, and the major inner and outer pseudofaults associated with it are shown to meet at a point (Fig. 6.16a-c). Not much remains of the scarps which define the Southwest Rift (Chapter 2, Fig. 2.1), which has just started to form at this time. The anomaly pick for the start of chron 2A (i.e. 2.48 Ma) has just disappeared, and slow strike-slip movement between the Nazca and Easter plates along the northern boundary appears to be continuing.

2.5-2.75 Ma. Few GLORIA data now remain on the Pacific plate to the west of the West Rift, but where they do, a good match is found between the rotated lineaments of the microplate interior and the tectonic fabric on the Pacific plate (Fig. 6.17a-c). There is no gap at all along the northern boundary of the microplate. This indicates that there has been no compression of lithosphere prior to this time, as expected, since the Nz-Ea pole is close to the East Pacific Rise.

2.75-3.0 Ma. The interior of the Easter Microplate has now been rotated some 45°, and the contemporaneous basement fabric of the northeast of the interior now appears to have the same trend as the material on the Nazca plate, and thus is assumed to be of the same age (i.e the end of anomaly 2A time) (Fig. 6.18a-c). The tip of the East Rift has retreated south of 24°S (in the Pacific reference frame) and although the shape of the major pseudofaults that remain do not appear entirely identical, the match is acceptable. So few GLORIA data are now available on the Pacific plate, that the configuration of the West Rift is poorly constrained.

3.0-5.0 Ma. Reconstructions back in time beyond 3.0 Ma are only carried out using the magnetic data, since the few GLORIA data that remain on the Pacific and Nazca plates provide no extra constraints (Fig. 6.19a-h). The tip of the East Rift continues to retreat southwards as the East Rift closes up and presumably the West Rift becomes more north-south oriented back in time, while the transform offsets between the individual segments become shorter. The East Rift pseudofaults remain a good match right up to the last, until they finally disappear at 5.25 Ma.

6.5 Discussion

6.5.1 Microplate Rotation

Throughout the rigid reconstructions of the microplate, the rotation rates have been kept the same. Though this implies that spreading rates on the East and West Rifts remain constant despite frequent ridge jumps and reorientations, it provides a good fit for the magnetic data. Naar and Hey (1991) invoked a slowing down of the microplate rotation rate from 20 to 15°/myr, which intuitively makes sense as the microplate grows in size (see Schouten et al., 1991), yet the present data set used here suggests that the rotation rate has remained constant at 15°/myr since 5.25 Ma. Schouten et al.'s (1991) "roller-bearing" model (see Chapter 1 and below) invokes a somewhat faster average rotation rate of around 18°/myr during their proposed two-stage development of the microplate.

The shape of the microplate during these reconstructions remains roughly equant (see Fig. 6.20) as growth occurs to the east, west and north, maintaining a quasi-triangular or shield shaped configuration throughout. As the microplate rotates, it may initially cause the transforms on the West Rift to re-orient in a clockwise manner (Engeln & Stein, 1984; Engeln et al., 1988), as is possibly indicated by a recent northward ridge jump at the western ridge transform intersection of the Raraku Transform (Chapter 4,

Figure 6.19 (a) - (h) Reconstructions back in time from 3.0 Ma to 5.0 Ma using only the magnetic data, since there are few GLORIA data left on the Nazca and Pacific plates to constrain the reconstructions. At 5.25 Ma, the East Rift pseudofaults finally disappear, and the Easter Microplate no longer exists.

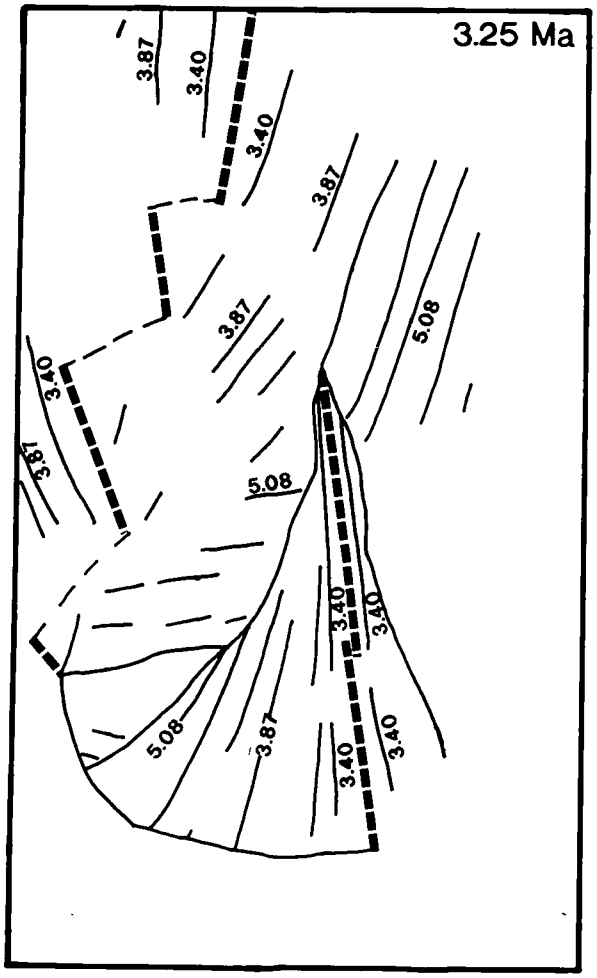
3.25 Ma
3.87
3.40
3.40
3.87
3.87
5.08
3.40
3.87
5.08
5.08
3.40
3.40
5.08
3.87
3.40
3.40

A

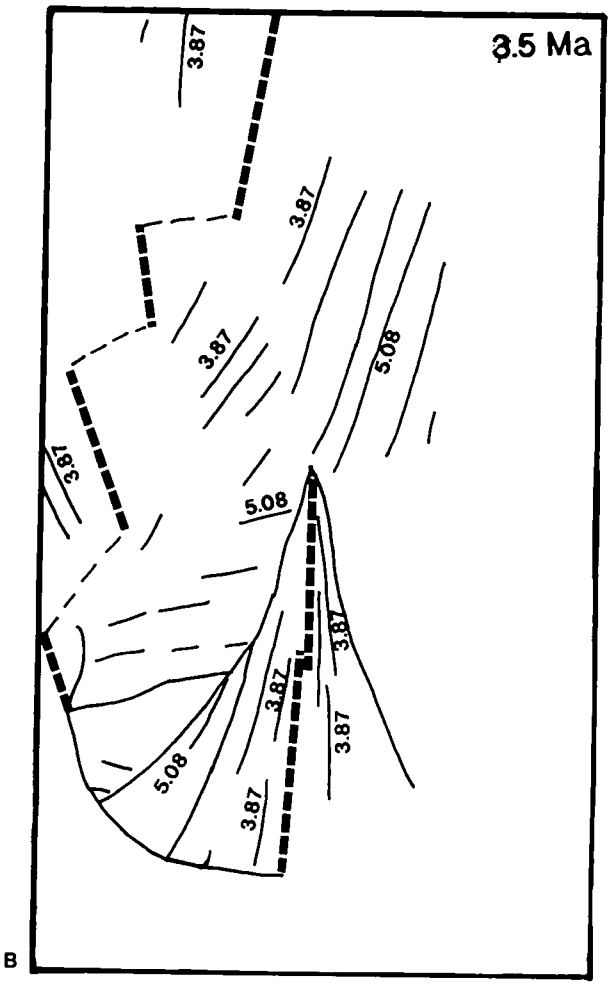
3.5 Ma
3.87
3.87
3.87
5.08
3.87
5.08
3.87
3.87
3.87
3.87
3.87

B

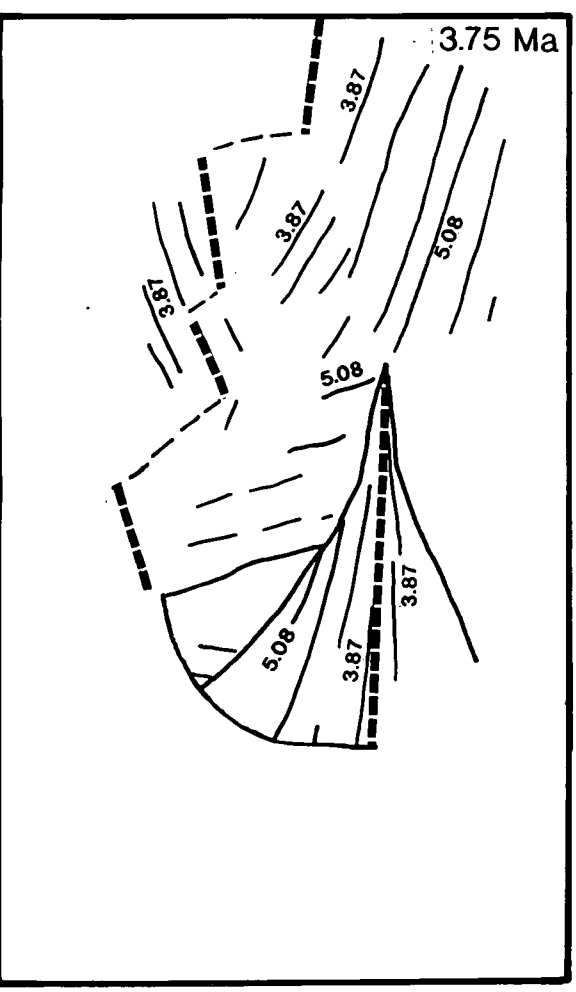
3.75 Ma
3.87
3.87
5.08
3.87
5.08
5.08
3.87
5.08
3.87

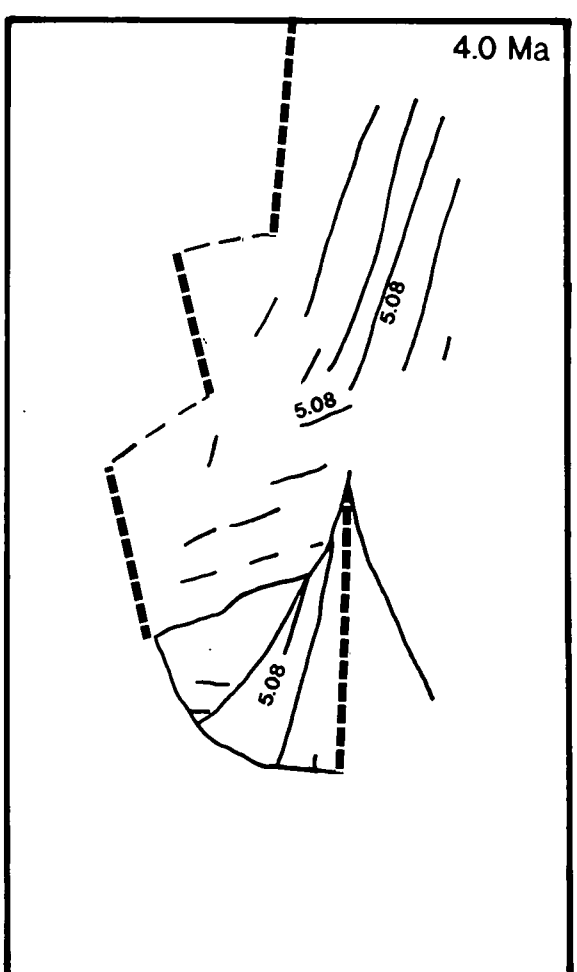
4.0 Ma
5.08
5.08
5.08

D

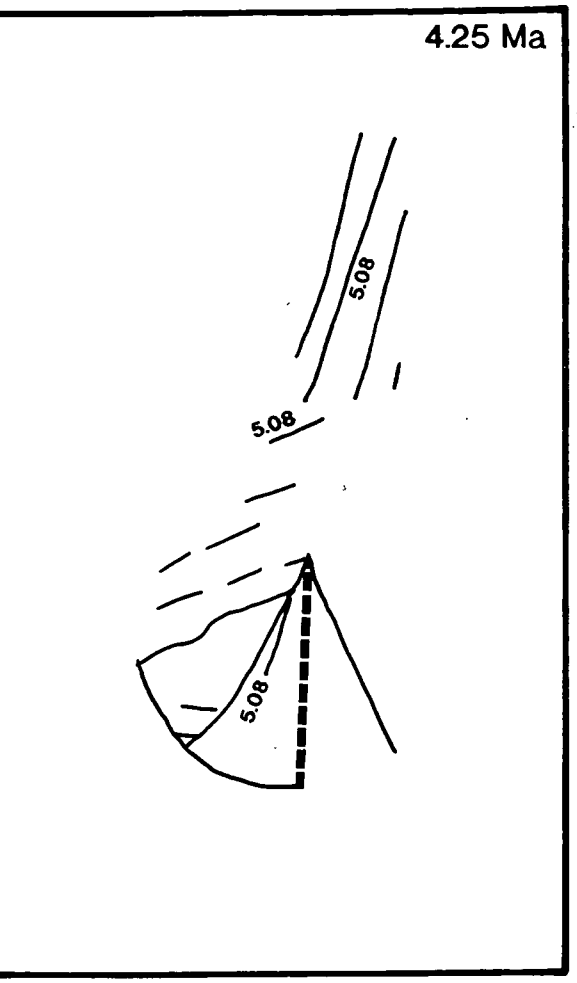

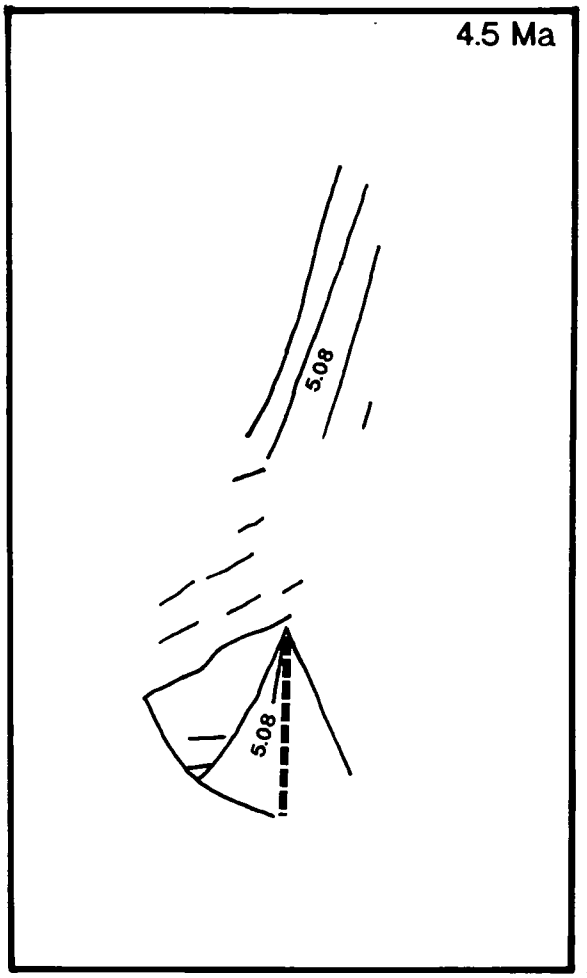

F

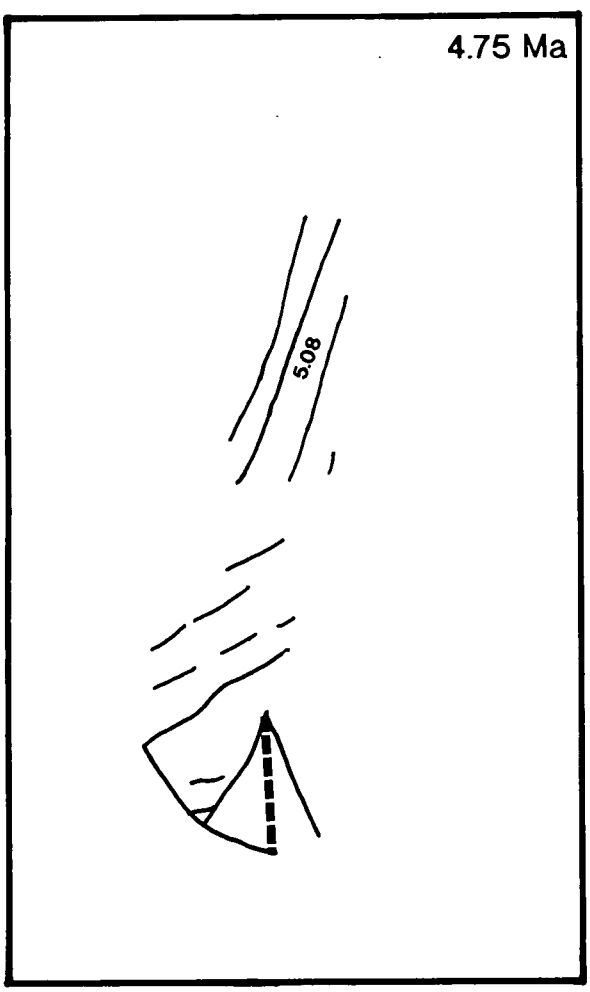

G

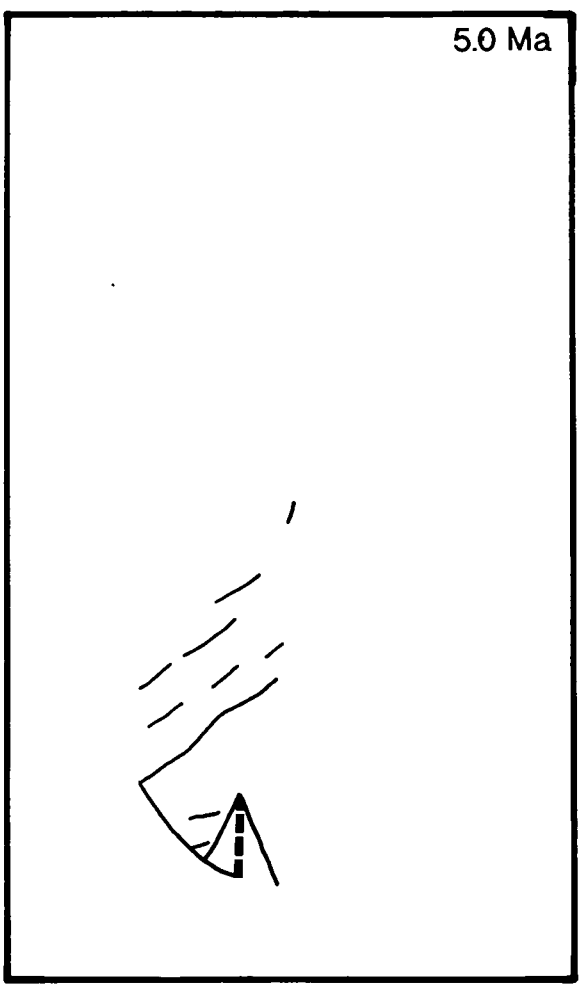

H

Figure 6.20 Change in shape and size of the Easter Microplate through time, at intervals of 0.5 myr, from 3.5 Ma to the present. After 2.5 Ma, when the East Rift ceases northward propagation, the microplate stops growing in a north-south direction, and although it does continue to grow in an east-west sense due to spreading, this growth is kept to a minimum by the propagation along the East and West Rifts of small rift segments to the inside (microplate side) of the dying rifts they replace.

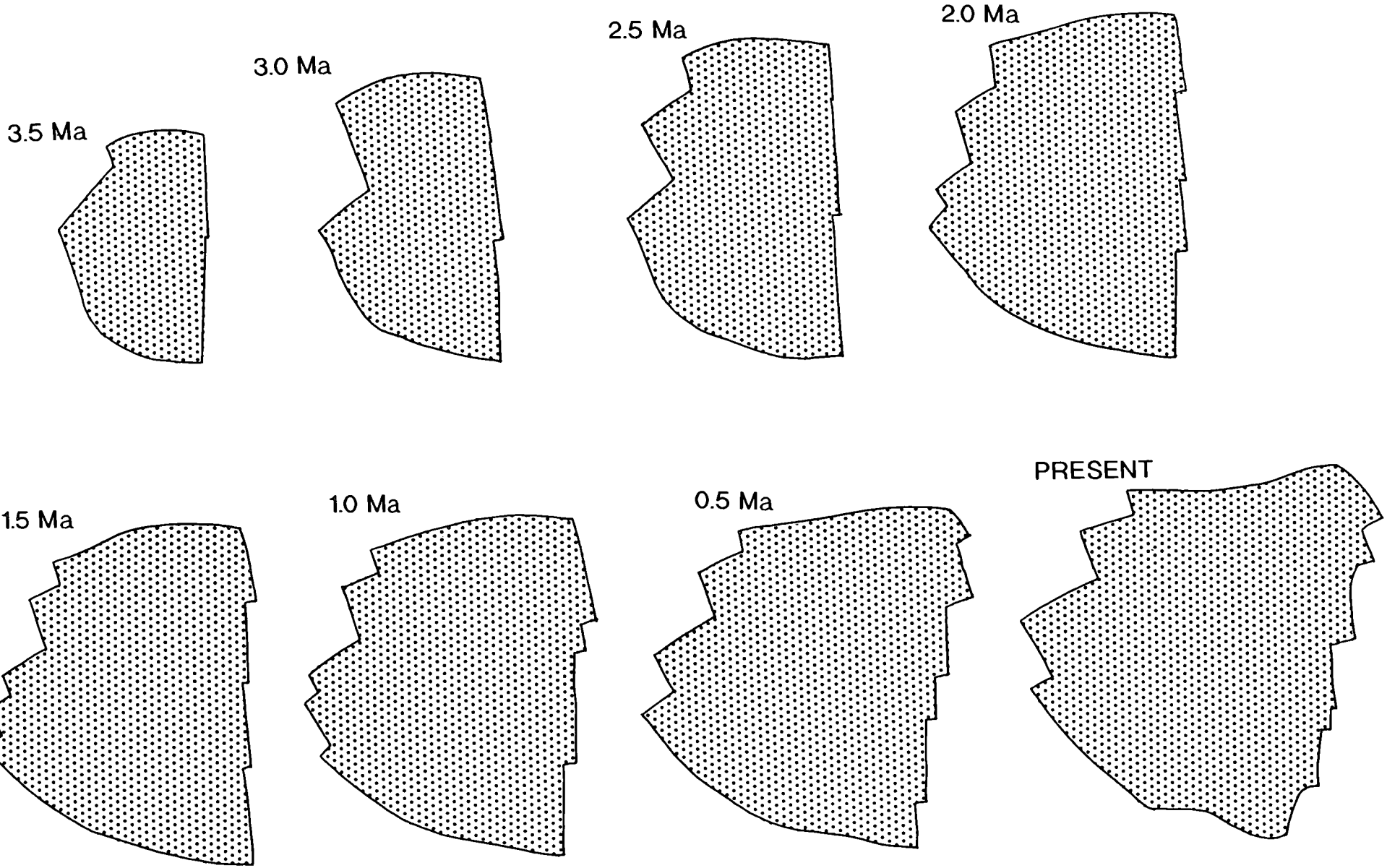
3.5 Ma
3.0 Ma
2.5 Ma
2.0 Ma
1.5 Ma
1.0 Ma
0.5 Ma
PRESENT

section 4.2); however, subsequently they appear to re-organise themselves in an anti-clockwise direction in order to remain orthogonal to the spreading direction.

The traces of these transforms on the interior of the microplate seem to have been obscured by the curvature of tectonic fabric through ridge propagation and "bookshelf" rotation (see below), as is also seen on GLORIA data to the west of the Juan de Fuca - Blanco transform intersection in the northeast Pacific (EEZ-SCAN 84 Scientific Staff, 1986; R.I. Rusby, 1988, unpublished dissertation). Also to be noted is the fact that there are no other transforms present south of the Terevaka transform on the West Rift. I suggest that at the tip of the small propagator south of this transform, another transform fault will develop here in the future. Although Francheteau et al. (1988) suggest that the Southwest Rift may be offset by one or more transforms, there is no evidence for this on the existing GLORIA and SeaMARC II data (Naar & Hey, 1991).

6.5.2 "Roller-bearing" model

Schouten et al.'s (1990) "roller-bearing" model (Chapter 1, section 1.5) presently cannot be used to describe completely the kinematics of the microplate. The instantaneous poles of rotation for Pacific-Easter and Nazca-Easter motion lie some 50 km from the microplate boundaries, though not actually on them as predicted, which implies that some strike-slip movement occurs between the microplate and the Pacific and Nazca plates (i.e. along the Pito and Orongo fracture zones of Francheteau et al., 1988 at the present-day). According to Schouten et al., this strike-slip movement should result in a slower rotation rate than that predicted by dividing the Pacific-Nazca spreading rate by the distance between the two poles. However, if we take the predicted Pacific-Nazca spreading rate to be 160 mm/yr (from Naar & Hey, 1989), and the distance between the two present-day instantaneous Euler poles to be 610 km, a rotation rate of 15°/myr (0.26 radians/myr) is implied which is the same as that used in the reconstructions. The timing of events used in Schouten et al.'s model is not compatible with my data. Their first stage, propagation of the East Rift while the West Rift opens about a hinge between the Pacific and Easter plates, is from 5.0-3.4 Ma, and their second phase, when the Southwest Rift and Pito Deep regions are assumed to form, is from 3.4 Ma to the present-day. However, the basic principal of a two-stage history is confirmed by the reconstructions, i.e. that as the East Rift propagates, the West Rift opens about a hinge (near the Terevaka transform) from 5.25-2.5 Ma, and then as the Southwest Rift opens up along the pre-existing transform, the Pito Deep region begins to rift apart the Nazca plate, from 2.5 Ma to the present. The resulting pseudofaults formed during the two stages are supposed to trace the location of the microplate's instantaneous relative rotation axes back in time, but since it is shown that the Pa-Ea and

the Nz-Ea poles need not be at the tips of the propagating ridges, these pseudofaults may only describe the path of the tips of the ridges throughout time.

One of the most interesting predictions made by Schouten et al. is that as the Southwest Rift is propagating 3-4 times faster than the Pito Rift, it will soon break through to the East Pacific Rise south of the microplate. When this happens the coupling between the microplate and the Pacific plate will cease, and thus the rotation of the microplate will also cease. Since dual spreading is no longer required, spreading will only continue along either the East or the West Rift. If the present West Rift is unable to accommodate Pacific-Nazca spreading (which would involve a reorganization to allow clockwise rotation of the axis by some 25°-45° if spreading were to be orthogonal), the East Rift might become the dominant ridge, and a permanent transform would form between the tip of the East Rift and the EPR, while the West Rift and microplate interior is abandoned on the Pacific plate (Schouten, pers. comm.). This new idea provides an interesting alternative to all previous ideas that used the propagating rift hypothesis to predict that the more recent East Rift will eventually take over from the failing West Rift. It also provides a much neater explanation for the lack of failure and apparent robustness of the West and Southwest Rifts.

6.5.3 Rift Propagation and Segmentation

Throughout the reconstructions, propagation of small spreading segments appears to be an essential part of the evolutionary process, allowing ridges and transforms to re-orient themselves in order to remain orthogonal to spreading directions. In the northwest corner of the microplate, the fabric produced by the northern segments of the West Rift has formed separate "morphotectonic" domains of different trends which have become juxtaposed as the segments forming them have re-oriented. These domains provide a strong control on the positioning of the earlier segments, and with additional data on the Pacific plate, it may be possible to match trends back to 5 Ma or so. On the East Rift, there is less control on the history of segmentation, except where magnetic lineations are clearly offset. However, it is assumed that orthogonal spreading has been accommodated in the past by ridge segmentation, in the same manner that it is accommodated today. Evidence for rift propagation both along isochrons, and into progressively younger fabric can be seen by careful examination of the tectonic fabric insonified by GLORIA to the west of the present East Rift. Here subtly different trends of lineaments can be seen to intersect, marking small changes in rift orientation produced by propagation in a less obvious manner than seen to the east of the West Rift.

6.5.4 Relation of Microplate to Easter Hotspot

Previous studies in the region have suggested that the microplate formed at 3.2 Ma (Handschumacher et al., 1981), or around 4.5 Ma (Naar & Hey, 1991) (section 6.3). If the initiation of the East Rift (and Easter Microplate) occurred at the same time as the formation of Easter Island, and these events were triggered by the presence of a hotspot situated beneath Easter Island, and on the East Rift at the start of its propagation (Pilger & Handschumacher, 1981; Engeln et al.,1984; Hey et al., 1985; Hagen et al., 1989), then the age at which these events occurred is significant. To examine the consequences I assume: (a) 5.25 Ma as the initial age of formation for the East Rift and Easter Island, as given by the above reconstructions, (b) an average half spreading rate of the southern end of the East Rift between 5.25-0.0 Ma of 67.5 mm/yr and (c) a Nazca - Easter Island hotspot rate of 50 mm/yr (from the Nazca-hotspot pole calculated by adding my three-plate Nz-Pa pole to the Pollitz (1986) Pacific-hotspot pole for 0-3.2Ma). Then the following predictions may be made (see Fig. 6.21). If the East Rift accelerates to its maximum half spreading rate of greater than 50 mm/yr almost instantaneously, then the hotspot will always be west of Easter Island and east of the East Rift between 5.25-0.0 Ma. Conversely, if the East Rift gradually accelerates to its maximum half rate, then initially the hotspot will lie to the west of the East Rift, until the East Rift begins to spread fast enough to allow the hotspot to cross over to the east of it. Whilst situated to the west of the East Rift, the hotspot may be unable to feed Easter Island, which would account for some of the age discrepancy between the oldest rocks found on Easter Island (3.3 Ma, Clark & Dymond, 1977) and the 5.25 Ma age of initiation of the East Rift. If the southern end of the East Rift has opened at 67.5 mm/yr (half rate) for 5.25 Ma and the Nazca plate (and Easter Island) has moved at 50 mm/yr for the 5.25 myr, then the East Rift would be presently situated the 354 km west of Easter Island which it is, and the hotspot should lie about 263 km west of Easter Island, which would place it at around 112°W, i.e. to the west of the Ahu volcanic field. A more likely position of the hotspot might be beneath the Ahu volcanic field, near 111°W (Hagen et al., 1990). This, however, would imply a slower Nazca absolute motion of 33 mm/yr and would mean that the hotspot is less likely to have been west of the East Rift during the early stages of propagation, or that Easter Island formed after the East Rift propagated.

6.5.5 Plate Deformation

The rigid reconstructions of the Easter Microplate appear to have provided a good fit to the existing GLORIA and magnetics data. The only major gap to form during the reconstructions is along the northern boundary of the microplate, implying compression has taken place. As mentioned above (section 6.4), the amount of compression that

Figure 6.21 This figure shows the relation of the Easter hotspot (assumed fixed) relative to the East Rift of the microplate and the Nazca plate with increasing time. The basic assumptions are: that the East Rift of the Easter Microplate formed at the same time as Easter island, i.e. at 5.25 Ma; that these two events were triggered by the presence of a hotspot beneath Easter Island at that time; that the oldest part of the outer pseudofault of the East Rift is at Easter Island, so that the East Rift has propagated away from the hotspot and Easter Island. Then if the Nazca-hotspot motion is 50 mm/yr (see text) and the average half spreading rate for the East Rift is 67.5 mm/yr the following predictions may be made: (1) If the East Rift accelerates to a half spreading rate of greater than 50 mm/yr almost instantaneously, the hotspot will always be west of Easter Island and east of the East Rift. However, if the East Rift gradually accelerates to its full half rate, then for a while the hotspot will be situated to the west of both the East Rift and Easter Island, and the hotspot may be unable to feed Easter Island. The hotspot will never be east of Easter Island. (2) If the southern end of the East Rift has opened at an average of 67.5 mm/yr (half rate) for 5.25 Ma and the Nazca plate (and Easter Island) has moved at 50 mm/yr for 5.25 Ma, the East Rift should lie about 350 km west of Easter Island (which it does) and the hotspot should presently be about 260 km west of Easter Island, i.e at around 112°W. If the hotspot is assumed to lie beneath the Ahu volcanic field, then a slower Nazca-hotspot rate of 33 mm/yr is required, which would mean that the hotspot is less likely to have been to the west of the East Rift, and that either the Nazca-Pacific Euler pole or the Pacific-hotspot pole is wrong.

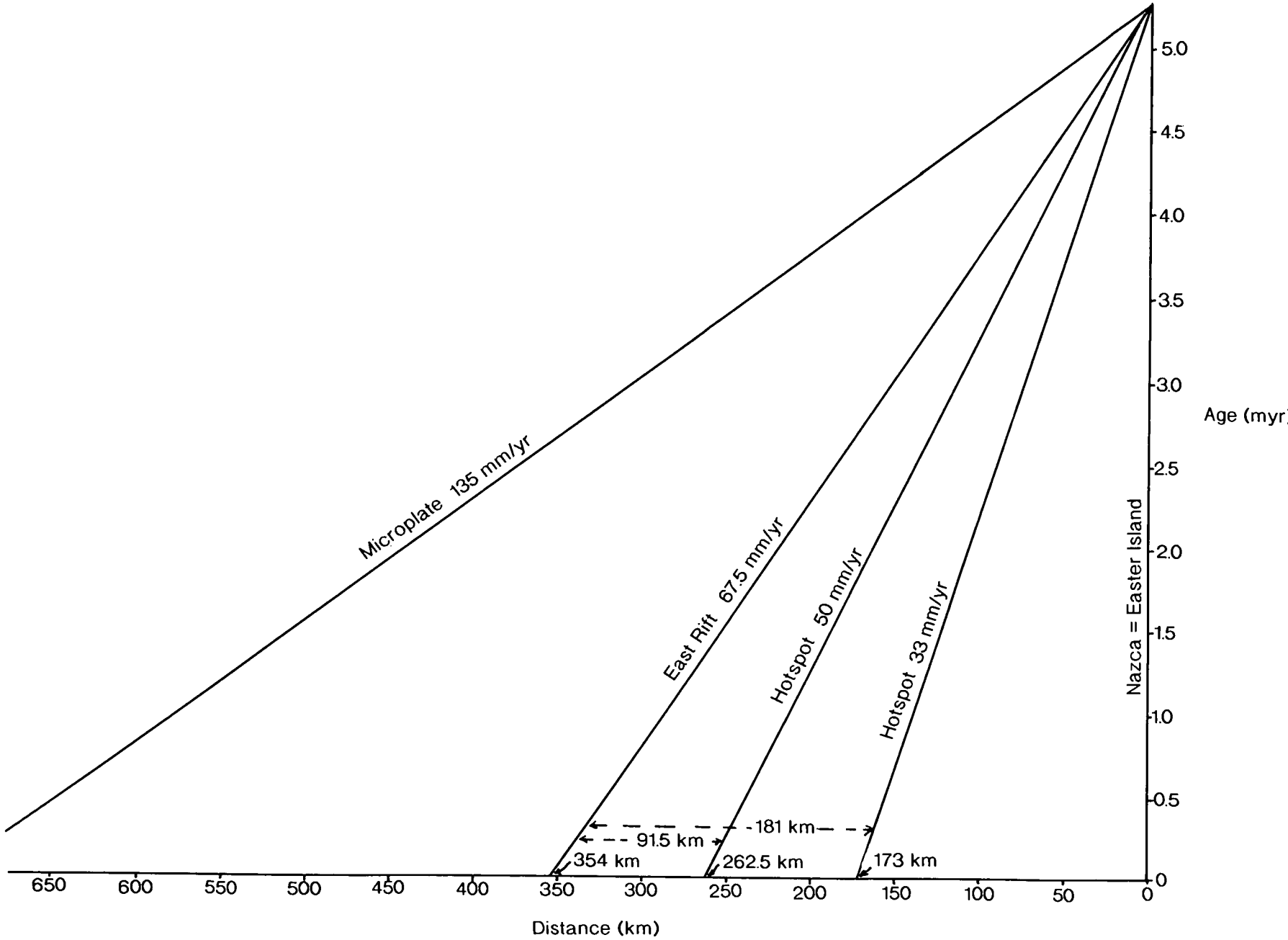
Microplate 135 mm/yr
East Rift 67.5 mm/yr
Hotspot 50 mm/yr
Hotspot 33 mm/yr
Nazca = Easter Island
181 km
91.5 km
354 km
262.5 km
173 km
650
600
550
500
450
400
350
300
250
200
150
100
50
0
Distance (km)
5.0
4.5
4.0
3.5
3.0
2.5
2.0
1.5
1.0
0.5
0
Age (myr)

occurs per given time increment decreases from the present-day maximum of about 14 km in 0.25 Ma (56 mm/yr) near the northern triple junction back to zero compression (and no gap formed) at around 2.5 Ma. As discussed in Chapter 7, much of the predicted Nazca-Easter motion associated with this boundary actually takes place to the north on the Nazca plate, and the shortening is believed to be accommodated by a series of thrust faults as well as by clockwise rotation of pre-existing normal-faulted fabric. During the last million years or so, thrust faulting has generally predominated in the west, while transpressional rotation of fabric has occurred in the east. One possibility is that where the strain rates are higher in the west, brittle failure of the uppermost crust occurs more readily, while in the east slower strain rates favour transpressional rotation of fabric.

There is little evidence within the microplate of crustal shortening having been accommodated in the past by thrust faulting, although a series of high relief roughly N-S trending ridges do exist in the region around 23.5°S, 112.5°W. These might have been created earlier on the Nazca plate as E-W ridges analogous to those forming there now, and subsequently transferred to the microplate and rotated with it as the East Rift propagated north past them (Naar, 1990; Naar et al., 1991, in press). One set of these (near 23°45'S, 112°45'W) dips steeply to the west, as expected if they were analogous to the faults on the Nazca plate to the north, suggesting that they are thrust faults with the same sense of overthrusting as occurring now. Other anomalous ridges within the microplate interior are less obviously asymmetric in their morphology, and may be compressional folds, rather than thrust faults. Although the magnetic anomalies are not readily identified within this region, the tectonic fabric on which the ridges lie appears to roughly span the time period from the end of chron 2a, and part of anomaly 3, say from 3.5-4.5 Ma, while the ridges themselves may have formed at a later date, possibly around 3 Ma.

Within the microplate interior there is little obvious indication of previous locations of earlier northern boundaries, which would presumably join the tip of the East Rift with the northern end of the West Rift. However, dextral shear between the Nazca and Easter plates must have been accommodated in the past by some mechanism. In the absence of any evidence for earlier through-going transform faults, it seems probable that this movement is accommodated by the "bookshelf" faulting mechanism employed by Searle and Hey (1983) and Kleinrock and Hey (1989) to explain the migration of the 95.5°W propagator, which is offset sinistrally. In Kleinrock and Hey's model an approximately 15 to 20 km wide zone accommodates the required 58 mm/yr dextral shear between the inner pseudofault and the failing rift by rotating pre-existing abyssal hill fabric in a clockwise direction (resulting in antithetic sinistral strike-slip movement along the original ridge-parallel normal faults) while the propagator migrates westward along the Cocos-

Nazca plate boundary at a rate of 52 mm/yr. The amount of rotation required to achieve this is on the order of 45° as shown by the rotated abyssal hill fabric. The amount of dextral strike-slip predicted along the northern boundary of the Easter Microplate through time, however, is about an order of magnitude smaller than that presently occurring at the 95.5°W propagator, and so the amount of rotation required within the transfer zone will be considerably less, and not readily discriminated from that occurring through rigid microplate rotation. Naar and Hey (1991) speculate that there has been pervasive simple shear across the entire microplate as the East Rift propagated northward until at least 3.4 Ma, before the rift offset distance grew sufficiently to allow the microplate to behave as a rigid body. Applying the same idea to the data presented here would mean that the microplate did not begin to behave rigidly until at least 2.5 Ma, which seems unlikely in the light of my reconstructions.

In conclusion, the reconstructions carried out here have given a valuable insight into the history of the Easter Microplate during the last 5.25 Ma. I have shown that it is not necessary for the Pacific-Easter and Nazca-Easter instantaneous Euler poles to migrate with the ridge tips of the propagating East and Southwest Rifts in order to match the magnetic anomalies, and instead the ridges are allowed to propagate towards their respective poles which remain fixed relative to the major plates. The evolution of the microplate occurs in two stages, the first in which the East Rift propagates northward, while the West Rift (formerly the East Pacific Rise) continually adjusts to accommodate a dual spreading system, and the second in which the East Rift ceases propagation, and Pito Deep and the Southwest Rift open up. Throughout these reconstructions I have shown that the microplate can be treated essentially as a rigid body. The history of the microplate as presented here is by no means the definitive version. However, based on the large data set available at present, it provides the most plausible story. The best way to improve on, or convincingly contradict, my understanding of the evolution of the Easter Microplate, would be to make an aeromagnetic survey over the entire microplate and surrounding region.

TABLE 6.1 Euler Poles Used to Reconstruct the Easter Microplate

	Plate	*Latitude*	*Longitude*	*Rotation(°)*
Fig. 6.7 (0-0.25Ma)	Pacific	0.00	0.00	0.00
	Nazca	56.80	-82.48	-0.35
	Easter	27.67	65.94	-3.70
Fig. 6.8 (0.25-0.5Ma)	Pacific	0.00	0.00	0.00
	Nazca	58.38	-88.71	-0.35
	Easter	27.67	65.94	-3.70
Fig. 6.9 (0.5-0.75Ma)	Pacific	0.00	0.00	0.00
	Nazca	59.62	-95.50	-0.35
	Easter	27.67	65.94	-3.70
Fig. 6.10(0.75-1.0Ma)	Pacific	0.00	0.00	0.00
	Nazca	60.48	-102.66	-0.35
	Easter	27.67	65.94	-3.70
Fig. 6.11 (1.0-1.25Ma)	Pacific	0.00	0.00	0.00
	Nazca	60.93	-110.24	-0.35
	Easter	27.67	65.94	-3.70
Fig. 6.12 (1.25-1.5Ma)	Pacific	0.00	0.00	0.00
	Nazca	60.94	-117.88	-0.35
	Easter	27.67	65.94	-3.70
Fig. 6.13 (1.5-1.75Ma)	Pacific	0.00	0.00	0.00
	Nazca	60.53	-125.41	-0.35
	Easter	27.67	65.94	-3.70
Fig. 6.14 (1.75-2.0Ma)	Pacific	0.00	0.00	0.00
	Nazca	59.72	-132.48	-0.36
	Easter	27.67	65.94	-3.70
Fig. 6.15 (2.0-2.25Ma)	Pacific	0.00	0.00	0.00
	Nazca	58.51	-139.33	-0.36
	Easter	27.67	65.94	-3.70
Fig. 6.16 (2.25-2.5Ma	Pacific	0.00	0.00	0.00
	Nazca	56.96	-145.59	-0.36
	Easter	27.67	65.94	-3.70
Fig. 6.17 (2.5-2.75Ma)	Pacific	0.00	0.00	0.00
	Nazca	55.14	-151.32	-0.36
	Easter	27.67	65.94	-3.70
Fig. 6.18 (2.75-3.0Ma)	Pacific	0.00	0.00	0.00
	Nazca	53.05	-156.50	-0.36
	Easter	27.67	65.94	-3.70

Fig. 6.19a (3.0-3.25Ma)	Pacific	0.00	0.00	0.00
	Nazca	50.73	-161.26	-0.36
	Easter	27.67	65.94	-3.70
Fig. 6.19b (3.25-3.5Ma)	Pacific	0.00	0.00	0.00
	Nazca	48.28	-165.43	-0.36
	Easter	27.67	65.94	-3.70
Fig. 6.19c (3.5-3.75Ma)	Pacific	0.00	0.00	0.00
	Nazca	45.63	-169.30	-0.36
	Easter	27.67	65.94	-3.70
Fig. 6.19d (3.75-4.0Ma)	Pacific	0.00	0.00	0.00
	Nazca	42.96	-172.71	-0.36
	Easter	27.67	65.94	-3.70
Fig. 6.19e (4.0-4.25Ma)	Pacific	0.00	0.00	0.00
	Nazca	40.06	-175.95	-0.36
	Easter	27.67	65.94	-3.70
Fig. 6.19f (4.25-4.5Ma)	Pacific	0.00	0.00	0.00
	Nazca	37.21	-178.79	-0.36
	Easter	27.67	65.94	-3.70
Fig. 6.19g (4.5-4.74Ma)	Pacific	0.00	0.00	0.00
	Nazca	34.19	-178.49	-0.36
	Easter	27.67	65.94	-3.70
Fig. 6.19h (4.75-5.0Ma)	Pacific	0.00	0.00	0.00
	Nazca	31.91	-176.01	-0.37
	Easter	27.67	65.94	-3.70

CHAPTER 7
INTRAPLATE THRUSTING NEAR THE EASTER MICROPLATE

7.1 Introduction

Until recently it has been considered unlikely that compressional intraplate deformation of young oceanic crust could occur (e.g. Park, 1988). Plate tectonic theory assumes that plates behave rigidly. However, on the Nazca plate just to the north of the northern boundary of the Easter Microplate there is evidence that compressional deformation is taking place.

Previous work in the area, using earthquake focal mechanisms (Anderson, et al., 1974; Engeln & Stein, 1984), Seabeam swath-bathymetry mapping (Francheteau et al., 1988) and calculations of recent plate motions (Naar & Hey, 1989), has shown that compressional movement may be occurring along the northern boundary of the microplate and on the Nazca plate to the north. The GLORIA data obtained during cruise CD35 reveal a series of high-relief, east-west, southward-facing ridges, forming a discontinuous chain from around 22°S, 114°W near the EPR to around 23°S, 112°W near the northern end of the East Rift of the microplate (the Pito Deep region) (Fig. 7.1a,b). As a result of our findings, some of these ridges have subsequently been mapped using Seabeam (Marchig et al., 1990).

I give evidence below that these ridges have occurred through brittle failure of the uppermost crust resulting in southward overthrusting of young oceanic lithosphere.

7.2 Evidence for Thrust Faulting

7.2.1 GLORIA Data

The anomalous ridges imaged by GLORIA (Fig. 7.1a,b) are oriented parallel/sub-parallel to the spreading direction, with generally brighter backscatter to the south. Those that are insonified from the north are revealed by a shadow facing away from the sonar vehicle, but are less readily distinguished. At least ten of these ridges are observed, varying between about 20 and 50 km in length, and with reliefs sometimes in excess of 1 km, as shown by bathymetric data. Some of them appear to be linked by NNE trending transcurrent faults, so that they form pairs throughout the region, with the western ridge

Figure 7.1(a) GLORIA image of part of the Nazca plate to the north of the Easter Microplate, with line drawing interpretation in (b). Note: the series of anomalous ridges that extend from around 22°S near the East Pacific Rise in an overall southeasterly trend toward the Pito Deep region in the east; the brighter backscatter to the south of most of these features, indicating a steeper slope to the south. Those that are insonified from the north show a shadow facing away from the sonar vehicle, but are less readily distinguished; at least ten of these features exist, and some appear to be linked, forming pairs; much of the abyssal hill fabric is oblique to the overall regional (ridge-parallel) trend, as if it has been rotated locally in a clockwise sense; the pair of ridges labelled 'a' are later referred to in detail.

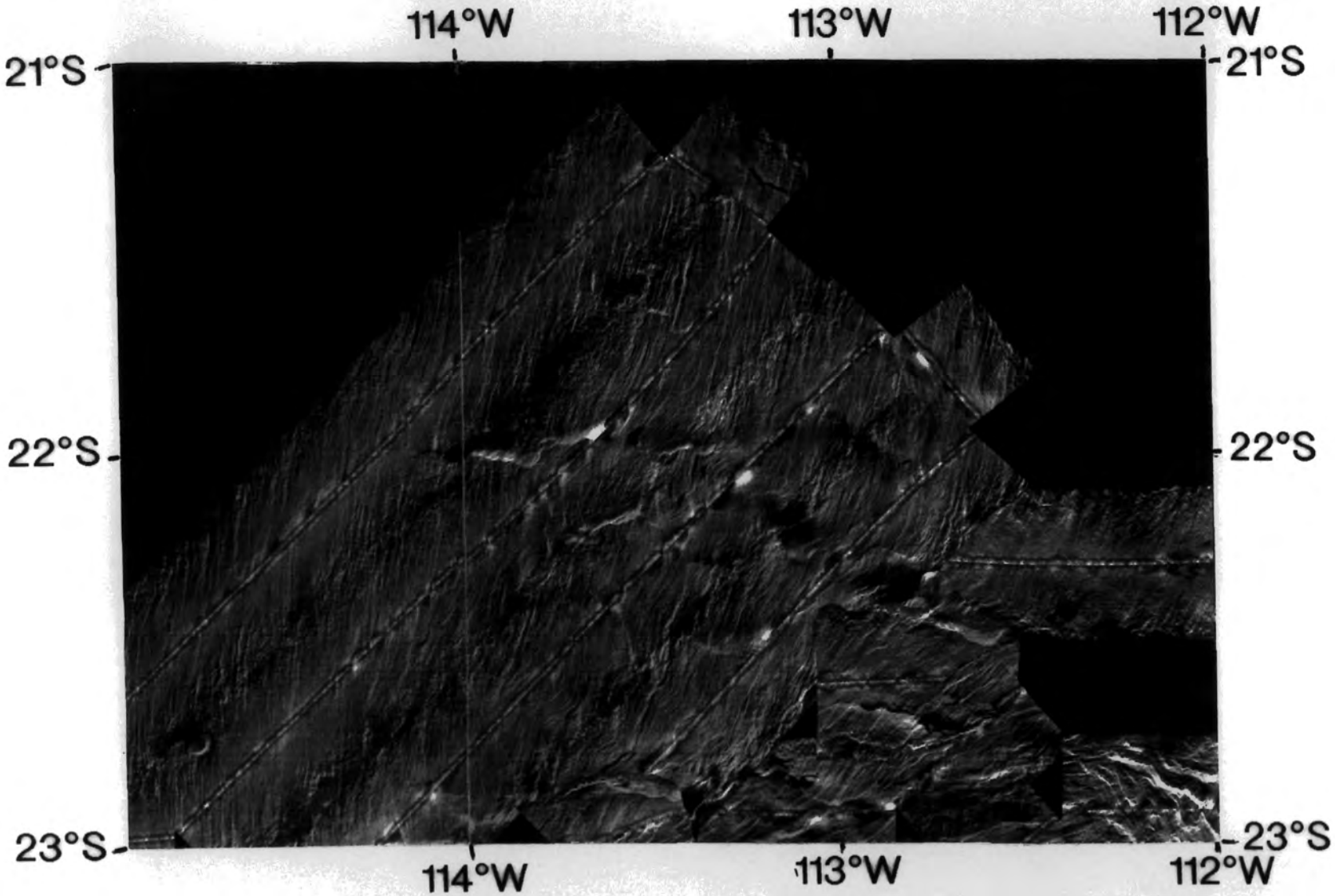
114°W
113°W
112°W
21°S
22°S
23°S

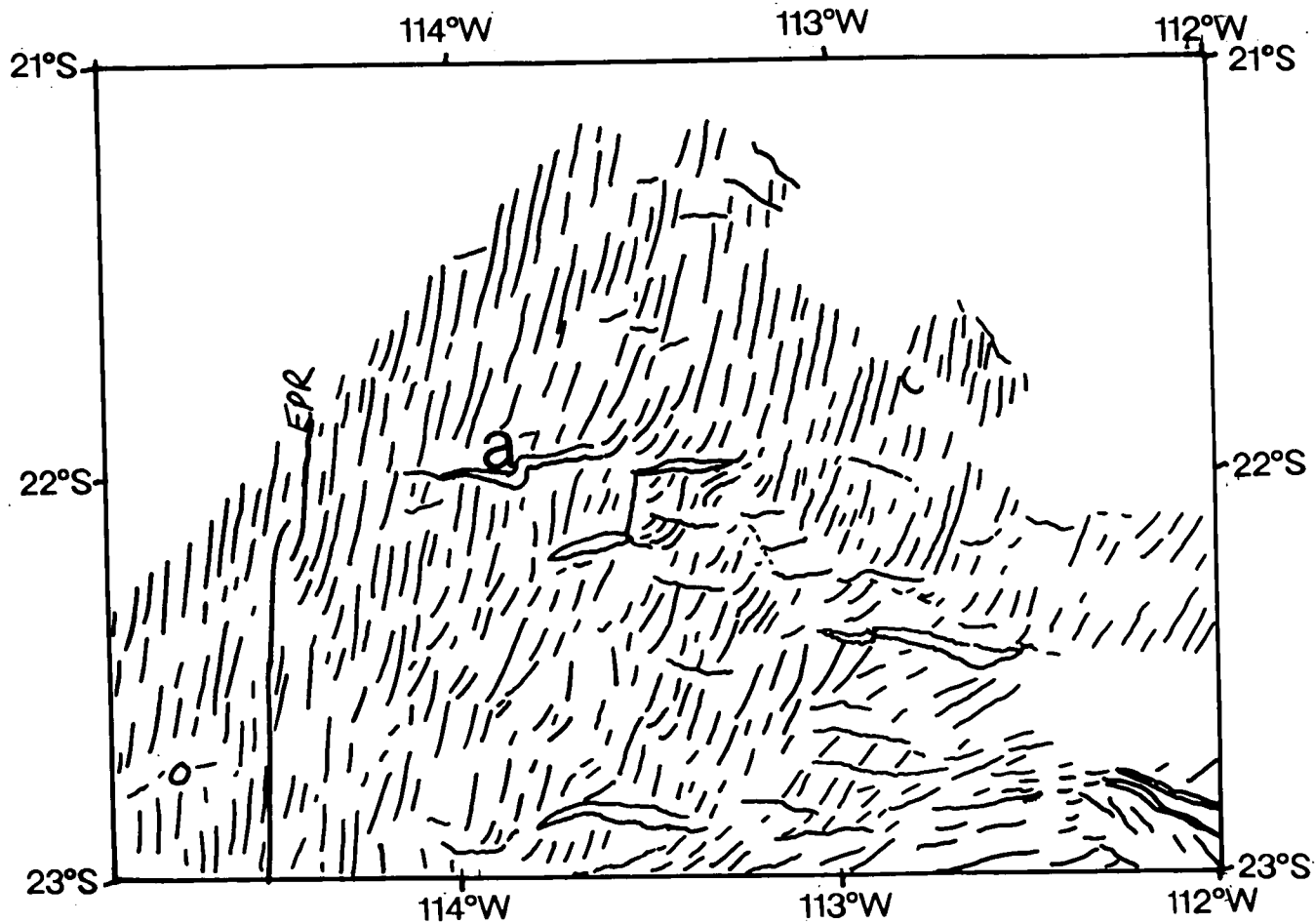
114°W
113°W
112°W
21°S
22°S
23°S
EPR
a
o

lying some 20 km to the south of its eastern counterpart. The westernmost pair, labelled 'a' in Fig. 7.1a,b is referred to below. The stronger backscattering to the south of each ridge indicates a steeper slope facing the sonar vehicle. Bathymetric data throughout the region are fairly scarce, but the 10 kHz and 3.5 kHz data collected concurrently with the GLORIA data show that many fairly high-relief ridges crossed obliquely do not show up clearly on the GLORIA mosaic, due to variations in the sidescan look direction. The asymmetric nature and steepness of the ridges suggests that they may have formed by some type of faulting mechanism.

Throughout this region to the north of the microplate, much of the abyssal hill fabric is oblique to the overall regional (ridge-parallel) trend, as if it has been rotated in a clockwise sense by some mechanism. This oblique fabric is also seen at the ends of some of the large east-west ridges, which, if this has occurred by a bookshelf faulting mechanism, may indicate that they are able to accommodate an element of dextral strike-slip movement.

7.2.2 Bathymetric Data

The bathymetric data that were available from the area prior to the CD35 cruise were compiled by Naar (1990) in his bathymetric map of the Easter Microplate (Fig. 1.2, Chapter 1), which has subsequently been published (Naar & Hey, 1991). Part of this map has been enlarged in Fig. 7.2. Although the individual ridges imaged by GLORIA are not obvious, the complexity of this region is suggested by the anomalous valleys and hills throughout the area which cut across the normal ridge-parallel trends. As a result of the GLORIA survey of this region, a broad Seabeam zig-zag was made through this area. This extended from Pito Deep in the southeast to the EPR in the west, as part of the transit passage from Easter Island to the EPR, at the start of the second leg of Geometep 5, cruise SO63 (Marchig, 1989) (see Fig. 4.18, Chapter 4). In Fig. 7.3, a Seabeam swath is shown over the westernmost pair of thrust faults imaged by GLORIA (labelled 'a' in Fig. 7.1a,b). These two major faults lie close to the EPR and dip steeply to the south (30-40°) and gently to the north (7°). Faults mapped further to the east also show this asymmetry, although this may decrease slightly nearer the Pito Deep region.

7.2.3 Seismicity

Earthquake data from the region are shown in Fig. 7.4 along with plate motion vectors and the Euler pole for Nazca-Easter rotation as discussed above. Earthquakes reported by the International Seismological Centre since 1971 are shown, with two

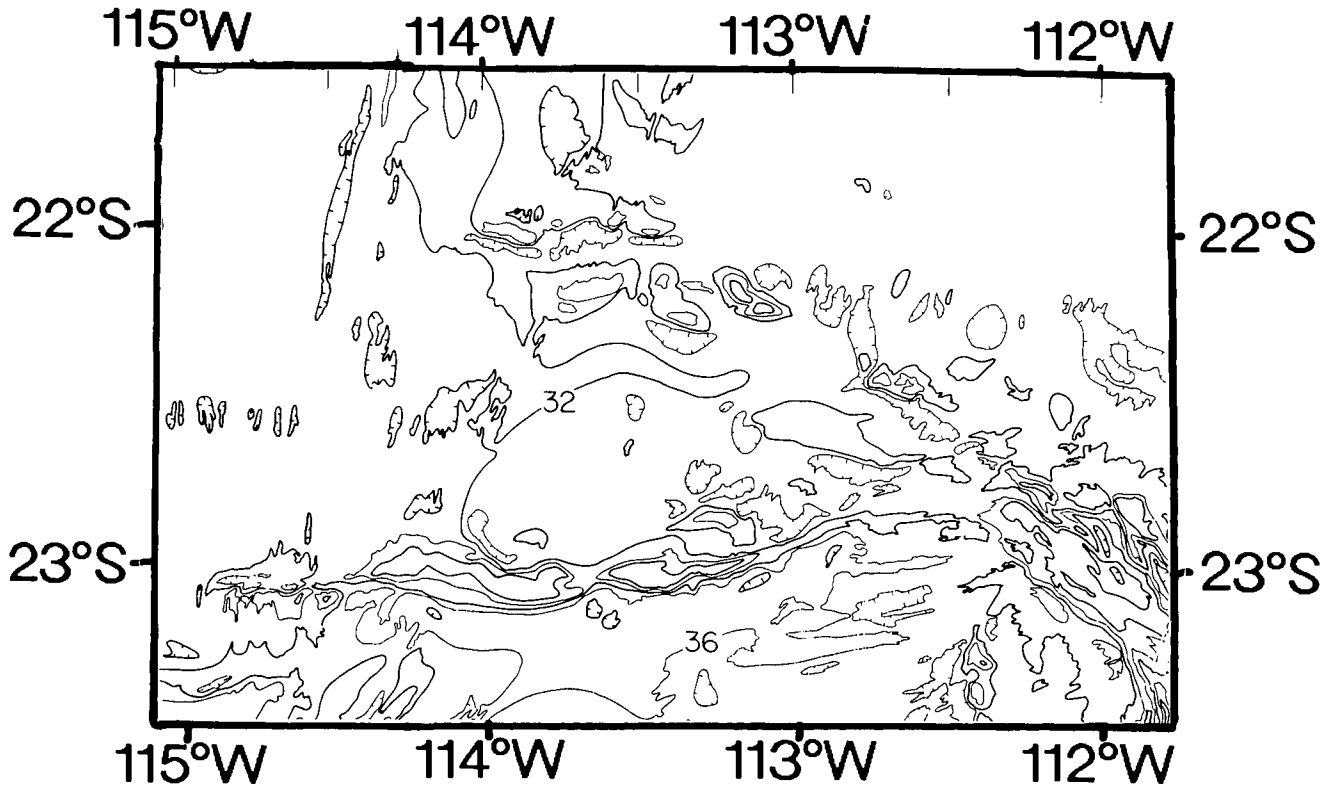

Figure 7.2 General bathymetry of the region showing the anomalous elevation of the northern boundary of the Easter Microplate and parts of the Nazca plate to the north. Contour interval is 400 m (Pito Deep 800 m) (modified from Naar, 1990).

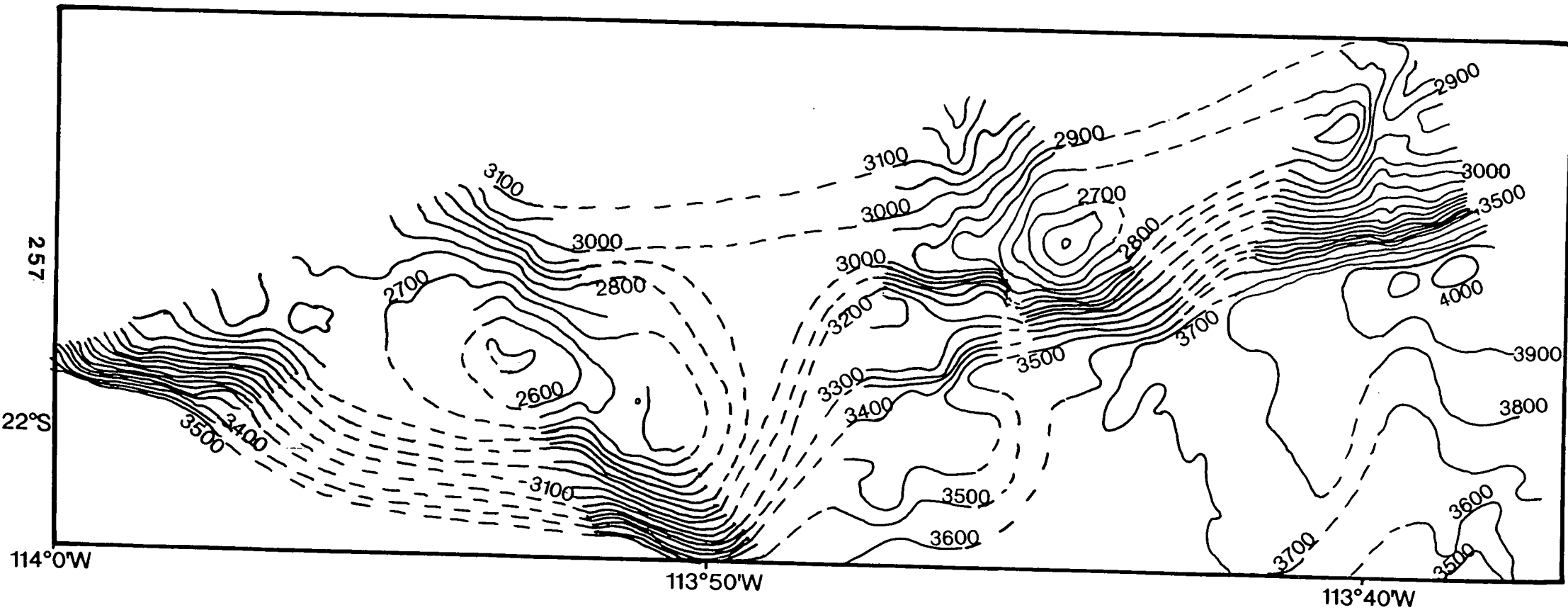

Figure 7.3 Seabeam zig-zag over the pair of ridges labelled 'a' in Fig. 7.1. Note the asymmetric morphology of the ridges, which dip steeply to the south (30-40°) and gently to the north (<10°).

Figure 7.4 Seismicity, fault plane mechanisms and plate motion vectors for area shown in Figs. 7.1a & b. Asterisks denote earthquakes reported by the International Seismological Centre (ISC) since 1971. Seismic activity within the region is not restricted to the plate boundaries. Locations and focal mechanisms of six earthquakes are shown. Those numbered 1 - 4 are from Engeln & Stein (1984), while 5 and 6 are published moment tensor solutions (CMT). Of the six focal mechanisms, one has a thrust faulting mechanism (3). The other five indicate either sinistral strike-slip movement on planes oriented 232°-247°, or dextral strike-slip on orthogonal planes. Plate motion vectors have been calculated for ten points in the region, and arrows show the result of assigning one third of the total compression for 1 Ma between the Nazca and Easter plates in this region (assumed constant for the last 1Ma) to individual faults (see text). The three-plate Nz-Ea Euler pole (Chapter 5) is indicated by a star.

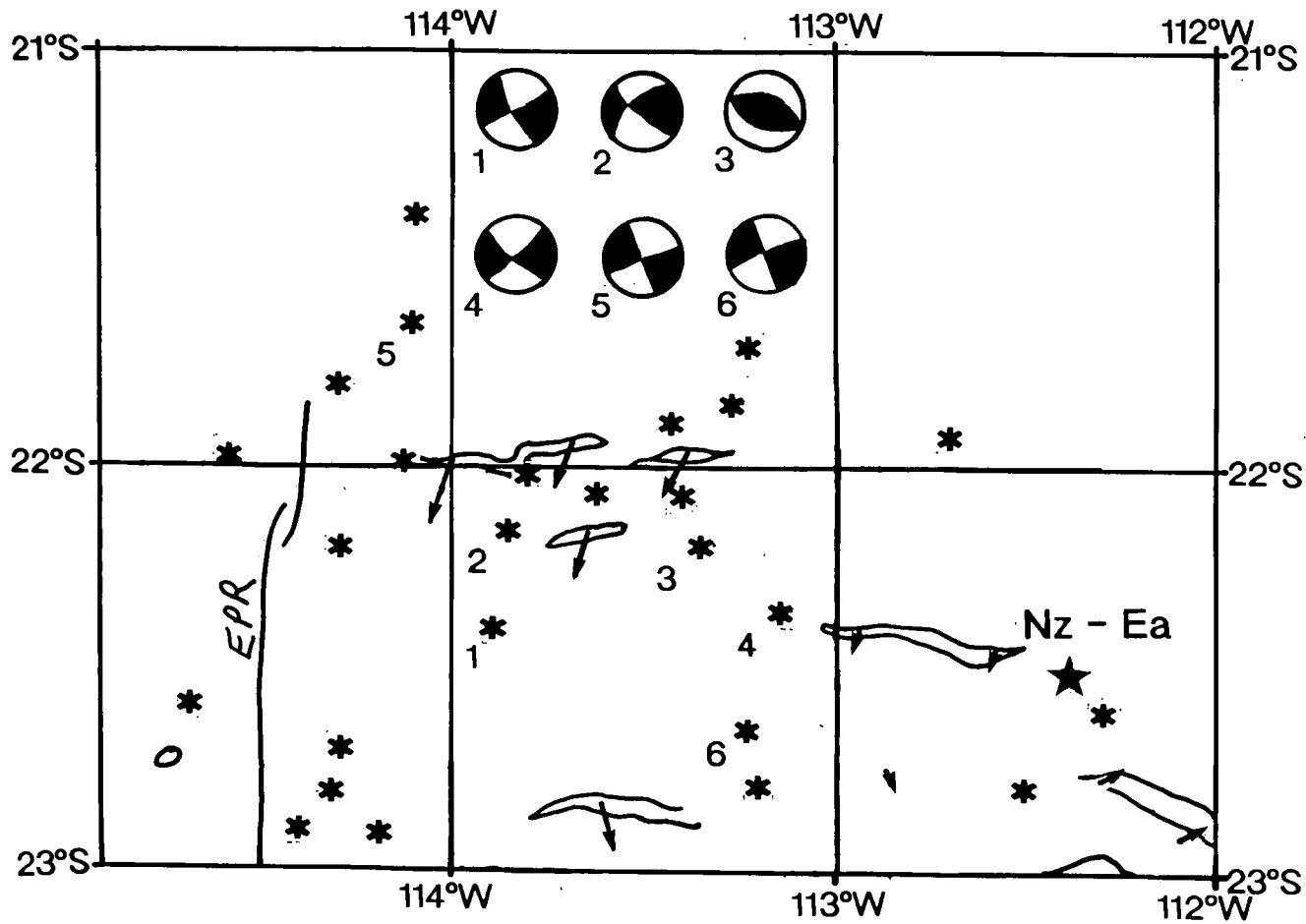
114°W
113°W
112°W
21°S
22°S
23°S
1
2
3
4
5
6
EPR
Nz - Ea

published moment-tensor solutions and four focal mechanisms from Engeln & Stein (1984).

Of the six focal mechanisms, one shows compression along 294° (3), but is poorly constrained, with possibly up to 30° of strike slip motion (Engeln & Stein, 1984). The other five are all strike-slip events with either sinistral movement on planes oriented 232°-247°, or dextral movement on orthogonal planes. If the rotated abyssal hill fabric imaged by GLORIA (section 7.2.1) resulted from a clockwise rotation of normal ridge-parallel fault blocks, this would have involved sinistral strike-slip movement along the edges of the blocks. This would then explain the occurrence of the five earthquakes with strike-slip focal mechanisms. The most obvious explanation for the earthquake with the thrust faulting mechanism is that the prominent, east-west trending ridges are in fact thrust faults, in the same way that thrust faults are believed to exist along the northern boundary of the microplate (see section 4.2.5, Chapter 4).

Fig. 7.5 shows the orientation patterns of faults and fold axes during (a) simple dextral shear, and (b) dextral north-south transpression (from Sanderson and Marchini, 1984). Transpression results in clockwise rotation of the stress axes, and with increasing compression, the axes would be rotated further. With further compression, the oblique basement fabric (described above) along which secondary sinistral strike-slip movement appears to be taking place would correspond to the antithetic Riedel shears (R') in Fig. 7.5, while the east-west ridges would correspond to the thrust faults (T) in the diagram.

7.2.4 Spreading Rates

Spreading rate data for the region during the last c. 3 million years (Chapter 5) show that for the last approximately 2 myr, spreading rates east of the EPR have decreased from north to south, despite increasing distance from the Pacific-Nazca Euler pole. The effect of this has been to produce a dextral shear couple over the region. Also, for the last 3 myr or so, spreading appears to have been consistently faster to the east, as is also the case elsewhere along the EPR (e.g. Naar & Hey, 1989). Asymmetric spreading of this nature may have been accommodated through subtle ridge propagation moving the East Pacific Rise westwards. Curved fabric extending in a southeastward direction away from a small OSC along the EPR, at 22°10'S (Fig. 7.1a,b), suggests that northward migration of the OSC has taken place, with older spreading ridge tips being rafted off (see Macdonald, et al. 1988). However, the lack of any similar rafted off rift tips to the west of the EPR, suggests that the ridge has consistently migrated westwards at the same time.

The velocity triangle predicted for the northern triple junction by the three-plate Nz-Pa and Nz-Ea Euler poles (section 5.4.2, Chapter 5) shows that the northern triple junction

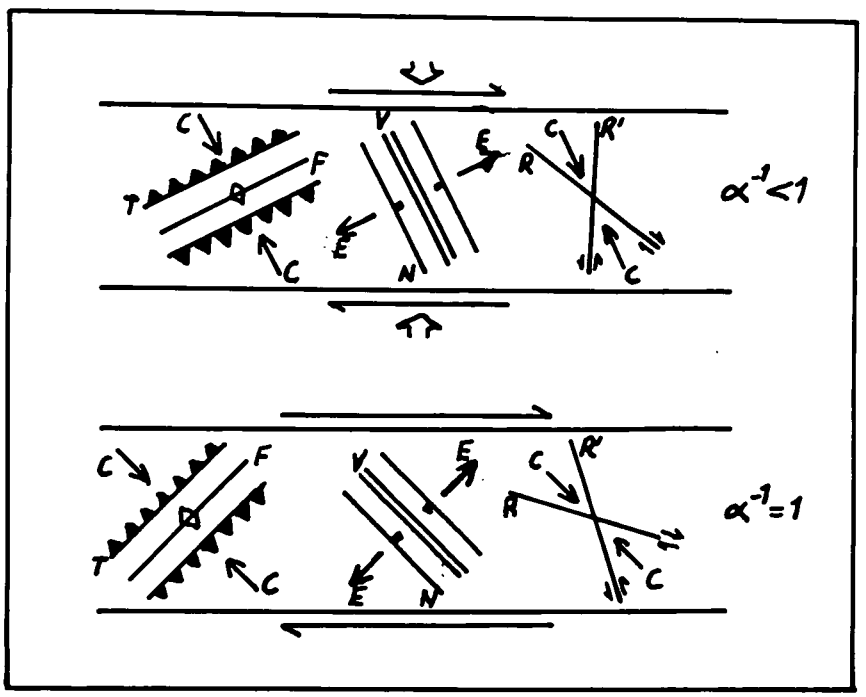

Figure 7.5 Diagrams showing the orientation patterns of faults and fold axes during dextral simple shear (bottom diagram) and under dextral transpression (top diagram). From Sanderson and Marchini (1984). C, compression axis; E, extension axis; N, normal faults; T, thrust faults; R, R', Riedel shears or strike-slip faults; V, veins, dykes or extension fractures; F, fold axes. Note that transpression results in clockwise rotation of compression and extension axes. The anomalous ridges imaged by GLORIA are thought to be thrust faults (corresponding to T in these diagrams), whereby the slightly younger Nazca lithosphere in the north has overthrust the slightly older lithosphere to the south (see text). If this is the case, then the oblique abyssal hill fabric seen on the GLORIA data may have been rotated by a "bookshelf" faulting mechanism to accommodate sinistral strike-slip movement (predicted by the earthquakes) as the antithetic Riedel faults (R') in the upper diagram.

may only be stable if the northern boundary is treated as a trench striking about 087°, assuming that spreading is orthogonal to the strike of the axes and is symmetric (Fig. 7.6a). The maximum predicted convergence between the Nazca and Easter plates is about 63 mm/yr along a strike of 115°. However, the Pacific-Nazca and Pacific-Easter spreading vectors measured from the magnetic anomaly data in the vicinity of the northern triple junction have considerably lower rates than those predicted by the Euler poles. These imply a maximum Nazca-Easter convergence rate near the triple junction of about 29 mm/yr along a strike of 110°, and the triple junction is shown to be stable if this northern boundary trends 080° (Fig. 7.6b), which in fact it does (Fig. 4.16a,b, Chapter 4). Measured spreading rates and azimuths at around 22°S along the EPR also predict a small amount of convergence between the Nazca plate to the north of 22°S and the deformed Nazca plate to the south (Fig. 7.6c). A maximum convergence of 8 mm/yr (along 116°) is predicted between these two parts of the Nazca plate (assuming spreading is strictly orthogonal), which appears to be taken up along a series of thrust faults.

The reconstructions carried out in Chapter 6 have shown that the East Rift ceased northward propagation between 2.25 Ma and 2.5 Ma. At this time, the northern boundary of the microplate stopped migrating northwards, and no more lithosphere was transferred to the Easter plate from the Nazca plate. As this happened, the northern boundary as it is known today began to form, accommodating convergence between the Nazca and Easter plates, presumably by means of thrust faulting. The total amount of convergence that is predicted to have occurred along this northern boundary is on the order of 7500 km². It is not known how much of this convergence may have been accommodated by the northern boundary itself during this time, but I suggest that much of this has been taken up by the Nazca plate to the north by rotation of originally ridge-parallel abyssal hill fabric and by southward overthrusting along the anomalous ridges imaged by GLORIA. In Fig. 7.4, plate motion vectors have been calculated for ten points in the region, and the arrows show the result of assigning one third of the total compression predicted for 1 myr between the Nazca and Easter plates in this region to individual faults.

7.2.5 Rheology of the Lithosphere

The rheology of the oceanic lithosphere is assumed to be controlled almost entirely by the deformation of olivine. Fig. 7.7 shows a critical stress vs. heat flow curve for compressional applied stress with a maximum ridge push stress source, and a probable maximum net stress force (by simple interaction of slab-pull, ridge-push and mantle drag) (Kusznir and Park, 1984). With this assumption, the curve shows that in order to deform the oceanic lithosphere by compression, heat flow values in the region of 90-100 mWm^{-2}

Figure 7.6 (a) Velocity triangle for the northern triple junction of the microplate, as predicted by the Euler vectors. These assume symmetric spreading and a ridge-normal spreading direction. Note the fast rate of convergence between the Nazca and Easter plates (63 mm/yr). In order for the triple junction to be stable, the northern boundary of the microplate must act as a trench trending 087°. (b) Velocity triangle for the northern triple junction based on measured spreading rates from the EPR and the northern end of the West Rift. Note the reduced convergence rate predicted between the Nazca and Easter plates (29 mm/yr). The triple junction may be stable if the northern boundary acts as a trench trending 080°. (c) Velocity triangle centred at 22°S along the EPR based on measured spreading rates. A subtle change in trend of the EPR occurs which is sufficient to accommodate local convergence between the northern and southern parts of the Nazca plate (8 mm/yr). The decreasing spreading rates southwards along the EPR, together with the shortening predicted, indicate that the region to the north of the microplate is under dextral transpression.

Northern Triple Junction 23.47°S 114.53°W

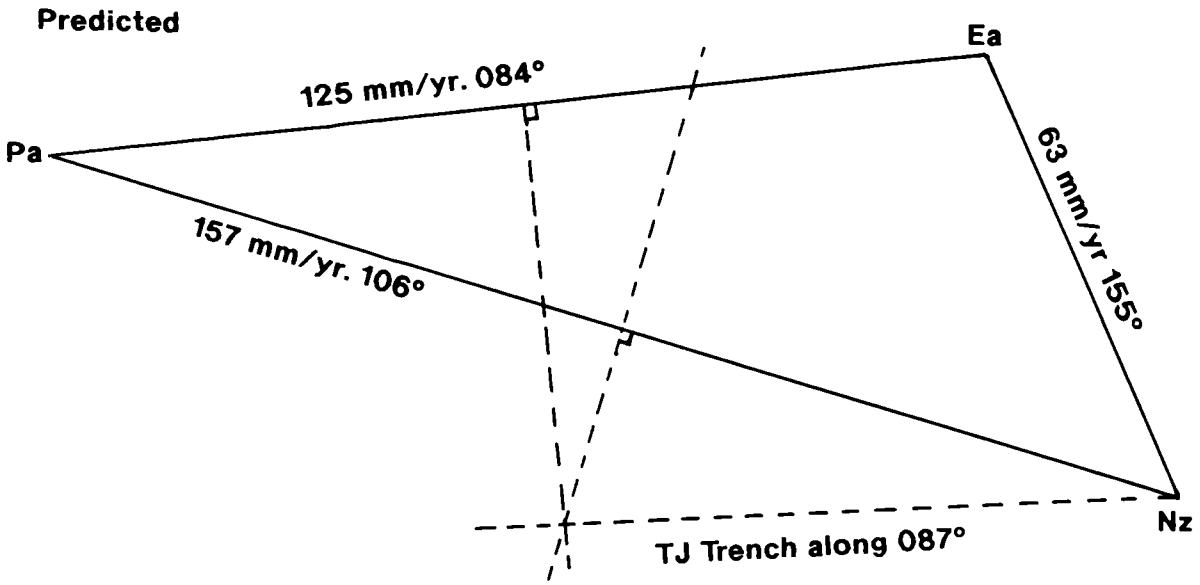

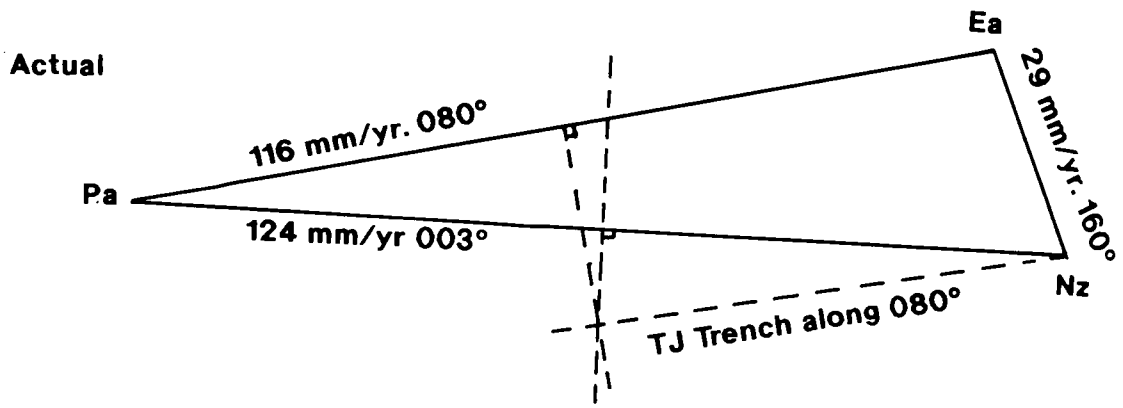

"22°S Triple Junction"

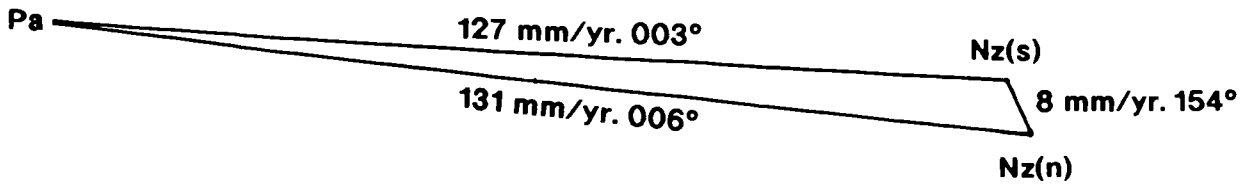

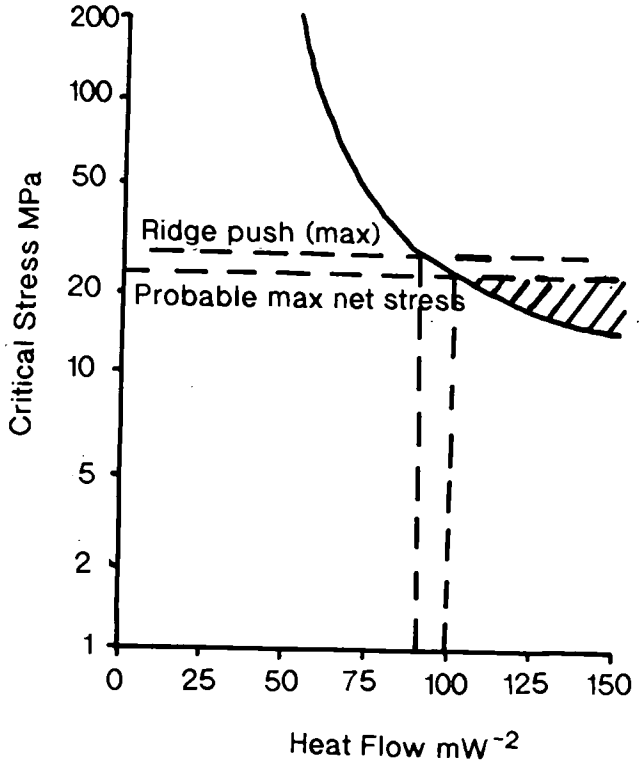

Figure 7.7 Curve of critical stress vs. lithospheric heat flow for compressional applied stress, compared with a possible ridge push source and probable maximum stress levels. Shaded area is region of potential deformation. Numerical model; after Kusznir and Park (1984). This shows that in order to deform the oceanic lithosphere by compression using a reasonable stress source, heatflow values in the region of 90-100 mWm^{-2} are required. Values greatly in excess of this have been found elsewhere along the EPR, which suggests that thrust faulting may be possible in this region.

are required. Unfortunately, there are no heat flow data within the deformed zone of the Nazca plate, and only a few within the area of the Easter Microplate, none of which are close to spreading axes. However, published heatflow values greatly in excess of 90-100 mWm^{-2} have been found elsewhere along the EPR, which suggests that thrust faulting may be possible in this region, especially as it is within the zone of influence of the Easter hotspot (see Chapter 4).

From the GLORIA mosaic, we can see that the nearest thrust fault to the EPR has its western end some 24 km from the spreading axis, corresponding to an age of ~0.3 myr. The westernmost extent of thrust faulting along the northern boundary of the Easter Microplate lies only 19 km from the EPR, corresponding to an age of ~0.25 myr. I suggest that these similar age offsets may correspond to a minimum period required for sufficient stress to build up within the lithosphere before thrust faulting can take place, or for the lithosphere to grow strong enough to deform by brittle faulting, i.e. the age at which the lithosphere has cooled and thickened sufficiently.

7.2.6 Thrust Faulting

Fig. 7.8a shows a close-up of a GLORIA image of a pair of thrust faults, labelled 'a' in Fig. 7.1, with a line-drawing interpretation in Fig. 7.8b. These east-west trending faults appear to be linked by a NNE-SSW trending strike-slip transfer fault. At the western end of the northern fault, a small sliver of lithosphere appears to have been overridden by the main fault. A schematic block diagram illustrating this is shown in Fig. 7.9. This shows my interpretation of the intraplate thrust faulting which is taking place on the Nazca plate. The faults shown are from the middle of Fig. 7.8, where two episodes of thrust faulting have enabled an earlier smaller thrust to be overridden by a larger later thrust. The sole of thrusting is arbitrarily shown as being at the base of the dykes, but may have occurred at other levels within the lithosphere.

The surface morphology of some of the thrust faults is known from the single Seabeam zig-zag throughout the area, but this tells us little about the nature of the faulting itself. The earthquake locations are all shallow (< 10 km depth) but are not constrained beyond this. Cann (1974) has suggested that as spreading rate increases, the interval between successive dyke intrusions decreases so that dykes cool less between injections, and a decrease in the thickness of the sheeted dyke unit results. Also as spreading rate increases stresses are concentrated in a thinner layer and fracturing will occur more frequently. Park (1988) notes that major rheological boundaries in the lithosphere (especially at mid-crustal levels) form important zones of low ductile strength. These zones may provide detachment horizons during deformation, with higher

Figure 7.8 (a) Close-up of a pair of thrust faults, labelled 'a' in Fig. 7.1, with line drawing interpretation in (b). These east-west trending thrust faults are linked by a NNE-SSW trending strike-slip transfer fault. At the western end of the northern fault, a small sliver of lithosphere appears to have been overridden by the main fault.

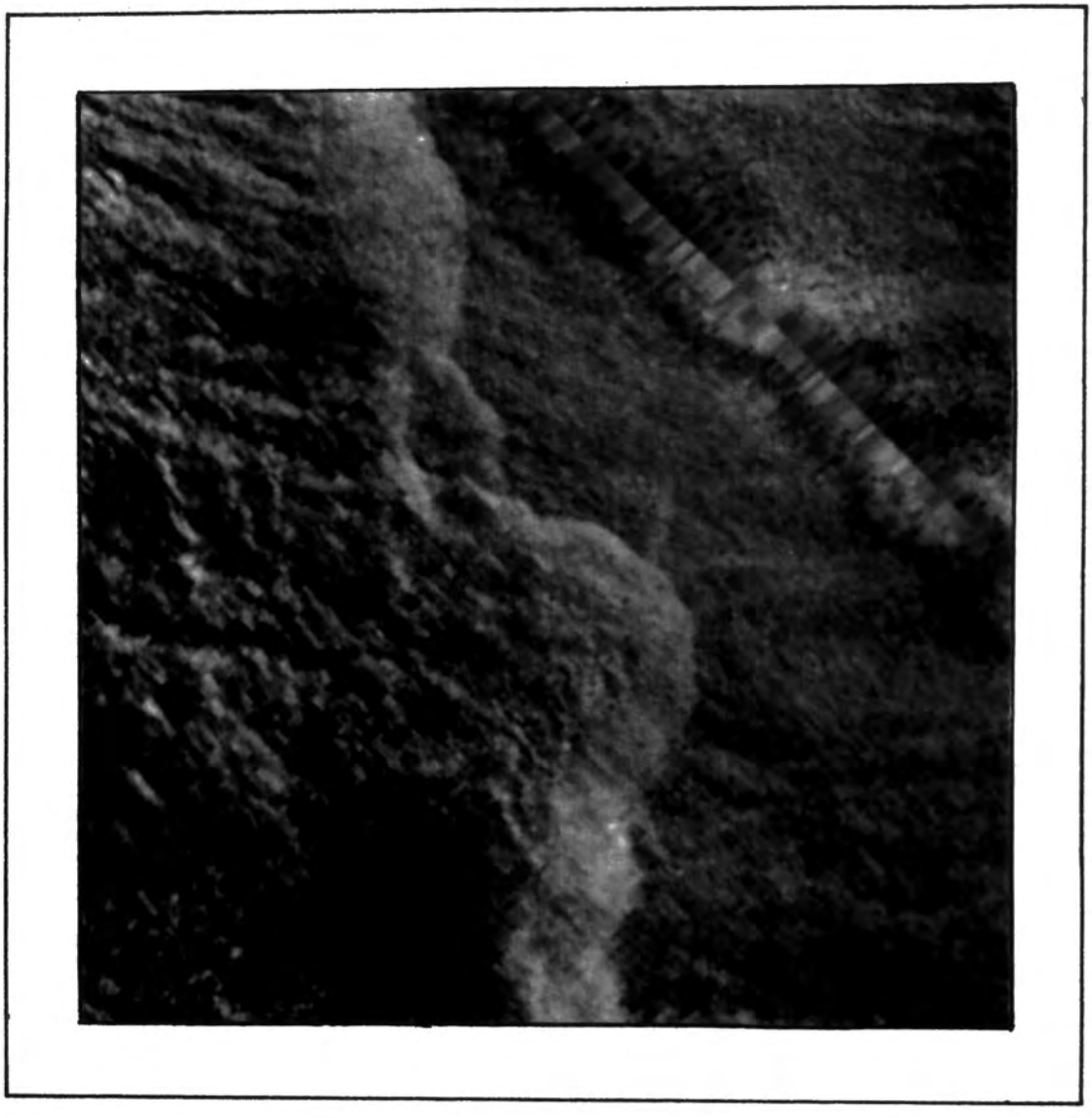

A

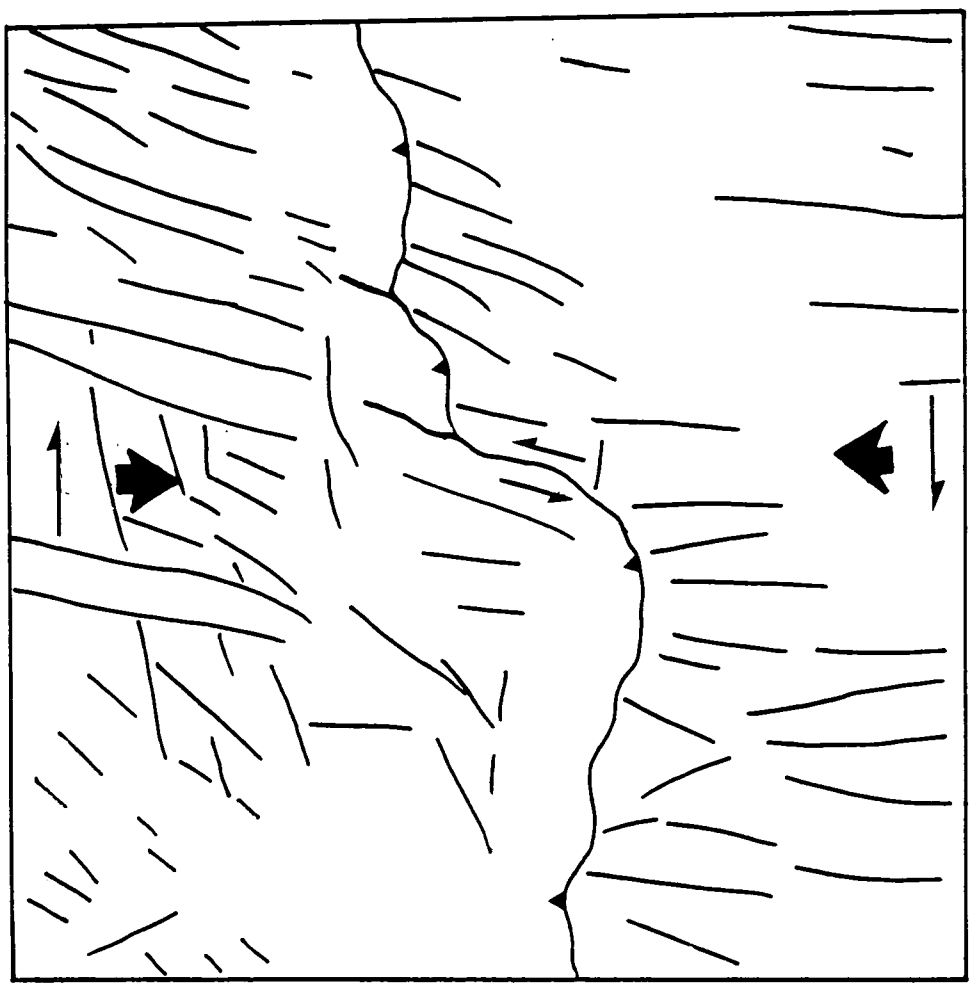

B

detachment levels being favoured in warmer lithosphere with a young thermal age, such as is the case within the Nazca plate to the north of the Easter Microplate.

One-, two- and three-dimensional seismic velocity representations of the crustal structure beneath and adjacent to the EPR (e.g. Rosendahl et al., 1976; Harding et al., 1989; and Toomey et al., 1990) show the top of layer 3 near the spreading axis to be only about 1 km below the seafloor. One possibility is that detachment of the thrust faults occurs at this rheological boundary, between the sheeted dykes and gabbros of layers 2 and 3, as shown in Fig. 7.9. Another possibility is that detachment occurs at Vera's (1990) seismic layer 2-3 transition, i.e. within the dyke unit, a few hundred metres above the dyke-gabbro transition. This transition may mark the maximum depth of penetration by a cracking front and associated hydrothermal circulation, and provide a convenient detachment horizon. For a large amount of lateral convergence to be taken up along these thrust faults, it seems likely that the sole of thrusting does occur at a fairly shallow level within the lithosphere, allowing detachment on low angle fault planes.

7.3 Discussion

Evidence from earthquake focal mechanisms and the predicted plate motions within the region to the north of the Easter Microplate suggest that the anomalous east-west trending ridges imaged by GLORIA are in fact thrust faults. It is widely acknowledged that intraplate compressional deformation within continental lithosphere is uncommon. However, the fact that intraplate deformation of this type may and does occur within young oceanic lithosphere has never before been considered.

Other examples of reverse thrust faulting within the oceanic lithosphere do exist, but these tend to occur in much older lithosphere due to the reactivation of pre-existing faults. One example of this is at the Gorringe Bank (northeast Atlantic) at the eastern end of the Azores-Gibraltar plate boundary where thrusting may have occurred on deep planes within lithosphere that is 120 Ma old, bringing dense mantle rocks nearer to the surface (Purdy, 1975; Souriau, 1984). Convergence between the Pacific and Caroline plates in the southwest Pacific is apparently accommodated by overthrusting of small slivers of the seafloor (Weissel & Anderson, 1978), however, again this is within much older lithosphere, and may involve reactivation of pre-existing faults.

The intraplate thrusting within the young, warm Nazca plate is likely to be a thin-skin phenomenon, with only the uppermost 1-2 km or so of crust being detached and overthrusted. It seems unlikely that a permanent zone of subduction will develop, as the lithosphere is young and buoyant, but rather that these thrust faults should occur when

Figure 7.9 Schematic block diagram showing the interpretation of intraplate thrust faulting that is taking place on the Nazca plate. The faults shown are from the middle of Fig. 7.8, where two episodes of thrust faulting have enabled an earlier, smaller thrust to be overridden by a larger later thrust. The sole of the thrusting is arbitrarily shown as being at the base of the dykes, but detachment may have occurred at the base of hydrothermal alteration within the crust, or at deeper rheological contrasts within the lithosphere.

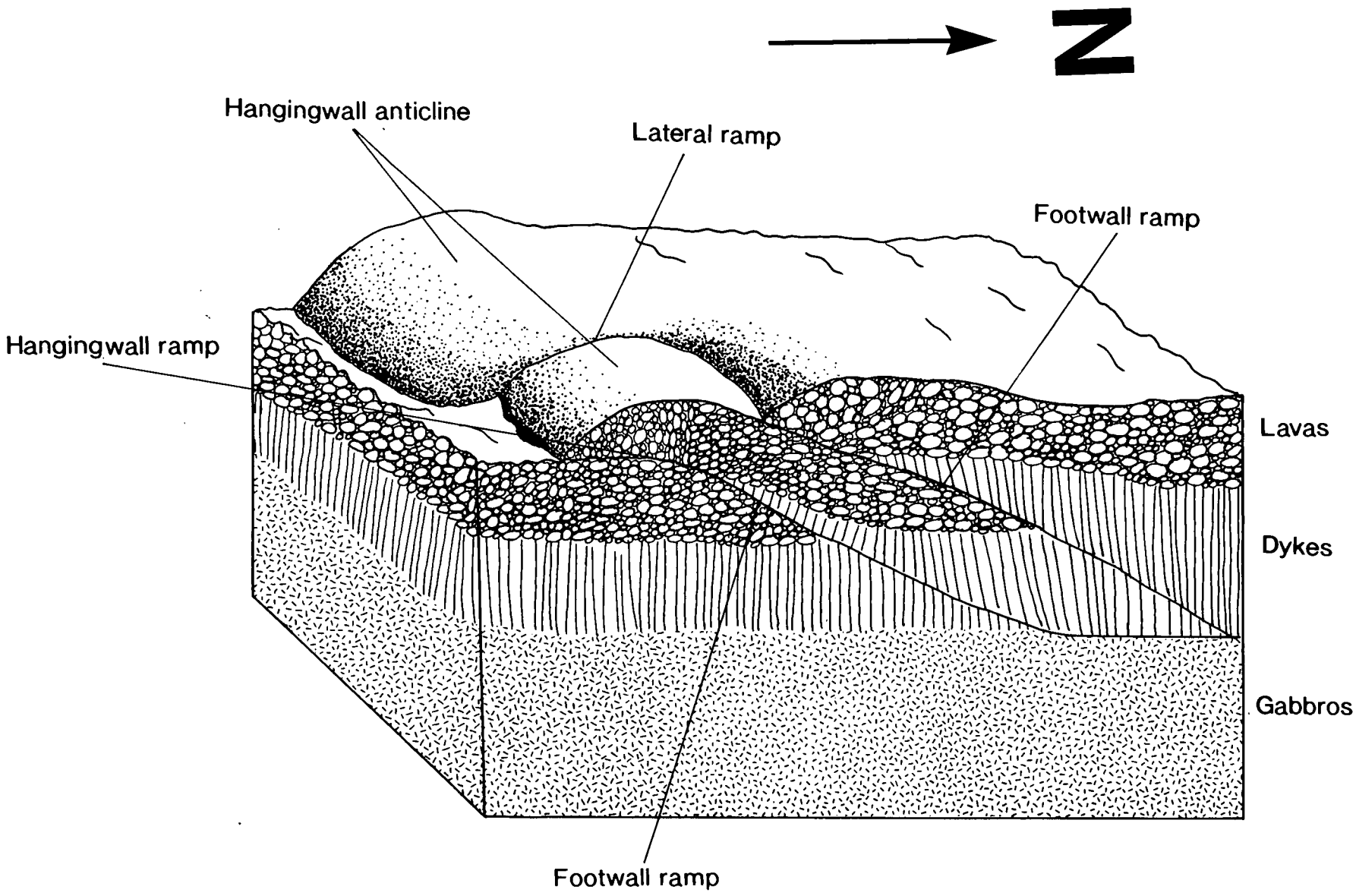
Z
Hangingwall anticline
Lateral ramp
Footwall ramp
Hangingwall ramp
Lavas
Dykes
Gabbros
Footwall ramp

and where they are needed in order to accommodate changing stress regimes within the region.

At the Juan Fernandez microplate, Anderson-Fontana et al. (1986) have located the Nazca-Juan Fernandez Euler pole at the tip of the east rift. This then requires that most of the northern boundary of this microplate is in compression. A recent GLORIA survey of the microplate (Bird et al., 1991; Larson et al., submitted, 1991) has revealed a series of large, high-relief east-west trending ridges at the northern boundary. The morphology of these ridges, combined with the predicted plate motions in the region, suggests that they have resulted from compressional tectonics. However, the lack of asymmetry may mean that they have not formed through brittle failure and faulting of the uppermost crust, but rather have formed by ductile folding of the lithosphere. Crustal shortening may have been associated with microplates in the past, such as with the Bauer, Mendoza, Roggeveen and the Mathematician palaeoplates.

Evidence for the formation of intraplate thrust faults or compressional ridges must be examined closely in order to understand the conditions required for this to occur. The fact that thrusting has been shown to occur within oceanic lithosphere suggests that some observations of thrusting within ophiolites should be carefully re-examined. Sites of thrusting within obducted oceanic lithosphere that were previously assumed to have been part of the obduction process itself may in fact have resulted from intraplate thrusting of young oceanic lithosphere prior to its obduction. Further detailed mapping and gravity surveys are required to determine the extent of shortening within young oceanic lithosphere which can be accommodated by thrust faulting. Detailed rock sampling along the steep scarp slopes of the thrust faults may shed light on the level of detachment of the fault planes within the lithosphere. Plutonic rocks were retreived from the base of one of the compressional ridges in the region of the Juan Fernandez microplate (D. Stakes, pers. comm.), which actually suggests that these ridges result from detachment at deeper levels within the lithosphere.

The fact that intraplate thrusting within young oceanic lithosphere has not been previously reported, despite our increasing knowledge of mid-oceanic rift systems, suggests that it is not a common occurrence. Whether this phenomenon is restricted to the vicinity of rapidly evolving, fast-spreading regions of the mid-oceanic ridge, and more specifically to the occurrence of microplates has yet to be examined. However, it seems unlikely that intraplate thrusting near the Easter Microplate remains a unique example.

CHAPTER 8
DISCUSSION

8.1 Introduction

The GLORIA survey of the Easter Microplate enabled the nature of all the microplate boundaries to be determined and showed evidence of rapid plate boundary evolution. Earthquake focal mechanisms have confirmed the idea that thrust faulting is not only taking place along the northern boundary of the microplate, but also in the Nazca plate to the north, and have shown that the microplate may not always behave rigidly. Interpretation of magnetic anomaly data and the complex structural information offered by the GLORIA images have permitted a detailed history of the microplate to be determined. Euler poles have been calculated for Nazca-Easter and Pacific-Easter relative motion, and the relative plate velocities they predict for the microplate boundaries are listed in Table 8.1 and shown on Fig. 8.1.

8.2 Evolution and the Future of the Easter Microplate

8.2.1 Microplate Evolution

The reconstructions described in Chapter 6 have shown that a reasonable understanding of the Easter Microplate's history can be established by rigidly rotating the three plates back in time around calculated Euler poles.

A constant rate of rotation was used for all of the reconstructions (15°/myr) and this enabled conjugate magnetic isochrons to be closed with reasonable accuracy throughout the microplate's evolution. Schouten et al.'s "roller-bearing" model predicts that the microplate rotated faster when it was smaller. However, the reconstructions described here show that faster rotation rates are not required to match the isochrons and structures observed back in time. In addition to this, Schouten et al.'s (1990) "roller-bearing" model predicts that the Nazca-Easter and Pacific-Easter instantaneous motion poles should migrate with the rift tips (i.e. southward along the East Rift and northwestward along the Southwest Rift) as the rifts were closed back in time. However, for these reconstructions, the relative motion poles were kept fixed with respect to the major plates on which they are situated, but not fixed relative to each other. Thus the major inner and outer pseudofaults of the East Rift and the initial rifting scarps of the Southwest Rift do not trace the loci of the Nz-Ea and Pa-Ea poles throughout the microplate's evolution. The idea that

TABLE 8.1 Current Spreading Rates and Azimuths for Easter Microplate

	Latitude/°S	*Longitude°W*	*Rate*	*Azimuth*
EPR Pa-Nz				
	22.00	114.38	155.70	106°
	22.50	114.47	156.04	106°
	23.00	114.49	156.36	106°
Pa-Ea				
	23.12	114.87	136.10	261°
	23.39	115.26	130.45	256°
	23.78	115.48	121.07	252°
	24.33	116.00	111.50	243°
	24.88	116.11	98.98	237°
	25.73	116.00	77.24	229°
	26.22	115.54	58.36	228°
	26.68	115.00	38.77	230°
	26.78	114.13	26.64	265°
	27.00	113.82	20.86	286°
	27.36	113.51	16.76	326°
	27.80	113.27	20.12	014°
Nz-Ea				
	27.22	113.04	138.57	097°
	26.50	112.60	116.55	092°
	26.00	112.49	101.76	091°
	25.50	112.47	87.03	090°
	24.78	112.11	66.43	082°
	24.27	112.09	51.68	079°
	23.92	111.82	43.89	067°
	23.41	111.67	33.06	050°
	23.00	112.00	18.06	047°
	23.00	112.51	-13.38	097°
	23.04	113.00	-20.81	136°
	23.08	113.50	-32.56	151°
	23.16	114.00	-45.83	157°

Figure 8.1 Simplified tectonic interpretation of the Easter Microplate, showing the plate motion vectors predicted by the Nz-Ea and Pa-Ea three-plate Euler poles. These two poles are indicated by stars; arrows indicate the magnitude of the plate velocity by their length (in km/yr, where 100 km/yr is drawn to the same scale as 100 km on the map), and the direction of plate movement is shown by the orientation of the arrows. The large black circle near the centre of the microplate indicates the present position of the absolute pole of microplate rotation, found by subtracting the Pa-Ea pole from the Pacific-hotspot pole of Pollitz (1986) to give the Easter-hotspot pole. This pole lies about 100 km NE of the centre of the microplate, and if correct, implies that movement relative to the asthenosphere will be faster in the southwest of the microplate than in the northeast. This pole lies slightly to the west of an imaginary line joining the Nz-Ea and Pa-Ea Euler poles, along which Schouten et al.'s (1990) second order motion pole would be expected to lie.

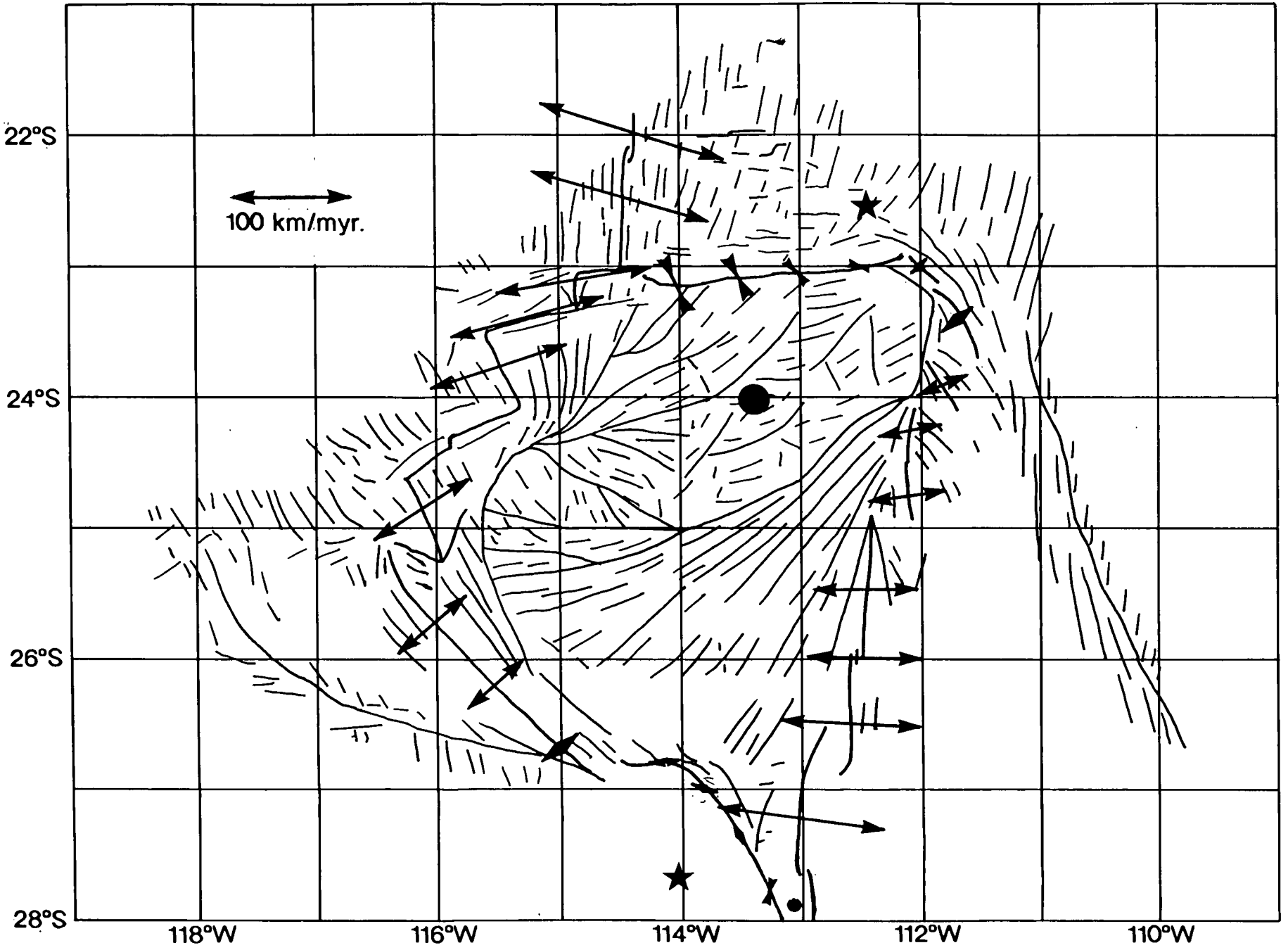
22°S
24°S
26°S
28°S
118°W
116°W
114°W
112°W
110°W
100 km/myr.

the Easter Microplate developed in two major phases as suggested by Schouten et al. (1990) is supported, but not the mechanism by which this occurs (see section 8.2.2).

The rigid reconstructions of the microplate back through time at intervals of 0.25 myr have revealed that the East Rift, and hence the microplate itself, started to form just after 5.25 Ma. Between 5.25 Ma and 2.5 Ma, the East Rift continually propagated northward at rates of between 170 mm/yr and 120 mm/yr. During this time, the continuously migrating, transpressive dextral shear couple between the tip of the East Rift and the EPR/West Rift was probably accommodated within a shear zone 15-20 km wide (north-south), analogous to those commonly found at propagator offsets (e.g. the Galapagos 95.5°W propagator). At the southern end of the growing microplate, transtensional, dextral strike-slip Pacific-Easter movement would have taken place along a possibly "leaky" transform fault which connected the southern end of the West Rift with the southern EPR/East Rift. This would have been along the site of the pre-existing Pacific-Nazca transform that was present prior to the formation of the microplate. Because the fast-slipping (160 mm/yr) Pacific-Nazca strike-slip movement was now taken up by dextral transtension along the southern boundary of the microplate and dextral transpression along the northern boundary, and by rapid clockwise rotation of the microplate, slip rates became minimal. Therefore, by comparison with the Galapagos 95.5°W propagator, the pre-existing abyssal hill normal fault blocks at the migrating northern boundary would only need to be rotated a few degrees to accommodate the required shear between the Nazca and Easter plates, and it may not be possible to distinguish this rotation from that caused by the rigid rotation of the microplate. The bookshelf faulting within the shear zone would also take up some of the resultant north-south convergence between the Easter and Nazca plates. The transform at the southern boundary of the microplate would have become increasingly transtensional as the microplate formed, and would have adjusted either by breaking up into smaller fault strands separated by extensional relay zones, or by becoming a "leaky" transform fault.

This study predicts that a fracture zone resulting from Nazca-Pacific motion prior to the formation of the microplate should be found in the relatively unmapped area to the east of Easter Island, where the few magnetic anomalies that exist to the north and south of the Easter Seamount Chain indicate a dextral offset of 1.5 - 2.0 myr. The fracture zone resulting from the proposed Easter-Pacific transform between 5.25 - 2.5 Ma would exist to the west of Easter Island where there is also an offset of about 120 km between anomaly 2A either side of the proposed fracture zone. The fact that no topographic feature has been mapped relating to this fracture zone may be due to lack of detailed mapping in most of the area and possibly because of the recent obliteration of earlier terrain by the Ahu Volcanic Field.

As the East Rift lengthened by rift propagation, in order to maintain the overall Nazca-Pacific motion around the growing microplate, the West Rift had to reorient itself in an anticlockwise direction. This it did by rotating up to 30° by rift propagation and the formation of transform faults to accommodate the offsets.

At sometime after 2.5 Ma, the East Rift ceased propagation. The reason and precise timing for this is not yet clear. One possibility is that if the Easter Microplate is likened to a large-scale overlapping spreading centre (Hey et al., 1985), Fig. 6.20 (Chapter 6) shows that the length to width ratio of the overlapped East and West Rifts at around 2.5 Ma was about 2:1. Although Macdonald et al. (1984) note that the length to width ratio of OSCs is generally 3:1, Sempere and Macdonald (1986) also observe that this is generally dependant on the initial offset of the two spreading centre limbs, that is, the closer the limbs are, the more elongate the overlap region will be. Thus for an extremely large initial offset on the order of 200 km at the Easter Microplate, the maximum length to width ratio obtainable may be 2:1, and after this is achieved, the rifts curve in towards one another, and finally one of the limbs dominates. Another possibility is that the driving force for the propagation of the East Rift lessened as the distance between the rift tip and the southern boundary increased. After about 450 km of northward propagation away from the influence of the Easter hotspot, the conditions necessary for further propagation were no longer met.

Whatever the reason for the cessation of propagation of the East Rift, the effect this had was significant. After 2.5 Ma, the Southwest Rift started to open up, presumably along the Easter-Pacific transform if it existed. At the same time, the transpressive shear zone in the north between the tip of the East Rift and the EPR/West Rift ceased migrating northwards, and so the northern boundary as we know it started to form. Since then, no more lithosphere from the Nazca plate north of the microplate was transferred to the microplate across the migrating northern boundary. The Pito Deep region was caused to open up by pervasively rifting apart pre-existing Nazca plate lithosphere. Since the microplate stopped growing northwards, it could now only broaden in an east-west sense by spreading and so its relative rate of expansion became less. This rate is further reduced by the continuous process of rift propagation to the inside (microplate side) of other rifts around the microplate, which transfers Easter Microplate lithosphere onto the surrounding major plates.

The position of the Easter hotspot remains unclear. However, it is becoming increasingly likely that it may either be situated beneath the Ahu Volcanic Field (at around 26.5°S, 111°W), as tentatively suggested by Hagen et al. (1990), or slightly closer to the East Rift. However, adding the Nazca-Pacific three-plate closure pole calculated in

Chapter 5 to the Pacific-Hotspot pole of Pollitz (1986) results in a predicted Nazca-Hotspot motion of about 50 mm/yr at the latitude of the Ahu Volcanic Field; if the hotspot was situated beneath Easter Island as the East Rift started to propagate northwards, this would place the hotspot some 260 km west of Easter Island now, at around 112°W, i.e. to the west of the Ahu Volcanic Field. If the hotspot is underneath the Ahu Volcanic Field now, this would imply a slower Nazca-Hotspot rate at this latitude of around 33 mm/yr (or that the hotspot was east of Easter Island at 5.25 Ma). Adding the Easter-Pacific pole to the Pacific-Hotspot pole produces an Easter-Hotspot pole (shown by the large black dot in Fig. 8.1) roughly 100 km NNE of the centre of the microplate. This pole is close to an imaginary line joining the Pacific-Easter and Nazca-Easter Euler poles, on which the secondary order microplate rotation pole should be located according to the Schouten et al. (1990) model, but the major East and West Rift pseudofaults do not form a small circle around it. The position of the Easter absolute motion pole suggests that the southwest corner of the microplate evolves slightly faster than the northeast.

8.2.2 Microplate Models

Initially, microplates were thought to behave non-rigidly, so that the whole of the microplate deformed internally by continuous simple shear (e.g. Hey, et al., 1985). As the present configuration of the Easter Microplate became more apparent, two hypothesis for the behaviour of microplates developed. Firstly, Engeln et al. (1988) modelled microplate evolution assuming both rigid and shear-deformed microplates, and stressing the effects of rift propagation, whereby the dominant East Rift would eventually replace the West Rift (Fig. 1.9a,b, Chapter 1). They found that the Easter Microplate behaved largely as a rigid plate, though there was some evidence of shearing within it. Their rigid microplate model predicted convergence along the northern boundary, and conversion of the initial southern boundary into a slow-spreading ridge, both of which have been observed at the Easter Microplate. Secondly, Schouten, et al. (1990), in contrast, have discussed microplates by analogy to a ball- (or roller-) bearing rotating between two major plates. They emphasise the torque applied by the major plates as an important driving force for microplate rotation. Ideally, the instantaneous relative poles of rotation between the major plates and the microplate must lie at the tips of the propagating East and West Rifts, and migrate with these rift tips as they propagate. Thus the pseudofaults formed should trace the loci of the relative motion poles throughout the microplate's evolution.

To a certain degree, both of these models are applicable to the Easter Microplate. The rigid model of Engeln et al. (1988) predicts the opening up of the Southwest Rift in response to the microplate rotation, as well as the formation of a convergent zone along the northern boundary of the microplate, both of which are clearly seen. The geometry of

this rigid plate model is largely dependant on the starting configuration, for if they had modelled a microplate that was originally round, as in Schouten et al.'s earlier simplified models, there would be no need for a compressive northern boundary nor a tensional southern one. Instead, there would always be compression ahead of the propagating tips and extension behind them, with continuous evolution of the plate boundary configuration to accommodate this. However, their assumptions that (a) prior to the formation of the microplate, the East Pacific Rise was offset along a ridge-normal transform and that (b) the East Rift originally propagated northwards seem valid, so that the starting configuration never was amenable to the microplate behaving as a ball-bearing. However, it could of course behave rather as a cam between the two major plates, as suggested by Searle et al. (1989).

The failure of the Engeln et al. (1988) model is that it assumes that the East Rift is propagating at the expense of the West Rift, as in a general propagating rift model, so that as the East Rift continues spreading, the West Rift is predicted to gradually fail and eventually cease propagation. This is clearly not the case, as the West and Southwest Rifts are actively propagating towards the southern EPR, and are known to be magmatically active at the present-day, around 5 Ma after the East Rift started to form. This is shown not only from the highly reflective sidescan sonar images obtained (both SeaMARC II and GLORIA), but also from recent camera runs and rock samples collected (Marchig et al., 1986; 1989). The Schouten et al. (1990) idea that the torque applied by the major plates is the major driving force for microplate rotation seems to be applicable, as the persistent rift propagation can not be readily explained by the usual mechanisms (such as propagation away from a hotspot, or due to a negative gravity gradient).

I have modelled the Easter Microplate's evolution with the two microplate-plate Euler poles fixed onto the respective major plates on which they lie, and using a constant angular rotation rate of the Easter Microplate throughout. This implies that if the size of the microplate decreases back in time, while the rate of separation between the Pacific and Nazca plates remains constant, and the distance between the Pacific-Easter and Nazca-Easter Euler poles does not vary significantly, there must be increasing slip along the northern and southern boundaries through progression back in time as shown by the reconstructions. I have thus taken the simplest model of microplate evolution, and shown that it can adequately explain the present pattern of tectonic lineaments revealed by the GLORIA data, and the magnetic isochrons that have been interpreted. I have shown that using this method, the Schouten et al. (1990) model cannot be applied, since the pseudofaults do not mark the loci of the Euler poles. Although Schouten et al. (1990) have attempted to show that the shapes of the major pseudofaults can be predicted from their model, little account is taken of the pattern of the abyssal hill fabric between these

pseudofaults, nor of the magnetic isochrons, which should be far less linear and more strongly rotated (especially to the west of the East Rift) if their model is applicable. Preliminary attempts to model these structures by assuming the Euler poles always remain at the tips of the propagators have not been unsatisfactory, as the conjugate isochrons fail to match up with increasing rotation back in time.

8.2.3 Future Evolution of the Easter Microplate

The future of the Easter Microplate can only be guessed at by comparison with mapped palaeoplates within the Pacific basin. Of the three palaeoplates found on the flank of the EPR, the Bauer microplate existed for less than 5 Ma, the Mathematician for around 7 Ma, and the Mendoza for less than 10 Ma, which may suggest that sometime within the next five million years the Easter Microplate will cease to exist. The same principles that were applied to the reconstructions of the microplate in Chapter 6 have also been applied in an attempt to model its future (i.e. at increments of 0.25 myr, and keeping the poles of rotation fixed relative to the plates on which they lie). The resulting configurations at "1 myr from now" and "2 myr from now" are shown in Fig. 8.2a,b. Unlike during the reconstructions, there is no control on the positioning of the transform faults on the West Rift, nor on rift propagation events on the West, Southwest and East Rifts. Hence all that is shown is the amount of lithosphere which may be accreted during the next 2 myr, providing there is no further evolution of the major- or microplate boundaries or poles.

Schouten et al. (1990) have suggested that as the Southwest Rift is propagating considerably faster than the tip of the East Rift, the Southwest Rift will propagate through to the EPR before long. Once this happens, the shear couple on the microplate will cease, and either the East or the West Rift will cease spreading, and the microplate will die. The amount of opening that is shown along the present day Orongo fracture zone and beyond in the "2 myr from now" representation of the microplate suggests that the Southwest Rift may well have propagated through to the EPR by this time. When this happens the East Rift will stop spreading and the microplate will be abandoned onto the Nazca plate. Alternatively, the West Rift will be unable to reorient itself parallel to the Pacific-Nazca spreading direction once again, and will become locked, so that the East Rift will have to take over, leaving the microplate on the Pacific plate. The abandoned Bauer, Mendoza and Roggeveen palaeoplates (Fig. 1.5, Chapter 1) appear to be mirror images of the Easter Microplate, in as much as they have evolved from rift propagation to the west of the original major plate boundary, have rotated in an anticlockwise direction, and have subsequently been abandoned onto the Nazca plate. By analogy with these palaeoplates, the Easter Microplate should thus eventually be abandoned onto the

Figure 8.2 Rotations of the Nazca and Easter plates relative to the Pacific plate, but in the opposite sense to those in Chapter 6, have been carried out in an attempt to model the future of the Easter Microplate. As before, the rotations were performed at time increments of 0.25 myr, and the poles of rotation were fixed relative to the major plates on which they are situated. Here the resulting configurations at '1 myr from now' and 2 myr from now' are shown in (a) and (b) respectively. Unlike during the reconstructions, there is no control on the positioning of the transform faults on the West Rift, nor on rift propagation events on the West, Southwest and East Rifts. Hence all that is shown is the amount of accretion which may occur during the next 2 myr, providing there is no further evolution of the plate boundaries or poles.

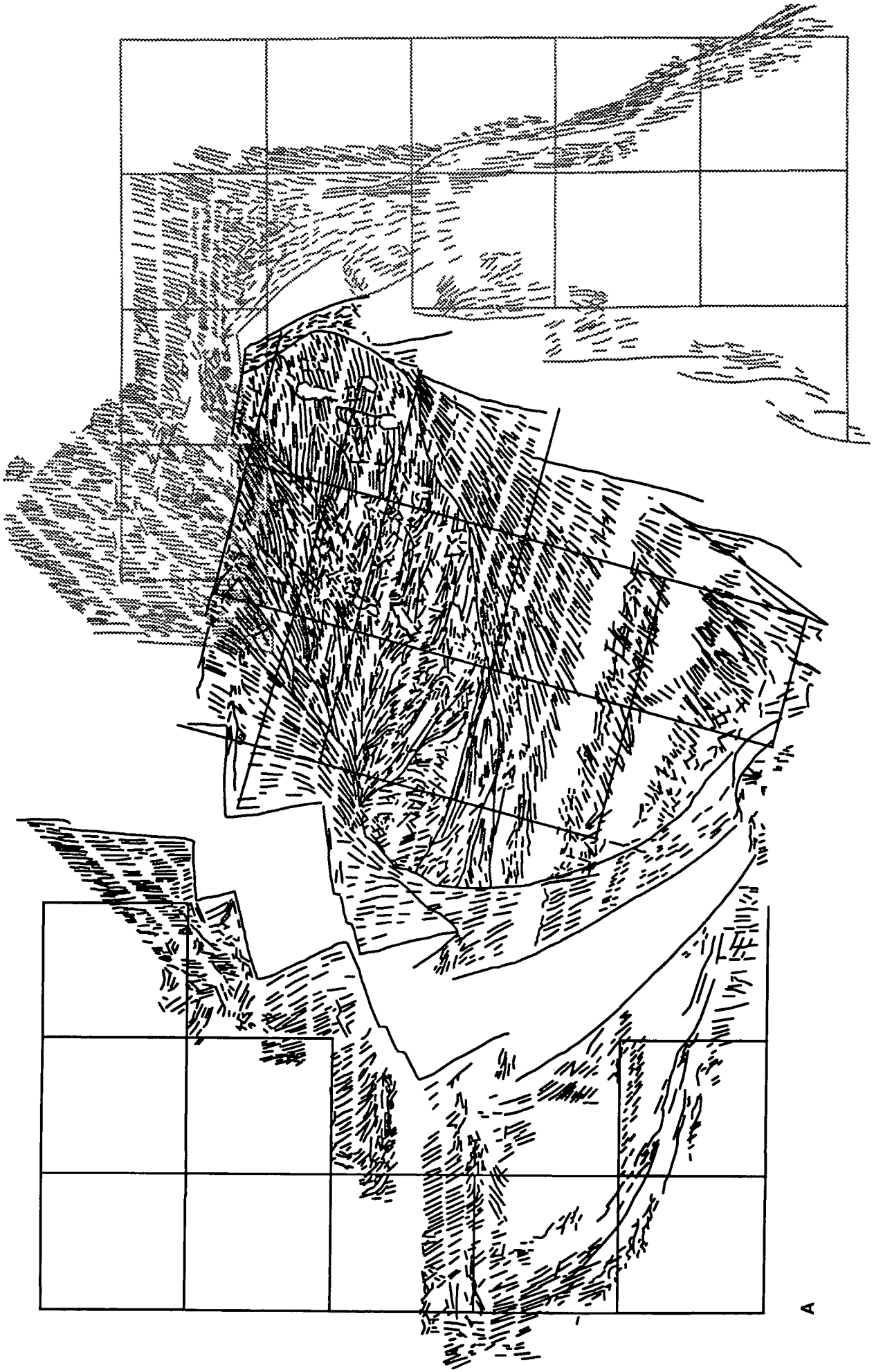
A

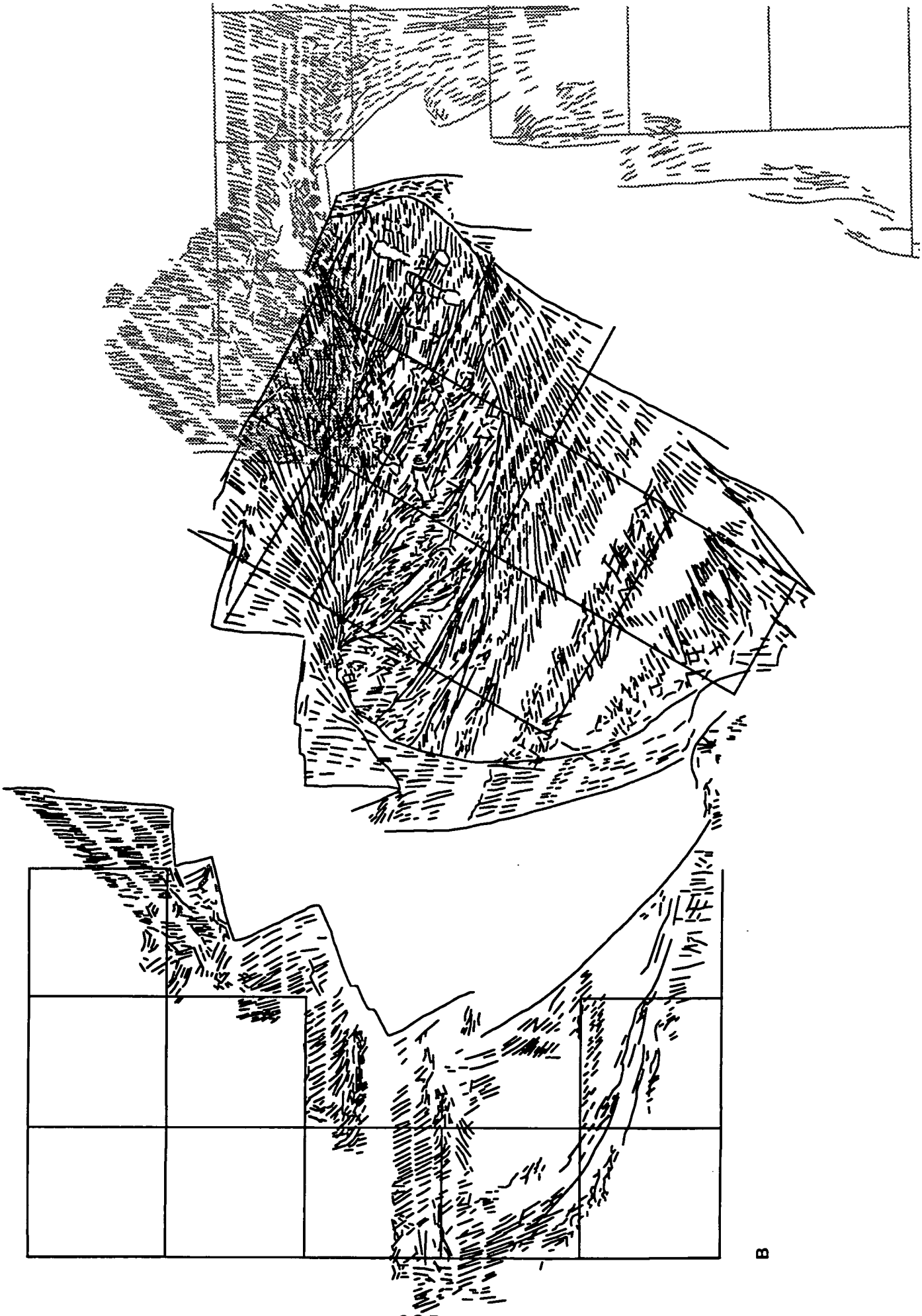
B

Pacific plate as the West Rift ceases spreading, and the East Rift becomes the new Pacific-Nazca plate boundary.

The reason for the formation of microplates is not yet firmly established. Hey et al. (1985) suggested that the Easter Microplate was the result of rift propagation on a very large scale. The microplate was viewed as a transient phenomenon between overlapping propagating and failing rifts. The West Rift was assumed to be failing as the East Rift took over. Mantle convection or superfast spreading were thought to be responsible for the rift propagation event, and the Easter Microplate was considered a present-day analogue for the re-organisation of the Pacific-Farallon to Pacific-Nazca system at 24 Ma.

A recent GLORIA survey has been conducted of the Juan Fernandez microplate (Bird et al., 1991; Larson et al., in press) situated at around 34°S, at the triple junction between the Pacific, Nazca and Antarctic major plates. One of the most remarkable discoveries has been the striking similarity between the Juan Fernandez and Easter microplates, despite their apparently different tectonic settings. Both these microplates have formed at around the same time (approximately 5 Ma ago), and both have formed as the result of the northward propagation of a new East Rift. This perhaps signifies a common cause. The most obvious explanation for the formation of two similar microplates along the EPR at about the same time would be a change in absolute motion of either the Pacific or Nazca plates at around 5 Ma. Lonsdale's (1989) study of ridge segmentation along the EPR has led to the conclusion that changes in major plate boundary configurations are intimately linked to the formation of microplates, and that the latter phenomenon may allow the former to occur.

Several authors (Stock & Molnar, 1982; Cox & Engebretson, 1985; Pollitz, 1986; Harbert & Cox, 1989) have proposed changes in absolute motion of the Pacific plate at varying times between 3 Ma and 9.8 Ma, depending on the data examined. Cox and Engebretson (1985) proposed a change in the motion of the Pacific plate at around 5 Ma, based changes in Pacific-North American, Pacific-Juan de Fuca and Pacific-Antarctic relative plate motions at this time. They propose that the observed clockwise change in motion of the Pacific plate could be produced by the detachment of a piece of seafloor which had been subducted beneath the Fiji plateau during the Tertiary. The other authors suggest similar changes in subduction at the western edge of the Pacific plate to explain the observed clockwise rotation of the Pacific plate at some time around 5 Ma. Such a clockwise change in motion would place the pre-existing Pacific-Nazca transform under transpression, causing the initiation of rift propagation along the new East Rifts of the proto-microplate. Once this had happened, the West Rift could re-organise itself by rift

propagation and the formation of new transforms, and the southern transform would begin to open up.

There are several plausible explanations for the slowing down and eventual abandonment of microplates onto a major plate. Resistance to motion of the microplate may increase with its size. Microplates, even if they were initially circular, are unlikely to remain so, as some of theri edges are accreting new lithosphere. They therefore act more like cams than ball-bearings, trying to force the major plates apart and naturally being resisted. As this happens, viscous drag on the base of the microplate will increase with plate area. Variations in the configuration of the microplate boundaries may cause changes to either the driving or braking forces acting on the microplate, e.g. conversion of a transform (low stress) boundary to a compressive (strong braking) one.

8.3 Future Areas of Research

Evidence on the GLORIA images for previous locations of propagators and fracture zones has helped to constrain the reconstructions of the West Rift. More GLORIA data is needed to the west and the east of the microplate to fully constrain its evolution during the past few million years. The major inner and outer pseudofaults of the East Rift have provided the main control for determining the evolution of the East Rift. If additional GLORIA data were available between the East Rift and the outer pseudofault, the history of individual propagation events might be controlled. In addition to this, a detailed aeromagnetic or shipboard magnetic survey is required to the east and west of the Easter Microplate out to lithosphere that is at least 5.5 Ma old, in order to place greater constraint on the early history of the microplate. Also a couple of north-south track lines with magnetics across the microplate interior would enable the existing magnetic anomalies of this region to be interpreted with more confidence.

The Easter Microplate is the most extensively studied of the present-day microplates, and may be considered the "type" example. The obvious similarity between the Easter and Juan Fernandez microplates, and again between these microplates and the known structures of the Mathematician, Bauer, Mendoza, Roggeveen and Selkirk palaeoplates strongly suggests a common cause for their formation, and similar driving forces fot their evolution. If, as Lonsdale (1989) proposes, microplates are merely the mechanism by which major changes in orientation of fast-spreading mid-ocean ridges occur, involving large-scale rift propaagation, then the relative abundance of these events should allow this hypothesis to be tested.

"Picoplates" (or "protomicroplates") microplates and palaeoplates represent three stages of evolution of the same system: examination of the possible existence of to

"protomicroplates" along the EPR will permit a fuller understanding of not just why these microplates evolve, but also how they were initially formed; comparison of the presently existing Easter, Juan Fernandez and Galapagos microplates will allow the two models of microplate behaviour (Engeln et al., 1988; Schouten, et al., 1990) to be resolved; and further detailed analysis of the magnetic anomalies and structures of the palaeoplates will enable their kinematic histories to be established, thus shedding light on the process of maturation of microplates leading to their eventual slowing down and abandonment onto one of the major plates.

CHAPTER 9
CONCLUSIONS

The GLORIA and other geophysical data obtained during this study enabled the entire present-day tectonic pattern of the Easter Microplate to be determined. Interpretation of magnetic anomaly data and the complex structural information revealed by the GLORIA images have permitted a detailed account of the evolution of the microplate to be resolved. The principal conclusions reached in this study are :

1. Rapid evolution of the plate boundaries is accommodated by small changes in the orientation (< 10°) of the Anakena, Raraku and Terevaka transforms along the West Rift of the microplate, and by subtle changes in orientation of individual ridge segments by rift propagation along the East Rift. Earlier plate boundary reorganisations along the West Rift of more than a few degrees have been accommodated by the southward propagation of a new rift.

2. The GLORIA data provide the first unequivocal evidence that dextral transpression along the northern boundary is being accommodated by thrust faults connected by strike-slip transfer faults. Further evidence for this is given by an earthquake with a thrust fault focal mechanism. Pure strike-slip movement only occurs at the eastern end of the boundary, and possibly to the east of the northern triple junction.

3.Thrust faulting is taking place on the Nazca plate to the north of the microplate along a series of en echelon ridges imaged by GLORIA that extend from around 22°S, 114°W southeastwards towards the Nazca-Easter instantaneous Euler pole, and the Pito Deep region at 23°S, 112°W. The whole of this region is under dextral compression, which causes normal abyssal hill faults to be re-activated and rotated clockwise. Earthquake focal mechanisms confirm this idea.

4. Rigid rotations of the Pacific, Nazca and Easter plates back in time (with a constant rotation rate of 15°/myr.) has enabled a two-phase history of the microplate to be determined. The Nazca-Easter and Pacific-Easter instantaneous motion poles did not migrate along the closing rift tips, but instead were kept fixed with respect to the major plates on which they are situated. Thus Schouten et al.'s (1990) "roller-bearing" model, which predicts that the major inner and outer pseudofaults of the East Rift and the initial rifting scarps of the Southwest Rift trace the loci of the Nz-Ea and Pa-Ea poles throughout the microplate's evolution is not valid.

5. The East Rift of the microplate, and hence the microplate itself, started to form just after 5.25 Ma. The first phase of evolution of the microplate was between 5.25 Ma and 2.5 Ma. during this time the East Rift continually propagated northward so that the transpressive dextral shear couple between the tip of the East Rift and the EPR/West Rift had to migrate with it. At the same time a transtensional transform fault existed along the southern boundary of the microplate, which would have exploited the site of a pre-existing Nazca-Pacific transform. As the East Rift lengthened by rift propagation, the West Rift had to re-orient itself by up to 30° in an anticlockwise direction in order to keep the overall Nazca-Pacific velocities the same.

6. At sometime after 2.5 Ma, the East Rift ceased propagation and the Southwest Rift started to open up, presumably along the Easter-Pacific transform. During this second phase, the transpressive shear zone in the north between the tip of the East Rift and the EPR/West Rift ceased migrating northwards, and so the northern boundary as we know it started to form. Since then, no more lithosphere from the Nazca plate north of the microplate was transferred to the microplate across the migrating northern boundary and the Pito Deep region began to open up by pervasive rifting apart of pre-existing Nazca plate lithosphere.

7. Within the next 2 - 5 myr., the Southwest Rift may propagate through to the EPR. When this happens, either the East Rift or the West Rift will stop spreading, and the microplate will be abandoned onto the Nazca or the Pacific plate. By analogy to the Mendoza, Bauer and Mathematician palaeoplates, it seems likely that the West Rift of the Easter Microplate (i.e. the older, segmented rift) will stop spreading, and that the microplate will be abandoned onto the Pacific plate.

REFERENCES

Acton, G.,D., Stein, S. & Engeln, J.F., Block rotation and continental extension in Afar: a comparison to oceanic microplate systems, Tectonics, **10**, 501-526, 1991.

Anderson, R.N., Forsyth, D.W., Molnar, P., & Mammerickx, J., Fault Plane Solutions on the Nazca Plate Boundaries and the Easter Plate, Earth Planet. Sci. Lett., **24**, 188-202, 1974.

Anderson, R.N. & Sclater, J.G., Topography and evolution of the East Pacific Rise between 5°S and 20°S, Earth Planet. Sci. Lett., **14**, 433-441, 1972.

Anderson, R.N., Forsyth, D.W., Molnar, P., & Mammerickx, J., Fault Plane Solutions on the Nazca Plate Boundaries and the Easter Plate, Earth Planet. Sci. Lett., **24**, 188-202, 1974.

Anderson-Fontana, S., Engeln, J.F., Lundgren, P., Larson, R. & Stein, S., Tectonics and evolution of the Juan Fernandez Microplate at the Pacific-Nazca-Antarctic triple junction, J. Geophys. Res., **91**, 2005-2018, 1986.

Baker P.E., Buckley, F. & Holland, J.G., Petrology and geochemistry of Easter Island, Contr. Mineral. Petrol., **44**, 85-100, 1974.

Bird, R.T., Larson, R.L., Searle, R.C., Kleinrock, M.C., Schouten, H., Naar, D.F., Rusby, R.I., Hooft, E.E. & Lasthiotakis, H., The Juan Fernandez Microplate Unveiled, EOS Trans. AGU, **72**, 1991.

Bonatti, E., Harrison, C.G.A., Fisher, D.E., Honnorez, J., Schilling, J.-G., Stipp, J.J. & Zentilli, Easter volcanic chain (southeast Pacific): A mantle hotline, J. Geophys. Res., **82**, 2457-2478, 1977.

Burke, K., Kidd, W.S.F. & Wilson, J.T., Nature Phys. Sci., **241**, 128-129, 1973.

Byerly, G.R., Melson, W.G., and Vogt, P.R., Rhyodacites, andesites, ferrobasalts and ocean tholeiites from the Galapagos spreading center, Earth Planet. Sci. Lett., **30**, 215-221, 1976.

Byerly, G.R., The nature of differentiation trends in some volcanis rocks from the Galapagos spreading center, J. Geophys. Res., **85**, 3797-3810, 1980

Cann, J.R., A model for oceanic crustal structure developed, Geophys. J. R. astr. Soc., **39**, 169-187, 1974.

Caress, D.W., Menard, H.W. & Hey, R.N., Eocene reorganization of the Pacific-Farallon spreading center north of the Mendocino fracture zone, J. Geophys. Res., **93**, 2813-2838, 1988.

Carter, D.J.T., Echo-sounding correction tables, formerly Matthews' Tables, 150pp., Np 139, 3rd Edition, Taunton, England: Hydrographic Department, Ministry of Defense, 1980.

Chavez, P.S., U.S. Geological Survey Mini Image Processing System (MIPS), Open File Report 84-353, Reston, Virginia, 1984.

Chavez, P.S., Processing techniques for digital sonar images from GLORIA, Photogrammetric Engineering and Remote Sensing, **52**, 1133-1145, 1986.

Christie, D.M. & Sinton, J.M., Evolution of abyssal lavas along propagating segments of the Galapagos spreading center, Earth Planet. Sci. Lett., **56**, 321-335, 1981

Christie, D.M., & Sinton, J.M., Major element constraints on melting, differentiation and mixing of magmas from the Galapagos 95.5°W propagating rift system, Contrib. Mineral. Petrol., **94**, 274-288, 1986.

Clark, J.G., & Dymond, J., Geochronology and petrochemistry of Easter and Salay Gomez Islands: implications for the origin of the Sala y Gomez Ridge, J. Volcanol. Geotherm. Res., **2**, 29-48, 1977.

Cox, A. & Engebretson, D., Change in motion of Pacific plate at 5 Myr BP, Nature, **313**, 472-474, 1985.

Craig, H., Kim, K-R., & Rison, W., Easter Island Hotspot: I. Bathymetry, Helium Isotopes, and Hydrothermal Methane and Helium, EOS, **65**, 45, 1984.

Cross, W., Iddings, J.P., Pirsson, L.V., & Washington, H.S., Quantitative classification of igneous rocks. University of Chicago Press, 1903.

DeMets, C., Gordon, R.G., Argus, D.F. & Stein, S., Current Plate Motions, Geophys. J. Int., **101**, 425-478, 1990.

Dziewonski, A.M., Chou, T.-A. & Woodhouse, Determination of earthquake source parameters from waveform data for studies of global and regional seismicity, J. Geophys. Res., **86**, 2825-2852, 1981.

Dziewonski, A.M & Woodhouse, J.H., An experiment ifn systematic study of global seismicity: Centroid moment tensor solutions for 201 moderate and large earthquakes of 1981, J. Geophys. Res., **88**, 3247-3271, 1983

EEZ-SCAN 84 Scientific Staff, Physiography of the Western United States Exclusive Economic Zone, Geology, **16**, 131-134, 1988.

Engeln, J.F., & Stein, S., Tectonics of the Easter plate, Earth Planet. Sci. Lett., **68**, 259-270, 1984.

Engeln, J.F., Stein, S., Werner, J., & Gordon, R.G., Microplate and Shear Zone models for Oceanic Spreading Centre Reorganizations, J. Geophy. Res., **93**, 2839-2856, 1988.

Farr, H.K., Multibeam bathymetric sonar: Sea Beam and Hydrochart, Marine Geodesy, **4**, 77-93, 1980.

Fontignie, D. & Schilling, J.-G., 87Sr/86Sr and REE variations along the Easter microplate boundaries: application of multivariate statistical analyses to ridge segmentation, Chem., Geol., **89**, 209-241, 1991.

Forsyth, D. W., Mechanisms of earthquakes and plate motions in the east Pacific, Earth Planet. Sci. Lett., **17**, 189-193, 1972.

Fox, P.J. & Gallo, D.G., A tectonic model for ridge-transform-ridge plate boundaries: implications for the structure of oceanic lithosphere, Tectonophysics, **104**, 205-242, 1984.

Francheteau, J., Yelles-Chaouche, A., & Craig, H., The Juan Fernandez Microplate north of the Pacific-Nazca-Antarctic Junction at 35°S, Earth Planett. Sci. Lett., **86**, 253-268, 1987.

Francheteau, J., Patriat, P., Segoufin, J., Armijo, R., Doucoure, M.,Yelles-Chaouche, A., Zukin, J., Naar, D.F., & Searle, R.C., Pito and Orongo fracture zones: the northern and southern boundaries of the Easter microplate (southeast Pacific), Earth Planet. Sci. Lett., **89**, 363-374, 1988.

Hagen, R.A., Baker, N.A., Naar, D.F. & Hey, R.N., A SeaMARC II Survey of Recent Submarine Volcanism Near Easter Island, Mar. Geophys. Res, **12**, 297-315, 1990.

Hanan, B.B., & Schilling, J-G., Easter Microplate Evolution: Pb Isotope Evidence, J. Geophys. Res., **94**, 7432-7448, 1989.

Handschumacher, D. W., Post-Eocene Plate Tectonics of the Eastern Pacific. In: Sutton et al. (eds), Geophysics of the Pacific Ocean and Its Margin, AGU Geo,1976.

Handschumacher, D.W., Pilger, R.H., Foreman, J.A., & Campbell, J.F., Structure and evolution of the Easter plate, Geological Society of America, Memoir **154**, 1981.

Harbert, W. & Cox, A., Late Neogene Motion of the Pacific Plate, J. Geophys. Res., **94**, 3052-3064, 1989.

Harding, A.J. et al., Structure of Young Oceanic Crust at 13°N on the East Pacific Rise From Expanding Spread Profiles, J. Geophys. Res., **94**, 12163-12196, 1989.

Harland, W.B., Armstrong, R.L., Cox, A.V., Craig, L.E., Smith, A.G. & Smith, D.G., A geologic time scale, 1989, pub. Cambridge University Press, Cambridge, 1990.

Herron, E.M., Two Small Crustal Plates in the South Pacific near Easter Island, Nature Phys. Sci., **240**, 35-37, 1972a.

Herron, E. M., Sea-Floor Spreading and the Cenozoic History of the East-Central Pacific. Geol. Soc. America Bull., **83**, 1671-1692, 1972.Herron, E. M., 1972b.

Hey, R.N., Johnson, G.L. & Lowrie, A., Trans. Am. geophys. Un., **54**, 244, 1973.

Hey, R.N., A new class of "pseudofaults" and their bearing on plate tectonics: a propagating rift model, Earth Planet. Sci. Lett., **37**, 321-325, 1977.

Hey, R.N., Naar, D.F., Kleinrock, M.C., Phipps Morgan, W.J.Morales, E. & Schilling, J.-G., Microplate tectonics along a superfast seafloor spreading system near Easter Island, Nature, **317**, 320-325, 1985.

Hey, R.N. & Naar, D.F., Cruise Report, R/V Moana Wave, Leg 8711, SeaMARC II Investigation of the Easter Microplate, Hawaii Institute of Geophysics, University of Hawaii, Honolulu, 1-23, 1987.

Hey, R.N. & Wilson, D.S., Propagating rift explanation for the tectonic evolution of the northeast Pacific - the pseudomovie, Earth Planet. Sci. Lett., **58**, 167-188, 1982.

Hey, R.N., Sinton, J.M., Atwater, T.M., Christie, D.M., Johnson, H.P.Kleinrock, M.C., Macdonald, K.C., Miller, S.P., Neal, C.A., Searle, R.C., Sleep, N.H. & Yonover, R.N., ALVIN Investigation of an active Propagating Rift System, 95.5 W, Cruise proposal, 1989.

IAGA (International Association of Geomagnetism and Aeronomy, Division I, Working Group 1), International Geomagnetic Reference Field Revision 1985, EOS Trans. AGU, **67**, 523-524, 1986.

Jarrard, R.D., & Clague, D.A., Implications of Pacific island seamount ages for the origin of volcanic chains, Reviews of Geophysics and Space Physics, **15**, 57-76, 1977.

Klaus, A., Icay, W., Naar, D. & Hey, R.N., SeaMARC II Survey of a Propagating Limb of a Large Nontransform Offset Near 29°S Along the Fastest Spreading East Pacific RIse Segment, J. Geophy. Res., **96**, 9985-9998, 1991.

Kleinrock, M.C. & Hey, R.N., Migrating Transform Zone and Lithospheric Transfer at the Galapagos 95.5°W Propagator, J. Geophys. Res., **94**, 13, 859-13,878, 1989.

Kogan, M.G., Gravity anomalies and the origin of the Walvis Ridge, J. Geophys. Res., **84**, 6019-6025, 1979.

Kusznir, N.J. & Park, R.G., The strength of intraplate lithosphere, Phys. Earth Planet. Int., **36**, 224-235, 1984.

LaBreque, J.L. Kent, D.V., & Cande, S.C., Revised magnetic polarity time-scale for Late Cretaceous and Cenozoic time, Geology, **6**, 330-335, 1977.

Larson, R.L., Searle, R.C. Kleinrock, M.C., Schouten, H., Bird, R.T., Naar, D.F., Rusby, R.I., Hooft, E.E., & Lasthiotakis, H., The Juan Fernandez Microplate, Submitted to Nature, 1991.

Lonsdale,P., & Klitgord, K.D., Structure and tectonic history of the eastern Panama basin, Geol. Soc. Am. Bull., **89**, 981-999, 1978.

Lonsdale, P., Structural Pattern of the Galapagos Microplate and Evolution of the Galapagos Triple Junctions, J. Geophys. Res., **93**, 13551-13574, 1988.

Lonsdale, P., Segmentation of the Pacific-Nazca Spreading Center, 1°N - 20°S, J. Geophys. Res, **94**, 12197-12225, 1989.

Lonsdale, P.F., Overlapping rift zones at the 5.5 degree offset of the East Pacific Rise, J. Geophys., Res., **88**, 9393-9406, 1983.

Macdonald, K.C., Sempere, J.-C. & Fox, P.J., The East Pacific Rise from the Siqueiros to the Orozco fracture zone: Along-strike continuity of the neovolcanic zone and the structure and evolution of overlapping spreading centers, J. Geophys. Res., **89**, 6049-6069, 1984.

Macdonald, K.C., Fox, P.J., Perram, L.J., Eisen, M.F., Haymon, R.M., Miller, S.P., Carbotte, S.M., Cormier, M.-H. & Shor, A.N., A new view of the mid-ocean ridge from the behaviour of ridge-axis discontinuities, Nature, **335**, 217-225, 1988.

Macdonald, K.C., Haymon, R.M., Miller, S.P., Sempere, J.-C. &Fox, P.J., Deep-Tow and Sea Beam Studies of Dueling Propagating Ridges on the East Pacific Rise Near 20 40'S, J. Geophys. Res., **93**,2875-2898, 1988.

Macdougall, J.D. & Tanzer, M.O., Easter Island Hotspot: II. Isotopic and Chemical Evidence of its Influence on EPR Basalts, EOS, **65**, 45, 1984.

Mammerickx, J., Herron, E., & Dorman, L., Evidence for two fossil spreading ridges in the southeast Pacific. Geol. Soc. America Bull., **91**, 263-271, 1980.

Mammerickx, J., Naar, D.F. & Tyce, R.L., The Mathematician Paleoplate, J. of Geophys. Res., **93**, 3052-3040, 1988.

Mammerickx, J. & Sharman, G.F., Tectonic evolution of the north Pacific during the Cretaceous quiet period, J. Geophys. Res., **93**, 3009-3024, 1988

Mammerickx, J. & Carmichael, I.S.E., A Spreading Incursion in the Continent Near the Rivera Plate and Jalisco Block?, EOS Trans AGU, **43**, 1318, 1989.

Marchig, V., et al., Sonne 40 Cruise Report, Bundesanstalt fur Geowissenschaften und Rohstoffe, 1986.

Marchig, V. & Gundlach, H., and the Shipboard Scientific Party, Ore Formation at Rapidly Diverging Plate margins, Results of Cruise Geometep 4, BGR, Hannover, 1987.

Marchig, V., et al., Sonne 62 Cruise Report, Bundesanstalt fur Geowissenschaften und Rohstoffe, 1989.

Marchig, V., Wilke, M. & Holler, G., The Eastern Divergent Boundary of the Easter Microplate. Hydrothermal Activity and its affect on the Surrounding Sediments, Unpublished manuscript, 1988.

Martinez, F., Naar, D.F. & Hey, R.N., Lithospheric Extension at Pito Deep: Fault Block Tectonocs at a Large-Offset Propagating Rift Tip of the Easter Microplate. EOS Trans. AGU, **71**, 640-641, 1990.

Martinez, F., Naar, D.F., Reed IV, T.B. & Hey, R.N., Three-Dimensional SeaMARC II, Gravity, and Magnetics Study of Large-Offset Rift Propagation at the Pito Rift, Easter Microplate, submitted to Mar. Geophys. Res., November, 1990.

McKenzie, D.P. & Bowin, C., The relationship between bathymetry and gravity in the Atlantic Ocean, J. Geophys. Res., **81**, 1903-1915, 1976.

McKenzie, D.P. & Jackson, J., The relationship between strain rates, crustal thickening, paleomagnetism, finite strain and fault movements within a deforming zone, Earth Planet. Sci. Lett., **65**, 182-202, 1983.

McKenzie, D.P. & Sclater, J.G., The evolution of the Indian Ocean since the late Cretaceous, Geophys. J. R. astron. Soc., **24**, 437-528, 1971.

Minster, J.B., Jordan, T.H., Molnar, P. & Haines, E., Numerical Modelling of Instantaneous Plate Tectonics, Geophys. J. R. Astr. Soc., **36**, 541-576, 1974.

Minster, J. B., and Jordan, T. H., Present-day Plate Motions, J. Geophys. Res., **83**, 5331-5354, 1978.

Minster, J.B., Jordan, T.H., Molnar, P. & Haines, E., Numerical Modelling of Instantaneous Plate Tectonics, Geophys. J. R. Astr. Soc., **36**, 541-576, 1974.

Mitchell, N.C., Improving GLORIA Images Using Sea Beam Data, J. Geophys. Res., **96**, 337-351, 1991.

Morelli, C. (comp.), The International Gravity Standardization Net 1971, 194pp., International Association of Geodesy, Special Publication No. 4, Paris, 1974.

Morgan, W.J., Convection Plumes in the Lower Mantle, Nature, **230**, 42-43, 1971.

Morgan, W.J., Deep Mantle Convection Plumes and Plate Motions, The American Association of Petroleum Geologists Bulletin, **56**, 203-213, 1972.

Naar, D. F., & Hey, R. N., Fast Rift Propagation Along the East Pacific Rise Near Easter Island. J. Geophys. Res., **91**, 3425-3438, 1986.

Naar, D.F. & Hey, R.N., Speed limit for oceanic transform faults, Geology, **17**, 420-422, 1989.

Naar, D. F., & Hey, R. N., Recent Pacific-Easter-Nazca Plate Motions. In: Evolution of Mid Ocean Ridges, Geophysical Monograph 57, IUGG Volume **8**, 1989.

Naar, D.F., Large-scale plate boundary reorganization at the Easter Microplate, Ph.D. Thesis, University of California, San Diego, 1990.

Naar, D.F. & Hey, R.N., Tectonic Evolution of the Easter Microplate, J. Geophys. Res., **96**, 7961-7993, 1991.

Naar, D.F., Martinez, F., Hey., R.N., Reed IV, T.B., Stein, S., Pito Rift: How a large-offset rift propagates, Mar. Geophys. Res., **13**,1991.

Natland, J.H., Effect of axial magma chambers beneath spreading centers on the compositions of basaltic rocks, In: Rosendahl, B.R., Hekinian, R, et al., Init. Repts. DSDP, **54** (US Govt. Printing Office, Washington), 833-850, 1980.

Okal, E.A., & Cazenave, A., A model for the plate tectonic evolution of the east-central Pacific based on SEASAT investigations, Earth Planet. Sci. Lett., **72**, 99-116, 1985.

Park, R.G., Geological Structures and Moving Plates, pub. Blackie & Son Ltd., Glasgow, 1988.

Parsons, B. & Sclater, J.G., An analysis of the variation of ocean floor bathymetry and heat flow with age, J. Geophys. Res., **82**, 803-827, 1977.

Patriat, P., Reconstruction de l'Èvolution du systËme de dorsales de l'ocean Indien par les mÈthodes de la CinÈmatique des Plaques, Ph.D. Thesis, 308 pp., Paris, France: Institut de Physique du Globe de Paris, 1987.

Pilger, R.H. & Handschumacher, D.W., The fixed-hotspot hypothesis and origin of the Easter-Sala y Gomez trace, Geol. Soc. Am. Bull., Part 1, **92**, 437-446, 1981.

Pollitz, F.F., Pliocene change in Pacific-plate motion, Nature, **320**, 738-741, 1986.

Poreda, R.J., Schilling, J.-G. & Craig, H., Helium isotope ratios in Easter microplate basalts, submitted to Earth Planet. Sci. Lett., 1991.

Purdy, G.M., The Eastern End of the Azores-Gibraltar Plate Boundary, Geophys. J. R. Astr. Soc., **43**, 973-1000, 1975.

Renard,V. & Allenou, J.-P., Sea Beam, multi-beam echo-sounding in "Jean Charcot" description, evaluation and first results, International Hydrographic Review, Monaco, **56**, 35-67, 1979.

Richter, F.M, & Parsons, B., The interaction of two scales of convection in the mantle, J. Geophys. Res., **80**, 2529-2541, 1975.

Rosendahl, B.R., et al., Evolution of Oceanic Crust 1. A Physical Model of the East Pacific Rise Crest Derived From Seismic Refraction DataJ. Geophys. Res., **81**, 5294-5304, 1976.

Rusby, R.I., Searle, R.C., Engeln, J., Hey, R.N., Naar, D. & Zukin, J., GLORIA and other surveys of the Easter and Juan Fernandez microplates, EOS Trans. AGU, **69**, 1428, 1988.

Rusby, R.I., I: A long-range side-scan sonar (GLORIA) survey of the Blanco Fracture Zone, N.E. Pacific, II: Geophysical and core data from King's Trough Flank area, N.E., Atlantic, B.Sc.(Hons) dissertation, University of St. Andrews, 1988.

Rusby, R.I, GLORIA and other geophysical studies of the tectonic pattern and history of the Easter Microplate, S.E. Pacific, In: Parson,L.M., Murton, B.J. & Browning, P. (eds) Ophiolites and their Modern Oceanic Analogues. Geological Society Special Publication No. 60, pp.000-000, 1992 (in press).

Rusby, R.I. & Searle, R.C., Intraplate Thrusting Near the Easter Microplate, submitted to Geology, 1991

Sanderson, D.J. & Marchini, W.R.D., Transpression, J. Struct. Geol., **6**, 449-458, 1984.

Saunders, M.R., Miles, P.R. & Storey, M.W., The Graphical Simulation of Tectonic Plate Motion, Computers & geosciences, **9**, No. 2, 245-254, 1983.

Schilling, J.-G. et al., Cruise Report R/V Endeavor, EN-113, 1984.

Schilling, J.-G., Thompson, G., Kingsley, R. & Humphris, S., Hotspot-migrating ridge interaction in the South Atlantic, Nature, **313**, 187-191, 1985.

Schilling, J.-G., Sigurdsson, H., Davis, A. N., and Hey, R. N., Easter microplate evolution, Nature, **317**, 325-331, 1985.

Schilling, J.-G., Mantle plume - migrating ridge interactions revisited: Implications on plume deflections, instabilities and upper-mantle flow, paper presented at: Intraplate volcanism: the Reunion Hot Spot meeting, organised by I.N.S.U, Universite de la Reunion and I.P.G.P., 1990.

Schouten, H. & McCamy, K., Filtering Magnetic Anomalies, J. Geophys. Res., **77**, 7089-7099, 1972.

Schouten, H., Klitgord, K. D., & Gallo, D. G., Roller-bearing microplate kinematics, submitted to Geology, 1990.

Searle, R.C. & Hey, R.N., Gloria Observations of the Propagating Rift at 95.5°W on the Cocos-Nazca Spreading Center, J. Geophys. Res., **88**, 6433-6447, 1983.

Searle, R.C., Rusby, R.I., Engeln, J., Hey, R.N., Zukin, J., Hunter, P.M., LeBas, T.P., Hoffman, H.-J. & Livermore, R., Comprehensive sonar imaging of the Easter microplate, Nature, **341**, 701-705, 1989.

Searle, R.C. et al., RRS Charles Darwin Cruise 35/88 13 October - 17 November 1988. GLORIA study of the Easter Microplate, East Pacific Rise, Institute of Ocenaographic Sciences, Deacon Laboratory Cruise Report No. 211, 1989b.

CORNAGLIA

Searle, R.C., Francheteau, J., Cavaglio, B. & Hofman, J., New observations on mid-plate volcanism and the tectonic history of the Pacific plate, Tahiti to Easter Microplate, In prep., 1990.

Searle, R.C., Le Bas, T.P., Mitchell, N.C., Somers, M.L., Parson, L.M. & Patriat, P.H., GLORIA Image Processing: The State of the Art, Mar. Geophys. Res., **12**, 21-39, 1990.

Sempere, J.C. & Macdonald, K.C., Overlapping spreading centers: Implications from crack growth simulation by the displacement discontinuity method, Tectonics, **5**, 151-163, 1986.

Sinton, J.M., Wilson, D.S., Christie, D.M., Hey, R.N., Delaney, J.R., Petrologic consequences of rift propagation on oceanic spreading ridges. Earth Planet. Sci. Lett., **62**, 193-207, 1983.

Somers, M.L., Carson, R.M., Revie, J.A., Edge, R.H., Barrow, B.J., and Andrews, A.G., GLORIA II - an improved long range sidescan sonar, paper presented at Oceanology International, Technical Session J, London, BPS Exhibitions, Ltd., pp16-24, 1978.

Souriau, A., Geoid anomalies over Gorringe Ridge, North Atlantic Ocean, Earth Planet. Sci. Lett., **68**, 101-114, 1984.

Stock, J. & Molnar, P., Uncertainties in the relative positions of the Australia, Antarctica, Lord Howe and Pacific plates since the Late Cretaceous, J. Geophys. Res., **87**, 4697-4714, 1982.

Stoffers, P., Hekinian, R., et al., Cruise Report SONNE 65- Midplate II, Hot Spot Volcanism in the Central Southpacific, Berichte - Reports, Geol.-Palaeont. Inst. Univ. Kiel., Nr. **40**, 1990.

Tamaki, K. & Larson, R.L., The Mesozoic tectonic history of the Magellan Microplate in the Western Central Pacific, J. Geophys. Res., **93**, 2857-2874, 1988.

Toomey, D.R., Purdy, G.M., Solomon, S.C. & Wilcock, W.S.D., The three-dimensional seismic velocity structure of the East Pacific Rise near latitude 9°30'N, Nature, 347, 639-645, 1990.

Vacquier, V., Geomagnetism in Marine Geology, pub. Elsevier, Amsterdam, Elsevier Oceanography Series, **6**, 1972.

Vera, E.E., Mutter, J.C., Buhl, P., Orcutt, J.A., Harding, A.J., Kappus, M.E., Detrick, R.S., & Brocher, T.M., The Structure of 0- to 0.2m.y.-old Oceanic Crust at 9°N on the East Pacific Rise From Expanded Spread Profiles, J. Geophys. Res, **95**, 15529-15556, 1990.

Watts, A.B., Gravity anomalies over oceanic rifts, In: Continental and Oceanic Rifts, ed. G. Palmason, AGU Geodynamics series, **8**, 99-106, 1982.

Weissel, J.K. & Anderson, R.N., Is there a Caroline Plate? Earth Planet. Sci. Lett., **41**, 143-158, 1978.

Wilke, M. & Lonsdale, P., In: Geometep 4 Bathymetry Report (Marchig et al.) Bundesanstalt fur Geowissenschaften und Rohstoffe, 1987.

Wilson, M., Igneous Petrogenesis A Global Tectonic Approach, pub. Unwin Hyman Ltd., London, 1989.

Winterer, E. L., & Sandwell, D. T., Evidence from en-echelon cross-grain ridges for tensional cracks in the Pacific, Nature, **329**, 534-537, 1987.

Woodhouse, J.H. & Dziewonski, A.M., Mapping the upper mantle:three-dimensional modeling of Earth structure by inversion of seismic waveforms, J. Geophys. Res., **89**, 5953-5986, 1984.

Zukin, J.H., Geophysical Study of the Easter Microplate, Doctoral Thesis, University of Paris VII, Institute de Physique du Globe de Paris, 1990.

Tapponier, P., Armijo, R., Manighetti, I. & Courtillot, V., Bookshelf Faulting and Horizontal Block Rotations between Overlapping Rifts in Southern Afar, Geophys. Res. Lett., **17**, -14, 1990.

Zukin, J.H. & Francheteau, J., A tectonic test of instantaneous kinematics of the Easter Microplate, Oceanologica Acta, in press, 1990a.

Zukin, J. & Francheteau, J., 3-D gravity and magnetic modeling at the Easter microplate, submitted to EOS Trans. AGU, **71**, 1636, 1990b.

Zukin, J.H. & Francheteau, J., A Tectonic Study of the Easter Microplate: The Northern and Southern Boundaries, submitted to J. Geophys. Res., 1990c.

Zukin, J.H. & Francheteau, J., Three-dimensional gravity and magnetic modelling of the Nazca-Easter propagating ridge-transfrom intersection near 23°S, 112°W, submitted to J. Geophys. Res., 1990d.

Zukin J.H. & Francheteau, J., Three-dimensional gravity and magnetic modeling of the Pacific-Easter propagating ridge-transform intersection near 26°30'S, 115°W, submitted to J. Geophys. Res., 1990e.

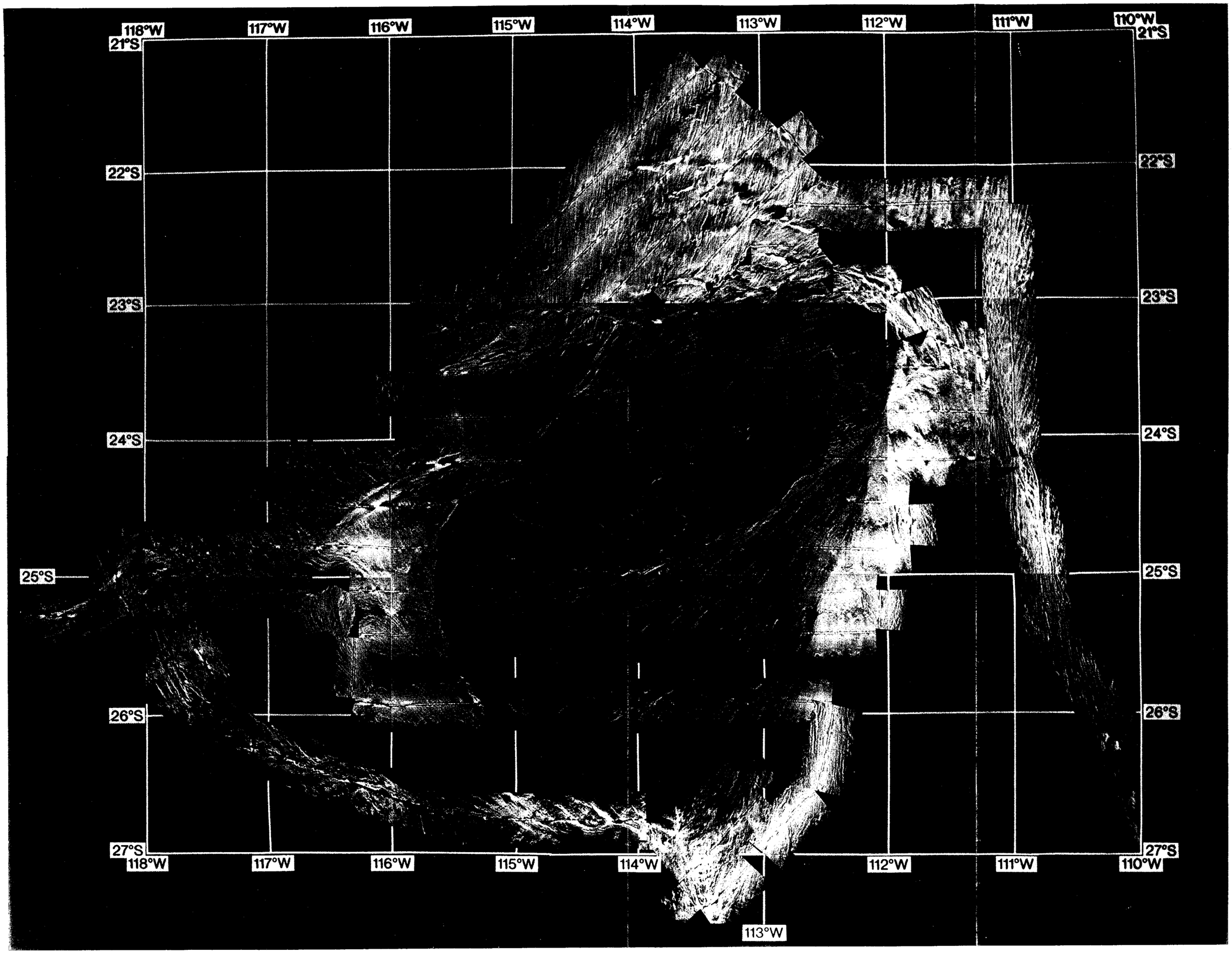
118°W
117°W
116°W
115°W
114°W
113°W
112°W
111°W
110°W
21°S
22°S
23°S
24°S
25°S
26°S
27°S

A

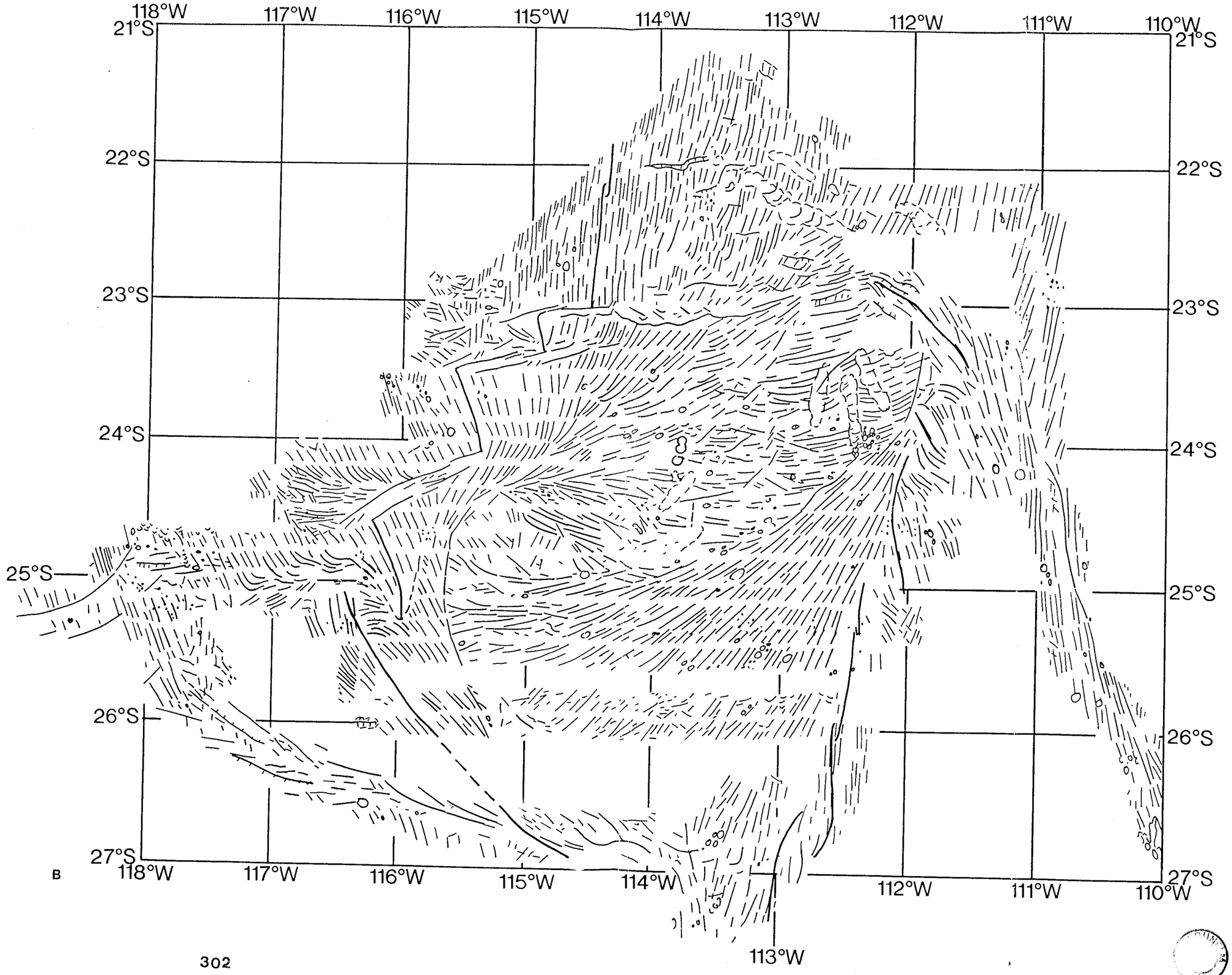
118°W
117°W
116°W
115°W
114°W
113°W
112°W
111°W
110°W
21°S
22°S
23°S
24°S
25°S
26°S
27°S

B